Exploring the faint source population at 15.7 GHz

Imogen Helen Whittam

Trinity Hall
University of Cambridge

June 2014

A dissertation submitted for the degree of Doctor of Philosophy

Contents

Summary

A sample of 296 faint (> 0.5 mJy) radio sources is selected from an area of the Tenth Cambridge (10C) survey at 15.7 GHz in the Lockman Hole. The 10C survey is complete to 0.5 mJy at 15.7 GHz and has a resolution of 30 arcsec. By matching this catalogue to several lower frequency surveys (e.g. including a deep GMRT survey at 610 MHz, a WSRT survey at 1.4 GHz, NVSS, FIRST and WENSS) I have investigated the radio spectral properties of the sources in this sample; all but 30 of the 10C sources are matched to a source in one or more of these surveys. I have found a significant increase in the proportion of flat spectrum sources at flux densities below $\approx$1 mJy – the median spectral index between 15.7 GHz and 610 MHz changes from 0.75 for flux densities greater than 1.5 mJy to 0.08 for flux densities less than 0.8 mJy. Thus a population of faint, flat spectrum sources is emerging at flux densities $\lesssim 1$ mJy.

The spectral index distribution of this sample of sources selected at 15.7 GHz is compared to those of two samples selected at 1.4 GHz from FIRST and NVSS. I find that there is a significant flat spectrum population present in the 10C sample which is missing from the samples selected at 1.4 GHz. The 10C sample is compared to a sample of sources selected from the SKADS Simulated Sky by Wilman et al.; this simulation fails to reproduce the observed spectral index distribution and significantly under predicts the number of sources in the faintest flux density bin. I conclude that it is likely that the observed faint, flat spectrum sources are a result of the cores of FRI sources becoming dominant at high frequencies, rather than the emergence of a new population of starforming galaxies.

I have used recent Very Long Baseline Interferometry (VLBI) observations by Middleberg et al. with a resolution of $\approx$ 10 mas to investigate the properties of these faint 10C sources in the Lockman Hole and find that 33 out of the 51 10C sources in the VLBI field (65 percent) are detected by the VLBI observations. The high brightness temperature of these VLBI-detected sources rules out the possibility that this faint, high frequency population is dominated by starbursting or starforming sources and indicates that they must be Active Galactic Nuclei.

The sources in the Lockman Hole 10C sample are matched to optical, infrared and X-ray data available in the field. A complete sample of 96 sources with high-resolution radio information available is defined; multi-wavelength counterparts are identified for 80 out of the

96 sources in this sample, for which is it possible to derive photometric redshifts. The radio-to-optical ratios of these sources show that the 10C sample is almost completely dominated by radio galaxies. 59/80 sources have luminosities greater than the FRI/FRII dividing luminosity.

The nature of these radio galaxies is investigated, using the multi-wavelength data to split the sources into high-excitation and low-excitation radio galaxies (HERGs and LERGs respectively). This shows that 34 sources are probably HERGs and 33 are probably LERGs, with 29 which could not be classified at this stage. The properties of these HERGs and LERGs are compared and I find that the HERGs tend to be found at higher redshifts, have flatter spectra, higher flux densities and smaller linear sizes.

This study is extended to lower flux densities using new, very deep, observations made with the Arcminute Microkelvin Imager in two fields. I use these observations to extend the 15.7-GHz source count down to 0.1 mJy, a factor of five deeper than the 10C count. These new deeper counts are consistent with the extrapolation of the fit to the 10C count, and do not show any evidence for an upturn. There is therefore no evidence for a new population (e.g. of starforming sources) contributing to the 15.7 GHz source count above 0.1 mJy, and suggesting that the faint, high-frequency population continues to be dominated by radio galaxies. Recent models of the high-frequency source counts under-predict the number of sources observed by a factor of two, consistent with the fact that these models fail to include the dominance of the cores and the faintness of the extended structures of these sources.

Declaration

This dissertation is the result of work carried out in the Cavendish Laboratory betweeen October 2010 and June 2014. The work in this thesis in my own except where stated otherwise. no part of this dissertation has been submitted for a degree, diploma or other qualification at this or any other university. The total length of this dissertation does not exceed 60,000 words.

Imogen Whittam, Cavendish Laboratory, June 2014

Acknowledgements

First, I'd like to thank my supervisor Julia for her constant time and support and for reading endless drafts of the thesis. Thank you to Dave for always being there to answer my many questions and for introducing me to the dark arts of AIPS (and, of course, for his help with the LaTeX!). I couldn't imagine a better pair to guide me through my PhD. Thank you to the other members of the AP group for providing stimulating tea and coffee conversations, and to Liz Waldram for her advice with the source counts. I'd also like to thank the members of the AMI consortium, particularly Clare and Michel, for providing me with the data for the last chapter and helping me explore the mysteries of AMI data.

Thanks must go to the Science and Technology Facilities Council for providing the studentship which has made this thesis possible. I'd also like to thank my college, Trinity Hall, for their invaluable support throughout my undergraduate and graduate studies. It has been a rewarding and stimulating community to be part of for the last eight years.

To my fellow students, Alex, Michel, Sam, Clare, Rena, Yvette, Tamela, Becky, Dave, Luke, Marion and many more, thank you for providing many entertaining lunchtimes and trips to the pub. I've learnt a lot from all of you, particularly the large gaps in my film-viewing history. Special thanks must go to Sam, for accompanying me in my descent into insanity in the last few months. Looks like we made it out the other side!

Thanks must go to everyone at CUYC, CURTC and THBC for providing many welcome distractions. I have spent many happy hours on some form of water or on the real tennis court, which as well as endless fun and many friends, has provided me with the space sometimes needed from my studies.

To Mum and Dad – thank you for your unconditional support throughout my many years of being a student, for the care packages and constant supplies of cake, and for always being at the end of the phone (or only a quick trip up the M11 away!). Thanks also to my brother Johannes for always being there for me.

Last, but by no means least, I'd like to thank my wonderful fiance Ian for making life so much fun, and for putting up with me, particularly during the last few months. I couldn't be more excited about the future...

Imogen Whittam
June 2014

CHAPTER 1

INTRODUCTION

This thesis explores the nature of the faint extragalactic radio source population selected at 15.7 GHz, using observations made with the Arcminute Microkelvin Imager (AMI; Zwart et al. 2008) in Cambridge. Early radio surveys were carried out at low frequencies due to the technology available at the time, e.g. the 3C survey at 178 MHz. As technology advanced and the need for higher resolution surveys increased, studies moved to higher frequencies, with a large number of surveys being conducted at GHz frequencies. As a result source counts, particularly at 1.4-GHz, are well constrained to flux densities below 0.1 mJy. The faint population at higher frequencies (tens of GHz), however, has been much less widely studied due to the increased time required to survey an area of sky to an equivalent depth at these frequencies[a].

High-frequency surveys have the potential to open a window on possible new classes of sources. They also provide further insights into the physics of sources detected in lower-frequency surveys, for example giving information on the break frequencies marking the transition from optically thick to optically thin regimes, and on any high-frequency steepening due to electron aging. Accurate knowledge of the high-frequency source population is also vital when removing contaminating foregrounds from Cosmic Microwave Background (CMB) maps.

In this introduction, I first discuss the different types of objects which make up the extragalactic source population, and outline how source counts of these objects can inform us about both the nature of these objects and the universe itself. I then summarise surveys of the high-frequency radio sky to date, discuss some recent models of this high-frequency pop-

[a]For a given instrument, the field of view scales with frequency as area $\propto \nu^{-2}$; combined with the typical synchrotron spectrum of a radio source ($S \propto \nu^{-0.7}$) this means the survey time scales as $\nu^{3.4}$

ulation and outline how multi-wavelength studies can provide valuable information about the high-frequency source population. Finally I summarise the contents of this thesis.

1.1 Extragalactic radio source types

Radio sources can be characterised by their radio spectra and angular sizes. The size of radio sources can vary widely, from very compact sources with linear sizes $\lesssim 1$ kpc to very extended sources spanning several Mpc. The radio spectra of many extragalactic sources can be described as power-laws, and characterised by their radio spectra index, α, where flux density S scales as frequency ν as $S \propto \nu^{-\alpha}$. Although the spectra of most radio sources are far more complex than a simple power-law, this provides a useful approximation. Sources are typically split into two main categories; 'steep' spectrum sources, with $\alpha > 0.5$, and 'flat' spectrum sources with $\alpha < 0.5$.

The majority of the radio emission observed at GHz-frequencies is synchrotron emission from relativistic electrons, although free–free emission can also play a role. Synchrotron radiation occurs when relativistic particles are accelerated in a magnetic field. For a single electron, the total radiated power scales as $\sin^2(\theta)\gamma^3\mathrm{B}^2$, where θ is the pitch angle between the electron velocity and the magnetic field, γ is the Lorentz factor of the electron, and B is the magnetic field strength. To get the full spectrum, this must be integrated over the total population of electrons, which can usually be described by a power-law distribution, $n_e(E) \propto E^{-p}$, where $n_e(E)$ is the number of electrons with energy E. This leads to a spectrum of the form $I_\nu \propto \nu^{-(p-1)/2}$, where I_ν is the specific intensity at frequency ν, which in practice usually gives a steep spectrum with spectral index of around 0.7.

In the optically thick regime, which occurs at lower frequencies or in dense regions, synchrotron self-absorption takes place. This causes a very different spectral shape, with a spectrum which rises with frequency and a spectral index of around -5/2. The synchrotron spectra in these two different regimes are demonstrated in Figure 1.1. Energy losses of relativistic electrons, known as spectral ageing (e.g. Kellermann 1966), can also be an important factor and produce spectral steepening (e.g. Carilli et al. 1991).

The objects associated with extragalactic radio sources range from massive elliptical galaxies with strong nuclear activity (active galactic nuclei or AGN) to starforming galaxies and normal spirals and ellipticals. In AGN the radio-emitting material originates in the nucleus, and at flux densities $S_{1.4\ \mathrm{GHz}} \gtrsim 1$ mJy the radio source population is dominated by such objects, referred to as radio galaxies or radio-loud AGN. However at lower flux densities starforming galaxies and a population of radio-quiet AGN make an increasingly important contribution (see Figure 1.2). Multi-frequency observations (radio to X-ray) are of great importance when

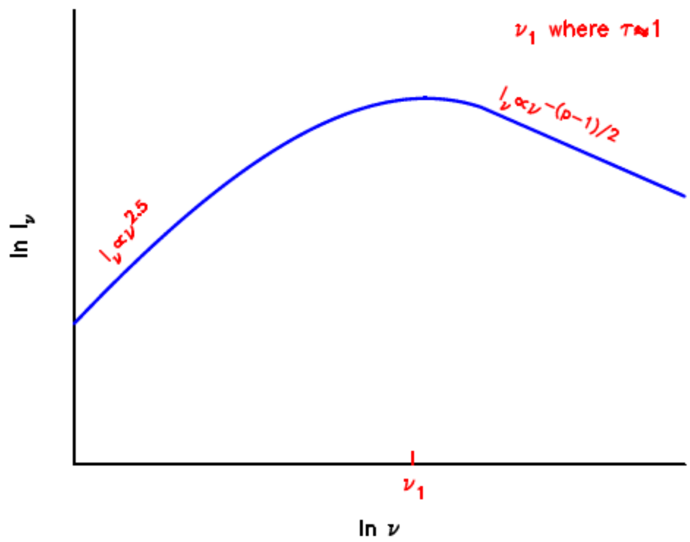

Figure 1.1: Typical synchrotron emission spectrum in the optically thick ($\nu < \nu_1$) and optically thin ($\nu > \nu_1$) regimes.

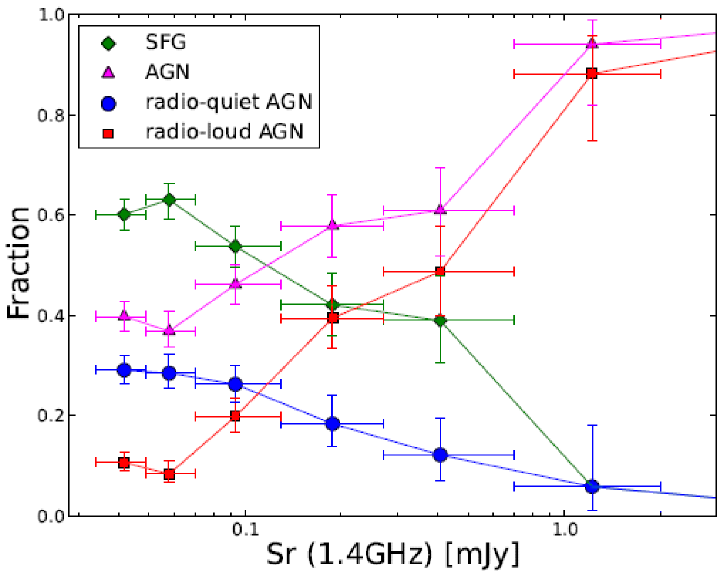

Figure 1.2: Relative fractions of different source-types as a function of flux density in the E-CDFS sample. Starforming galaxies (SFG) are shown by green diamonds, the total AGN population is shown together (magenta triangles), and split into radio-quiet and radio-loud populations (blue circles and red squares respectively). Taken from Padovani et al. (2014).

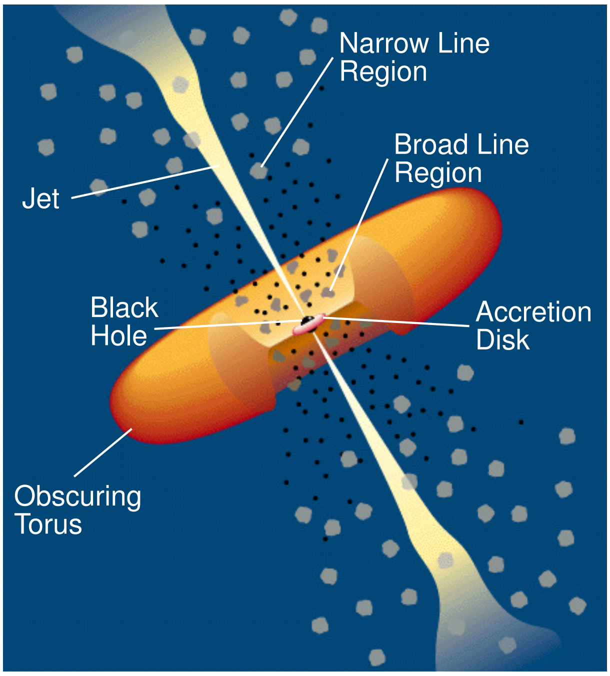

Figure 1.3: Schematic diagram of an Active Galactic Nucleus (AGN). From Urry & Padovani (1995).

distinguishing between these different types of objects.

1.1.1 Radio galaxies

At flux densities $S_{1.4\,\mathrm{GHz}} \gtrsim 1$ mJy the extragalactic radio sky is dominated by radio-loud AGN. Radio-loud AGN (often referred to as radio galaxies) have radio emission thousands of times more powerful than both their emission at other wavelengths and the emission of normal galaxies. These powerful sources are fuelled by accretion of matter onto the super-massive black hole at the centre of the galaxy, which results in the production of an accretion disc surrounded by a dusty torus, as shown in Figure 1.3. This produces characteristic emission lines in the optical spectrum, with broad emission lines produced in clouds of gas moving rapidly located close to the central black hole, and narrow emission lines produced in more slowly moving gas clouds further from the accretion disc (this is shown in Figure 1.3). The anisotropic structure of these objects means that the orientation of the object with respect to the observer dramatically changes the observed emission, and therefore results in different optical classifications. If the object is viewed face on (i.e. perpendicular to the jets), the dusty torus obscures the broad emission lines and the object is classified as a 'type II AGN'. If, however, the objects is viewed along the jet axis these broad lines are visible and it is classified as a 'type I AGN' (see Antonucci 1993 for a review). In both orientations narrow-line emission, which

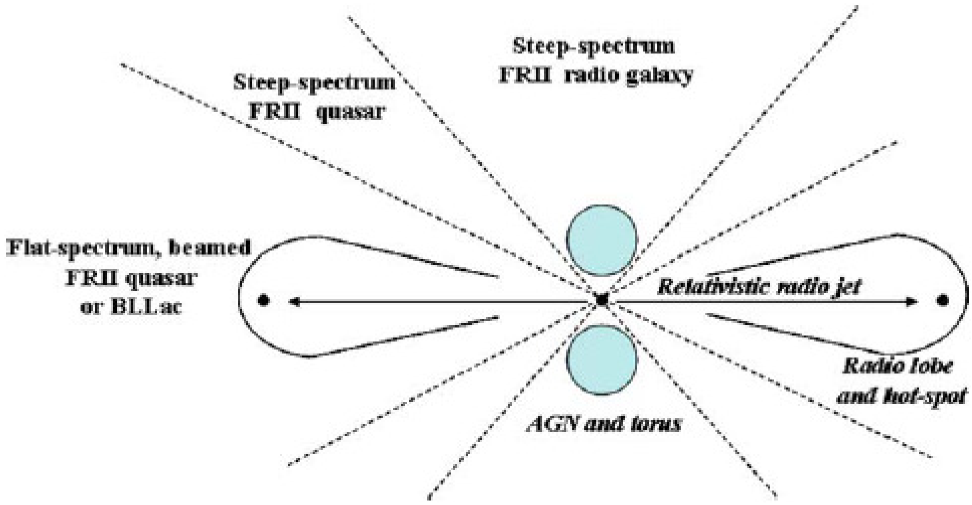

Figure 1.4: Unified scheme for FRII sources, from de Zotti et al. (2010).

originates further from the black hole, is visible.

More detailed studies (Hardcastle et al. 2007; Best & Heckman 2012) have suggested that radio galaxies accrete in two different modes; 'cold mode', which gives rise to the traditional picture of an AGN described above, and 'hot mode', where objects lack the expected optical emission lines and dusty torus (often referred to as high-excitation and low-excitation radio galaxies, HERGs and LERGs, respectively). This is explored in more detail in Chapters 6 and 7.

Radio galaxies typically produce bipolar relativistic jets which often extend far beyond the galaxy they originate from. This causes these sources to be also highly anisotropic in the radio, meaning that their appearance is strongly dependent on their axis of orientation with respect to the observer. Their radio emission can be modelled as a compact, flat spectrum core and two steep spectrum lobes, as shown in Figure 1.4. If a source is viewed perpendicular to the jet axis, the optically-thin, steep spectrum synchrotron emission from the twin jet-lobes is visible and will dominate the radio emission, so an extended, steep-spectrum source is observed. If, however, the source is viewed along the jet axis the Doppler-boosted base of the jet dominates the extended emission. The superposition of different self-absorbed components from the base of the jet causes it to have a flat spectrum, so the source appears compact and flat spectrum.

Fanaroff & Riley (1974) showed that there are two main types of radio-loud sources with distinct structures and luminosities; Fanaroff and Riley type I (FRI) sources are brightest along the jet axis and towards the core, while type II (FRII) sources have bright hot spots near the ends of their jets. There is a clear divide in luminosities between the two classes, with FRI sources typically having $L_{1.4\ \mathrm{GHz}} < 10^{24.5}$ W Hz^{-1}, while FRII sources have luminosities larger than

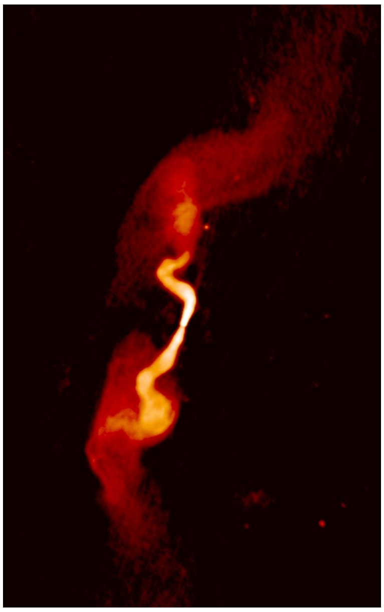
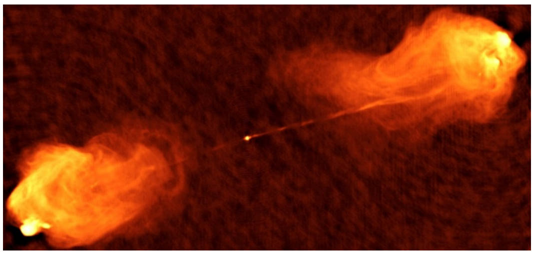

Figure 1.5: Examples of FRI (left) and FRII (right) sources (3C31 and Cygnus A respectively). Images taken with the Very Large Array (VLA) and courtesy of NRAO/AUI.

this dividing value. Example images of these two source types are shown in Figure 1.5. When viewed perpendicular to the jet axis, FRI and FRII sources appear as in Figure 1.5, however, when viewed along the jet axis their emission is dominated by the doppler boosted emission from the base of the jet, so the sources appear compact and flat spectrum and are referred to as BL Lacertae type objects (BL Lacs) and flat spectrum radio quasars (FSRQs) respectively (Urry & Padovani 1995).

There are several other types of radio-loud AGN; sources which have similar properties to FRI/II sources but on much smaller scales are known as compact steep-spectrum (CSS) sources and are thought to be younger versions of FRI/II sources. GHz-peaked spectrum (GPS) sources are compact and have spectra which rise at lower frequencies then peak at $\nu \gtrsim 1$ GHz. These sources are generally very compact, and the characteristic spectral shape is caused by synchrotron self-absorption, as discussed earlier in this section (see O'Dea 1998 for a review). Sources with $\alpha > 1.3$ are known as ultra steep spectrum (USS) sources and are often associated with very high redshift radio galaxies (e.g. de Zotti et al. 2010).

AGN which lack the powerful radio emission characteristic of radio-loud sources are known as 'radio quiet'. As these sources are not radio silent, they begin to make a significant contribution of the extragalactic radio sky below ~ 1 mJy (Jarvis & Rawlings 2004) as shown in Figure 1.2. Radio-quiet AGN tend to have steep spectra and no significant extended structure. It can be challenging to distinguish between radio-quiet AGN and starforming galaxies as both

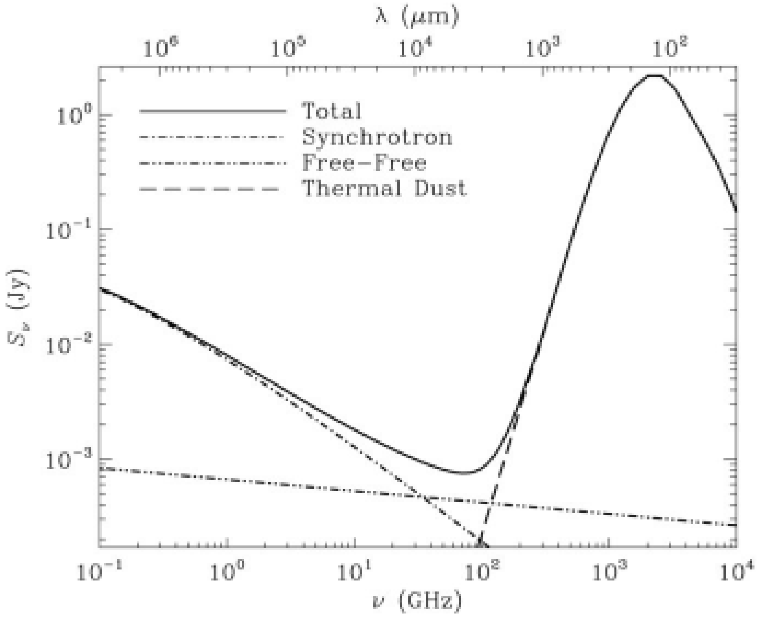

Figure 1.6: Typical radio and far-infrared spectrum of a normal galaxy. From Murphy (2009).

populations display similar radio properties. There has been some debate about the origin of the emission in radio-quiet AGN and there are two main possibilities; i) radio-quiet AGN are scaled-down versions of radio-loud AGN (e.g. Miller et al. 1993) or ii) the major contribution to their radio emission is starformation in the host galaxy (e.g. Sopp & Alexander 1991). Recent results from Padovani et al. (2011) support the second option – they found that the luminosity functions and cosmic evolution of the two types of AGN were significantly different, while they were indistinguishable for radio-quiet AGN and starforming galaxies.

1.1.2 Starforming galaxies

The radio emission from starforming galaxies (i.e. those not dominated by a central AGN) is dominated by synchrotron radiation from relativistic electrons accelerated by supernovae remnants, which has a steep spectrum ($\alpha \sim 0.75$). At higher frequencies ($\nu \gtrsim 30$) free–free emission from HII regions begins to play a role, causing the spectrum to flatten. Above $\nu \sim 200$ GHz thermal re-radiation of starlight by dust becomes dominant, causing the spectrum to rise steeply (Condon 1992) as shown in Figure 1.6. Starforming galaxies can be split into two classes; starburst galaxies, which are undergoing a period of intense starformation and are therefore more luminous, and the lower-luminosity quiescent starforming sources. Compact starbursts with high starformation rates tend to display flatter spectra than quiescent starforming sources due to increased free–free absorption (Murphy et al. 2013). At lower frequencies, it is known that starforming galaxies begin to make a significant contribution to the radio source population below $S_{1.4\ \mathrm{GHz}} \sim 1$ mJy and dominate below $S_{1.4\ \mathrm{GHz}} \sim 200$ µJy (e.g. Seymour et al. 2008; Smolčić et al. 2008; Padovani et al. 2009). However, their contribution to the population at higher frequencies is not known as observations at these flux densities have not been made at high frequencies.

1.1.3 Role of AGN in galaxy evolution

AGN activity can have a major impact on the formation and evolution of the host galaxy. For example, feedback from AGN plays a crucial role in quenching star formation in massive galaxies. There are two main mechanisms for this feedback: 'radiative mode' and 'radio mode' (Caputi 2014). Radiative mode feedback occurs during luminous AGN phases when the radiation pressure from the AGN drives a powerful, very energetic, nuclear wind which shocks and accelerates the inter-stellar medium of the host galaxy. This produces massive outflows which remove a substantial fraction of the available gas from the galaxy and therefore quench star formation (e.g. Hopkins et al. 2006). Radio mode feedback occurs when radio jets inject energy into the galaxy halo, preventing the halo gas from cooling. The halo gas therefore cannot replenish the galaxy with fresh fuel for further starformation. This causes most radio galaxies to be hosted by 'red and dead' elliptical galaxies, which are characterised by old stellar populations and very low star formation rates (e.g. Croton et al. 2006).

1.2 Source counts

Source counts of extragalactic radio sources can be used to investigate the cosmological evolution of the universe. Evidence from source counts was one of the key pieces of evidence in the Big Bang versus Steady State debate (Ryle & Clarke 1961), which was resolved when the discovery of the Cosmic Microwave Background (CMB) (Penzias & Wilson 1965) confirmed the Big Bang theory.

A non-expanding Euclidean Universe populated with non-evolving sources with number density n and luminosity L contains $N = 4\pi n d^3/3$ sources out to distance d. As the flux density (S) of each source is given by $S = L/4\pi d^2$, the number of sources brighter than flux density S should scale as $N(S) \propto S^{-3/2}$. The differential source count (i.e. the number of sources per unit area on the sky with flux densities in the interval $S \to S + dS$) should therefore scale as $dN/dS \propto S^{-5/2}$. Deviations from this simple result provide information about both the geometry of the universe and the evolution of radio sources. To aid the reader, source counts are often presented in Eucledian normalised form; i.e. the count in each bin is multiplied by $S^{-5/2}$, so $S^{-5/2} dN/dS$ is plotted as a function of flux densities.

Today, the main focus of the study of radio source counts is to understand the proportions of different types of source which make up our universe, and how these change with flux density. One of the main areas of recent debate has been the relative proportions of starforming galaxies and AGN, as understanding how these two populations evolve with time will be key to understanding how AGN and starformation processes interact.

Figure 1.7 shows differential source counts at 1.4 GHz and higher radio frequencies collated in the review by de Zotti et al. (2010). Note that there are many more observations at 1.4 GHz than at higher frequencies and the observations extend to much lower flux densities. This figure demonstrates that the 1.4-GHz counts show a flattening below $\sim$ 1 mJy, the cause of which has been the subject of much debate. It is now believed that this is because to both starforming galaxies and radio-quiet AGN are beginning to contribute significantly to the source population below $S_{1.4\ \mathrm{GHz}} \approx 1$ mJy (e.g. Seymour et al. 2008; Smolčić et al. 2008; Padovani et al. 2009). However, much less is known about the composition of the high-frequency source population at these faint flux densities, as it remains relatively unstudied. The observations of the high-frequency radio sky to date are summarised in the next section.

1.3 High-frequency radio surveys

As mentioned previously, there have been far fewer radio surveys at high frequencies than at lower radio frequencies due to the increased survey time required. However, in recent years several high-frequency surveys have been conducted and these are summarised in this section. The whole Southern sky has been surveyed by the Australia Telescope 20 GHz (AT20G) survey (Massardi et al. 2011a). This survey has a flux density limit of 40 mJy and is 93 percent complete above 100 mJy. Massardi et al. have made almost simultaneous observations at 4.8, 8.6 and 20 GHz for 3332 sources, which allows the spectral index distribution of this sample to be studied in detail.

Several high-frequency surveys have been carried out at higher flux densities and lower resolutions in conjunction with CMB experiments. Recent examples include the South Pole Telescope (SPT), which has surveyed 87 deg^2 at 150 and 200 GHz to flux density limits of 4.4 and 11 mJy at the two frequencies (Vieira et al. 2010), and the *Planck* satellite has surveyed the whole sky at 30, 44, 70, 100, 143 and 217 GHz to completeness levels of between 0.4 – 1 Jy, depending on the band (Planck Collaboration et al. 2011).

Waldram et al. (2003, 2010) carried out the Ninth Cambridge (9C) survey at 15 GHz using the Ryle Telescope. This was the first high-frequency survey to cover a significant portion of the sky, covering 520 deg^2 to a completeness limit of $\approx$ 25 mJy. A series of deeper regions were also observed (Waldram et al. 2010), with 115 deg^2 complete to $\approx$ 10 mJy and 29 deg^2

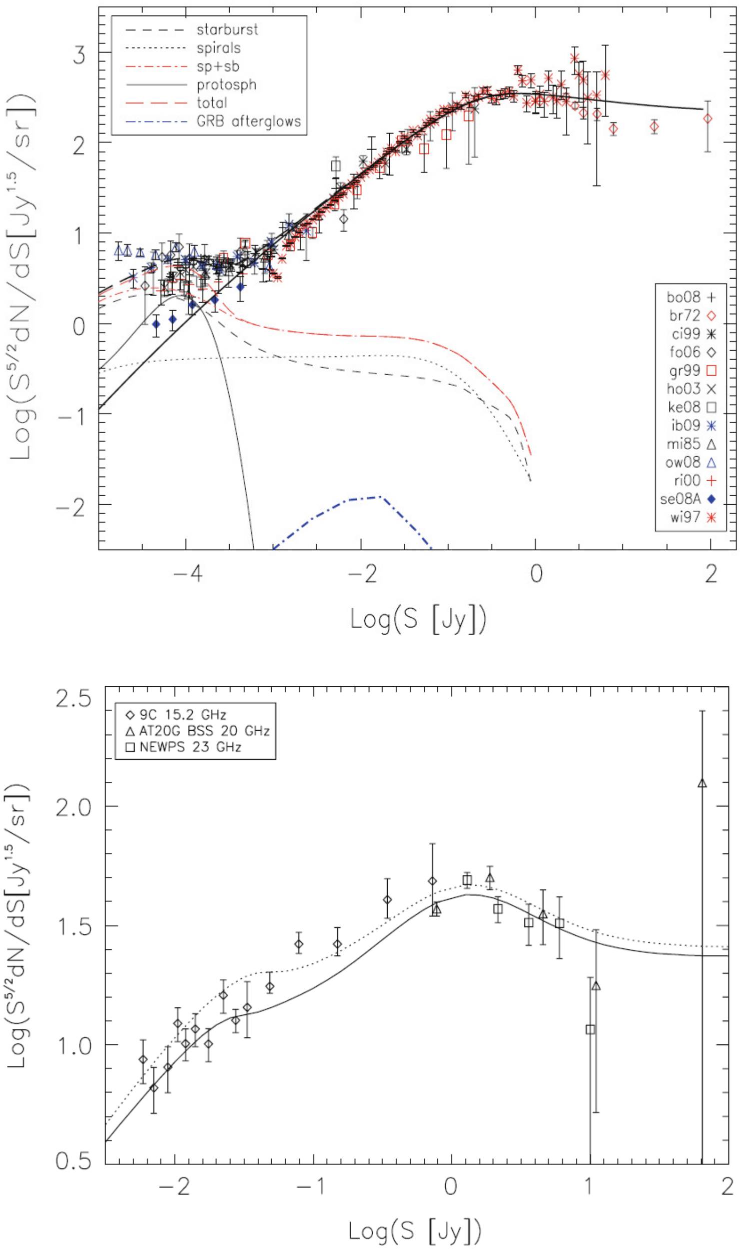

Figure 1.7: Collated differential source counts from observations at 1.4 GHz (top) and higher frequencies (bottom). From de Zotti et al. (2010). Top panel; the thick solid line is the contribution from radio-loud AGN predicted by the Massardi et al. (2010) model, the other lines are the predicted contributions from different source types as described in the legend. Bottom panel; lines indicate the de Zotti et al. (2005) model at 20 GHz (solid line) and 15 GHz (dotted line).

complete to $\approx$ 5.5 mJy. Bolton et al. (2004) followed up a sample of 9C sources with multi-frequency simultaneous observations to study the spectral shapes of the sources.

More recently, the Tenth Cambridge (10C) survey was observed with the Arcminute Microkelvin Imager (AMI; Zwart et al. 2008) at 15.7 GHz with a resolution of 30 arcsec. The observations, mapping and source extraction is described in Franzen et al. (2011) and the source counts and other results are presented in Davies et al. (2011). The 10C survey is complete to 1 mJy in ten different fields covering a total of $\approx$ 27 deg^2; a further $\approx$ 12 deg^2, contained within these fields, is complete to 0.5 mJy, making the 10C survey the deepest high-frequency radio survey published to date. This survey therefore enables us to study the faint source population at 15.7 GHz, a parameter space which has not been explored in any detail. The properties of samples of sources selected from the 10C survey are the subject of this thesis.

Recently, even deeper observations have been made in two of the 10C fields, enabling the study of the high-frequency source population to be extended by a factor of five in flux density. This work is presented in Chapter 8.

1.4 Models of the high-frequency source population

There have been several attempts to model the high-frequency radio sky, often extrapolating from lower frequencies. Early evolutionary models of radio sources (Dunlop & Peacock 1990; Jackson & Wall 1999; Toffolatti et al. 1998) successfully fitted the available data at frequencies $\lesssim$ 10 GHz down to flux densities of a few mJy. The model by Toffolatti et al. (1998) was particularly successful and was used to estimate the radio source contamination of the *Wilkinson Microwave Anisotropy Probe* (WMAP) CMB maps. More recently, de Zotti et al. (2005) produced a model of the radio source counts at frequencies $\gtrsim$ 5 GHz (up to 30 GHz) which successfully fitted the data available at the time. (Massardi et al. 2010 provide a complementary model of the source population at frequencies $\lesssim$ 5 GHz.) The de Zotti et al. model splits the sources into flat and steep spectrum populations, with the flat-spectrum population further divided into FSRQs and BL Lacs, and determines the epoch-dependent luminosity function for each population. Starforming galaxies, GPS sources and objects in the late stages of AGN evolution are also included in the model.

A more recent model by Tucci et al. (2011) used physically grounded models to extrapolate the 5-GHz source count, which is well known observationally, to higher frequencies. They focus on the spectral behaviour of blazars and compare three different models which treat flat spectrum sources differently. This scheme is successful at high flux densities but does not accurately reproduce the observed 15 GHz source count below $\approx$ 10 mJy, as demonstrated in Figure 1.8. The number of sources is significantly underestimated (by a factor of $\sim$ 2), indicat-

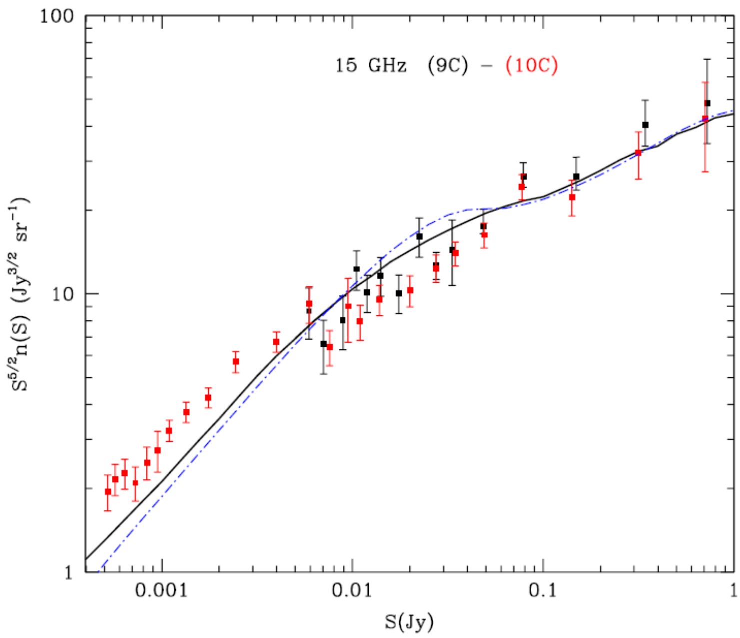

Figure 1.8: Predicted and observed differential source counts at 15 GHz (Euclidean normalised). The blue dot-dashed line shows the de Zotti et al. (2005) model and the black solid line shows the Tucci et al. (2011) model. The points show the 9C (black) and 10C (red) counts. Taken from Tucci et al. (2011).

ing that the properties of these sources are not well understood, largely due to the complexity and diversity of the high-frequency spectra of individual sources.

Wilman et al. (2008, 2010) have produced a semi empirical simulation of the extragalactic radio continuum sky (the SKADS Simulated Sky; S^3). This simulation serves two purposes (Norris et al. 2013); i) it is an approximation of the real radio sky and can therefore be used to optimise the design of telescopes and future radio surveys, and ii) it represents the 'best knowledge' of the radio sky to date and can therefore be used to test models of radio source evolution. The simulation splits the radio sources into separate populations;

- radio-quiet AGNs,
- FRI sources,
- FRII sources,
- starforming galaxies, which are then split into quiescent starforming and starbursting galaxies.

The observed (and extrapolated) radio continuum luminosity functions are used to generate a catalogue of $\approx$ 320 million simulated sources. This simulation covers 20×20 deg^2 out to a cosmological redshift of $z = 20$ and down to a flux density of 10 nJy at 151, 610 MHz, 1.4, 4.86 and 18 GHz. This simulation is discussed further and compared to the 10C sample later in this thesis.

Although good progress has been made in recent years when modelling extragalactic radio sources, there is still no model which accurately describes the high-frequency radio source population down to low flux densities. To understand the nature of the faint, high-frequency population and constrain the models better, a multi-frequency study is required. In this thesis I describe just such a study, examining the radio properties of a sub-sample of 10C sources at a wide range of wavelengths.

1.5 Multi-wavelength studies

Although they provide valuable insights into the source population, radio surveys alone do not provide sufficient information to fully characterise the extragalactic sky. For example, it is generally not possible to distinguish between radio-quiet AGN and starforming galaxies using radio surveys alone. Data at other wavelengths is therefore vital to provide a better understanding of the objects which make up our universe. Some examples of the complementary information which can be provided by surveys at a range of other wavelengths are given below. The specific examples used in this thesis are described in more detail in Chapter 6.

Radio-loud AGN can easily be distinguished from radio-quiet AGN and starforming galaxies using far-infrared or optical data, as for the same optical or infrared magnitude, radio-loud AGN have significantly larger radio powers (usually by more than two orders of magnitude) than either radio-quiet AGN or starforming galaxies. For example, either the radio-to-optical ratio R, where $R = S_{1.4\ \mathrm{GHz}} \times 10^{0.4(m-12.5)}$ (where m is the optical magnitude, typically in the i-band) or the q_{IR} parameter, where $q_{\mathrm{IR}} = \log(S_{\mathrm{IR}}/S_{1.4\ \mathrm{GHz}})$ (where S_{IR} is the infrared flux density) can be used to classify sources as radio loud. Radio-quiet AGN can be separated from starforming galaxies using mid-infrared observations; the dusty torus which surrounds an AGN produces a characteristic signal in the mid-infrared from warm dust emission, meaning that mid-infrared colour–colour diagrams can efficiently separate AGN from starforming galaxies (Lacy et al. 2004). X-ray power, emission lines in the optical spectra and Polycyclic Aromatic Hydrocarbon (PAH) features can also be using to distinguish different source types.

Recent work in the Extended *Chandra* Deep Field-South (E-CDFS) has used data at a range of wavelengths (including optical, mid- and far-infrared and X-ray) to investigate the properties of radio sources with $S_{1.4\mathrm{GHz}} > 30$ μJy (Bonzini et al. 2012; Vattakunnel et al. 2012; Bonzini et al. 2013, summarised in Padovani et al. 2014). The relative proportions of different source-types as a function of flux density resulting from this study are shown in Figure 1.2, which shows our current best understanding of the nature of the faint radio sky at 1.4 GHz. The composition of the faint radio sky at higher frequencies, however, remains unconstrained and, as mentioned in Section 1.4, models extrapolated from lower frequencies fail to accurately reproduce the observed source properties. This demonstrates the need for a comprehensive multi-wavelength study of the faint, high-frequency radio sky.

As well as helping to identify source type, multi-wavelength data can also provide valuable information about the host galaxies of radio sources. For example, Bonzini et al. (2013) found that radio-loud AGN are found in red elliptical galaxies which have often undergone recent mergers, while radio-quiet AGN are almost exclusively hosted by bluer spiral galaxies. This supports the suggestions that radio-quiet and radio-loud AGN are intrinsically different objects.

The availability of data at a range of optical and infra-red wavelengths allows photometric redshifts to be estimated. Photometric redshifts are important if the source populations from deep surveys are to be characterised, as the large number of optically faint objects detected in these surveys makes acquiring spectroscopic redshifts for the whole sample unfeasible. Significant improvements have been made in the methods used to estimate photometric redshifts in recent years and there are several publicly available photometric redshift codes, such as EAZY (Brammer et al. 2008), Le Phare (Arnouts & Ilbert 2011), HyperZ (Bolzonella et al. 2011) and ZEBRA (Feldmann et al. 2006). Six different codes are discussed and compared in Abdalla et al. (2011).

For starforming galaxies, which are the dominant population in optical and infrared surveys, these codes produce reliable results, typically with catastrophic outliers of only ~ 5 percent. However, producing reliable results for AGN, which dominate radio-selected surveys, presents a number of challenges (Salvato et al. 2011). Firstly the SEDs of powerful AGN are dominated by power-laws, meaning that their shape produces a colour-redshift degeneracy (complete and deep multi-wavelength coverage is needed to break this degeneracy). Secondly, in most cases, the galaxy which hosts the AGN contributes to the global SED of the source. There are a large number of possible combinations of different type of host galaxies and AGN, which can combine in a continuous variation of ratios, resulting in large degeneracies between templates and redshifts. Thirdly, AGNs are variable, so it is difficult to combine photometric data from different epochs. Salvato et al. (2011) have had some success by identifying AGN through a combination of X-ray data, optical morphology and variability information, and then fitting a separate template library to those sources identified as hosting an AGN. In this work, Le Phare photometric code is used to estimate the photometric redshifts of a sample of 10C sources, as described in Chapter 5.

1.6 The Lockman Hole

The Lockman Hole is a region of the sky centred near $10^{\mathrm{h}}45^{\mathrm{m}}$, $+58°$ (J2000 coordinates, which are used throughout this work) with exceptionally low HI column density (Lockman et al.

1986). The low infrared background (0.38 MJy sr^{-1} at 100 μm; Lonsdale et al. 2003) in this area of the sky makes it ideal for deep extragalactic infrared observations. As a result, as part of the *Spitzer* Wide-area Infrared Extragalactic survey (SWIRE; Lonsdale et al. 2003) sensitive infrared observations of ≈ 14 deg^2 of the Lockman Hole area have been made. The availability of deep infrared observations in the Lockman Hole has triggered deep observing campaigns at optical, X-ray and radio wavelengths (e.g. Biggs & Ivison 2006; Brunner et al. 2008; Ciliegi et al. 2003; Ishisaki et al. 2001; Lonsdale et al. 2003; Mauduit et al. 2012; Wright et al. 2010) These will be discussed in more detail later in this thesis.

The availability of data at such a wide range of frequencies makes the Lockman Hole a particularly good area for study. The properties of a sample of sources selected from the 10C survey in the Lockman Hole are the subject of the bulk of this thesis.

1.7 Thesis outline

In this chapter I have outlined the need for a multi-frequency study of the faint, high-frequency radio sky. The rest of this thesis is laid out as follows.

Chapter 2 describes the radio properties of a sample of 296 sources selected from the 10C survey in the Lockman Hole.

Chapter 3 analyses the radio properties of these sources, focusing on the variation in spectral index with flux density. These properties are then compared to a sample selected at 1.4 GHz and to the SKA Simulated Sky.

Chapter 4 uses recent very long baseline interferometry (VLBI) observations of part of the Lockman Hole to further investigate the nature of 10C sources.

Chapter 5 outlines the multi-wavelength data available in the Lockman Hole and computes photometric redshifts for a sub-sample of 10C sources. Radio-to-optical light ratios are calculated, and the properties of the sample are discussed in light of the redshift information.

Chapter 6 outlines how the data described in Chapter 5 is used to split the 10C sources into high-excitation and low-excitation radio galaxies.

Chapter 7 presents the properties of the different sources types identified in Chapter 6, then compares the properties of the 10C sample to other studies.

Chapter 8 outlines results from new, very deep, 15.7-GHz observations in two 10C fields. These are the deepest high-frequency radio observations to date.

Chapter 9 presents the conclusions from this work and describes some possible extensions to this project.

CHAPTER 2

DERIVING THE RADIO PROPERTIES OF 10C SOURCES IN THE LOCKMAN HOLE

As discussed in Chapter 1, the availability of data at such a wide range of frequencies makes the Lockman Hole a particularly good area for study. In this chapter, the radio properties of sources detected in the 10C survey at 15.7 GHz in the Lockman Hole are investigated. The 10C data are combined with those at lower frequencies, such as deep surveys at 610 MHz made with the Giant Meterwave Radio Telescope (GMRT; Garn et al. 2008, 2010) and at 1.4 GHz made with the Westerbork Synthesis Radio Telescope (WSRT; Guglielmino et al. 2012), along with other available data over a range of radio frequencies. The surveys used are described in more detail in Section 2.1 along with the process for matching them to the 10C catalogue. Section 2.2 describes how the parameters of the 10C sources are investigated using these surveys, including calculating the radio spectral indices and investigating the extent of the radio emission. The data are analysed and the radio properties of the 10C sources are discussed in Chapter 3. Optical identifications, redshift estimates and detailed discussions of the source types will be presented later in this thesis.

2.1 Sample selection

2.1.1 Surveys used

The 10C radio survey at 15.7 GHz was made with the Arcminute Microkelvin Imager (AMI; Zwart et al. 2008) with a beam size of 30 arcsec. It covers $\approx$27 deg^2 complete to 1 mJy and $\approx$12 deg^2 complete to 0.5 mJy across ten different fields; a full description of the 10C survey and the source catalogue can be found in Franzen et al. (2011) and Davies et al. (2011). Two of the fields are in the Lockman Hole, covering an area of 4.64 deg^2 (see Figure 2.1) and detecting a total of 299 sources.

To investigate the properties of these 10C sources I have matched the 10C catalogue to other lower-frequency, but usually higher-resolution, radio catalogues as detailed below. This not only enables me to determine the radio spectral properties of the sources but also allows me to investigate the extent and structure of the radio sources in more detail. The greater positional accuracy of these higher-resolution catalogues is also vital for finding the counterparts of the 10C sources at optical and infrared wavelengths; this is explored further in Chapters 5, 6 and 7. The other radio surveys of the Lockman Hole used in this work are listed in Table 2.1 and briefly described below.

A series of deep observations at 610 MHz made with the GMRT covers the whole 10C Lockman Hole area except for a small corner of the field containing five 10C sources (Figure 2.1). The GMRT image has an rms noise of ≈60 μJy per beam in the central area (see Garn et al. 2008, 2010, for details of the data reduction and source extraction). This deep image and the catalogue derived from it are used here.

A deep survey at 1.4 GHz carried out with the WSRT overlaps a large portion of the 10C survey (Figure 2.1) in the Lockman Hole (Guglielmino et al. 2012). The rms noise in the centre of the map is ≈11 μJy; this map and the associated source catalogue are used in this study.

I also make use of several other catalogues and surveys covering the Lockman Hole region. The Faint Images of the Radio Sky at Twenty cm (FIRST; White et al. 1997), NRAO VLA Sky Survey (NVSS; Condon et al. 1998) and Westerbork Northern Sky Survey (WENSS; Rengelink et al. 1997) cover the whole area. There are also several deep observations made with the VLA within the Lockman Hole area: Owen et al. (2009) at 324 MHz (OMK2009) and Biggs & Ivison (2006) and Owen & Morrison (2008) at 1.4 GHz (BI2006 and OM2008). The locations of these surveys are shown in Figure 2.1 and are summarised in Table 2.1.

Sixteen 10C sources in the Lockman Hole are labelled in the 10C catalogue as part of a 'group' (see Davies et al. 2011 for details) – in this case consisting of eight pairs. Contour maps of these eight pairs were examined by eye, along with images of their counterparts in FIRST and/or GMRT. For three of these pairs, there is evidence of structure connecting the two components, so it was decided to combine the two components into one source (an example of one such source is shown in Figure 2.2). The positions listed in the catalogue for these three pairs is the point mid-way between the two components. For the remaining five pairs the components were left as separate sources. This leaves a total of 296 sources in the 10C sample.

These 296 sources, selected at 15.7 GHz, are the subject of this chapter. A subsample of 89

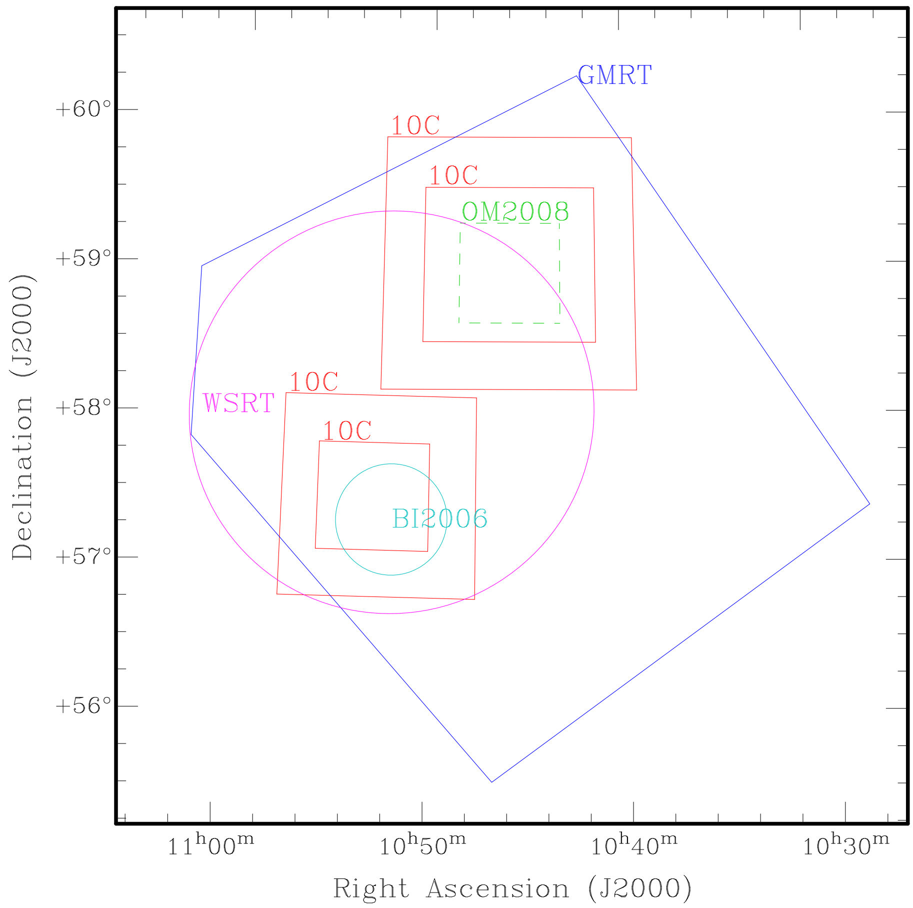

Figure 2.1: The deep radio surveys in the Lockman Hole region. The two larger (red) squares show the shallow region of the 10C survey fields, complete to 1 mJy. The two smaller squares contained within the larger squares are the deep 10C regions, complete to 0.5 mJy. The pentagon (dark blue) shows the GMRT survey area, the dashed square (green) shows the OM2008 survey area, the smaller circle (pale blue) shows the BI2006 survey area and the larger circle (pink) shows the WSRT survey area. FIRST, NVSS and WENSS are not shown as they cover the whole region. See Table 2.1 for details of the different surveys shown.

sources, with flux densities greater than 0.5 mJy, selected from the region complete to 0.5 mJy is defined as ‘Sample A’. A second subsample of 118 sources, ‘Sample B’, which has some overlap with Sample A, forms a sample complete to 1 mJy. A further sample, ‘Sample W’, is defined in Chapter 5 and used when matching to optical and infrared catalogues. Table 2.2 contains a summary of the different subsamples used in this thesis.

2.1.2 Matching the radio catalogues

2.1.2.1 Choosing a match radius

The TOPCAT software package[a] was used to match the catalogues. The match radius was chosen so as to maximise the number of real associations and avoid false matches. The error in the 10C positions is ≈ 6 arcsec, which is larger than the errors in the other catalogues used here (for example the error in the GMRT positions is $\lesssim 1$ arcsec), so the errors in the 10C positions tend to dominate. Here I describe the process by which I chose a suitable match radius and assessed the probability of genuine and random matches for the 10C and GMRT catalogues. To create a random distribution of sources the 10C sources were shifted by 5 arcmin in declination. Both this shifted catalogue and the true 10C catalogue were then matched to the GMRT catalogue and the angular separation between a shifted or true 10C source and its nearest GMRT source was recorded. Once a shifted or true 10C source was matched to a source in the GMRT catalogue no further matches were sought for that source. The matches were then binned according to their separation for both the true and shifted sources. The resulting distribution is shown in Figure 2.3. It can be seen that beyond 15 arcsec the numbers of random matches become comparable for both the true and shifted catalogues; thus 15 arcsec was chosen as the match radius. The number of matches with the shifted distribution within a separation of 15 arcsec is 4 (out of 296 sources), meaning the probability of a random match within 15 arcsec is $\approx$1.5 percent of the total number of sources being matched. 15 arcsec corresponds to 2.5σ, where σ is the typical error in the 10C source positions, suggesting that the matching is limited by the error in the 10C source positions.

This process was repeated for the other catalogues and it was decided that 15 arcsec was a suitable match radius to use when matching each of the catalogues to the 10C catalogue. The number of random matches within 15 arcsec for each catalogue is shown in Table 2.3.

2.1.2.2 Results of the matching

A summary of the matching between the 10C sources and the other radio catalogues is shown in Table 2.3. In total, 266 out of the 296 10C sources are detected at at least one other wavelength. Table 2.4 summarises the number of sources with matches in more than one other catalogue.

For the 30 10C sources with no other detections, upper limits on the flux density at 610 MHz from GMRT and at 1.4 GHz from WSRT and FIRST can be used, as described in Section 2.2.1. All of the 10C sources with no other detections have a low flux density (see Figure 2.4), with the majority below 1 mJy and all below 2 mJy. All of the 10C sources in the regions with deep VLA observations available (BI2006 and OM2008) are detected, and all 10C sources are

[a] see: http://www.starlink.ac.uk/topcat/

Table 2.1: Radio catalogues in the Lockman Hole

Catalogue	Reference(s)	Epoch of observation	Frequency /GHz	Beam size /arcsec	rms noise /mJy	Area covered /deg^2
10C – shallow	Franzen et al. (2011); Davies et al. (2011)	Aug 2008 – June 2010	15.7	30	0.1	4.64 (deep areas included)
10C – deep	Franzen et al. (2011); Davies et al. (2011)	Aug 2008 – June 2010	15.7	30	0.05	1.73
GMRT	Garn et al. (2008); Garn et al. (2010)	Jul 2004 – Oct 2006	0.610	6×5	0.06	13
WSRT	Guglielmino et al. (2012)	Dec 2006 – Jun 2007	1.4	11×9	0.011	6.6
OM2008	Owen & Morrison (2008)	Dec 2001 – Jan 2004	1.4	1.6	0.0027	0.011
OMK2009	Owen et al. (2009)	Feb 2006 – Jan 2007	0.324	6	0.07	3.14
BI2006	Biggs & Ivison (2006)	Jan 2001 – Mar 2002	1.4	1.3	0.0046	0.089
FIRST	White et al. (1997)	1997 – 2002	1.4	5	0.15	Whole area
NVSS	Condon et al. (1998)	1997	1.4	45	0.45	Whole area
WENSS	Rengelink et al. (1997)	1991 – 1996	0.325	54	3.6	Whole area

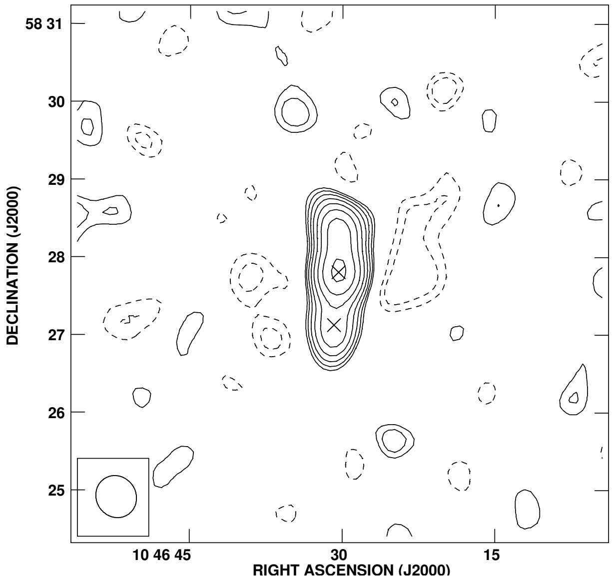

Figure 2.2: 15.7-GHz image of an example extended source listed as two components in the 10C catalogue. The contours are plotted at $(\pm 2\sqrt{2^n}, n = 0, 1 \ldots 7) \times 0.136$ mJy. The crosses mark the positions of the two sources in the 10C catalogue. There are three such pairs of sources in the 10C Lockman Hole fields; in each case the flux densities of the separate components are combined.

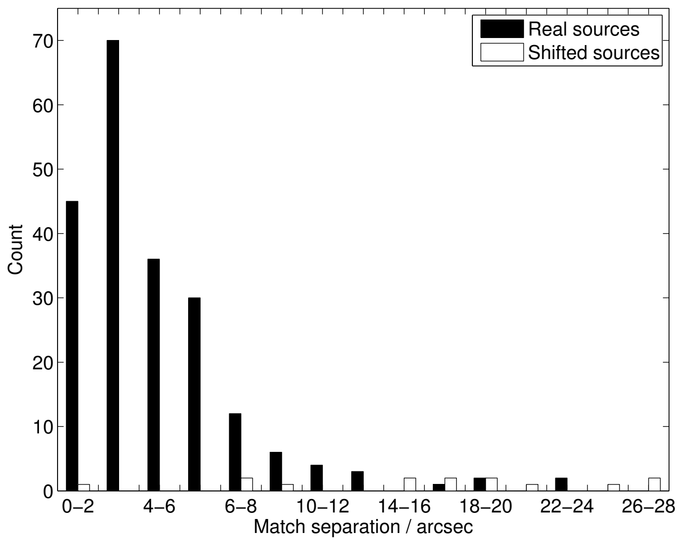

Figure 2.3: The number of matches with a given separation between the 10C and GMRT catalogues for the true and shifted distribution of 10C sources. Beyond 15 arcsec the number of true and shifted matches becomes comparable so 15 arcsec is chosen as the match radius.

Table 2.2: The different subsamples in the Lockman Hole used in this thesis.

Sample	Description	Number of sources
All sources	All sources detected at 15.7 GHz. Includes sources below 0.5 mJy.	296
Sample A	Complete to 0.5 mJy at 15.7 GHz	89
Sample B	Complete to 1.0 mJy at 15.7 GHz	118
Sample W	Sources in Sample A or B in either the WSRT deep area or the BI2006 or OM2008 survey areas. (Sample used when matching to multi-wavelength catalogues. See Chapter 5 for details.)	96

Table 2.3: A summary of the matching between the 10C catalogue and other radio catalogues in the Lockman Hole. Column (2) shows the number of matches to 10C sources within 15 arcsec and column (3) shows the number of 10C sources in the survey area. Column (4) shows the number of random matches within 15 arcsec, i.e. the number of matches to the shifted 10C sources.

Catalogue (1)	Number of matches (2)	Number of 10C sources (3)	Number of random matches (4)
GMRT	205	291	8
WSRT	160	182	10
FIRST	196	296	0
NVSS	166	296	0
WENSS	86	296	6
OM2008	27	27	2
OMK2009	116	156	2
BI2006	35	35	3

Table 2.4: A summary of the number of 10C sources with multi-frequency matches.

Number of matches	Number of sources
10C only	30
One match only	46
Two matches	36
Three matches	27
Four matches	55
Five matches	78
Six matches	23
Seven matches	1

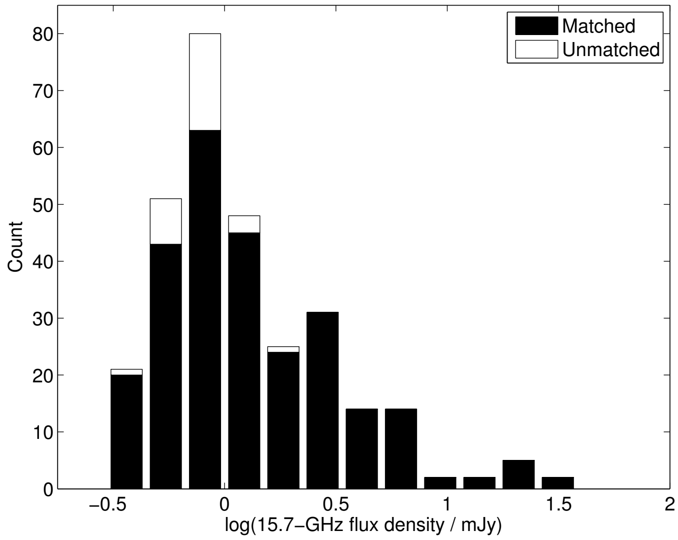

Figure 2.4: The distribution of 10C sources with and without associations in the other radio catalogues as a function of flux density. This diagram contains all 296 sources detected, some of which are below the completeness levels of the 10C survey. All of the 10C sources with no matches have a flux density below 2 mJy.

detected in the deeper observations made in Chapter 8, which shows that the 10C catalogue has a very low false-detection rate and the 30 undetected 10C sources are therefore likely to be real.

2.2 Deriving the source parameters

2.2.1 Flux density values

2.2.1.1 GMRT

The large difference in resolution between the 10C (beam size 30 arcsec) and GMRT (beam size 6 arcsec) observations means that care must be taken when comparing flux densities. As illustrated in Figure 2.5, many 10C sources are extended or resolved into multiple components at 610 MHz. The components of such sources will be listed as separate entries in the GMRT catalogue. In addition, for some of the sources in the GMRT catalogue there may be extended low brightness structure too faint to be seen in the high resolution images. In order to reduce these problems, contour plots of all the GMRT sources which matched to a source in the 10C catalogue (using a 15 arcsec match radius as described in Section 2.1.2.1) were examined by eye. For the 50 sources which appeared multiple or extended, the GMRT images were convolved in AIPS[b] to a 30-arcsec gaussian to create an image of comparable resolution to the

[b]Astronomical Image Processing System, see http://www.aips.nrao.edu/.

10C data (see Figure 2.5). The total 610-MHz flux density of each source (which had already been matched to a 10C source from the higher resolution image) was then estimated from the smoothed GMRT image. The integrated 610-MHz flux densities were estimated by fitting a Gaussian using the AIPS task JMFIT. In the few cases where JMFIT did not converge (due to the presence of another bright source in the subimage) the integrated flux density was found by hand using the AIPS task TVSTAT.

For the 84 10C sources for which a counterpart was not present in the full resolution GMRT catalogue the GMRT images were used to place an upper limit on the source flux density at 610 MHz. A sub image of 2.5 arcmin was extracted and smoothed (as described in above) to check for any large scale structure which might have been resolved out in the original image. In eight cases a source could be seen in the smoothed GMRT images with a peak within 15 arcsec of the 10C source position; for these sources a value for the integrated flux density was obtained manually using TVSTAT. For the remaining sources, the upper limit on the flux density was taken to be three times the noise in this smoothed image. It was not possible to get any information about the flux density at 610 MHz for the five 10C sources outside the GMRT area so these sources are excluded from all discussions relating to 610-MHz data.

2.2.1.2 NVSS

NVSS has a resolution comparable to the 10C survey so the flux densities can be directly compared without any problems caused by resolution differences. Because of this, it is useful to be able to calculate spectral indices using NVSS and 10C values only, so upper limits were found for all sources not matched in the NVSS catalogue despite the fact that some of these sources have a counterpart in one of the deeper 1.4-GHz surveys used. NVSS images of all 10C sources without a match in the NVSS catalogue were examined to see if there was a source present which was below the catalogue limit and for the few sources where this was the case, the flux density of the NVSS source was found manually using the AIPS task TVSTAT. For the remaining unmatched sources, an upper limit of three times the local noise in the NVSS image was placed on the flux density.

2.2.1.3 WSRT and FIRST

As the WSRT synthesised beam (12 arcsec) is smaller than the 10C synthesised beam (30 arcsec), several sources were resolved into multiple components in the WSRT catalogue but appeared as a single component in the 10C catalogue. In order to reduce the effects of resolution when comparing the flux densities, sub-images of the WSRT image at the position of each 10C source were examined by eye; for those sources where there were multiple WSRT

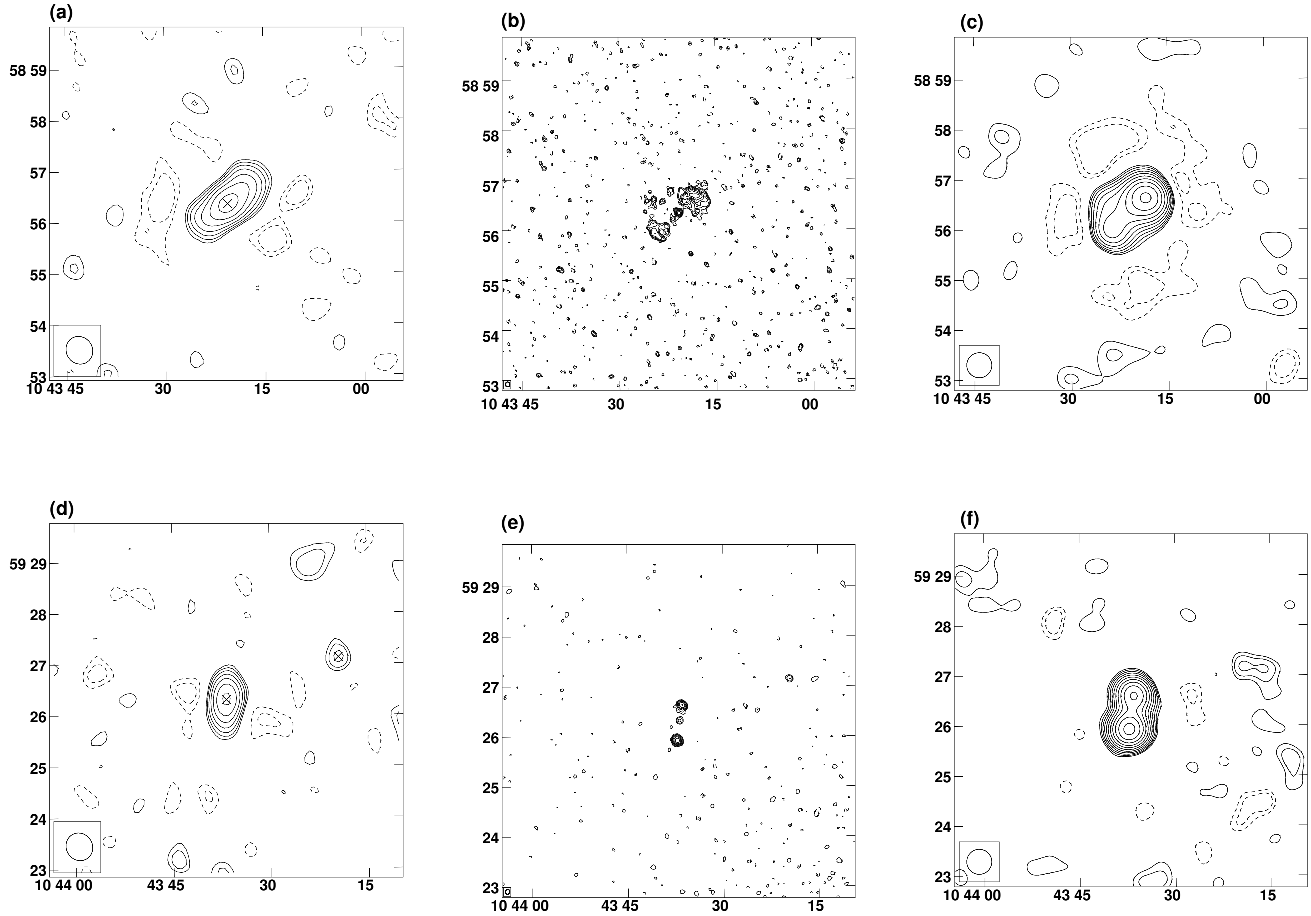

Figure 2.5: The difference in resolution between AMI Large Array (used for the 10C survey) and the GMRT. Figures (a) and (d) each show a source imaged with AMI, Figures (b) and (e) show the same sources imaged with GMRT. In both cases several sources in the GMRT catalogue correspond to one source in the 10C catalogue, so care must be taken when comparing the catalogues. In Figures (c) and (f) the GMRT images have been smoothed to create an image with a resolution comparable to the 10C images. This allows for a more direct comparison between the two surveys. The contours are drawn at $(\pm 2\sqrt{2^n}, n = 0, 1 \ldots 7) \times x$ mJy where $x = 0.074$ for (a), 0.1 for (b), 0.3 for (c), 0.086 for (d), 0.16 for (e) and 0.3 for (f).

components associated with one 10C source, the flux densities of the WSRT components were added together. (In fact, in all cases except one, the WSRT sources in question were listed as a multi-component source in the WSRT catalogue and the total flux density from the catalogue was used). This process was also carried out for FIRST sources.

For those 10C sources in the WSRT survey area without a match to the WSRT catalogue, the WSRT image was examined to see if there was a source present which was below the catalogue limit. This was not the case for any of the unmatched 10C sources in the WSRT area. The upper limit of flux density was taken to be three times the local noise in the WSRT image. For the 28 sources which were unmatched at 1.4 GHz and outside the WSRT area, an upper limit of 1 mJy was placed on the flux density because this is the FIRST completeness limit and these sources are all within the FIRST survey area but not detected.

2.2.1.4 OM2008 and BI2006

The two deep 1.4 GHz surveys made with the VLA (OM2008 and BI2006) have very small synthesised beams ($\approx$ 1.5 arcsec) compared to the 10C survey. As images are not available for these surveys, the flux density values from the catalogues were used. OM2008 do account for the fact that some of the sources may be extended when calculating flux densities. They convolve the full resolution images to an effective beam size of 3, 6 and 12 arcsec and compare the flux densities derived from the four images. BI2006 do not attempt to account for extended sources when calculating the flux densities, however there is only one 10C sources which has a counterpart in BI2006 and not in any other 1.4-GHz catalogue so this will not significantly affect these results.

2.2.2 The effects of variability

The different surveys used in this paper were not carried out simultaneously so it is important to consider the possible effects of variability on the observed spectral index distributions. The epoch of observation for each survey is shown in Table 2.1. The time interval between the 15-GHz and the 610-MHz observations is in the region of 4 – 6 years and between the 15-GHz and 1.4-GHz observations 5 – 10 years.

Whilst there is currently no data on the variability of sources at 15 GHz at the low flux density end of my sample, there have been some systematic studies at higher flux densities. Bolton et al. (2006) studied the 15-GHz variability of 51 9C sources with flux densities > 25 mJy over a 3-year period. They found that while there was no evidence for variability (above the ~6 percent flux calibration uncertainties) in steep spectrum sources, half of the flat spectrum objects were variable. In total, 29 percent of the sources studied were found to vary. Sadler et al. (2006) observed 173 20-GHz sources with flux densities > 100 mJy over a 2-year period and found that 42 percent varied by more than 10 percent. However, they found no correlation between variability and radio spectral index. More recently, Bonavera et al. (2011) investigated the variability of 159 sources with 20-GHz flux densities > 200 mJy and found the variability to be slightly larger than that found by Sadler et al., with an rms amplitude of 38 percent at 20 GHz on a timescale of a few years. Bonavera et al. note that there is some indication that the variability decreases as flux density decreases. Massardi et al. (2011b) studied the variability of a brighter sample ($S_{20\mathrm{GHz}} > 500$ mJy) at 20 GHz and found similar levels of variability to Sadler et al. At higher flux densities still, Franzen et al. (2009) have looked at variability at 16 GHz in a complete sample of 97 sources with flux densities > 1 Jy over timescales of about 1.5 years. They found that 15 percent of the sources vary by more than 20 percent; however, in contrast to the results of Sadler et al. but in agreement with those of Bolton et al., the spectra of the variable sources are flatter than those of the non-variable ones.

The variability properties of the population studied here are not known. However, on the assumption that the faint sources in the 10C sample exhibit the same sort of flux densiy variations as shown in the higher flux density samples discussed above, a significant fraction of them are likely to have varied over the period between the observations. Thus the spectral indices of individual objects may be unreliable. However, given that the sources are probably equally likely to increase or decrease in flux density this should not have a major effect on the overall spectral index distribution.

2.2.3 Spectral indices

To investigate the spectral properties of the source sample in a quantitative way, the spectral index was calculated between 15.7 GHz and 1.4 GHz ($\alpha_{1.4}^{15.7}$) and 15.7 GHz and 610 MHz ($\alpha_{0.61}^{15.7}$) for each source. For $\alpha_{1.4}^{15.7}$ all 296 sources are studied, for $\alpha_{0.61}^{15.7}$ the 5 sources outside the GMRT area are excluded as there is no 610-MHz flux density information available. For the sources with no match in GMRT, a limiting spectral index was calculated from the upper limit placed on the flux density from the GMRT image, as described in Section 2.2.1.1.

The distributions of $\alpha_{1.4}^{15.7}$ were investigated in two ways, using slightly different procedures, to check the effects of resolution on the data. The first, $\alpha_{1.4}^{15.7}M$, makes use of all of the 1.4-GHz data available; for the sources where there is more than one 1.4-GHz flux density, flux densities are chosen according to resolution in the following order of preference: NVSS, WSRT, OM2008, FIRST, BI2006; FIRST and BI2006 are last as they are the most likely to resolve out some of the flux of the 10C sources because of their small beam sizes (5 and 1.5 arcsec respectively). OM2008 also has a small beam (1.6 arcsec) but the sources have been convolved with gaussians of varying radius to try and overcome the resolution problem. NVSS and WSRT have larger beam sizes (30 and 12 arcsec respectively) which are more comparable to the 10C beam. For the sources with no match in any of the 1.4-GHz catalogues which are in the WSRT survey area, the upper limit from the WSRT image (as described in Section 2.2.1.3), is used to calculate a limiting spectral index. For the remaining sources, an upper limit of 1 mJy from the FIRST survey is used.

The second value, $\alpha_{1.4}^{15.7}N$, only uses values from the NVSS catalogue as this has a resolution comparable to the 10C survey. For the 10C sources which do not appear in NVSS, the

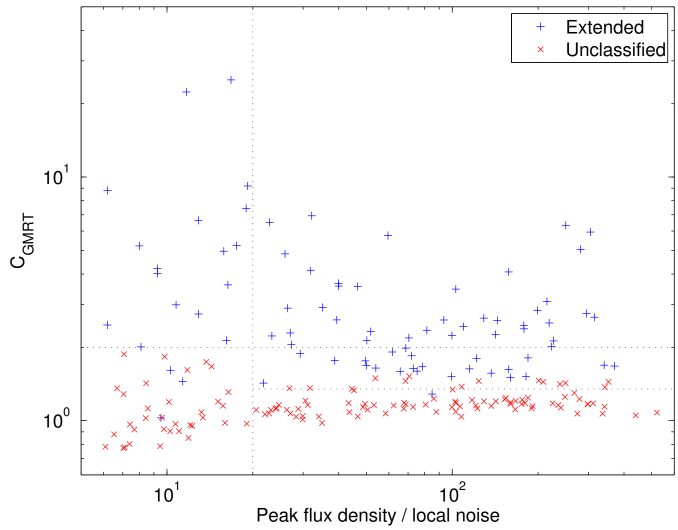

Figure 2.6: Compactness ratio calculated using GMRT data, C_{GMRT}, against the signal to noise ratio from the GMRT catalogue. The vertical line shows the divide at peak flux density / noise = 20 and the horizontal lines at C = 1.35 and 2.00 indicate the cutoffs in C used when classifying the extended sources, see text for details.

limit is derived from the NVSS image (see section 2.2.1.2). These values of the spectral index contain a larger number of upper limits but provide a useful comparison when considering the effects of resolution.

Possible effects of variability on the spectral indices are discussed in Section 2.2.2.

2.2.4 Extent of the radio emission

To determine in a quantitative manner whether a source is extended or not, a compactness ratio C is often used. This is usually taken as the ratio of the integrated or total flux density of a source S_{int} and its peak flux density on a map S_{peak} i.e. $C = S_{int}/S_{peak}$. For the 10C sample considered here I do not use the 10C observations to find C because the large beam size of $\approx$ 30 arcsec means that the majority of the sources are unresolved. Instead, I use the matched data from the lower frequency catalogues, which have smaller beam sizes and can therefore provide more information about the angular size of a source. Four values of C are calculated, using data from the GMRT, FIRST and OMK2009 (324 MHz VLA observations) catalogues, which all have beam sizes $\approx$ 6 arcsec, and the WSRT catalogue which has a beam size of 12 arcsec. The deep 1.4 GHz VLA observations (OM2008 and BI2006) are not used in this analysis because their beam sizes are considerably smaller ($\approx$ 1 arcsec) so that the data are not comparable with those from the other catalogues used here.

To take account of the effects of noise, several other studies (e.g Bondi et al. 2007, Prandoni

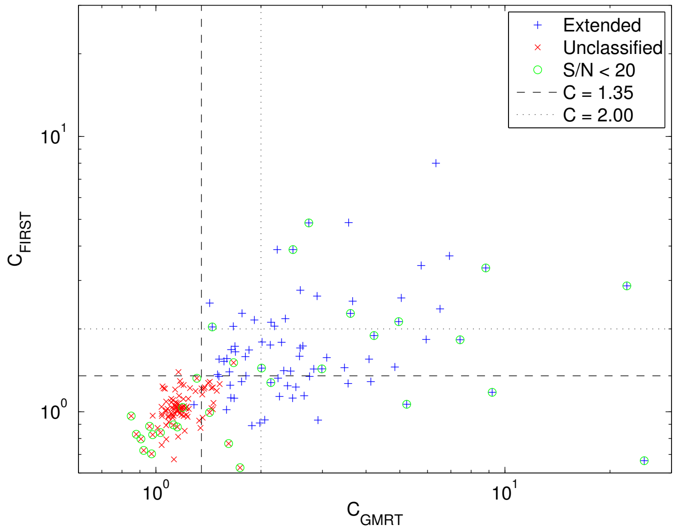

Figure 2.7: Value of the compactness ratio, C, calculated using FIRST and GMRT data. The horizontal and vertical lines indicate the values used when identifying the extended sources; see text for details. Sources classified as extended and those not classified are shown separately. Sources with a signal to noise ratio $<$ 20 in the GMRT data are indicated with a green circle.

et al. 2006) plot C against the signal to noise ratio and fit a lower envelope to the data; reflecting this about $C = 1$ gives a curve which provides the cutoff between the extended and compact sources. I have not used this method for the sample of sources studied in the chapter due both to the relatively small number of sources in the sample and to the range of different surveys used. Instead, each source was examined by eye and the criteria described below were decided upon to identify the extended sources.

At lower signal to noise ratios the errors in the C values become larger, due to the larger errors in the integrated and peak flux density values. This is evident in Figure 2.6 for the GMRT data, where the number of sources with values of $C < 1$, which must be due to errors in the flux density values, increases at lower signal to noise ratios. Therefore different criteria are used to identify the extended sources at high and low signal to noise. Sources were classified as extended if they had a signal to noise ratio greater than 20 in the GMRT data and values of $C > 1.35$ in at least two of the datasets used, or a value of $C > 2$ in at least one of the datasets. Sources with a signal to noise ratio less than 20 in the GMRT data were classified as extended if the value of C was greater than 2 in any of the datasets. A comparison of two of the C values used is shown in Figure 2.7. For most sources the two values are similar and some of the largest variations are for those sources with low signal to noise values, which is expected because the errors in the integrated flux densities are larger for the fainter sources.

I am confident that all the sources which fulfil these criteria are extended; however, as I have erred on the side of caution, there will be some sources which have not been classified as extended but do in fact have extended emission on the scale investigated here. In particular, sources which only have a value of C from the WSRT catalogue are not classified as extended as the WSRT beam is larger than that of the other catalogues used here. For this reason, those sources which are not classified as extended are placed in the 'unclassified' bin. The 36 sources which do not have a counterpart in any of the four catalogues used here are classified as 'no information'. The criteria used to select the extended sources here is roughly equivalent to selecting sources with angular sizes larger than ≈ 6 arcsec.

2.2.5 Angular sizes

Angular size information is available on a range of scales from the different catalogues available in the field. Best estimates of the angular sizes are compiled from these catalogues for the 96 sources in Sample W (sources in the 10C complete catalogue in the BI2006, OM2008 or the WSRT deep areas). The two deep VLA surveys, BI2006 and OM2008, are the highest resolution surveys, with resolutions of 1.3 and 1.6 arcsec respectively, so provide information on the smallest angular scales. However, the angular sizes from these two catalogues may not be reliable for significantly extended sources, as some structure may be resolved out due to a lack of short baselines. Additionally, some sources may be resolved into multiple components which are then listed separately in the catalogue, so the size listed in the catalogue would be only for part of the source. For this reason, for any source which was classified as extended in Section 2.2.4 the angular size was taken from the Garn et al. (2008) GMRT observations instead. The angular sizes for these sources were measured by hand, to avoid any problems caused by fitting Gaussians to extended sources with complicated structures. For the remaining sources (which are not classified as extended) the angular size was taken from the catalogue with the highest resolution available. The maximum angular size from the relevant catalogue is used, with the catalogues being used in the following order of preference: OM2008/BI2006, FIRST, WSRT (highest to lowest resolution). A value is flagged as an upper limit on the angular size if the size listed is less than the synthesised beam size for those observations.

Two sources required different treatment. The very extended source 10CJ105437+565922 is not detected in FIRST or GMRT as it has diffuse low-brightness structure; its size is measured from the NVSS map. The other source, 10CJ104927+583830, is only in the 10C catalogue, so for this source the 10C beam size (30 arcsec) is used as an upper limit on the angular size of the source.

The angular size distribution is shown in Figure 2.8 for the 96 sources in Sample W; the left panel shows the total distribution split into two groups, those with measured sizes and

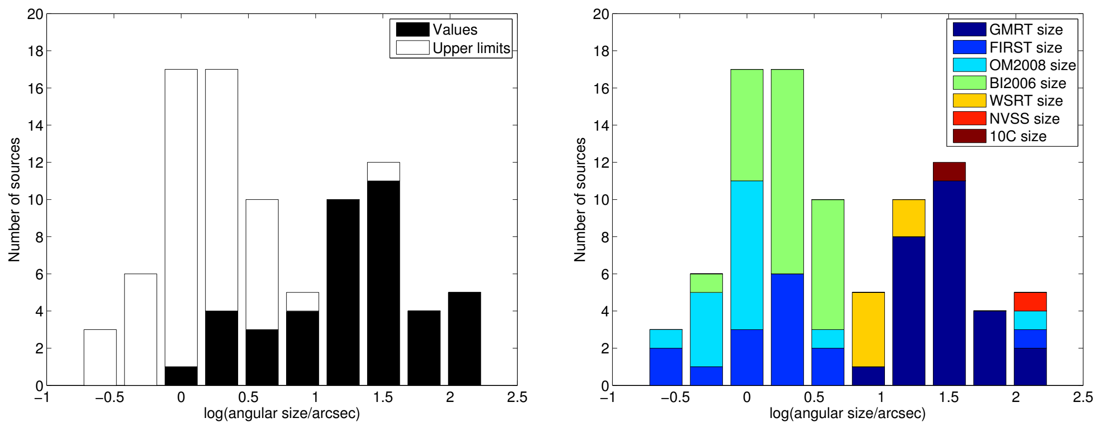

Figure 2.8: Angular size distribution for sources in Sample W. The left panel shows upper limits and values separately and the right panel shows the sample split according to the catalogue from which the angular size value originates.

those with upper limits used, and the right panel shows the distributions split according to the catalogues used.

2.3 Summary

A sample of 296 sources were selected at 15.7 GHz in the Lockman Hole. I matched this sample to several lower-frequency (and higher resolution) radio catalogues available in the field. Matches were found for 266 sources; upper limits were placed on the flux densities at 1.4 GHz and/or 610 MHz for the 30 unmatched sources. This allowed spectral index values (or limits) $\alpha_{0.61}^{15.7}$ and $\alpha_{1.4}^{15.7}$ to be calculated for the sample and the morphology of the sources to be investigated. The sources were split into three samples based on their radio morphology; 'extended' (85 sources), 'not classified' (containing the more compact sources, 170 sources) and 'no information' (36 sources). Matching to these lower frequency catalogues also provides more accurate positions for the sources, which are vital when matching to optical and infrared catalogues, as is done in Chapter 5.

A catalogue containing the flux density and spectral index values can be found in Appendix A. The properties of all 296 sources are discussed in the next chapter.

CHAPTER 3

ANALYSIS OF THE RADIO PROPERTIES OF 10C SOURCES IN THE LOCKMAN HOLE

One area of particular interest in studies of the radio sky has been the variation with flux density of the spectral index distribution for the samples selected at 15 – 20 GHz. For example, in the Ninth Cambridge survey (9C; Waldram et al. 2003) the proportion of sources with flat or rising spectra decreased as the flux density decreased. The median spectral index between 15.2 and 1.4 GHz ($\alpha_{1.4}^{15.2}$) changed from 0.23 for the highest flux density bin ($S_{15\ \mathrm{GHz}} \geq 100$ mJy) to 0.79 for the lowest flux density bin (5.5 mJy $\geq S_{15\ \mathrm{GHz}} > 25$ mJy).

The Australia Telescope 20 GHz survey (AT20G; Massardi et al. 2011a) found a similar variation of spectral index with flux density for a sample with a flux density limit of 40 mJy. The 10C survey (Davies et al. 2011) enables these studies to be extended to lower flux densities. Although the study by Davies et al. (2011) contains a larger number of limits, it is clear that the fraction of flat spectrum sources increases again as flux density decreases further. The data described in Chapter 2 enables this study to be extended.

In Chapter 2 a sample of 296 radio sources selected from the 10C survey at 15.7 GHz was matched to several lower frequency catalogues. Matches were found for 266 out of 296 sources and upper limits were placed on the lower-frequency flux densities for the 30 unmatched sources. These data are used to investigate the radio spectral properties of the sample in Section 3.1.1 and the morphology of the sources in 3.1.3. The 10C source population is compared to samples selected at 1.4 GHz in Section 3.2 and to the Wilman et al. (2008, 2010) simulated model of the radio sky in Section 3.3.

Table 3.1: The $\alpha_{0.61}^{15.7}$ results for three 15.7-GHz flux density bins.

Bin name	15.7-GHz flux density range / mJy	Number of sources	Number of upper limits	Median α	Mean α	% $\alpha > 0.5$
$S_{\rm low}$	$0.300 < S \leq 0.755$	99	45	0.08	0.25 ± 0.04	25 ± 4
$S_{\rm med}$	$0.755 < S \leq 1.492$	97	29	0.36	0.31 ± 0.05	40 ± 5
$S_{\rm high}$	$1.492 < S \leq 45.700$	95	4	0.75	0.57 ± 0.05	67 ± 5

Table 3.2: The $\alpha_{1.4}^{15.7}M$ results for three 15.7-GHz flux density bins.

Bin name	15.7-GHz flux density range / mJy	Number of sources	Number of upper limits	Median α	Mean α	% $\alpha > 0.5$
$S_{\rm low}$	$0.300 < S \leq 0.755$	99	27	0.10	0.11 ± 0.07	29 ± 4
$S_{\rm med}$	$0.755 < S \leq 1.492$	99	13	0.43	0.30 ± 0.07	46 ± 5
$S_{\rm high}$	$1.492 < S \leq 45.700$	98	2	0.79	0.66 ± 0.05	76 ± 4

3.1 Sample analysis

3.1.1 Radio spectral properties

Radio spectral indices were calculated for all 296 10C sources in the Lockman Hole, as described in Chapter 2. Some example radio spectra are shown in Figure 3.1, demonstrating the different spectral types observed. The spectral index $\alpha_{1.4}^{15.7}M$ against 15.7-GHz flux density for all sources is shown in Figure 3.2. It is clear from this plot that there is a greater proportion of flat spectrum sources at lower flux densities. This trend is further investigated by calculating the median spectral indices $\alpha_{0.61}^{15.7}$ and $\alpha_{1.4}^{15.7}M$ in three different flux density bins containing equal numbers of sources and the results are shown in Tables 3.1 and 3.2. Upper limits are included by using the ASURV Rev 1.2 package which implements the survival analysis methods presented in Feigelson & Nelson (1985). The distributions of both $\alpha_{0.61}^{15.7}$ and $\alpha_{1.4}^{15.7}M$ as a function of 15.7-GHz flux density show a sharp change at flux densities between 1 and 2 mJy. The spectral index distributions for these three flux density bins for both $\alpha_{0.61}^{15.7}$ and $\alpha_{1.4}^{15.7}M$ are shown in Figure 3.6 and are very similar. There is a distinct peak at $\alpha \sim 0.7$ in the highest flux density bin ($S_{\rm high}$). As flux density decreases the peak broadens as the contribution from flat spectrum sources becomes much more significant. In the lowest flux density bin ($S_{\rm low}$) the sources display a wide range of spectral index values, with a broad peak at $\alpha \sim 0.3$. The sources shown in white are upper limits and could only move to the left in these plots, making the $S_{\rm low}$ distribution even more different from the $S_{\rm high}$ distribution.

This is illustrated in Figure 3.3 which shows the median $\alpha_{0.61}^{15.7}$, $\alpha_{1.4}^{15.7}M$ and $\alpha_{1.4}^{15.7}N$ and the percentage of sources with $\alpha > 0.5$ in narrower 15.7-GHz flux density bins – there is a

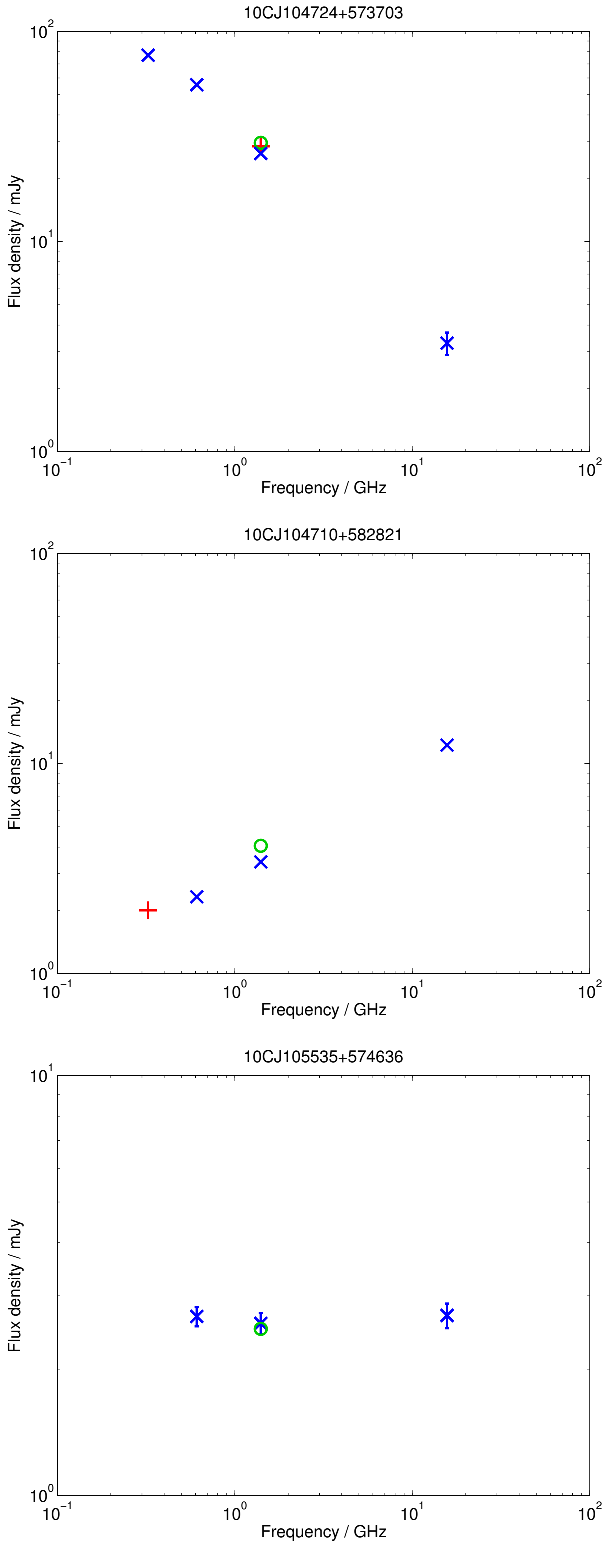

Figure 3.1: Example spectra. 10CJ104724+573703 is an example of a steep spectrum object, 10CJ104710+582821 is a rising spectrum object and 10CJ105535+574636 is an example of a flat spectrum object. The blue cross at 324 MHz (if present) is from WENSS, the red plus at 324 MHz is from OMK2009 and the value at 610 MHz is from GMRT. The blue cross at 1.4 GHz is from FIRST, the green circle is from WSRT and the red plus is from NVSS. The value at 15.7 GHz is from 10C. Error bars are not shown when they are smaller than the symbol plotted.

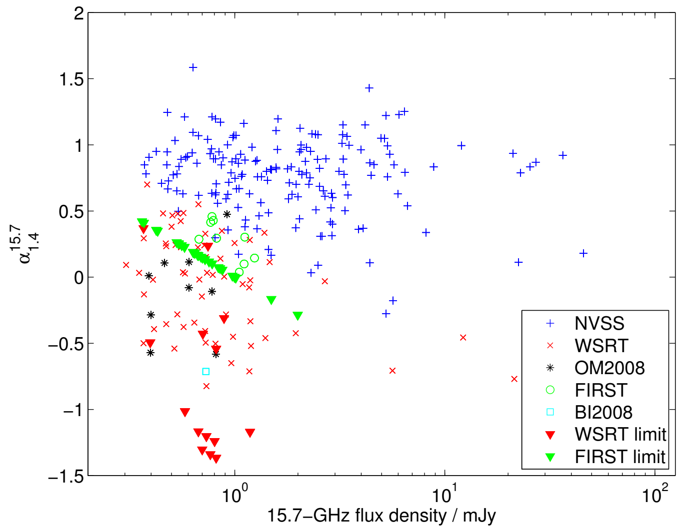

Figure 3.2: The spectral index $\alpha^{15.7}_{1.4}M$ against 15.7-GHz flux density, showing which catalogue the 1.4-GHz flux density values come from.

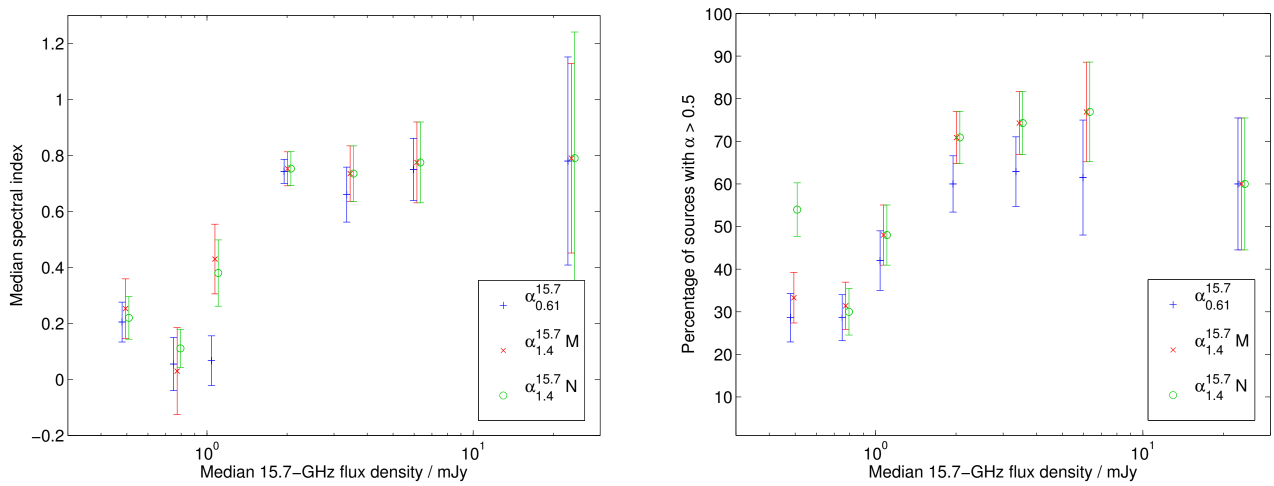

Figure 3.3: The median spectral index and percentage of sources with $\alpha > 0.5$ as a function of 15.7-GHz flux density for all 10C sources. The values of $\alpha^{15.7}_{1.4}M$ are calculated using the best 1.4-GHz flux density values available (order of preference = NVSS, WSRT, OM2008, FIRST, BI2006) while the values of $\alpha^{15.7}_{1.4}N$ are calculated using 1.4-GHz flux density values from NVSS only. The points are plotted at the median flux density in each bin but are offset for clarity. Limiting spectral indices are included in the median using survival analysis (see text). The error bars in the median spectral index plot show the interquartile range divided by $\sqrt{N}$ to give an indication of the errors in the medians. Note the large change in spectral index between 1 and 2 mJy.

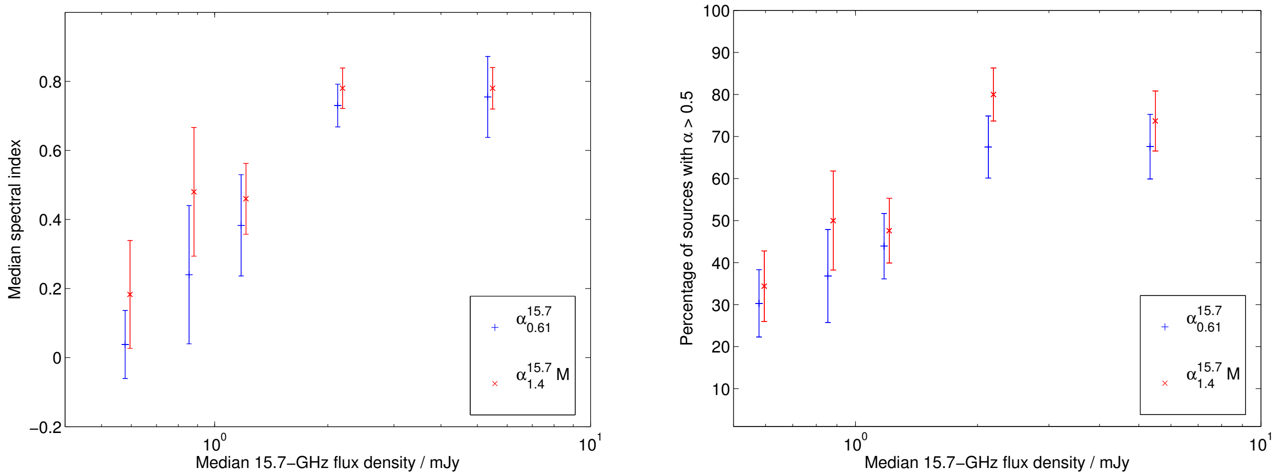

Figure 3.4: The median spectral index and percentage of sources with $\alpha > 0.5$ as a function of 15.7-GHz flux density for sources in the complete samples A and B. The values of $\alpha^{15.7}_{1.4}M$ are calculated using the best 1.4-GHz flux density values available (order of preference = NVSS, WSRT, OM2008, FIRST, BI2006). The points are plotted at the median flux density in each bin but are offset for clarity. The sources in the lowest two flux density bins are from Sample A, which is complete above 0.5 mJy and the remaining three flux density bins contain sources from sample B, complete above 1 mJy. Limiting spectral indices are included in the median using survival analysis (see text). The error bars in the median spectral index plot show the interquartile range divided by $\sqrt{N}$ to give an indication of the errors in the medians.

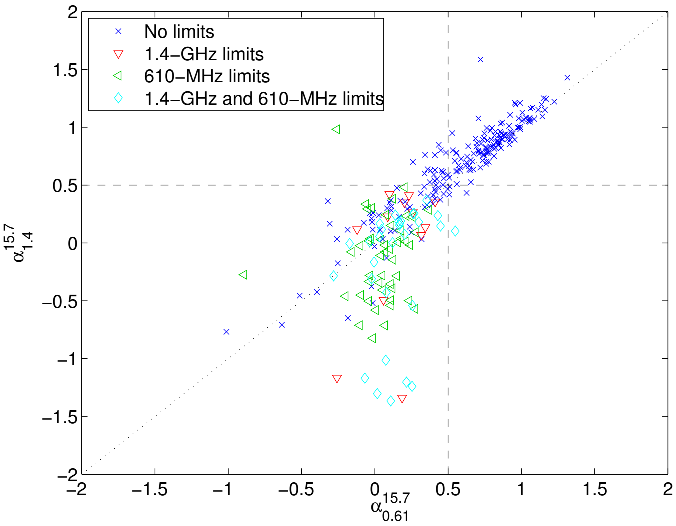

Figure 3.5: Values of $\alpha^{15.7}_{0.61}$ and $\alpha^{15.7}_{1.4}M$, showing which values are upper limits. The arrows indicate the direction in which the points which are upper limits could move. The dashed lines at $\alpha = 0.5$ illustrate the division between steep and flat spectrum sources; sources with $\alpha > 0.5$ are classified as steep spectrum while sources with $\alpha < 0.5$ are classified as flat spectrum. The dotted line illustrates $\alpha^{15.7}_{0.61} = \alpha^{15.7}_{1.4}M$.

far higher proportion of flat spectrum sources at lower flux densities. The values for $\alpha_{1.4}^{15.7}N$ (using NVSS flux densities only) are very similar to those for $\alpha_{1.4}^{15.7}M$, except in the lowest flux density bin which is dominated by upper limits in the NVSS-only case. This implies that resolution differences between 10C and the other surveys is not having a major effect on the derived spectral indices. The same plots for the complete samples A and B are shown in Figure 3.4. There are fewer sources in this sample so the uncertainties are larger but the general trend towards decreasing spectral indices below ≈ 2 mJy remains the same.

A plot of $\alpha_{1.4}^{15.7}M$ against $\alpha_{0.61}^{15.7}$ and for all sources is shown in Figure 3.5. There is a good correlation between the two values of spectral index. The majority of the points in the bottom left corner which deviate from the correlation are upper limits and therefore could move closer to the one-to-one correlation line shown. Of the points which are not upper limits, slightly more lie above the one-to-one correlation line than below it, indicating a slight spectral steepening at higher frequencies.

Possible effects of variability are discussed in Chapter 2. The variability properties of the population studied here are not known, but it seems likely that, if anything, variability would increase the proportion of steep spectrum sources rather than producing the decrease observed. It is possible, for example, that variability in some of the genuinely flat spectrum sources over the epochs covered by the surveys used here could make them appear to have steep spectra. On the other hand, the genuinely steep spectrum sources in my faint sample are unlikely to be variable (unless their properties differ markedly from the steep spectrum sources at higher flux densities) so their spectral indices will not be affected at all.

3.1.2 Comparison with other spectral index studies

The variation in spectral index with flux density at higher (~10 mJy – 1 Jy) flux densities has been investigated by Waldram et al. (2010) and Massardi et al. (2011a). Waldram et al. and Massardi et al. used samples selected at 15 and 20 GHz respectively and, by matching them to catalogues at 1.4 GHz, found that the median spectral index becomes rapidly larger with decreasing flux density; for example Waldram et al. found that the median $\alpha_{1.4}^{15}$ changed from around 0 at 1 Jy to 0.8 at 10 mJy. This study of 10C sources shows that as the flux density decreases further the median spectral index drops again, with the median $\alpha_{1.4}^{15}$ decreasing from around 0.8 for flux densities > 1.5 mJy to around 0.1 at 0.5 mJy. As discussed in Section 3.1.1 the change occurs fairly abruptly at $\approx$ 1mJy, indicating that the nature of the 15-GHz source population is changing at this flux density. The relationship between spectral index and flux density is summarised in Figure 3.7 which shows the Waldram et al. results from the Ninth Cambridge survey (9C) along with the results from this study.

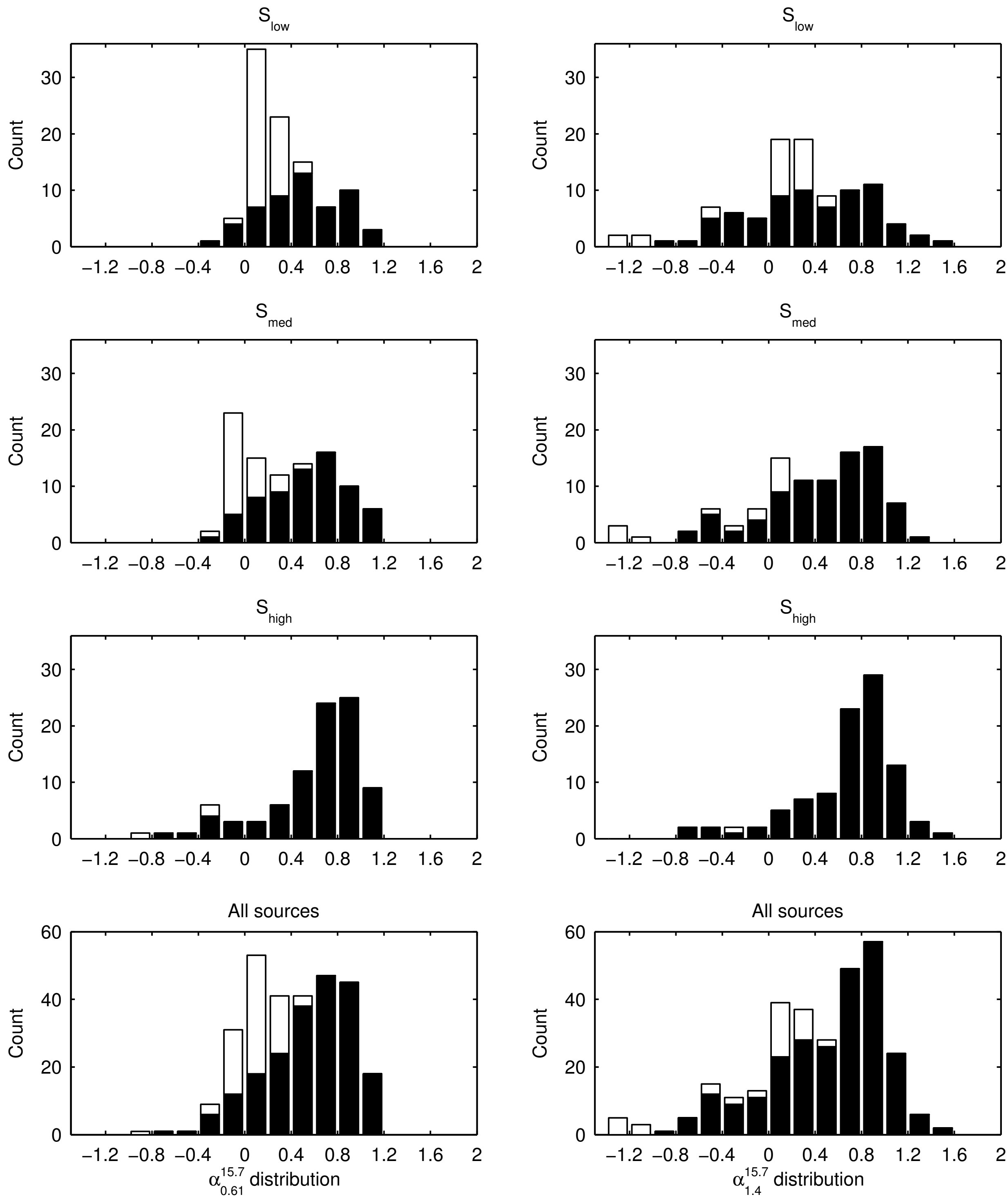

Figure 3.6: The spectral index distribution for three different flux density bins are shown in the top three panels. S_{low} : $0.300 < S_{15.7\mathrm{GHz}} \leqslant 0.755$ mJy, S_{med} : $0.755 < S_{15.7\mathrm{GHz}} < 1.492$ mJy, S_{high} : $1.492 < S_{15.7\mathrm{GHz}} \leqslant 47$ mJy. The spectral index distribution for the whole 10C sample is shown in the bottom panel. $\alpha_{0.61}^{15.7}$ is calculated using the GMRT values and limits, accounting for the resolution difference as described in Section 2.2.1, and using the integrated flux density from the 10C catalogue. $\alpha_{1.4}^{15.7}$ was calculated using the best 1.4 GHz flux density available (order of preference = NVSS, WSRT, OM2008, FIRST, BI2006). In both cases upper limits on α are included for sources where no low frequency flux density data is available; these are shown in white while values are plotted in black.

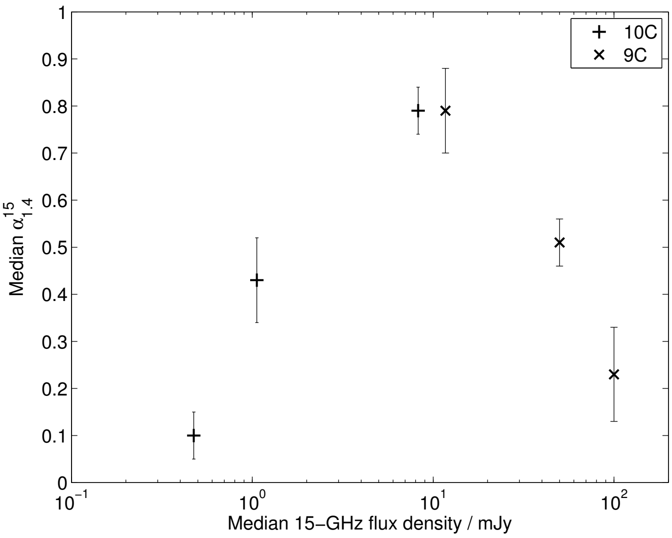

Figure 3.7: The median spectral index as a function of flux density from the study of 9C sources by Waldram et al. (2010) and the 10C sources studied in this paper. The points are plotted at the bin midpoint, except for the highest flux density bin (S > 100 mJy) where the point is plotted at the bin lower limit.

I have shown here that the spectral index distribution changes dramatically below ~1 mJy for a sample of sources selected at 15.7 GHz. A similar trend has been found by other studies at slightly lower frequencies. For example, Prandoni et al. (2006) studied a complete sample of 131 sources detected at 5 and 1.4 GHz with a comparable flux density range to the sample studied here. They found that the median spectral index between 5 and 1.4 GHz changed from 0.56 ± 0.06 for sources with $S_{5\mathrm{GHz}}$ > 4 mJy to 0.24 ± 0.06 for sources with $S_{5\mathrm{GHz}}$ < 4 mJy.

3.1.3 Extent of the radio emission

The sources were split into three groups (extended, unclassified and no information) as described in Chapter 2. A summary of the properties of these three groups of sources in terms of spectral index and flux density is given in Table 3.3 and the flux density distribution for the three groups is shown in Figure 3.8. A larger proportion of the brighter sources are extended, with extended sources making up 38 percent of the total number of sources with S > 1 mJy, compared to 19 percent of sources with S < 1 mJy. This could be a result of the more stringent criteria for classifying sources with low signal to noise as extended as well as the fact that extended low surface brightness emission is more likely to be missed at low signal to noise levels. As expected, the majority of the sources with no information are faint, with S < 1 mJy.

The spectral index distributions for the extended sources and those not classified are, as anticipated, significantly different, as shown in Figure 3.9 and Table 3.3. The majority (70/85)

Table 3.3: A summary of the properties of sources classified as extended, those not classified and those with no information. The value of spectral index used here is $\alpha_{0.61}^{15.7}$ so the five sources which are outside the GMRT survey area are not included. The numbers in brackets refer to the percentage of sources in each classification.

		Number of sources with ...			
Bin	Total	$S_{15.7} > 1$ mJy	$S_{15.7} < 1$ mJy	$\alpha > 0.5$	$\alpha < 0.5$
Extended	85	55 (65)	30 (35)	70 (82)	15 (18)
Unclassified	170	80 (47)	90 (53)	56 (33)	114 (67)
No info	36	5 (14)	31 (86)	2 (6)	34 (94)

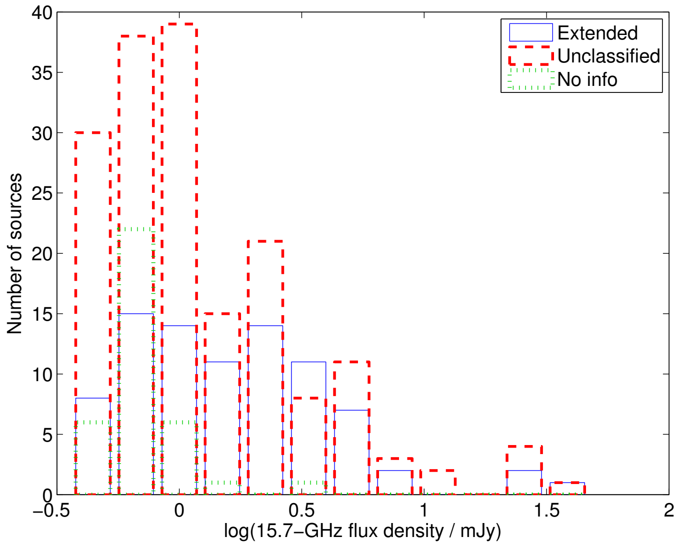

Figure 3.8: The 15.7-GHz flux density distribution for the extended sources, those which are unclassified and those with no information. The three histograms are overlaid.

of the extended sources are steep spectrum, with the spectral index distribution peaking at $\alpha \approx 0.8$. The distribution of the unclassified sources is much broader and is less peaked, with the distribution stretching between $\alpha \approx -0.2$ to $\alpha \approx +1$. The majority of the sources with no information display a flat spectrum, as these are the sources which are too faint to be detected at the lower frequencies of 610 MHz/1.4 GHz. For these sources the value of α plotted is an upper limit, which explains the large peak at $\alpha \approx 0$. Figure 3.10 shows $C_{\rm GMRT}$ against $\alpha_{0.61}^{15.7}$ for all sources matched to the GMRT catalogue. It is evident from this plot that, as expected, a greater number of the extended sources have a steep spectrum.

The distribution for extended sources displays a flat spectrum tail, 15 sources having $\alpha_{0.61}^{15.7} < 0.5$. It is likely that these extended, flat spectrum sources are extended sources with a flat spectrum core which dominates at high frequency. We might therefore expect that the lower frequency images of most of these sources would display a dominant core surrounded by

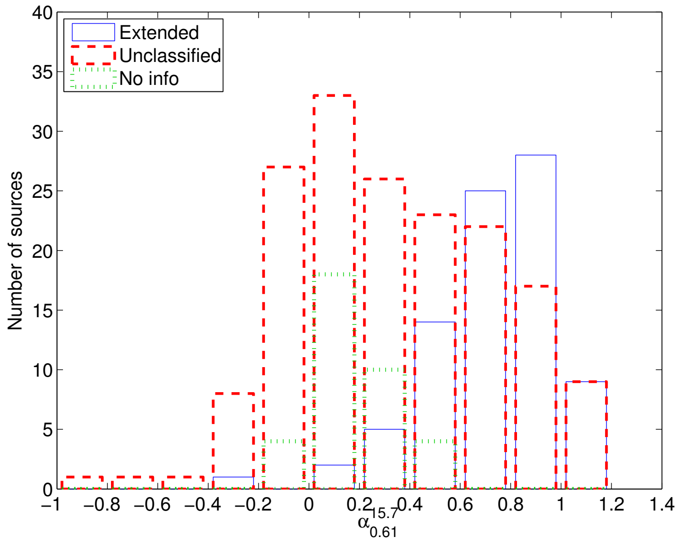

Figure 3.9: The spectral index distribution for sources classified as extended and unclassified, and those with no information. The three histograms are overlaid. Upper limits in α are plotted for the sources with no information which explains the apparent peak at $\alpha \approx 0$.

some, possibly fainter, extended emission, whereas the steep spectrum extended sources would have relatively more pronounced lobes. Examination of the images shows this to be the case for most sources; typical examples of steep and flat spectrum extended sources are shown in Figure 3.11.

3.1.4 Correlations between size and spectral index

In Section 3.1.3 it is shown that the majority of the flat spectrum sources are not classified as extended and therefore probably compact. However, a small but significant number (15 out of 163) of the flat spectrum sources are clearly extended, indicating a variety of source types. There are also a significant number of sources (34) for which I have no information about their structure.

Recent work by Massardi et al. (2011a) using the AT20G survey found that for α_1^5 there was a clear divide between the extended, steep spectrum sources and the compact, flat spectrum sources. However, when looking at the higher frequency spectral index, α_8^{20}, they found that the extended sources displayed a much broader range in spectral index. This is consistent with the flat spectrum tail in the spectral index distribution for extended sources observed here and supports the idea that a flat spectrum core is becoming increasingly dominant at higher frequencies. A study by Prandoni et al. (2006) investigated the properties of a sample of 111 sources using data at 1.4 and 5 GHz and found that nearly all the extended or multiple sources

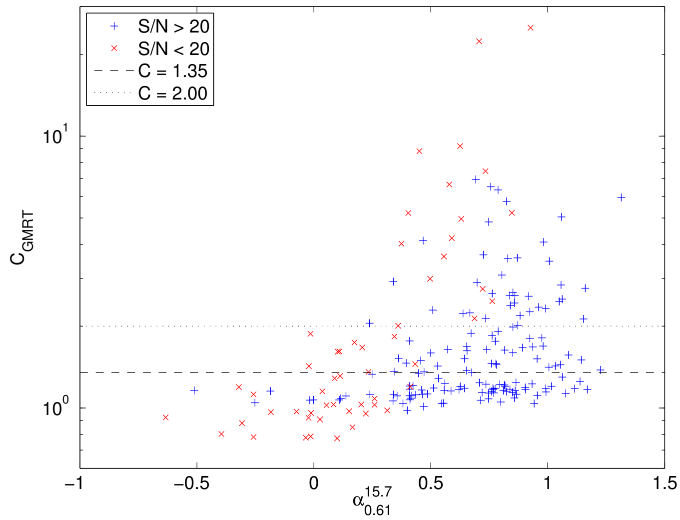

Figure 3.10: $C_{\rm GMRT}$ as a function of $\alpha^{15.7}_{0.61}$ for all sources in the GMRT area. Sources with peak flux / noise < 20 in the GMRT catalogue are shown separately and the horizontal lines at $C = 1.35$ and 2.00 indicate the cutoffs in C used when classifying the extended sources, see text for details.

were steep spectrum. The lack of flat spectrum extended sources in the Prandoni et al. study is probably due to the lower frequencies used, as at these frequencies the flat spectrum core has not yet become dominant.

3.1.5 Effect on the source counts

The 15.7-GHz source count derived from the full 10C survey is presented in Davies et al. (2011). The function fitted to the source count is a broken power law, as shown in equation 3.1,

$$n(S) \equiv \frac{dN}{dS} \approx \begin{cases} 24 \left(\frac{S}{\rm Jy}\right)^{-2.27} \ {\rm Jy^{-1}\ sr^{-1}} & \text{for } 2.8 \leq S \leq 25 \text{ mJy}, \\ 376 \left(\frac{S}{\rm Jy}\right)^{-1.80} \ {\rm Jy^{-1}\ sr^{-1}} & \text{for } 0.5 \leq S < 2.8 \text{ mJy}. \end{cases} \tag{3.1}$$

It is significant that the break in this power law occurs at 2.8 mJy i.e. at approximately the same flux density as the change in the spectral index distribution observed here.

To examine this further, the source counts for the complete sample of sources (made up of Samples A and B) studied in this paper are presented in Table 3.4. The counts for steep and flat spectrum sources are shown separately; the flux density bins are double the bins used in presenting the full 10C counts in Davies et al. (2011). No attempt is made to fit the source count due to the small number of sources in each bin. However, it is clear that the source counts are significantly different for the two populations, with, as expected, a greater proportion of flat spectrum sources in the fainter flux density bins ($S_{\rm 15GHz} \lesssim 1$ mJy), while the steep spectrum sources dominate at the higher flux densities. Taken with the flattening of the overall counts

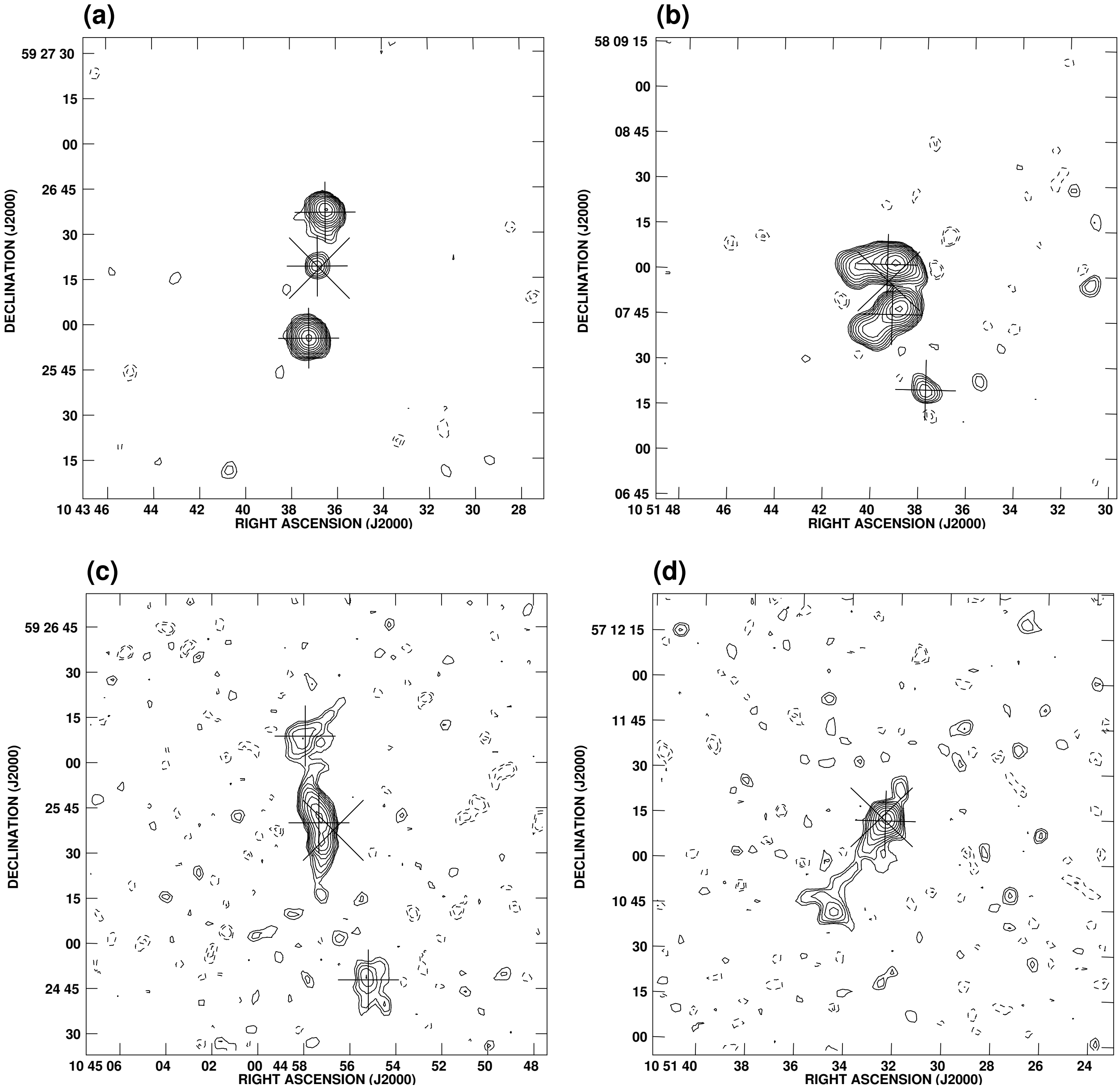

Figure 3.11: GMRT images of some example extended sources. The contours are drawn at $(\pm 2\sqrt{2^n}, n = 0, 1 \ldots 7) \times x$ mJy where $x = 0.16$ for (a), 0.15 for (b), 0.086 for (c) and 0.076 for (d). The $\times$ marks the position of the 10C source and the + mark the positions of the components listed in the GMRT catalogue for each source. Sources (a) and (b) are steep spectrum sources with $\alpha_{0.61}^{15.7} = 0.93$ and 1.08 respectively. Sources (c) and (d) have flatter spectra with $\alpha_{0.61}^{15.7} = 0.49$ and 0.34 respectively.

Table 3.4: Source counts for the complete 10C sample from the Lockman Hole fields (made up of samples A and B). Steep and flat spectrum sources (with $\alpha_{0.61}^{15.7} > 0.5$ and $\alpha_{0.61}^{15.7} < 0.5$ respectively) are shown separately. Each flux density bin corresponds to two of the flux density bins used in presenting the full 10C source counts in Davies et al. (2011) (except for the highest flux density bin).

Bin start /mJy	Bin end /mJy	No. of sources with $\alpha > 0.5$	No. of sources with $\alpha < 0.5$	Area /deg^2
9.000	25.000	4	4	4.64
2.900	9.000	22	11	4.64
1.500	2.900	27	10	4.64
1.000	1.500	18	24	4.64
0.775	1.000	5	11	1.73
0.600	0.775	5	11	1.73
0.500	0.600	6	12	1.73

for flux densities < 2.8 mJy, this indicates that the source counts for the steep spectrum sources must be flattening significantly at flux densities below about 1 mJy.

There is evidence from other studies that the FRII population is dropping out at around the flux density where I observe the flattening of the steep spectrum source count. For example, Gendre & Wall (2008) used a sample of Combined NVSS-FIRST Galaxies (CoNFIG) to construct a 1.4-GHz source count for FRI and FRII sources. They found that the FRII population is dropping out as flux density decreases below approximately 20 mJy at 1.4 GHz, leaving a source population dominated by FRI sources at lower flux densities. This change in the population at $S_{1.4\mathrm{GHz}} \approx 20$ mJy corresponds to $S \approx 3$ mJy at 15 GHz for a steep spectrum source ($\alpha = 0.75$). The simulated source counts produced by Wilman et al. (2008) (which are discussed in more detail in Section 3.3) also show that the FRII population drops out at a few mJy at 18 GHz. It therefore seems likely that the changes in the spectral index distributions at around 1 mJy in my 15 GHz sample are due in part to the disappearance of the FRII sources. However, as discussed in Section 3.3, the dominance of a flat spectrum population at flux densities below 1 mJy is in clear disagreement with the models of Wilman et al., de Zotti et al. and Tucci et al..

3.2 Comparison with samples selected at 1.4 GHz

The source population at 1.4 GHz has been much more widely studied than the higher frequency population and models of the faint population at higher frequencies are often extrapolated from this lower frequency data. It is therefore useful to see how the spectral index distribution of the 10C source population compares to that for sources selected at 1.4 GHz.

Two samples of sources at 1.4 GHz were used; the first sample was selected from the

FIRST catalogue (Sample P) and the second from the NVSS catalogue (Sample Q). The FIRST catalogue is deeper so Sample P provides more information about the faint source population; the NVSS survey on the other hand has a beam size comparable to the 10C survey so provides more reliable spectral indices.

Some consideration needs to be given to the limiting flux densities of the FIRST and NVSS catalogues and the 10C catalogue which they are being matched. A source with a 1.4-GHz flux density of 3.4 mJy (the completeness limit of NVSS) should be detected in 10C unless it has a spectral index greater than 0.8. It is therefore expected that counterparts will be found at 15.7 GHz for the majority of the NVSS sources. FIRST, however, has a completeness limit of 1 mJy; a source with a 1.4-GHz flux density of 1 mJy could be detected at 15.7 GHz if it had $\alpha_{1.4}^{15.7} < 0.3$. I therefore expect a larger proportion of lower limits on the spectral indices for FIRST sources.

3.2.1 Sample selected from FIRST

All FIRST sources in the 10C deep fields (the areas containing Sample A) were selected (see Figure 2.1) giving a sample of 127 sources selected at 1.4 GHz. These sources were matched to the full 10C catalogue using a match radius of 15 arcsec, as described in Section 2.1.2. The difference in resolution between the two catalogues meant that there were several sources which were resolved into multiple components in FIRST but unresolved in 10C. For those cases where several FIRST sources matched to one 10C source, the flux densities of the individual FIRST sources were combined, giving a sample of 105 FIRST sources, 70 of which have a match to 10C.

10C maps of the unmatched FIRST sources were examined by eye. In ten cases, a source was visible in the 10C image – however its flux was clearly below the 10C completeness limit; the flux density of such a source was found using TVSTAT in AIPS. For the remaining unmatched sources, an upper limit of three times the local noise was placed on the flux density. This allows a lower limit to be placed on the spectral index.

The flux density distribution of the 105 sources in Sample P is shown in Figure 3.12.

3.2.2 Sample selected from NVSS

In order to have enough NVSS sources to be able to draw statistically significant conclusions, sources were selected from the deep areas of four 10C fields. Two of these are the fields in the Lockman Hole studied in this thesis, the other two fields are centred on $17^{h}33^{m}$, $+41°48^{m}$ and $00^{h}24^{m}$, $+31°52^{m}$. There are 292 sources in these four fields, giving a sample of comparable size to the sample of 10C sources studied in this chapter. The NVSS sources were matched to

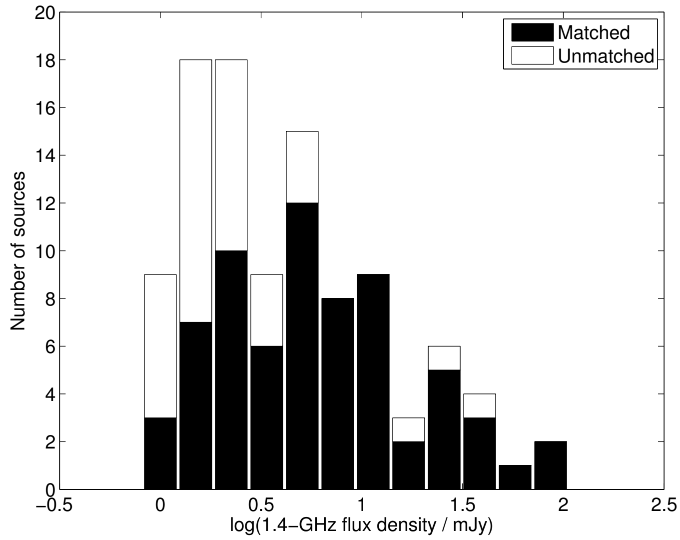

Figure 3.12: The flux density distribution of the sources in Sample P, selected from the FIRST catalogue. Sources with and without a match to the 10C catalogue are shown separately.

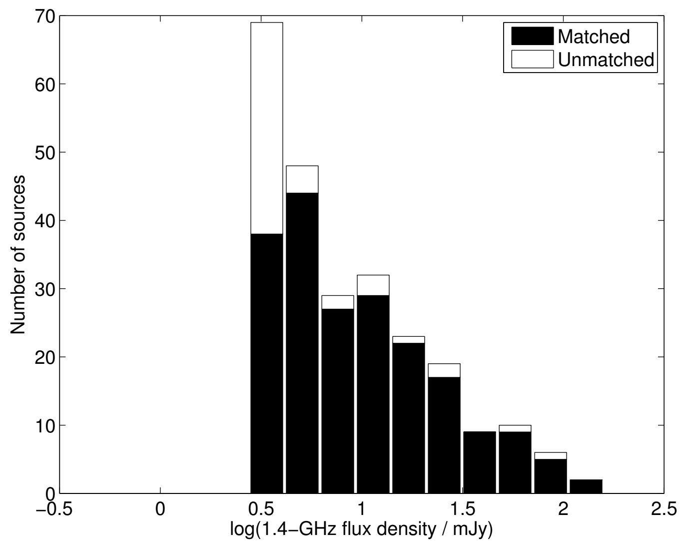

Figure 3.13: The flux density distribution of the sources in Sample Q, selected from the NVSS catalogue. Sources with and without a match to the 10C catalogue are shown separately.

the 10C catalogue, with limits placed on the unmatched sources as described in Section 3.2.1. This sample (Sample Q) contains 292 NVSS sources, 223 of which have a match to the 10C catalogue. The flux density distribution of Sample Q is shown in Figure 3.13.

3.2.3 Spectral index distribution of samples selected at 1.4 GHz

The spectral index $\alpha_{1.4}^{15.7}$ was calculated for all sources in Samples P and Q with a match in 10C. For the unmatched sources, a lower limit was placed on the spectral index using the upper limit from the 10C map. Figure 3.14 shows a comparison of the spectral index distributions of the sources selected at 15.7 GHz and those selected at 1.4 GHz. As expected the distributions are noticeably different; the sources selected at 1.4 GHz show one peak at $\alpha_{1.4}^{15.7} \approx 0.7$, while the sample selected at 15.7 GHz displays an additional peak at $\alpha_{1.4}^{15.7} \approx 0.3$. The additional population of flat spectrum sources, as expected, are poorly represented by selecting at 1.4 GHz. This is the challenge that extrapolating from lower frequencies to predict the high-frequency radio population presents. It relies on accurate modelling of the source population and of how the spectral behaviour of sources varies with frequency; it is particularly unreliable when there are no observations at nearby frequencies at the required flux density. The 10C sample is compared to one such model in Section 3.3.

3.3 Comparison with the SKADS Simulated Sky

Wilman et al. (2008, 2010) produced a semi-empirical simulation of the extragalactic radio continuum sky which contains $\approx$ 320 million sources. This simulation covers a sky area of 20×20 deg^2 out to a cosmological redshift of $z = 20$ and down to flux density limits of 10 nJy at 151, 610 MHz 1.4, 4.86 and 18 GHz. The sources in the simulation are split into six distinct source types: radio-quiet AGN (RQQ), radio loud AGN of the Fanaroff-Riley type I (FRI) and type II (FRII), GHz-peaked spectrum (GPS) sources, quiescent starforming and starbursting galaxies. These simulated sources are drawn from the observed or extrapolated luminosity functions. In order to produce a sub-sample of simulated sources comparable to the sources observed in this work, sources with a flux density greater than 0.5 mJy at 18 GHz were selected from the simulation. This produced a simulated sub-sample of 16235 sources (sample S^3). The spectral index between 610 MHz and 18 GHz was calculated from the flux densities in the catalogue.

The S^3 sample is dominated by FRI sources, which make up 71 percent of the source population (Table 3.5) in agreement with the discussion in Section 3.1.5. The second largest source population are FRII sources, while radio quiet AGN, GPS sources and starforming galaxies each make only small contributions to the simulated source population. The S^3 sample covers a region of area 400 deg^2 while the deep 10C regions from which Sample A is drawn cover 1.73 deg^2. In order to investigate the possible impact of clustering on these results, five regions of the S^3 sample with areas of 1.73 deg^2 were selected at random. The fraction of different sources types in each of these five regions was calculated and the range of values

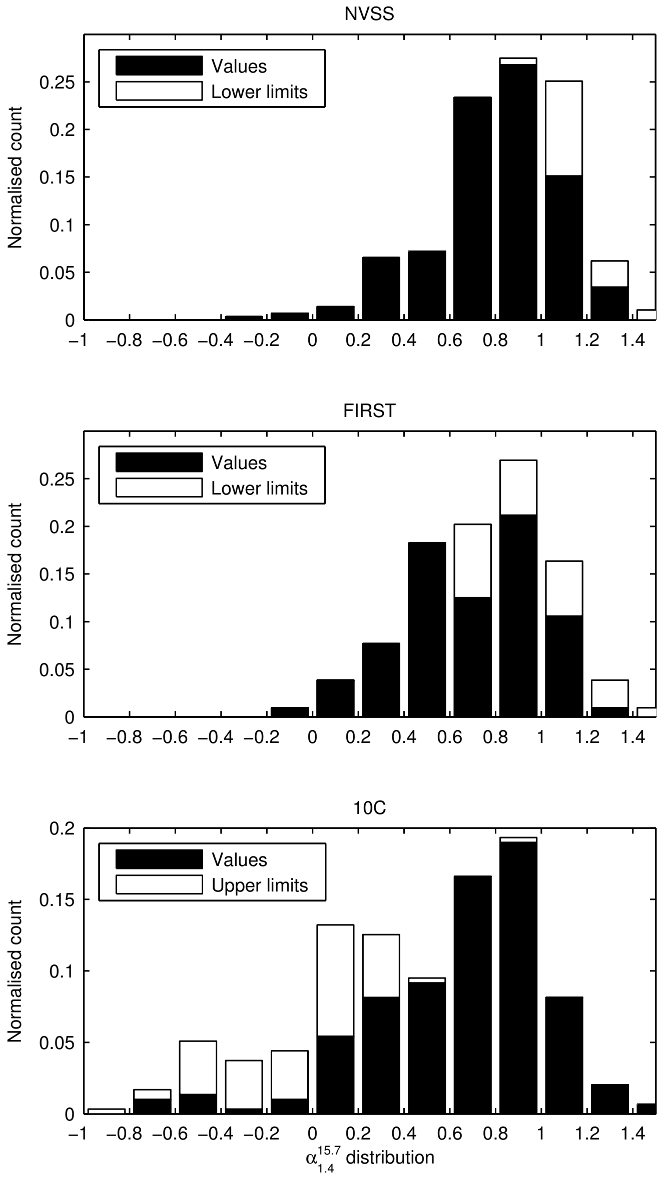

Figure 3.14: The spectral index distributions for sources selected at 1.4 GHz from NVSS (sample Q, shown in the top panel) and FIRST (sample P, middle panel) and 10C sources selected at 15.7 GHz (bottom panel). Limiting spectral indices for the unmatched sources are shown in white – note that these are lower limits in the FIRST and NVSS cases, therefore could only move to the right, and upper limits in the 10C case.

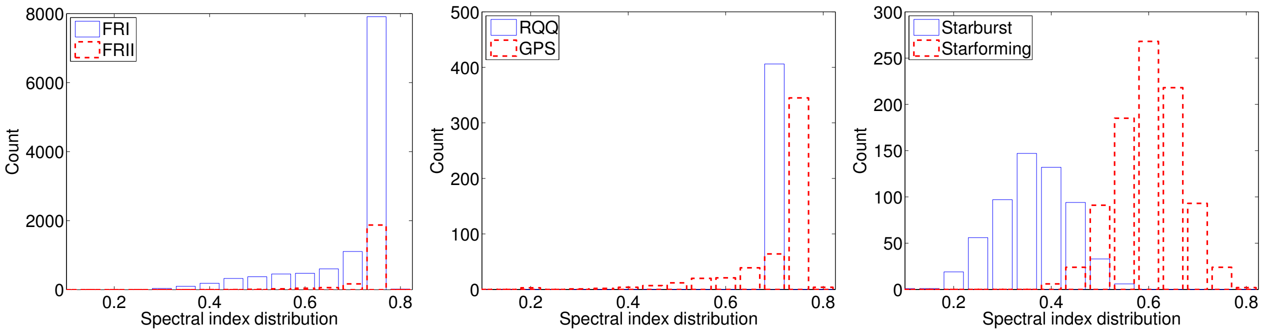

Figure 3.15: The spectral index distribution of the different source population in the S^3 sample with $S_{18\ \mathrm{GHz}} > 0.5$ mJy. The left panel shows FRI and FRII sources, the middle panel shows radio quiet AGNs and GHz-peaked sources and the right panel shows starburst and quiescent starforming sources.

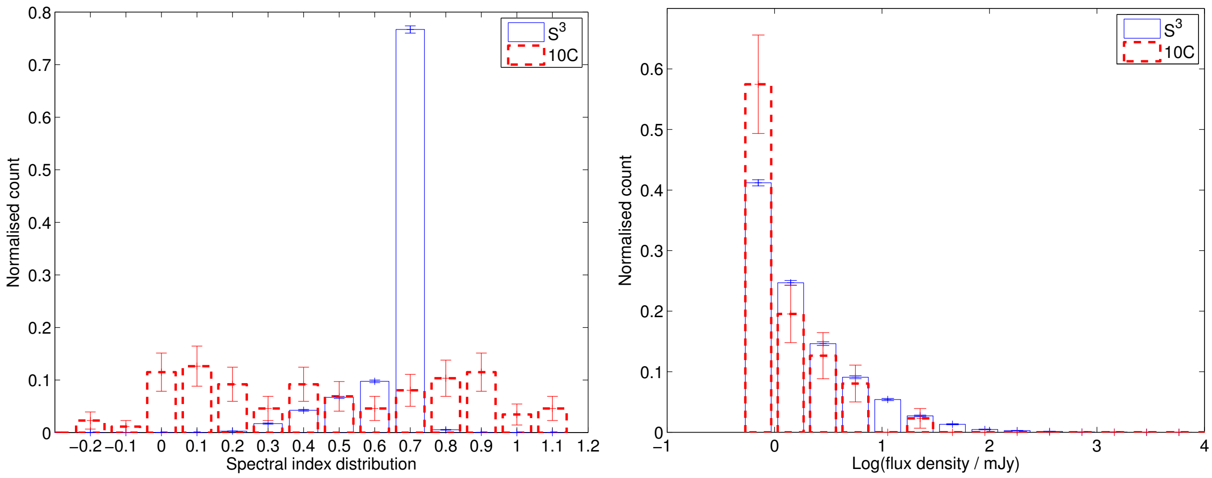

Figure 3.16: Comparison of the 10C and the simulated samples. The spectral index distribution (left) and flux density distribution (right) for sources in the S^3 sample with $S_{18\ \mathrm{GHz}} > 0.5$ mJy and for 10C sources with $S_{15.7\ \mathrm{GHz}} > 0.5$ mJy is shown. Note that for the S^3 sample the values plotted are $\alpha_{0.61}^{18}$ and 18-GHz flux density while for the 10C sources $\alpha_{0.61}^{15.7}$ and 15.7-GHz flux density are plotted. I do not expect this to make any difference to the results. Error bars show the poisson errors.

this gave is shown in Table 3.5. Although the exact percentages of source vary across the five regions, the general proportions remain the same, indicating that clustering will not have a major effect on the 10C results.

The spectral index distributions of the different groups of sources in the simulation are shown in Figure 3.15. All FRI, FRII and GPS sources have been modelled assuming their extended emission has a constant spectral index of 0.75, hence the prominent peaks at $\alpha = 0.75$. An orientation-dependent relativistic beaming model is used to find the contribution of the flat-spectrum core to the overall emission from each source; this gives the flatter spectrum

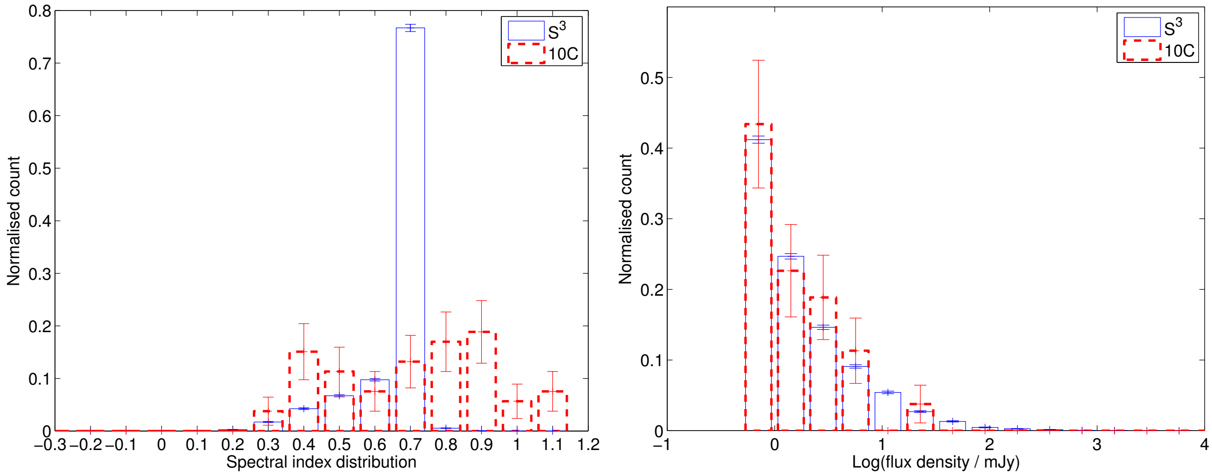

Figure 3.17: Comparison of the spectral index distribution and flux density distribution for sources in the S^3 sample with $S_{18\ \mathrm{GHz}} > 0.5$ mJy and for 10C sources with $S_{15.7\ \mathrm{GHz}} > 0.5$ mJy and a spectral index ($\alpha_{0.61}^{15.7}$) greater than 0.3 only. Note that for the S^3 sample the values plotted are $\alpha_{0.61}^{18}$ and 18-GHz flux density while for the 10C sources $\alpha_{0.61}^{15.7}$ and 15.7-GHz flux density are plotted. I do not expect this to make any difference to the results. Error bars show the poisson errors.

Table 3.5: The proportion of different source types in the sub-sample of simulated sources selected to be directly comparable to the sources observed in this study. This sub-sample contains 16235 sources with a flux density at 18 GHz greater than 0.5 mJy. The range of percentages calculated from five regions of equivalent size to the 10C deep survey area is also given.

Source type	Percentage	Range
FRI	71	57 – 85
FRII	13	6 – 30
Radio quiet AGN	3	0 – 6
GPS	3	0 – 8
Starburst	4	0 – 11
Quiescent starforming	3	1 – 11

tail in each spectral index distribution. The radio-quiet AGN have been assumed to have a constant spectral index of 0.7. The spectra of the starburst and starforming galaxies have been modelled using thermal and non-thermal components and in the case of starbursts a thermal dust component has been included.

Figure 3.16 shows a comparison of the spectral index and flux density distributions of the observed 10C sources (Sample A, complete to 0.5 mJy) and S^3 sample. It is clear that the simulation fails to reproduce the spectral index distribution of the 10C sources. The discrepancy for $\alpha > 0.7$ is due to the input assumption of the model that all sources have $\alpha = 0.75$; however the model fails to reproduce the distribution for $\alpha < 0.7$ with a conspicuous absence of sources with $\alpha < 0.3$. There are two main possibilities here; either the distribution of sources has not been modelled correctly and FRI sources do not dominate at this frequency and flux density level, but instead a new population with flat spectra is becoming important, or the emission from FRI sources has not been modelled correctly and that their flat spectrum cores are more dominant than predicted by the model in this frequency range. It is also possible that starburst galaxies may be causing this flattening in spectral index, although this is unlikely as it would require the contribution of starbursts to be greater than modelled by at least a factor of ten. This possibility is explored further in Chapter 4.

The actual and simulated flux density distributions are similar, but the 10C distribution contains a larger proportion of sources with flux densities less than 1 mJy. To test the possibility that there is a population of faint flat spectrum sources observed here which are missing from the simulation, the spectral index and flux density distributions were replotted, this time excluding all sources in the 10C sample with $\alpha < 0.3$ (Figure 3.17) as essentially no sources with $\alpha < 0.3$ are predicted by the model. The distributions are now more similar.

This analysis indicates that the extrapolations of the luminosity functions coupled with the models for the effects of beaming on the spectra of the radio-loud AGN used in this simulation have failed to reproduce the observed properties of the high-frequency population. It is worth noting that the recent models of the source population at 15 GHz by de Zotti et al. (2005) and Tucci et al. (2011) also fail to reproduce the observed source count at flux densities $\lesssim 10$ mJy, significantly under-predicting the observed number of sources. The updated version of the model of the 15-GHz source count by de Zotti et al. (2005), extracted from their website[a], shows that steep spectrum sources outnumber flat spectrum sources until the flux density drops below approximately 2 μJy, in clear disagreement with the counts in Table 3.4. The de Zotti et al. model predicts that at $S_{15\mathrm{GHz}} = 1$ mJy steep spectrum sources outnumber flat spectrum sources by nearly a factor of three. The results in Table 3.4 show that for $S_{15\mathrm{GHz}} < 1$ mJy there are twice as many flat spectrum sources as steep spectrum sources. The recent high frequency predictions of the source counts by Tucci et al. (2011) significantly under predict the number of sources observed at 15 GHz below approximately 5 mJy. This underprediction of the total number of sources could be explained by there being a greater number of flat spectrum sources at faint flux densities than are included in the model. These results highlight the difficulties inherent in predicting the behaviour of the high-frequency radio source population by extrapolating from lower frequencies.

[a]http://web.oapd.inaf.it/rstools/srccnt_tables

3.4 Conclusions

The radio spectral properties of 296 sources detected as part of the 10C survey at 15.7 GHz in the Lockman Hole are investigated in detail using a number of radio surveys, in particular a deep GMRT image at 610 MHz and a WSRT image at 1.4 GHz.

There is a clear change in spectral index with flux density – the median $\alpha_{0.61}^{15.7} = 0.75$ for flux densities greater than 1.5 mJy while the median $\alpha_{0.61}^{15.7} = 0.08$ for flux densities less than 0.8 mJy. This demonstrates that there is a population of flat spectrum sources emerging below 1 mJy. This result is consistent with results from other studies of the spectral indices of sources at lower frequencies.

The 10C source population was compared to two samples selected at 1.4 GHz from FIRST and NVSS at a comparable flux density. The spectral index distribution of these two samples is significantly different from that of the 10C sample selected at 15.7 GHz, the flat spectrum population present at 15 GHz being poorly represented in the 1.4-GHz samples. This demonstrates the well-known problem with extrapolating from lower frequencies to predict the properties of the high-frequency population.

The 10C sample was compared to a comparable sample selected from the SKADS Simulated Sky constructed by Wilman et al. (2008). The spectral index distributions of the two samples differ significantly; there are essentially no sources in the simulated sample with $\alpha < 0.3$ while 40 percent of the 10C sample have $\alpha_{0.61}^{15.7} < 0.3$. There is also a larger proportion of sources with flux densities below 1 mJy in the 10C sample than in the simulated sample – 57 percent of the 10C sources have a flux density below 1 mJy compared to 40 percent of simulated sources. This indicates that the simulation does not accurately reproduce the observed population at 15.7 GHz. I conclude that either there is a population of faint, flat spectrum sources which are missing from the simulation or the high-frequency radio emission of a known population is not modelled correctly in the simulation. If the relative contributions of the different populations are modelled correctly, it is likely that the observed flat spectrum population is due to cores of FRI sources being much more dominant than the model suggests.

These unique, faint 15 GHz samples are of great value when investigating the faint, high-frequency source population. The milliarcsecond-scale properties of this sample are investigated using VLBI observations in the next chapter. This provides further insights into the nature of this faint, high-frequency source population.

CHAPTER 4

MILLIACRSECOND PROPERTIES OF 10C SOURCES IN THE LOCKMAN HOLE

4.1 Introduction

In Chapter 3 I studied a sample of 296 faint (> 0.5 mJy) sources selected from the 10C survey at 15.7 GHz in the Lockman Hole. The properties of the 10C sample were compared with those of a sample of sources selected from the SKADS Simulated Sky (S^3; Wilman et al. 2008, 2010). I found that this simulation fails to reproduce the observed spectral index distribution and underpredicts the number of sources in the faintest flux density bin ($0.5 < S < 1$ mJy). I discussed two possible origins for this discrepancy. The first is that the source population at this flux density level is not dominated by AGN in the form of FRI sources, as predicted by the S^3 model, and is instead dominated by a population with flatter spectra, such as, for example, a population of starburst galaxies with unusually flat high-frequency spectra (Murphy et al. 2013). The second possibility is that FRI sources are not modelled correctly in the simulation and in fact themselves have much flatter spectra at high frequencies. In Chapter 3 I suggested that the first option is unlikely, as it would require the number of starburst sources to be incorrect in the simulation by at least a factor of ten. In this chapter this is explored further using high resolution images of a subsample of 10C sources.

Information about the structure of the sources in a sample can provide useful information about their nature, meaning that high resolution studies are valuable when investigating the properties of a population. The angular size of sources in the high frequency (20 GHz) source population at much higher flux densities ($S > 40$ mJy) has recently been investigated by Chhetri et al. (2013). They used data from a 6 km baseline to split the sample into different populations and investigate their properties. They found that 77 percent of their sample are compact AGNs and 23 percent are extended AGN-powered sources. Here I study a sample of high-frequency sources which are considerably fainter on even smaller angular scales.

In this chapter I use recently published VLBI data (Middelberg et al. 2013, hereafter M2013) to investigate further the nature of this faint 15.7-GHz source population. M2013 have recently conducted wide-field observations with the Very Long Baseline Array (VLBA) at 1.4 GHz of part of the Lockman Hole. The VLBA provides milliarcsec-scale resolution, so if a source is detected the emission must come from a very compact region and the brightness temperature must be very high ($\gtrsim 10^6$ K). Any stellar non-thermal sources, such as supernova remnants, at redshift $\gtrsim 0.1$ cannot have a surface brightness this high and thus any objects with $z \gtrsim 0.1$ which are detected must originate in AGN.

In Section 4.2 the different samples used in this chapter are defined and the methods used to investigate the properties of these samples are described. The results and discussion are split into two parts – the first part, Section 4.3, discusses the properties of the 10C sources in the VLBA survey area and the second part, Section 4.4, contains further insights into the nature of the M2013 VLBA sources. The conclusions are given in Section 4.5.

4.2 Sample definition and properties

4.2.1 Middelberg et al. observations

M2013 used a 1.4-GHz VLA image of the Lockman Hole field by Ibar et al. (2009) to identify a sample of sources which could in principle be detected with the VLBA observations provided all the flux comes from a very compact (milliarcsecond scale) region. They defined a source as 'detectable' if its peak VLA flux density is $\gtrsim$ 6 times the noise in the VLBA image at that point. They found that 217 sources fitted these criteria – I refer to this sample as the Middelberg sample.

M2013 made naturally weighted images, with a median resolution of 11.9×9.4 mas^2, at the positions of each of the 217 sources to detect, or place limits on, any milliarcsecond-scale components. Images with uniform weighting, with a median resolution of 7.4×5.5 mas^2, were used to calculate the integrated flux density of each detected source. Sixty-five of the sources in the Middelberg sample were actually detected in the VLBA observations, using the 6 σ threshold for detection. These sources form the 'VLBA-detected' sample.

Redshift information is available for 47 out of the 65 VLBA-detected sources from the Fotopoulou et al. (2012) photometric redshift catalogue. The redshift values for these sources

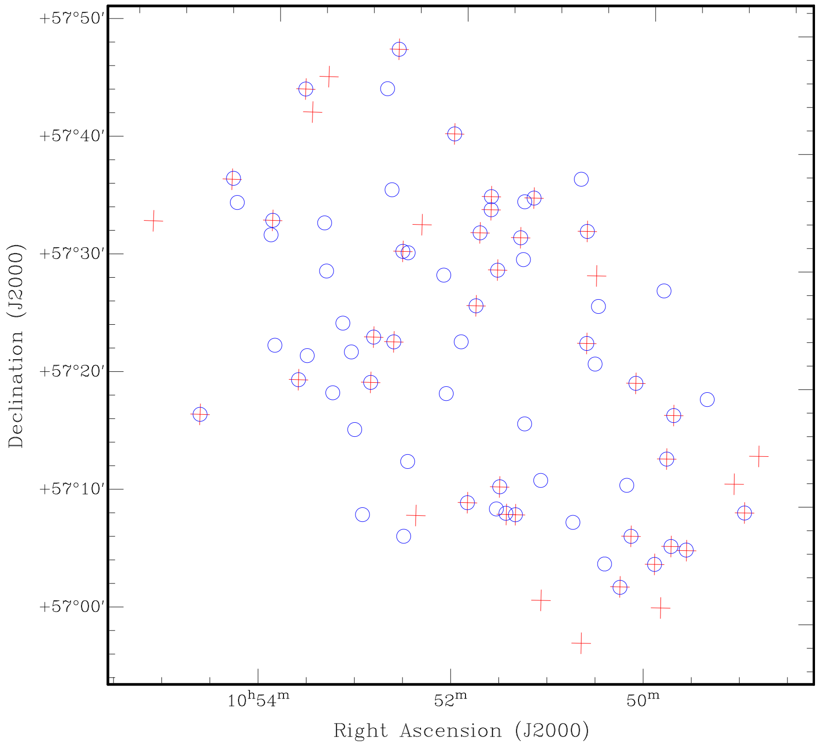

Figure 4.1: Positions of 10C and VLBI sources in the Lockman Hole. Red crosses show 10C sources in the Middelberg sample (i.e. the 10C sources which should, in theory, be detectable by the VLBA observations if they are compact). Blue circles show the 65 Middelberg sources which are detected by the VLBA.

all lie in the range $0.2 < z < 4.2$, meaning that all VLBA-detected sources must have the very high brightness temperatures which can only be found in AGN (see Section 4.1).

4.2.2 Data used and sample definition

The M2013 observations consist of three pointings with an rms noise of 24 μJy beam^{-1} towards the pointing centre. The 10C survey is complete to 0.5 mJy in the region covered by the M2013 observations. The 10C and Middelberg catalogues were matched in TOPCAT using a match radius of 15 arcsec. This match radius was chosen to minimise the number of false detections by matching to a shifted distribution of sources in the same way as described in Chapter 2. There are 51 10C sources in the VLBA survey area, of which 44 match to a source in the Middelberg sample. These 44 sources should therefore be bright enough at 1.4-GHz to be detectable with the VLBA if all their flux is in a compact core. Thirty-three of these 44 10C sources are actually detected by the VLBA observations.

The seven 10C sources which are not in the Middelberg sample (which would therefore not be detectable by the VLBA observations) have rising spectra, with typical values of $\alpha \sim -0.5$,

Table 4.1: Summary of the different samples used in this chapter.

Description	Number of sources
Middelberg VLBA-detectable sources	217
Middelberg sources in 10C sample	44
Middelberg sources detected by VLBA	65
10C sources detected by VLBA	33

and therefore fall below the VLBA-detectable flux density limit at 1.4 GHz (note that all 10C sources are found in the Ibar et al. (2009) deep VLA image).

In two separate cases a second VLBA source falls within the contours of a 10C source which is already matched to a different VLBA source. In both cases, the second VLBA source is more than 15 arcsec (the radius used for matching) away from the 10C source position, so is not counted as a match. The first case (10C ID 10CJ105115+573552) appears as an extended source in the 10C map (resolution $\approx$ 30 arcsec). In the higher-resolution GMRT map (synthesised beam 5×6 arcsec) this source is resolved into two separate compact sources and the two VLBA sources correspond to these two separate sources. It is likely that both VLBA sources are seen in the 10C map but they are blended together. If this is the case, it will mean that the 15.7-GHz flux density of the matched VLBA source is over estimated, as it also contains some contribution from the second VLBA source. The matched VLBA source has a steep spectum ($\alpha_{1.4}^{15.7} = 0.65$), so if the 15.7-GHz flux density is over-estimated the spectrum may be steeper still. In the second case (10C ID 10CJ105237+573058), the higher-resolution GMRT images reveal that the VLBA source which is closer to the 10C source position corresponds to the core of an extended double-lobed radio source, while nothing is visible in the GMRT map at the position of the second VLBA source. This is probably because this source is very faint ($S_{1.4\ \mathrm{GHz}} = 0.14$ mJy), so falls below the detection limit of the GMRT observations.

The positions of the 10C sources in the Middelberg sample and the VLBA-detected sources are shown in Figure 4.1 and the different samples are summarised in Table 4.1.

4.2.3 VLBA sources without a match in 10C

Thirty of the Middelberg sources which are detected by the VLBA observations do not have a match in the 10C catalogue. For each of these unmatched VLBA sources the 10C image was examined to see if there was a source present which was below the 10C catalogue limit. In 14 cases a source was visible within 15 arcsec of the VLBA position with a peak flux density greater than 3σ. For these 14 sources the 15.7-GHz flux density was estimated from the 10C image using the AIPS task JMFIT. In four cases JMFIT did not converge due to the presence of a nearby bright source; for these sources the flux density was found manually using the AIPS task TVSTAT. For the remaining unmatched sources an upper limit of three times the local noise in the 10C map was placed on the 15.7-GHz flux density.

4.2.4 Spectral index

In Sections 4.3 and 4.4 radio spectral index, α, (where $S = \nu^{-\alpha}$ for flux density S at frequency ν), is used to investigate source properties.

In Section 4.3, for sources in the 10C sample, $\alpha_{1.4}^{15.7}$ and $\alpha_{610}^{15.7}$ values calculated in Chapter 2 are used.

In Section 4.4 the spectral index, or a lower limit on the spectral index, between 15.7 GHz and 1.4 GHz ($\alpha_{1.4}^{15.7}$) was calculated for all 65 sources detected by the VLBA observations. For consistency, the 1.4-GHz flux densities used were the integrated flux densities from the VLA observations by Ibar et al. (2009) used in M2013. The 15.7-GHz flux densities were either the integrated flux densities taken from the 10C catalogue or, for those sources without a match in the 10C catalogue, the values determined from the 10C map or the upper limit on the 10C flux density derived from the 10C map (see Section 4.2.3).

4.2.5 Morphology

In this study I use two different measures of source morphology, which provide information about the size of the source on different scales, as follows.

(1) VLA size, $\theta_{\rm VLA}$ – the maximum angular size taken from the Ibar et al. (2009) 1.4-GHz VLA catalogue. For single sources this value corresponds to twice the maximum Full Width Half Maximum (FWHM) of the fitted Gaussian and gives information about whether or not the source is resolved on an arcsecond scale. The FWHM synthesised beam size is $\approx$ 4 arcsec so values of $\theta_{\rm VLA} \gtrsim 9$ arcsec indicate that the source is resolved.

(2) Ratio R of the VLA integrated flux density to the VLBA integrated flux density ($R = S_{\rm VLA}/S_{\rm VLBA}$). This gives information about whether the source is dominated by compact emission ($\lesssim$ 10 mas), in which case $R \approx 1$, or whether there is significant emission from a more extended region.

4.3 Properties of the 10C sources

4.3.1 VLBA detections

The spectral index and morphology properties of the 44 10C sources in the Middelberg sample are summarised in Table 4.2. Thirty-three out of the 44 sources (75 percent) in this sample

Table 4.2: Properties of 10C sources in the Middelberg sample (which should be detectable by the VLBA if they are compact). Sources which are detected by the VLBA observations are marked with a ∗. All flux densities listed are integrated flux densities. All spectral index values are from Chapter 2.

10C ID[a]	RA (J2000)	Dec (J2000)	S_{10C} /mJy	σ_S_{10C} /mJy	$\alpha_{0.61}^{15.7}$	$\sigma\_\alpha_{0.61}^{15.7}$	Flag1[b]	$\alpha_{1.4}^{15.7}$	$\sigma\_\alpha_{1.4}^{15.7}$	Flag2[c]	$\alpha_{0.61}^{1.4}$	$\sigma\_\alpha_{0.61}^{1.4}$	Name[d]	S_{VLA} /mJy	σ_S_{VLA} /mJy	S_{VLBA} /mJy	σ_S_{VLBA} /mJy	θ_{VLA}[e] /arcsec	R[f]
10CJ104849+571417	10:48:49.47	+57:14:17.48	1.82	0.17	0.74	0.03	0	0.71	0.04	1	0.8	0.06	J104849.8+571415	10.84	0.048			9.0	
∗10CJ104858+570933	10:48:58.99	+57:09:33.03	0.50	0.16	0.50	0.14	0	0.47	0.13	2	0.59	0.39	J104858.3+570925	1.384	0.046	0.642	0.121	8.8	2.16
10CJ104906+571156	10:49:06.21	+57:11:56.35	1.86	0.21	0.69	0.04	0	0.83	0.05	1	0.29	0.06	J104905.1+571151	14.612	0.730			37.9	
∗10CJ104934+570613	10:49:34.42	+57:06:13.69	2.09	0.17	0.76	0.03	0	0.78	0.04	1	0.72	0.05	J104934.3+570608	14.787	0.082	0.295	0.080	19.6	50.13
∗10CJ104943+571739	10:49:43.82	+57:17:39.14	1.17	0.13	−0.16		1	−0.08	0.05	2	−0.39		J104943.8+571737	1.013	0.025	0.666	0.084	8.9	1.52
∗10CJ104944+570635	10:49:44.12	+57:06:35.92	0.81	0.16	0.08	0.07	0	0.30	0.08	1	−0.54	0.11	J104944.1+570628	1.275	0.034	0.916	0.113	9.1	1.39
∗10CJ104947+571355	10:49:47.49	+57:13:55.24	0.68	0.12	0.07		1	−0.02	0.07	2	0.32		J104947.8+571354	0.607	0.026	0.490	0.073	9.0	1.24
10CJ104950+570117	10:49:50.50	+57:01:17.79	0.66	0.12	0.70	0.06	0	0.86	0.08	1	0.22	0.13	J104950.4+570120c	1.047	0.083			28.1	
∗10CJ104954+570456	10:49:54.30	+57:04:56.77	5.64	0.32	−0.63	0.04	0	−0.71	0.03	2	−0.42	0.14	J104954.2+570456	1.376	0.034	0.633	0.091	8.9	2.17
∗10CJ105007+572020	10:50:07.93	+57:20:20.28	1.18	0.10	0.11	0.04	0	0.28	0.04	2	−0.38	0.09	J105008.1+572018	1.668	0.019	1.195	0.127	9.9	1.70
∗10CJ105009+570724	10:50:09.71	+57:07:24.56	1.05	0.18	0.57	0.05	0	0.67	0.08	1	0.29	0.12	J105010.4+570724b	2.302	0.023	2.335	0.240	8.6	2.40
∗10CJ105015+570258	10:50:15.38	+57:02:58.44	0.51	0.13	0.68	0.08	0	0.77	0.11	1	0.39	0.15	J105015.6+570258	3.155	0.045	0.983	0.117	13.9	3.21
10CJ105034+572922	10:50:34.05	+57:29:22.91	1.20	0.12	−0.01	0.04	0	−0.52	0.04	2	1.46	0.12	J105034.2+572922	0.336	0.019			9.3	
10CJ105038+565810	10:50:38.75	+56:58:10.04	0.54	0.14	0.43	0.09	0	0.48	0.11	2	0.30	0.10	J105039.1+565806	1.520	0.043			9.9	
∗10CJ105039+572339	10:50:39.56	+57:23:39.77	1.08	0.12	0.34	0.04	0	0.76	0.08	1	−0.88	0.19	J105039.6+572336	4.936	0.022	3.972	0.399	13.1	1.24
∗10CJ105040+573308	10:50:40.65	+57:33:08.68	0.89	0.12	0.16		1	0.00	0.06	2	0.61		J105040.7+573308	0.703	0.019	0.984	0.112	8.7	0.71
10CJ105104+570148	10:51:04.45	+57:01:48.35	0.54	0.15	0.64	0.09	0	0.84	0.13	1	0.06	0.16	J105104.7+570150b	1.409	0.051			14.5	
∗10CJ105115+573552	10:51:15.54	+57:35:52.32	0.53	0.14	0.72	0.08	0	0.65	0.11	1	0.92	0.03	J105115.0+573552	2.362	0.020	0.133	0.049	9.1	17.76
∗10CJ105122+570854	10:51:22.18	+57:08:54.76	1.26	0.12	0.84	0.03	0	0.87	0.05	1	0.73	0.06	J105122.1+570854	10.644	0.532	10.562	0.921	25.8	1.01
∗10CJ105123+573229	10:51:23.11	+57:32:29.40	0.38	0.10	0.49	0.08	0	0.78	0.13	1	−0.38	0.21	J105122.9+573228	1.434	0.016	1.343	0.138	8.9	1.07
∗10CJ105128+570901	10:51:28.10	+57:09:01.68	2.25	0.16	0.67	0.02	0	0.70	0.03	1	0.56	0.05	J105127.8+570854	12.570	0.628	0.506	0.062	29.4	24.84
∗10CJ105132+571114	10:51:32.63	+57:11:14.59	2.92	0.19	0.34	0.03	0	0.60	0.04	1	−0.42	0.13	J105132.4+571114	12.756	0.637	1.157	0.120	158.7	11.03
∗10CJ105136+572944	10:51:36.99	+57:29:44.40	1.12	0.10	0.41	0.03	0	0.38	0.08	1	0.50	0.22	J105137.0+572940	2.532	0.012	0.402	0.049	10.2	6.30
∗10CJ105142+573447	10:51:42.02	+57:34:47.81	0.79	0.10	−0.04		1	0.02	0.05	2	−0.21		J105142.0+573447	1.090	0.015	1.168	0.122	8.9	0.93
∗10CJ105142+573557	10:51:42.07	+57:35:57.97	1.95	0.15	0.45	0.02	0	0.37	0.05	1	0.67	0.10	J105142.1+573554	1.268	0.017	1.243	0.130	11.8	3.97
∗10CJ105148+573245	10:51:48.76	+57:32:45.04	0.52	0.10	0.08		1	0.24	0.08	2	−0.41		J105148.7+573248	0.807	0.018	0.944	0.099	8.6	0.85
∗10CJ105150+572637	10:51:50.02	+57:26:37.10	0.30	0.09	0.28		1	0.09	0.12	2	0.82		J105150.1+572635	0.118	0.009	0.272	0.036	9.2	0.43
∗10CJ105152+570950	10:51:52.33	+57:09:50.63	0.37	0.11	0.81	0.09	0	0.85	0.14	1	0.70	0.17	J105152.4+570950	3.118	0.019	2.965	0.216	8.8	1.05
∗10CJ105206+574111	10:52:06.40	+57:41:11.78	3.35	0.20	0.46	0.02	0	0.50	0.03	1	0.35	0.06	J105206.5+574109	10.542	0.021	8.420	0.555	8.7	1.25
10CJ105224+570837	10:52:24.96	+57:08:37.66	0.42	0.12	0.53	0.09	0	0.95	0.14	1	−0.69	0.19	J105224.5+570838	2.157	0.028			15.4	
10CJ105225+573323	10:52:25.84	+57:33:23.31	0.58	0.15	0.85	0.08	0	0.90	0.11	1	0.69	0.10	J105225.6+573322	4.873	0.024			13.1	
∗10CJ105237+573058	10:52:37.01	+57:30:58.85	5.16	0.30	1.06	0.02	0	1.05	0.03	1	1.09	0.04	J105237.3+573103	63.323	3.166	0.607	0.066	48.4	104.32
∗10CJ105240+572322	10:52:40.87	+57:23:22.96	0.54	0.09	0.42	0.06	0	0.50	0.07	1	0.19	0.07	J105241.4+572320	1.740	0.012	0.184	0.030	9.9	9.46
∗10CJ105243+574817	10:52:43.34	+57:48:17.11	1.00	0.13	−0.01	0.05	0	0.26	0.05	2	−0.80	0.13	J105243.3+574813	1.857	0.039	1.237	0.159	9.0	1.50
∗10CJ105253+572348	10:52:53.86	+57:23:48.65	0.47	0.08	0.11		1	−0.36	0.07	2	1.46		J105254.2+572341	0.157	0.010	0.140	0.028	8.9	1.12
∗10CJ105255+571949	10:52:55.07	+57:19:49.35	0.39	0.11	0.75	0.09	0	0.91	0.13	1	0.28	0.18	J105255.3+571950	3.107	0.013	2.921	0.293	8.8	1.06
10CJ105327+574546	10:53:27.36	+57:45:46.09	0.81	0.12	0.73	0.05	0	0.89	0.07	1	0.28	0.09	J105327.6+574543	6.618	0.330			30.7	
10CJ105337+574242	10:53:37.29	+57:42:42.26	0.38	0.09	0.26	0.08	0	0.70	0.10	2	−1.02	0.14	J105337.3+574240	0.995	0.026			10.5	
∗10CJ105341+571951	10:53:41.01	+57:19:51.29	0.55	0.09	0.47	0.06	0	0.42	0.07	2	0.60	0.06	J105340.9+571952	1.554	0.015	0.283	0.044	8.9	5.49
∗10CJ105342+574438	10:53:42.19	+57:44:38.11	1.80	0.14	0.50	0.03	0	0.59	0.04	1	0.23	0.09	J105342.1+574436	7.825	0.391	2.152	0.194	40.4	3.64
∗10CJ105400+573324	10:54:00.97	+57:33:24.63	0.67	0.13	0.55	0.06	0	0.62	0.10	1	0.37	0.17	J105400.5+573321	3.016	0.025	0.222	0.043	14.8	13.59
∗10CJ105425+573700	10:54:25.05	+57:37:00.78	25.47	0.92	0.79	0.01	0	0.83	0.02	1	0.65	0.01	J105427.0+573644	181.160	9.058	1.658	0.176	67.6	109.26
∗10CJ105441+571640	10:54:41.45	+57:16:40.84	0.78	0.10	0.67	0.04	0	0.63	0.07	1	0.78	0.14	J105442.1+571639	2.778	0.037	0.945	0.136	8.9	2.94
10CJ105515+573256	10:55:15.50	+57:32:56.87	0.63	0.10	0.89	0.05	0	0.94	0.07	1	0.75	0.08	J105516.0+573257	7.104	0.355			29.6	

Notes:

a) ID and positions from the 10C catalogue.

b) Flag1 = 1 if value of $\alpha_{0.61}^{15.7}$ is an upper limit, Flag1 = 0 otherwise.

c) Indicates 1.4-GHz flux density used to calculate $\alpha_{1.4}^{15.7}$. Flag2 = 1 if value is from NVSS, Flag2 = 2 if value is from Guglielmino et al. (2012) WSRT map.

d) Source name from M2013 and Ibar et al. catalogues.

e) Maximum angular size taken from the Ibar et al. (2009) 1.4-GHz VLA catalogue. For single sources this value corresponds to twice the maximum Full Width Half Maximum (FWHM) of the synthesised beam (see Section 4.2.5).

f) Ratio of the VLA integrated flux density to the VLBA integrated flux density (see Section 4.2.5).

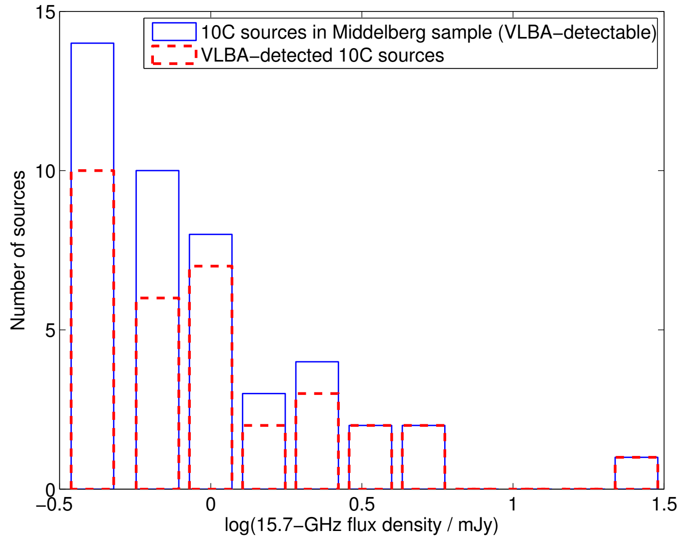

Figure 4.2: 15.7-GHz flux density distribution for the 44 10C sources in the Middelberg sample, showing the 33 sources which are detected by the VLBA observations separately.

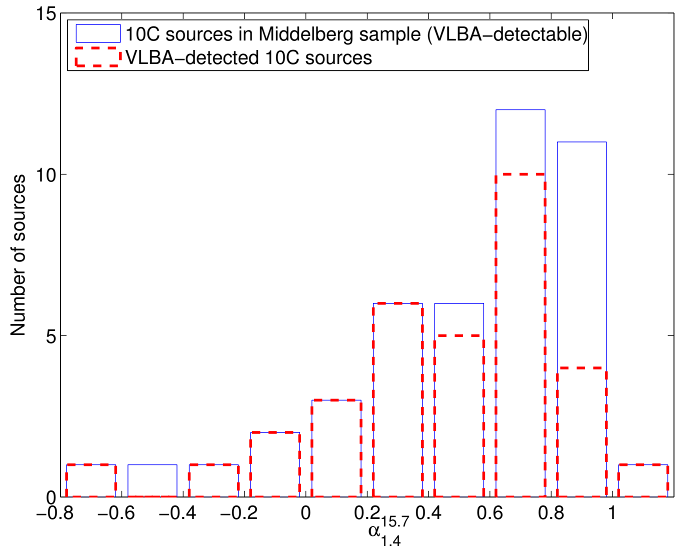

Figure 4.3: Spectral index distribution for the 44 10C sources in the Middelberg sample, showing the 33 sources which are detected by the VLBA observations separately. Spectral index values are taken from Chapter 2.

are detected by the VLBA observations. This is much higher than the percentage of sources in the total Middelberg sample which are detected by the VLBA observations (65 out of 217 i.e. 30 percent). However nothing significant can be deduced from this since the sources in the 10C sample have higher 1.4-GHz flux densities than the majority of sources in the Middelberg sample (e.g. 14 percent of the 10C sources in the Middelberg sample have $S_{1.4\mathrm{GHz}} < 1$ mJy compared with 75 percent of sources in the total Middelberg sample) and, as shown in M2013, the probability of detection is a strong function of flux density.

The 15.7-GHz flux density distributions of the 44 10C sources in the Middelberg sample and the 33 10C sources which are detected in the VLBA observations are shown in Fig 4.2. The flux density distribution of the 10C VLBA-detected sources is similar to that of the 10C sources in the Middelberg sample (although, significantly, all seven of the brightest sources with $S_{15.7\ \mathrm{GHz}} > 2$ mJy are detected by the VLBA observations). There are VLBA-detected sources with 15.7-GHz flux densities as low as $S_{15.7\ \mathrm{GHz}} = 0.3$ mJy so VLBI components are being found in the majority of the faintest 10C sources.

The fact that 75 percent of the 10C sources in the Middelberg sample are detected by the VLBA observations, and therefore must be AGN, rules out the possibility discussed in Chapter 3 that the 10C population is dominated by starburst galaxies. These results therefore support the conclusions in Chapter 3 that the majority of the 10C population are AGN, such as FRI sources. Thus the proportions of sources in S^3, which predicts that the faint, high-frequency population is dominated by FRI sources, may well be correct. If this is the case, the emission from the FRI sources must be modelled incorrectly, because, as described in Section 4.1, the simulation does not accurately reproduce the observed spectral index distribution. This is probably due to incorrect modelling of the emission from the cores of FRI sources (for example, there is no attempt to include the effects of self-absorption in compact objects), as well as the lack of spectral ageing in the overall source model.

4.3.2 Spectral properties

The spectral index distribution of the 44 10C sources in the Middelberg sample and the 33 detected in the VLBA observations are shown in Figure 4.3, using the values from Chapter 2. The sources which are not detected in the VLBA observations tend to have steeper spectra than those which are detected, with 9 of the 11 undetected sources having $\alpha_{1.4}^{15.7} > 0.5$ (of the other two, one has $\alpha_{1.4}^{15.7} = 0.47$ and the other has a rising spectrum and is discussed below). However, many of the sources which are detected by the VLBA observations also have steep spectra. In fact, out of the 26 steep spectrum 10C sources, 17 (65 percent) are detected by the VLBA observations.

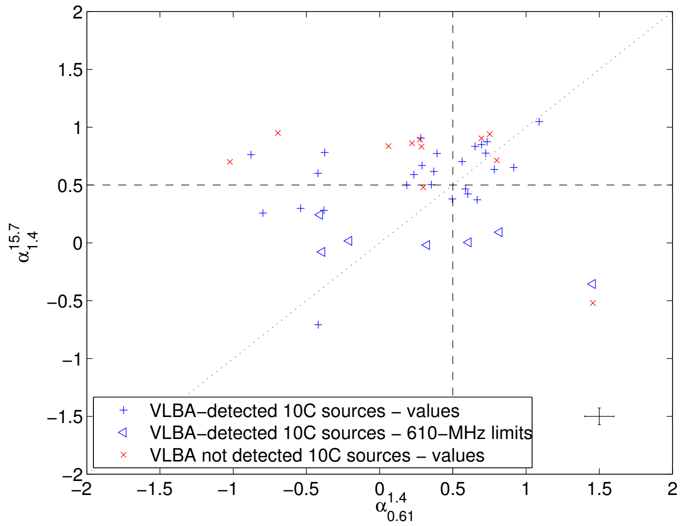

Figure 4.4: Colour–colour plot for 10C sources in the Middelberg sample, showing those which are and are not detected by the VLBA observations separately. Spectral index values for all sources are taken from Chapter 2. Sources which have an upper limit at 610 MHz are shown by triangles and could move to the left. The horizontal and vertical dashed lines are at $\alpha = 0.5$, the cutoff between steep and flat spectrum sources. The diagonal dotted line is at $\alpha^{15.7}_{1.4} = \alpha^{1.4}_{0.61}$, sources which lie above and to the left of this line have spectra which are steeper between 15.7 and 1.4 GHz than between 1.4 GHz and 610 MHz. For clarity individual error bars have been omitted but a point representing the median errors is shown in the bottom right hand corner for reference.

Further insights into the spectral shape of 10C sources in the Middelberg sample can be gained from Figure 4.4, a radio colour–colour plot which uses the spectral index values $\alpha^{15.7}_{1.4}$ and $\alpha^{1.4}_{0.61}$ from Chapter 2. The majority (9 out of 11) of the sources which are not detected by the VLBA observations (shown by red crosses) have $\alpha^{15.7}_{1.4} > \alpha^{1.4}_{0.61}$ and therefore have spectra which steepen at higher frequencies. There is a larger spread in values of $\alpha^{1.4}_{0.61}$ than of $\alpha^{15.7}_{1.4}$, particularly towards negative values; 14 of the sources which display a flat or rising spectrum between 610 MHz and 1.4 GHz ($\alpha^{1.4}_{0.61} < 0.5$) have turned over and have a steep spectrum ($\alpha > 0.5$) by 15.7 GHz. These sources could therefore be GPS sources.

All but two of the 10C sources detected by the VLBA observations have flat spectra; this is not suprising as flat spectrum emission generally originates from compact core regions, which are much more likely to have a high enough surface brightness to be visible in the VLBA observations. Conversely, steep spectrum emission tends to come from more extended regions, which do not have high enough surface brightness to be detectable with the VLBA observations – consistent with the fact that most of the 10C sources not detected by the VLBA observations have steep spectra. The majority of these undetected sources have a spectrum which steepens with frequency, supporting the idea that these sources do not have a dominant core, as this

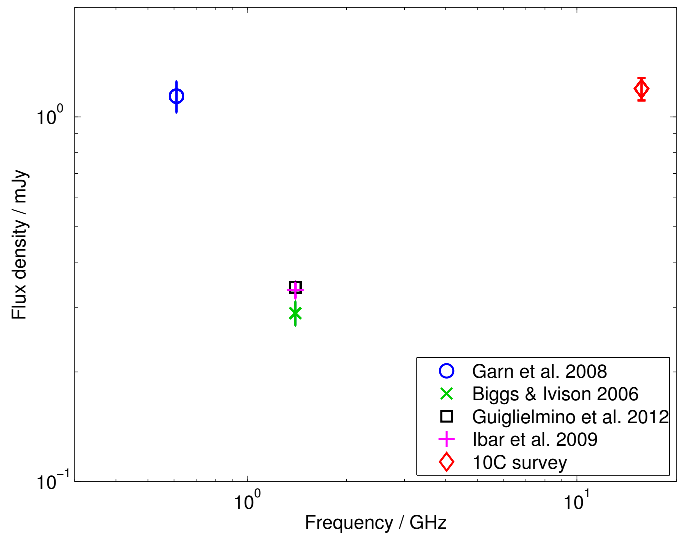

Figure 4.5: Spectrum for source 10CJ105034+572922 which has an unusual spectral shape and is not detected by the VLBA observations. Where error bars are not shown they are smaller than the symbol plotted.

would contribute more to the flux density at higher frequencies.

As mentioned above, one 10C source not detected by the VLBA observations has a rising spectrum, with $\alpha_{1.4}^{15.7} = -0.5$. The spectrum of this source is shown in Figure 4.5; the source has an interesting spectrum as it is very steep ($\alpha_{0.61}^{1.4} = 1.5$) at lower frequencies, but then it turns up and rises at higher frequencies ($\alpha_{1.4}^{15.7} = -0.51$). The likely explanation for the rise at high frequencies is the presence of a compact core which dominates the emission at 15 GHz; however the emission at 1.4 GHz is likely still to be dominated by the more extended steep spectrum region with the core being too faint to be detected by the VLBA observations. This source highlights the complicated spectral shapes manifested at higher frequencies and the difficulties this presents when understanding and modelling this population.

4.3.3 Source morphology

The two measures used to probe source morphology on different scales are described in Section 4.2.5. In Chapter 2 I investigated the extent of the radio emission of the 10C sources on arcsec scales using FIRST and GMRT data (beam size ≈ 5 arcsec) along with WSRT data (beam size ≈ 11 arcsec). These new VLBA data allow me to probe the structure of these sources on much smaller scales (≈ 10 milliarcsec).

Figures 4.6 and 4.7 show these measures against spectral index for the 33 10C sources detected in the VLBA observations. Figure 4.6 shows that, as expected, all of the significantly extended sources (with $\theta_{\rm VLA} > 12$ arcsec) have a steep spectrum. There are, however, four

Table 4.3: Properties of sources detected by the VLBA which are not in the 10C catalogue. All flux densities listed are integrated flux densities. The two sources without any spectral index information are the two sources which lie very close to (but do not match to) a bright 10C source, meaning I am unable to place a limit on their flux density (see Section 4.2.2 for more details).

Name[a]	RA (J2000)	Dec (J2000)	$S_{\rm VLA}$ /mJy	$\sigma\_S_{\rm VLA}$ /mJy	$S_{\rm VLBA}$ /mJy	$\sigma\_S_{\rm VLBA}$ /mJy	$S_{\rm 10C}$ map[b] /mJy	$\sigma\_S_{\rm 10C}$ map[b] /mJy	10C 3σ limit[c] /mJy	$\alpha_{1.4}^{15.7}$	$\sigma\_\alpha_{1.4}^{15.7}$	Flag[d]	$\theta_{\rm VLA}$[e] /arcsec	R[f]
J104922.9+571901	10:49:22.87	+57:19:01.8	2.425	0.038	2.209	0.234			0.28	0.89		1	8.6	1.10
J104951.3+572812	10:49:51.33	+57:28:12.3	1.083	0.037	0.922	0.119	0.181	0.050		0.74	0.01	2	9.0	1.17
J105012.6+571137	10:50:12.56	+57:11:37.0	0.616	0.019	0.415	0.059	0.232	0.057		0.40	0.01	2	9.2	1.48
J105025.5+570453	10:50:25.52	+57:04:53.4	0.250	0.023	0.271	0.061			0.27	−0.04		1	8.3	0.92
J105032.7+572646	10:50:32.67	+57:26:46.6	0.466	0.015	0.497	0.064	0.194	0.035		0.36	0.01	2	8.7	0.94
J105034.0+572152	10:50:34.03	+57:21:52.4	1.005	0.017	0.220	0.042			0.12	0.87		1	8.9	4.57
J105045.2+573734	10:50:45.23	+57:37:34.0	0.858	0.034	0.290	0.081			0.15	0.74		1	9.1	2.96
J105045.9+570822	10:50:45.90	+57:08:22.4	0.344	0.017	0.153	0.042			0.19	0.25		1	8.9	2.25
J105106.7+571152	10:51:06.71	+57:11:52.8	0.355	0.017	0.282	0.043	0.468	0.150		−0.11	0.03	2	9.1	1.26
J105117.6+571639	10:51:17.63	+57:16:39.3	0.398	0.011	0.411	0.049	0.279	0.080		0.15	0.02	2	8.6	0.97
J105120.8+573037	10:51:20.82	+57:30:37.4	0.336	0.014	0.294	0.044			0.17	0.29		1	8.8	1.14
J105120.9+573532	10:51:20.85	+57:35:32.5	8.496	0.025	8.966	0.898							8.7	0.95
J105134.1+570922	10:51:34.12	+57:09:22.1	0.348	0.025	0.278	0.044			0.24	0.15		1	9.0	1.25
J105158.9+572330	10:51:58.92	+57:23:30.1	0.234	0.009	0.304	0.038			0.13	0.25		1	8.6	0.77
J105207.5+571903	10:52:07.49	+57:19:04.0	0.324	0.011	0.269	0.036	0.126	0.051		0.39	0.01	2	9.0	1.20
J105211.0+572908	10:52:11.03	+57:29:08.0	1.713	0.012	1.585	0.160	0.121	0.035		1.10	0.01	2	8.7	1.08
J105230.6+571312	10:52:30.61	+57:13:12.4	0.282	0.012	0.291	0.042			0.14	0.30		1	9.0	0.97
J105231.8+570650	10:52:31.81	+57:06:50.5	1.137	0.020	1.015	0.113	0.464	0.098		0.37	0.02	2	8.8	1.12
J105234.0+573057	10:52:34.00	+57:30:57.2	0.144	0.018	0.143	0.029							8.0	1.01
J105245.3+573616	10:52:45.34	+57:36:16.3	0.448	0.016	0.267	0.041	0.187	0.052		0.36	0.01	2	10.4	1.68
J105250.0+574450	10:52:50.02	+57:44:51.0	0.988	0.024	0.309	0.072	0.265	0.041		0.54	0.01	2	8.7	3.20
J105258.0+570834	10:52:58.02	+57:08:34.9	0.375	0.018	0.471	0.070	0.263	0.063		0.15	0.01	2	8.8	0.80
J105304.5+571547	10:53:04.49	+57:15:47.6	0.198	0.011	0.155	0.034			0.18	0.04		1	8.9	1.28
J105308.1+572222	10:53:08.08	+57:22:22.9	0.317	0.012	0.145	0.029	0.153	0.040		0.30	0.01	2	9.2	2.19
J105314.0+572448	10:53:13.98	+57:24:48.6	0.127	0.012	0.142	0.029	0.167	0.020		−0.11	0.01	2	9.8	0.89
J105319.0+571851	10:53:19.02	+57:18:51.8	0.548	0.014	0.229	0.037	0.156	0.048		0.52	0.01	2	9.1	2.39
J105325.3+572911	10:53:25.31	+57:29:11.8	0.602	0.012	0.199	0.033			0.14	0.61		1	9.2	3.03
J105327.5+573316	10:53:27.49	+57:33:17.1	0.195	0.013	0.219	0.036			0.13	0.18		1	8.6	0.89
J105335.8+572157	10:53:35.85	+57:21:57.3	0.147	0.010	0.226	0.038			0.12	0.07		1	8.4	0.65
J105356.5+572244	10:53:56.46	+57:22:44.8	0.249	0.014	0.258	0.044			0.14	0.24		1	8.8	0.97
J105401.2+573207	10:54:01.21	+57:32:07.5	0.267	0.013	0.142	0.039			0.12	0.32		1	8.6	1.88
J105423.3+573446	10:54:23.32	+57:34:46.4	0.661	0.020	0.598	0.078			0.31	0.32		1	8.5	1.11

Notes:

a) Source name and positions from M2013 and Ibar et al. catalogues.

b) 15.7-GHz flux density value from 10C map (see Section 4.2.3 for details).

c) Three times the local rms noise in the 10C map.

d) The 15.7-GHz value used to calculate $\alpha_{1.4}^{15.7}$. Flag = 1, if upper limit is used, Flag = 2, if value from 10C map is used.

e) Maximum angular size taken from the Ibar et al. (2009) 1.4-GHz VLA catalogue. For single sources this value corresponds to twice the maximum Full Width Half Maximum (FWHM) of the synthesised beam (see Section 4.2.5).

f) Ratio of the VLA integrated flux density to the VLBA integrated flux density (see Section 4.2.5).

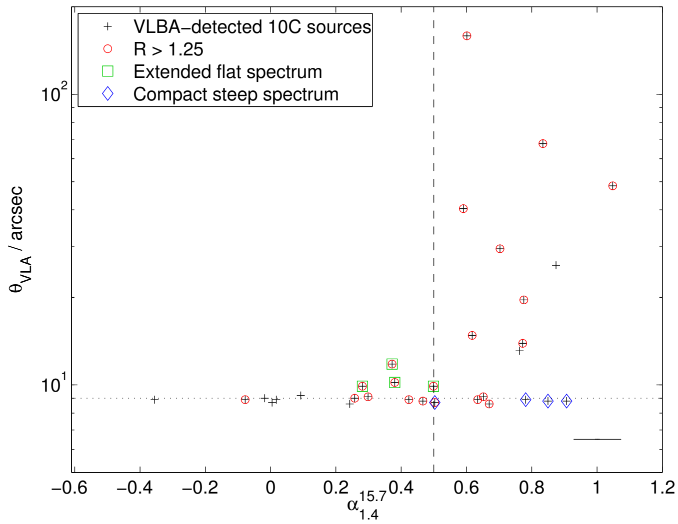

Figure 4.6: VLA size, $\theta_{\rm VLA}$, against spectral index, $\alpha_{1.4}^{15.7}$, for the 33 10C sources detected by the VLBA. Sources with $R > 1.25$ are circled in red (for comparison with Figure 4.7). The vertical dashed line is at $\alpha = 0.5$, the cutoff between steep and flat spectrum sources. The horizontal dotted line is at $\theta_{\rm VLA} = 9$ arcsec, and sources with values of $\theta_{\rm VLA}$ larger than this are resolved. The four extended, flat spectrum sources are marked by squares and the compact, steep spectrum sources are marked by diamonds. For clarity individual error bars have been omitted but a point representing the median error in the x axis is shown in the bottom right hand corner for reference.

sources which are resolved with the VLA ($9 < \theta_{\rm VLA} < 12$ arcsec) in the 10C sample which have flat spectra (these are marked with green squares in Figures 4.6 and 4.7). This is consistent with the findings in Chapter 3 that there is a small population of extended, flat spectrum sources present, indicating that emission from the cores of these extended sources is becoming dominant at higher frequencies.

Figure 4.7 shows $R = S_{\rm VLA}/S_{\rm VLBA}$ as a function of spectral index. All sources with $\theta_{\rm VLA} > 9$ arcsec are circled for comparison with Figure 4.6, this shows that unsurprisingly the majority of the sources with large values of R have $\theta_{\rm VLA} > 9$ arcsec and are therefore resolved on arcsec scales. This plot also shows that most of the flat spectrum sources have smaller values of $R = S_{\rm VLA}/S_{\rm VLBA}$ than the steep spectrum sources, indicating that they are more dominated by emission from a compact core. All of the sources with rising spectra ($\alpha < 0$) have values of R close to unity, indicating that all of the emission detected by the VLA is also detected by the VLBA observations and therefore, as expected, comes from a very compact region. There are six steep spectrum sources with values of R close to unity ($R < 1.25$). Two of these sources have values of $\theta_{\rm VLA} > 9$ arcsec therefore, although they may have a compact core, they are clearly extended on arcsec scales. Of the remaining four compact sources (which have $\theta_{\rm VLA} <$

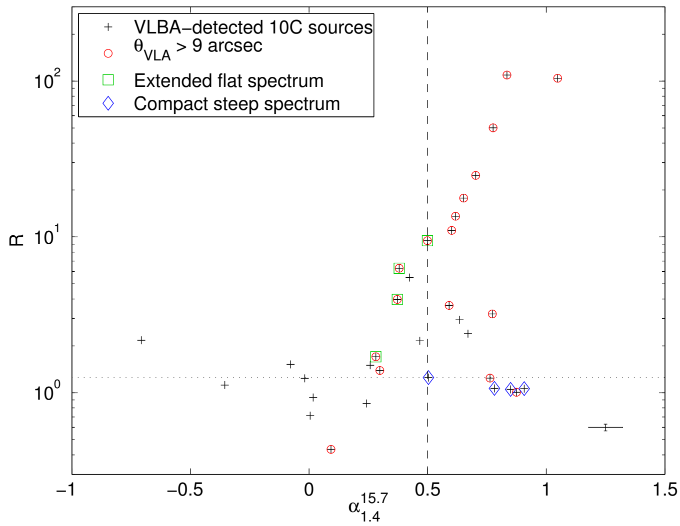

Figure 4.7: The ratio of the VLA integrated flux density to the VLBA integrated flux density ($R = S_{\rm VLA}/S_{\rm VLBA}$) against spectral index for the 33 10C sources detected by the VLBA. Sources with $\theta_{\rm VLA} > 9$ arcsec are circled in red (for comparison with Figure 4.6). The vertical dashed line is at $\alpha = 0.5$, the cutoff between steep and flat spectrum sources, and the horizontal dotted line is at $R = 1.25$. The four extended, flat spectrum sources are marked by squares and the compact, steep spectrum sources are marked by diamonds. For clarity individual error bars have been omitted but a point representing the median errors is shown in the bottom right hand corner for reference.

9 arcsec), one (10CJ105152+570950) has a steep spectrum down to 610 MHz ($\alpha_{1.4}^{15.7} = 0.85$, $\alpha_{0.61}^{1.4} = 0.70$), which is surprising for an object this compact. The lower frequency spectral index is slightly lower than the higher frequency spectral index so the spectrum may turn over below 610 MHz. One source has a spectrum which rises at lower frequencies (between 610 MHz and 1.4 GHz) so it therefore peaks between 1.4 GHz and 15.7 GHz, typical of a gigahertz peaked-spectrum (GPS) source, while the spectra of the other two sources peak at slightly lower frequencies, and are therefore more typical of compact, steep spectrum sources (O'Dea 1998).

In Chapter 3 I found in the faint 10C sample a small number of extended, flat spectrum sources, four of which are seen in this sample. Here I have also found that the faint 10C sample contains a number (4/33, 12 percent) of compact sources with steep spectra. This shows that although the majority of the steep spectrum sources are extended and the majority of the flat spectrum sources are compact, high frequency spectral index is not always a good indicator of source structure.

Chhetri et al. (2013) investigated the angular sizes of sources in the Australia Telecope 20 GHz (AT20G) catalogue, which has a flux density limit of 40 mJy so probes a population with higher flux densities than the 10C survey. Chhetri et al. found that 77 percent of sources in

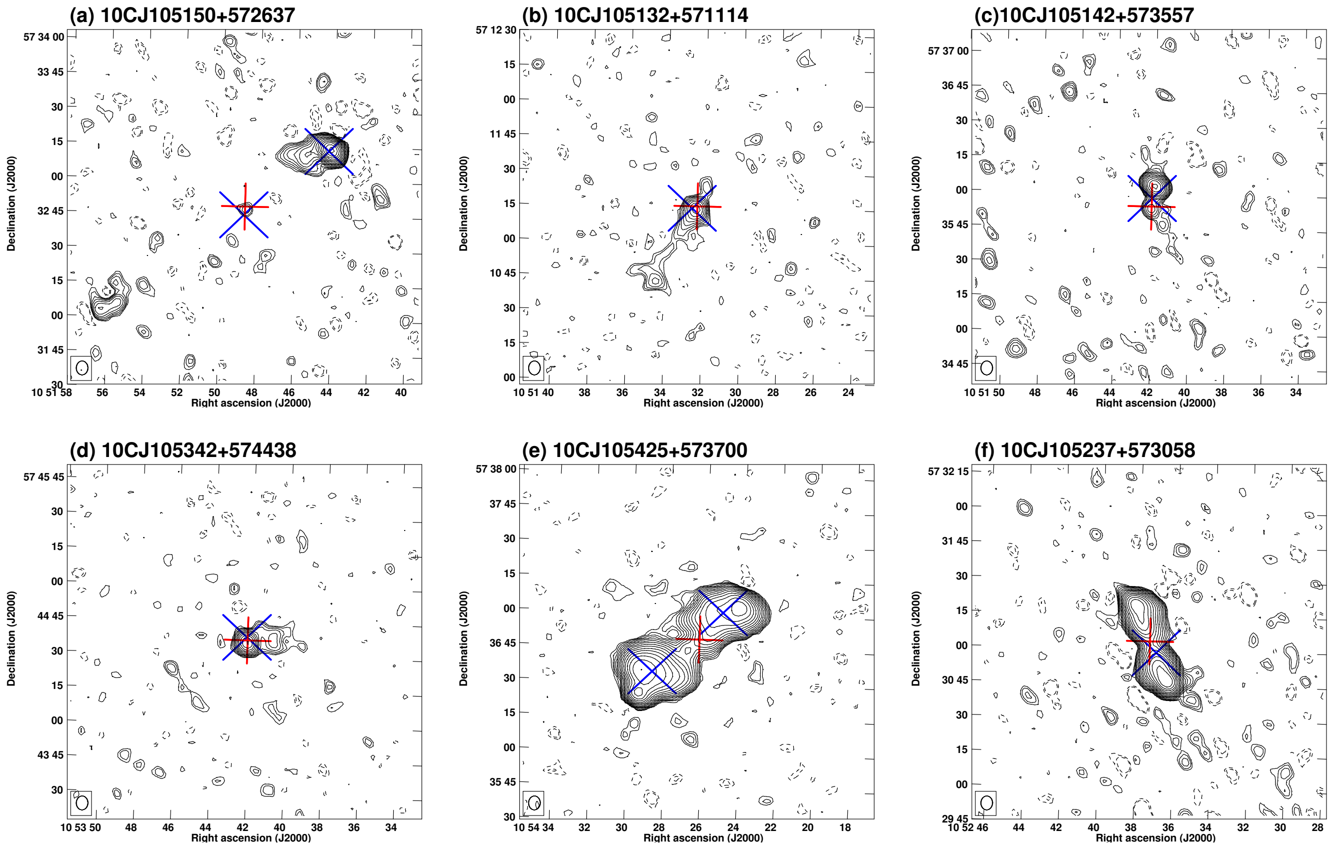

Figure 4.8: Example 610-MHz GMRT images of some extended sources detected by the VLBA (taken from (Garn et al. 2008, 2010) GMRT data). Source names are the IDs from the 10C catalogue, listed in Table 4.2. Crosses (×) show the positions of the 10C source, pluses (+) show the positions of the VLBA sources and are 20 arcsec across. The contours are drawn at $(\pm 2\sqrt{2^n}, n = 0, 1 \ldots 7) \times a$ mJy where $a = 0.062$ for (a), 0.077 for (b), 0.061 for (c), 0.087 for (d), 0.098 for (e) and 0.077 for (f).

the AT20G catalogue are compact, with angular sizes less than 0.15 arcsec. They produce a plot which is similar to Figure 4.7, in which most of the sources lie in approximately the same regions. They identify a population of compact steep-spectrum sources and find a smooth transition between this population and GPS sources.

4.3.4 Extended source structure

Further information about the structure of the extended sources can be gained by looking at GMRT images of these sources (from the Garn et al. 2008, 2010 data) which have a resolution of 6×5 arcsec^2; GMRT images of six extended sources detected in the VLBA observations are shown in Figure 4.8. In their discussion of the properties of the VLBA-detected sources, M2013 assume that all the extended emission comes from star-formation. There is evidence here that this assumption is not true in a significant number of cases; the six sources shown in Figure 4.8 display extended structures that appear to relate to the radio AGN, rather than star formation. Of the 33 10C sources detected by the VLBA, nine show evidence of extended structure relating to extragalatic radio activity. This is consistent with the idea discussed in Section 4.3.1 that this population is dominated by FRI and FRII sources, where the extended structure is due to emission produced by radio jets. M2013 use the assumption that all the extended emission originates from star formation to show that the most luminous AGN tend to have higher levels of star-formation activity; they conclude that this argues against quenching of star formation by AGN feedback and instead provides evidence that radio AGN activity might enhance star-formation. The results in this Chapter suggest that the underlying assumption is not correct in a significant number of cases and therefore these conclusions may not necessarily hold.

4.3.5 Optical properties

Fotopoulou et al. (2012) have calculated photometric redshifts for this part of the Lockman Hole field (this catalogue is described in more details in Chapter 5). Out of the 33 10C sources which are detected by the VLBA observations, 23 have photometric redshifts. The median redshift of these 10C sources is 0.91 ± 0.16, compared to a median redshift for all VLBA-detected sources of 0.91 ± 0.14. There is no significant difference in the source type classifications in the Fotopoulou et al. catalogue of the VLBA-detected sources which are and are not in the 10C catalogue – both samples are dominated by early-type or bulge dominated galaxies (along with heavily extinct starbursts, which is probably due to a degeneracy in the fit as discussed in M2013). A full analysis of the multi-wavelength properties of objects associated with 10C sources in the whole Lockman Hole field is presented in Chapters 5, 6 and 7.

4.4 Properties of VLBA sources

In this section I look at the 15 GHz properties of the Middelberg VLBA-detected sample of 65 sources. The spectral index and morphology properties of the VLBA-detected sources which match to the 10C catalogue are given in Table 4.2, the relevant rows being marked with an asterix. The properties of the 32 sources detected by the VLBA observations which are not in the 10C sample are summarised in Table 4.3. The 1.4-GHz flux density distributions of the VLBA-detected sources and those which are also in the 10C catalogue are shown in Figure 4.9, which shows that those sources which are in the 10C catalogue have larger 1.4-GHz flux densities than those which do not match to 10C. The sources which are not in the 10C catalogue for which a 15.7-GHz flux density value was calculated from the 10C map are also shown, these tend to be some of the brighter undetected sources. Figure 4.10 shows the VLA size

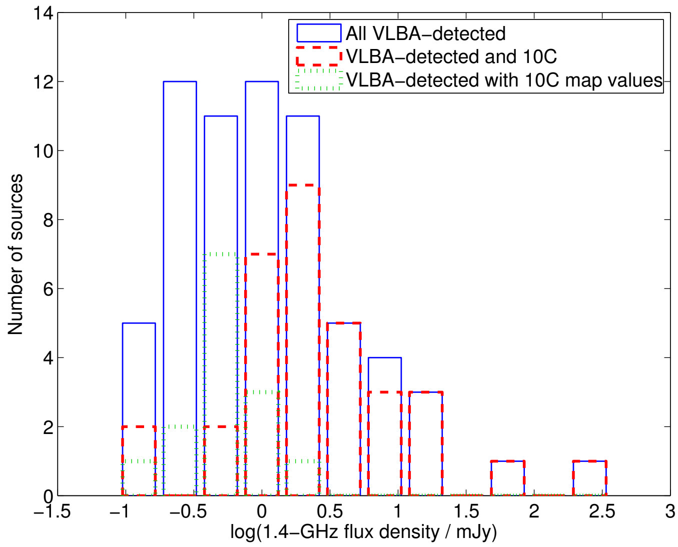

Figure 4.9: 1.4-GHz flux density distribution for all 65 sources detected by the VLBA observations, with the subsample of sources also in the 10C sample shown separately, as are those sources which are not detected in the 10C catalogue for which a 15.7-GHz flux density value is available from the 10C map.

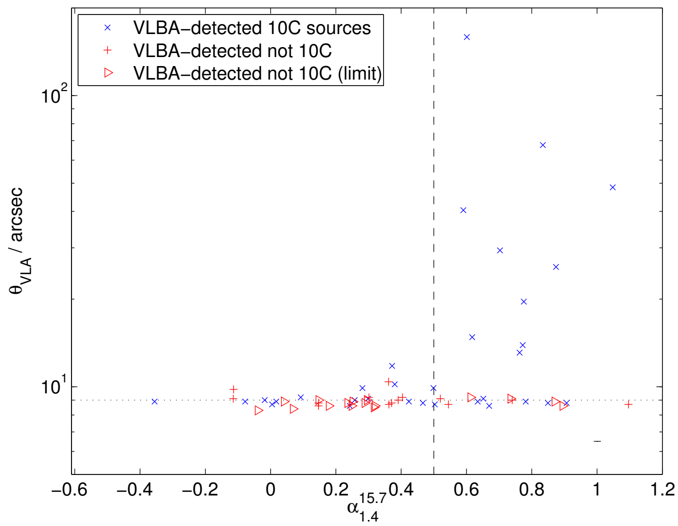

Figure 4.10: VLA size, $\theta_{\rm VLA}$, against spectral index, $\alpha_{1.4}^{15.7}$, for all sources detected by the VLBA observations. Sources which are also in the 10C sample are shown separately. Lower limits on spectral index are indicated by triangles. The vertical dashed line is at $\alpha = 0.5$, the cutoff between steep and flat spectrum sources. The horizontal dotted line is at $\theta_{\rm VLA} = 9$ arcsec, and sources with values of $\theta_{\rm VLA}$ larger than this are resolved. For clarity individual error bars have been omitted but a point representing the median error in the x axis is shown in black in the bottom right hand corner for reference.

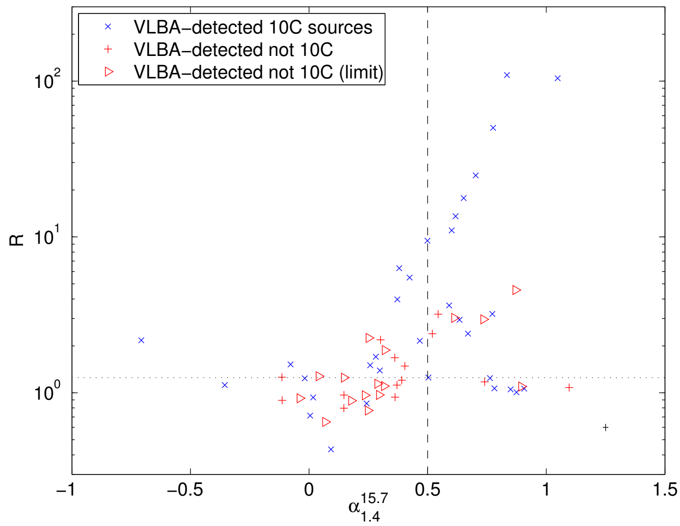

Figure 4.11: The ratio of the VLA integrated flux density to the VLBA integrated flux density ($R = S_{\rm VLA}/S_{\rm VLBA}$) against spectral index for all sources detected by the VLBA observations. Sources which are also in the 10C sample are shown separately. Lower limits on spectral index are indicated by triangles. The vertical dashed line is at $\alpha = 0.5$, the cutoff between steep and flat spectrum sources, and the horizontal dotted line is at $R = 1.25$. For clarity individual error bars have been omitted but a point representing the median errors is shown in black in the bottom right hand corner for reference.

($\theta_{\rm VLA}$) of all sources detected by the VLBA observations as a function of the spectral index $\alpha^{15.7}_{1.4}$. It indicates that *all* of the significantly extended sources are detected by 10C, whereas those which are not detected at 15.7 GHz are not extended; this arises because the significantly extended sources in this sample have higher integrated flux densities and are therefore more likely also be in the 10C sample. Figure 4.11 shows R against spectral index. The VLBA-detected sources which are not found in the 10C catalogue (shown by pluses and triangles) display a fairly uniform distribution of spectral indices, ranging from $\alpha = -0.11$ to 1.1. There are more flat spectrum sources than sources with steep spectra, but many of these values are lower limits so the spectra may be steeper in reality. There are at least three compact, steep spectrum sources (with $R < 1.25$) in addition to the four in the sample of 10C VLBA-detected sources, and there may be more as several of the other compact sources only have a lower limit on their spectral index.

4.5 Conclusions

Sixty-five percent (33/51) of the 10C sources in the VLBA survey area are detected by the VLBA observations, showing that these sources are AGN. The detected sources have a range of 15.7-GHz flux densities, with detected sources as faint as $S_{15.7\ \mathrm{GHz}} = 0.3$ mJy. These results rule out the possibility discussed in Chapter 3 that the 10C population is dominated by starforming or starbursting sources and provides strong evidence for the conclusion that the faint, high-frequency population is dominated by AGN, such as FRI sources. The proportions of sources in the S^3 model are therefore probably roughly correct, i.e. the population at 1 mJy at 15 GHz is dominated by FRI sources. The spectral properties of these sources are not modelled correctly in the simulation, both because the flat spectrum cores are not correctly modelled, and because no spectral ageing has been included in the source model.

These results also show that there is a small but significant population (four out of 33) of very compact, steep spectrum sources in the 10C sample. They also show that in a number of cases the extended emission displayed by the sources in the VLBA sample is not caused by star formation as assumed by Middelberg et al. and is instead synchrotron emission produced by the AGN jets.

CHAPTER 5

MULTI-WAVELENGTH DATA, PHOTOMETRIC REDSHIFTS AND DERIVED RADIO PROPERTIES

To provide a more thorough understanding of the faint radio source population, information at a range of wavelengths across the whole electromagnetic spectrum is required. In this chapter the Lockman Hole 10C catalogue studied in Chapter 2 is matched to optical, infrared and X-ray data available in the field. The range of multi-wavelength data available in the Lockman Hole is described in Section 5.1. The high density of sources in the optical and infrared catalogues compared to the radio catalogue presents a number of challenges when matching these different datasets; accurate positions are required for the radio sources to ensure the correct match is identified (the 10C positions cannot be used reliably as several multi-wavelength objects often fall within the error ellipse). Matching to extended radio sources is particularly challenging, as there are often several objects within the contours of one radio source. The methods used to minimise these problems when matching the 10C catalogue to other catalogues are described in Section 5.2.

In order to investigate the properties of the 10C sources in as unbiased a way as possible a sub-sample of 96 sources (Sample W) is defined, as all but one of these sources have accurate positions available so I am able to search for a counterpart for them in the multi-wavelength catalogues. Details of how this sample is defined are given in Section 5.3. The multi-wavelength data are then used to estimate photometric redshifts for these sources using the LE PHARE code (Section 5.4). In Section 5.5 the radio-to-optical ratio is estimated for all sources in this sample, which enables radio-loud and radio-quiet sources to be separated. The properties of the sample are discussed in light of the redshift information in Section 5.6 and compared to the S^3 simulation in Section 5.7. The properties of these objects are then discussed further in Chapters 6 and 7.

5.1 Summary of multi-wavelength data used

5.1.1 FUSED catalogue

The 'FUSED' multi-wavelength catalogue was compiled by Vaccari et al. (private communication) and contains most of the publicly available photometric data in the Lockman Hole. The FUSED catalogue combines data from the *Spitzer* Wide-Area Infrared Extragalactic survey (SWIRE; see Lonsdale et al. 2003), the *Spitzer* Extragalactic Representative Volume Survey (SERVS; see Mauduit et al. 2012) and the United Kingdom Infrared Telescope (UKIRT) Infrared Deep Sky Survey (UKIDSS; see Lawrence et al. 2007) with deep optical photometric data taken by González-Solares et al. (2011) (GS11) at the Isaac Newton Telescope (INT) and the Kitt Peak National Observatory (KPNO). For inclusion in the FUSED catalogue, a source must be detected at either 3.6 or 4.5 µm.

SWIRE (Lonsdale et al. 2003) is a wide-field high galactic latitude survey covering nearly 50 deg^2 in six different fields, one of which is the Lockman Hole. These fields have been surveyed by the *Spitzer Space Telescope* using both the Infrared Array Camera (IRAC) and the Multi-Band Imaging Photometer (MIPS) far-infrared camera. The FUSED catalogue contains data from IRAC, which made observations at 3.6, 4.5, 5.8 and 8.0 µm with 5σ sensitivities of 3.7, 5.4, 48 and 37.8 µJy respectively (the longer wavelength MIPS photometry is not included here).

SERVS (Mauduit et al. 2012) is a warm *Spitzer* survey which imaged $\approx$ 18 deg^2 using the 3.6 and 4.5 µm IRAC bands. It achieved limiting (5σ) magnitudes of 24.0 and 23.2 (AB) respectively (equivalent to flux densities of 0.91 and 1.74 µJy respectively).

UKIDSS (Lawrence et al. 2007) used the UKIRT Wide Field Camera (WFCAM) to map 7500 deg^2 in five different surveys in J, H and K bands. The Lockman Hole is part of the Deep Extragalactic Survey (DXS), which will cover 35 deg^2 to K magnitude of 21. The FUSED catalogue contains data from UKIDSS Data Release 9, which includes only J and K bands in the Lockman Hole.

The González-Solares et al. (2011) (GS11) deep optical data were taken with the Wide Field Camera (WFC) at the INT and the Mosaic-1 camera on the Mayall 4-meter Telescope at the KPNO in g, r, i and z-bands. The average magnitude limits in the g, r, i and z-bands are of 24.5, 24.0, 23.3 and 22.0 (AB, 5σ for a point-like object measured in a 2-arcsec aperture). Information about the optical morphology of the objects is included in the full published GS11

Table 5.1: A summary of the multi-wavelength information used in this work.

	Survey	Reference	Band	Flux density limit (5σ)
$*$	SWIRE	Lonsdale et al. (2003)	3.6, 4.5, 5.8, 8.0 μm	3.7, 5.4, 48, 37.8 μJy
$*$	SERVS	Mauduit et al. (2012)	3.6, 4.5 μm	24.0, 23.3 (AB) (0.91, 1.74 μJy)
$*$	UKIDSS	Lawrence et al. (2007)	J, K	21 (AB)
$*$	GS11	González-Solares et al. (2011)	g, r, i, z	24.5, 24.0, 23.3, 22.0 (AB)
	WISE	Wright et al. (2010)	3.6, 4.6, 12, 22 μm	0.08, 0.11, 1, 6 mJy

Note: $*$ indicates that the survey is included in the FUSED multi-wavelength catalogue.

catalogue but is not included in the FUSED catalogue. The full GS11 catalogue is therefore matched to the FUSED catalogue to include this information. A match radius of 1 arcsec is used and all of the objects with optical information in the FUSED catalogue found matches to the GS11 catalogue.

These catalogues are summarised in Table 5.1. Details of matching the radio data to the FUSED catalogue are given in Section 5.2. There are a maximum of ten photometric bands available for each source, these data are used to derive photometric redshifts, as described in Section 5.4.

5.1.2 WISE data

The Wide-field Infrared Survey Explorer (WISE; Wright et al. 2010) surveyed the whole sky at wavelengths of 3.6, 4.6, 12, 22 μm with 5σ point-source sensitivities of 0.08, 0.11, 1 and 6 mJy respectively. Details of matching to this catalogue are given in Section 5.3.2 and the 22 μm flux densities are used to investigate the far-infrared to radio correlation in Chapter 6.

5.1.3 Fotopoulou et al. photometric redshift catalogue (F12)

Fotopoulou et al. (2012) (F12) produced a deep photometric redshift catalogue covering 0.5 deg^2 contained within the southern 10C Lockman Hole field. This catalogue contains 187,611 objects and has up to 21 bands available, ranging from far-ultraviolet to mid-infrared. The far-ultraviolet (FUV) and near-ultraviolet (NUV) observations used in this work were made by the *Galaxy Evolution Explorer (GALEX)*, with limiting magnitudes of 24.5 in both bands. At optical wavelengths, they use data from the Large Binocular Telescope (LBT), Subaru, and the Sloan Digital Sky Survey (SDSS). The LBT data consists of five bands, U, B, V, Y and z′, and covers about 0.25 deg^2, the Subaru data contain R_c, I_c and z′-band observations and SDSS contains data in u', g', r', i' and z′-bands. Fotopoulou et al. also use the UKIDSS and *Spitzer* data which are used in this work and described in more detail in Section 5.1.1. X-ray observations are available for 0.2 deg^2 of the field, and the 388 X-ray-detected sources, presumed to be AGN, are treated differently in the fitting process. They use the Le Phare photometric redshift code and the template libraries used are the same as those used in the photometric redshift fitting described in Section 5.4.

5.1.4 Revised SWIRE Photometric Redshift Catalogue (RR13)

Rowan-Robinson et al. (2013) (RR13) produced an updated SWIRE photometric redshift catalogue, which is a revised version of the redshift catalogue produced by Rowan-Robinson et al. (2008). The revised catalogue uses the FUSED multi-wavelength catalogue (see Section 5.1.1), which provides deeper optical data and more photometric bands than the catalogue used in Rowan-Robinson et al. (2008). The redshifts are estimated using a two-pass template method based on six galaxy and three AGN templates in the first pass and 11 galaxy and three AGN templates in the second. AGNs are identified by their optical morphology – only objects which appear point-like are fitted with AGN templates. This reduces the risk of catastrophic outliers occurring when normal galaxies are erroneously fitted with AGN templates, but does mean that some AGN will be missclassified as normal galaxies. The main difference between the RR13 catalogue and the previous 2008 version is the treatment of AGNs, as dust torus emission is now included in the quasar templates. The RR13 catalogue only contains redshift values for objects which were included in the original SWIRE photometric redshift catalogue (Rowan-Robinson et al. 2008), so does not include redshifts for every object in the FUSED catalogue. There are also a small number of objects in RR13 catalogue which are not in the FUSED catalogue as these appear in the original SWIRE redshift catalogue.

RR13 contains redshift estimates for 1,009,607 sources in all eight of the SWIRE fields and covers all but a small section of the 10C Lockman Hole field.

5.1.5 Spectroscopic redshifts

Spectroscopic redshifts are available for six sources in this field from a range of different catalogues (these catalogues are listed in F12 and/or RR13). These redshift values and their origins are summarised in Table 5.2.

5.1.6 X-ray data

There are two separate X-ray survey fields in the Lockman Hole 10C survey area; one field is observed by *Chandra* (Wilkes et al. 2009) and one by *XMM-Newton* (Brunner et al. 2008). Figure 5.1 illustrates the positions of these two surveys. The *Chandra* Lockman Hole field covers 0.7 deg^2 and detected 775 X-ray sources to a limiting broadband (0.3 to 8 keV) flux $\sim 4 \times 10^{-16}$ erg cm^{-2} s^{-1}. The *XMM-Newton* field covers ~0.2 deg^2 and detects 409 sources

Table 5.2: Spectroscopic redshift values for sources in Sample W. Photometric redshifts from the RR13 and F12 catalogues along with the values from the fitting performed later in this chapter are included for reference.

			Photometric redshifts		
10C ID	Spec. z	Reference	RR13 z	F12 z	Le Phare z^a
10CJ104539+585730	0.390	Keck redshift, Smith et al., in prep (from RR13)	0.38	n/a	0.47
10CJ105039+572339	1.439	Lehmann et al. (2001)	1.69	0.27	0.80
10CJ105132+571114	0.318	SDSS DR2	0.32	0.40	0.52
10CJ105148+573245	0.990	Lehmann et al. (2001)	0.93	1.00	2.06
10CJ105206+574111	0.462	Ishisaki et al. (2001)	n/a	1.53	1.49
10CJ105240+572322	1.013	Keck/Deimos 2010 (from F12)	n/a	1.11	1.07

Note: a) Redshift value from the photometric redshift fitting described in Section 5.4.

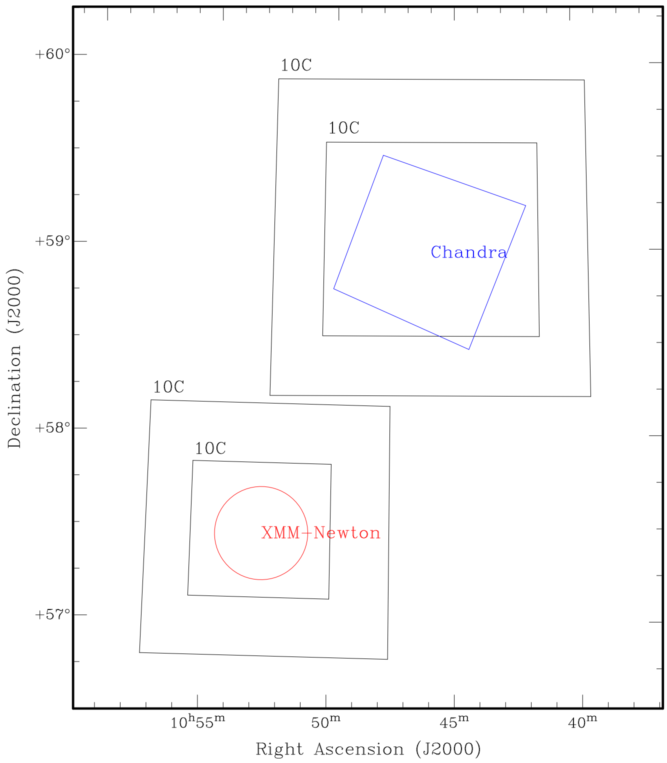

Figure 5.1: Positions of the two X-ray surveys in the Lockman Hole. The Wilkes et al. (2009) *Chandra* survey is shown in blue and the Brunner et al. (2008) *XMM-Newton* survey is shown in red. Positions of the 10C radio survey fields are shown in black for reference (the large rectangles indicate the regions complete to 1 mJy and small rectangles contained within shown the regions complete to 0.5 mJy).

with a sensitivity limit of 1.9, 9 and 180 $\times 10^{-16}$ erg cm^{-2} s^{-1} in the 0.5 to 2.0, 2.0 to 10.0 and 5.0 to 10.0 keV bands respectively.

5.2 Matching the catalogues

In Section 5.3 a complete sample of 96 radio sources with high resolution radio data available is defined (Sample W). Although this sample is used when discussing the multi-wavelength properties of the 10C sources, the FUSED multi-wavelength catalogue was matched to the full Lockman Hole 10C sample as this larger sample size provides better statistics when, for example, determining the match radius. In this section I describe the methods used to search for counterparts for the 245 10C sources which lie inside the FUSED survey area.

5.2.1 Morphology of the radio sources

Due to the high density of sources in the FUSED catalogue it is necessary to take into account the structure of the radio sources when matching the catalogues, as there may be several optical sources within the radio contours of extended sources. In Chapter 2 10C sources were classified as extended using the lower-frequency catalogues available in the field as these have higher resolution. The emphasis on the size classifications in Chapter 2 was to select only those which are definitely extended, while for the purposes of matching the aim is to select sources which are definitely compact as it is not necessary to examine these sources by eye. Therefore, a different classification scheme is used here to that described in Chapter 2.

In order to determine whether or not a source is extended the ratio of total flux to peak flux density ($C = S_{\rm int}/S_{\rm peak}$) was calculated for all sources with a match in either the FIRST, GMRT or WSRT surveys or the 324 MHz VLA survey by Owen et al. (2009) (OMK2009). FIRST, GMRT and OMK2009 have similar resolutions, with a synthesised beam of $\approx$5 arcsec, while WSRT has a larger beam of $\approx$10 arcsec. (OM2008 and BI2006 have significantly smaller beam sizes, $\approx$1 arcsec, meaning that values of C from these catalogues cannot be directly compared to the other C values so they are not used in this analysis). FIRST and GMRT cover the whole field while WSRT and OMK2009 only cover part of the field. Those sources with a match in either FIRST or GMRT were classified as extended if either $C_{\rm GMRT}$ or $C_{\rm FIRST} > 1.2$, otherwise they were classified as compact for the purpose of matching. Sources without a match in FIRST or GMRT but with a match to OMK2009 were classified as extended if $C_{\rm OMK2009} > 1.2$ and compact otherwise. All sources with a match in WSRT and not in the other three catalogues used here were classified as extended for the purpose of matching as the resolution of the WSRT map is not high enough to ensure these sources are not extended.

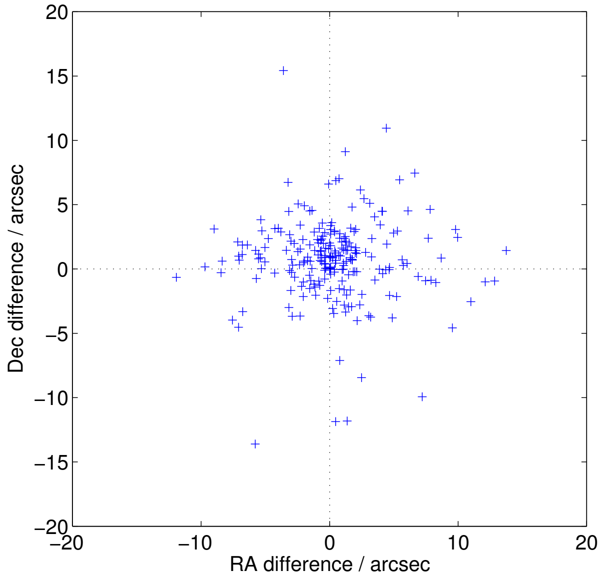

Figure 5.2: The separations in RA and Dec between the positions in the 10C catalogue and the best radio position used for matching to the FUSED catalogue.

There are six sources which are not classified as extended or compact because they do not have a counterpart in any of the four catalogues used when classifying the sources but which do have a match in OM2008 or BI2006, and therefore an accurate position. These sources all have angular sizes less than 3 arcsec in the OM2008 or BI2006 catalogues so were considered to be compact for this purpose.

There are therefore 84 (38 in Sample W) sources which are compact and 137 (57 in Sample W) sources which have been classified as extended for the purpose of matching but which may in fact not be significantly extended on these angular scales. These two groups of sources are treated separately when identifying optical matches.

There are a further 24 sources which only appear in the 10C catalogue; due to the lack of accurate positions available for these sources no attempt is made to find a match for them. Only one of these sources appears in Sample W. 52 10C sources lie outside the FUSED survey area so are not included in this discussion.

5.2.2 Matching the catalogues

All matching was carried out using the TOPCAT[a] software package. The density of sources in the FUSED catalogue is high compared to the potential error in the 10C source positions which means that care must be taken when matching the catalogues. I therefore use the more accurate positions from the lower frequency radio catalogues (typical error $\approx$ 1 arcsec) rather than those

[a]see: http://www.starlink.ac.uk/topcat/

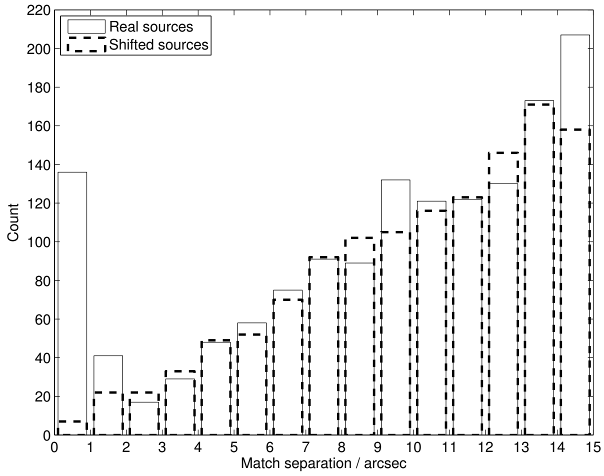

Figure 5.3: The separation distribution when the radio sources in the 10C catalogue and the simulated catalogue are matched to the FUSED catalogue, taking all matches to the radio sources within 30 arcsec. Note that the full 10C sample is matched here.

from the 10C catalogue (error $\approx$ 6 arcsec). When there are several positions available for a source, they are used in the following order of preference: FIRST, GMRT, BI2006/OM2008, WSRT, 10C. For sources which are resolved into multiple components in FIRST or GMRT, the position from the 10C catalogue was used instead as this gives a best estimate of the centre of the flux. For the three sources which have two separate components listed in the original 10C catalogue (see section 2.1.1 for details), the average of the two 10C positions is used. The separations in RA and Dec between the 10C source positions and the positions used for matching are shown in Figure 5.2.

The match radius needs to be chosen carefully to avoid false matches while still maximising the number of real matches. The 10C sources were shifted by 0.2 degrees in declination to produce a simulated sample of randomly positioned sources. Both this simulated sample and the real sample were matched to the FUSED catalogue, and all FUSED objects within 30 arcsec of each source were noted. The separation between the matches is shown in Figure 5.3; it is clear that beyond 2 arcsec the number of real and random matches becomes comparable.

For those sources classified as compact, the nearest match within 2 arcsec was accepted. If there was no match within 2 arcsec then the source in question was considered to have no optical counterpart. In total, 79 (36 in Sample W) of the compact sources have a match within 2 arcsec and 5 (2 in Sample W) do not.

For sources classified as extended the positions of all the optical sources were plotted on top of the radio contours (GMRT maps were used for those sources with a GMRT match, WSRT maps were used for the remaining sources). These images were then examined and the sources were also assigned one of the following flags:

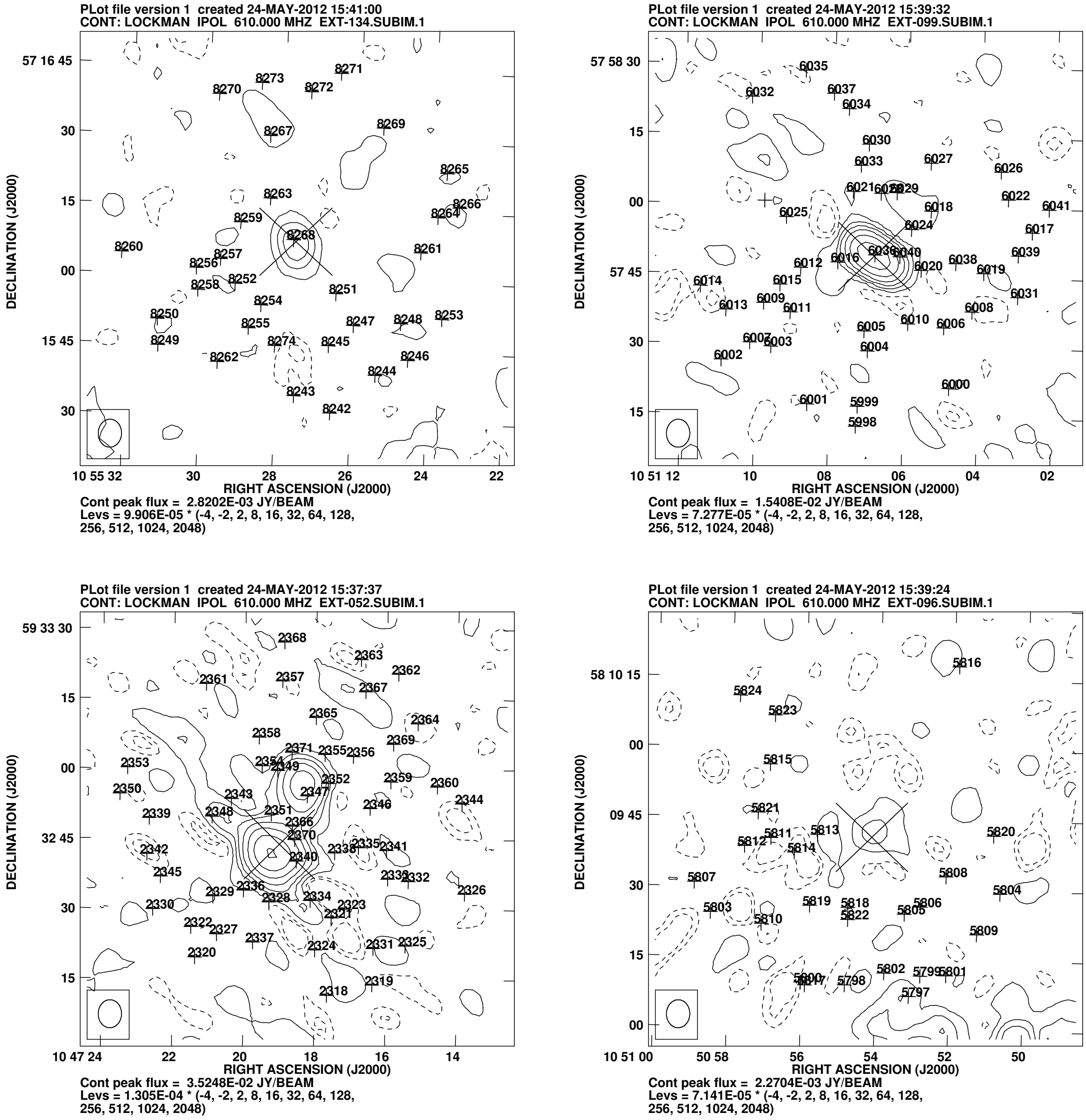

Figure 5.4: Examples of extended sources assigned each of the four flags. Top left = 1 (probable match), top right = 2 (possible match), bottom left = 3 (confused) and bottom right = 4 (no match).

1. probable match – only source within radio contours (48 sources in total, 21 in Sample W);
2. possible match – looks likely but there are other sources within the radio contours (58 sources in total, 23 in Sample W);
3. confused – several sources within the radio contours so cannot identify the correct match (18 sources in total, 8 in Sample W);
4. no match – no sources within the radio contours (13 sources in total, 5 in Sample W).

Table 5.3: A summary of the matches to the FUSED catalogue found for 10C sources.

Description	Number of sources in full sample	Number of sources in Sample W
Extended – probable match	48	21
Extended – possible match	58	23
Extended – confused	18	8
Extended – no match	13	5
Compact – match within 2 arcsec	79	36
Compact – no match within 2 arcsec	5	2
10C position only	24	1
Not in FUSED area	51	0

Examples of sources given each of these flags are given in Figure 5.4. Table 5.3 contains a summary of the number of matches to the FUSED catalogue and the flags used in the catalogue.

In summary, I have identified possible counterparts for 187 out of 245 10C sources in the FUSED survey area (76 percent), and 80 out of the 96 sources in Sample W (83 percent). The separation between the radio position of each source and the FUSED object associated with it are shown in Figure 5.5. Possible counterparts for those sources classified as confused are discussed in Section 5.3.3. I examined the contour plot of the one source in Sample W without an accurate position available; this shows that there are no possible counterparts within the radio contours. This source is therefore included in the group of sources without a match in future discussions of Sample W (giving a total of eight sources without a match in Sample W, and a further eight confused sources).

5.3 Radio sample used – 'Sample W'

Chapter 2 describes how the 10C catalogue was matched to several lower-frequency, and generally higher-resolution, radio catalogues in order to calculate radio spectral indices and investigate the morphology of the sources. As well as giving information about the radio properties of these sources, matching to these higher-resolution catalogues also provides more accurate positions (the positional accuracy of the GMRT and FIRST catalogues is ≈ 1 arcsec compared to ≈ 6 arcsec for the 10C catalogue). These are vital when identifying optical counterparts for the 10C sources, as discussed in Section 5.2.

For the purposes of this analysis it is useful to define a complete subset of sources from 1.4-GHz samples which have high sensitivity and very good positional accuracy. There are three such 1.4-GHz surveys in this field; Biggs & Ivison (2006) (BI2006) and Owen & Morrison (2008) (OM2008) have both made surveys with the VLA and Guglielmino et al. (2012)

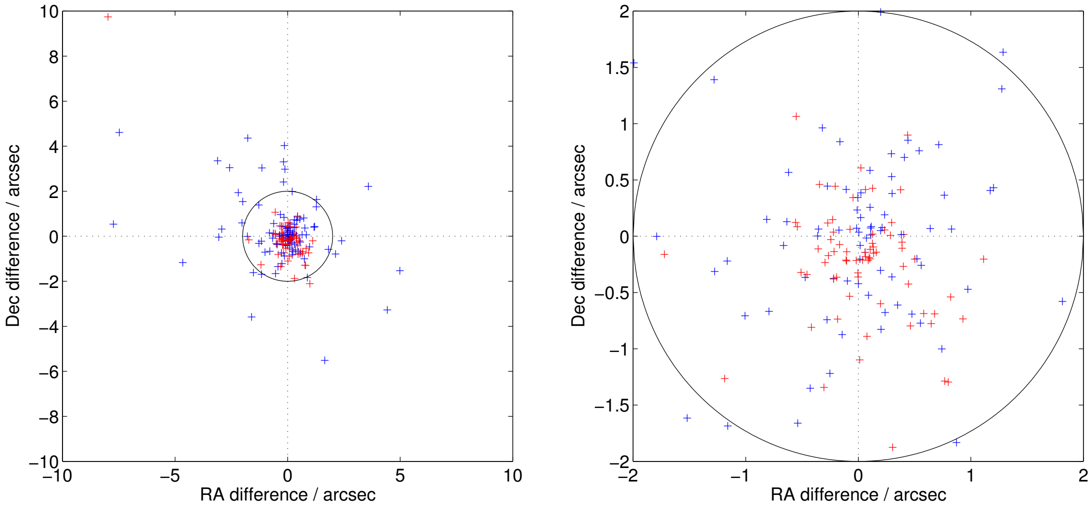

Figure 5.5: Separation between the best radio position for each source and the position of its counterpart in the FUSED catalogue for the full 10C catalogue. Sources which are considered extended for the purposes of matching are shown in blue, compact sources are shown in red. The left panel shows all sources with a match, the right panel is zoomed in on the central two arcsec. In both panels the circle indicates a separation of 2 arcsec (the match radius for compact sources).

surveyed a larger area of the field with the WSRT. Further details of these surveys are given in Chapter 2. OM2008 and BI2006 have rms noises of 2.7 and 6.0 μJy/beam respectively and all the 10C sources in these fields are detected at 1.4 GHz. The majority of the Guglielmino et al. WSRT map has an rms noise of < 15 μJy/beam and parts have an rms noise of 11 μJy/beam. This means that it should be possible to detect the faintest sources in the complete 10C sample (with $S_{15.7\mathrm{GHz}} = 0.5$ mJy) in the WSRT map provided they have spectral indices $\alpha_{1.4}^{15.7} > -1$ (assuming a 3σ WSRT detection). Sources with spectra which rise as steeply as this are very rare so the vast majority of the 10C sources in the WSRT map are detectable – in fact, all but one of the sources in the complete 10C catalogue are detected in the WSRT map. I therefore define 'Sample W' – all 10C sources in the complete catalogue in the OM2008, BI2006 or WSRT deep survey areas. Sample W contains 96 sources and accurate positions and spectral index information is therefore available for all but one of the sources. The positions of the sources in Sample W are shown in Figure 5.6.

The spectral indices and flux density distributions of the full sample of 296 sources studied in Chapter 2 and the subsample of 96 sources in Sample W are plotted in Figure 5.7. The spectral index distributions of the two samples are relatively similar, although all nine of the very steeply rising sources, with $\alpha_{1.4}^{15.7} < -0.8$, in the full sample are not included in Sample W. Seven of these nine sources are below the 10C completeness limits (0.5 mJy in the deep regions and 1 mJy in the shallow regions) and are not detected at 1.4 GHz so the spectral indices

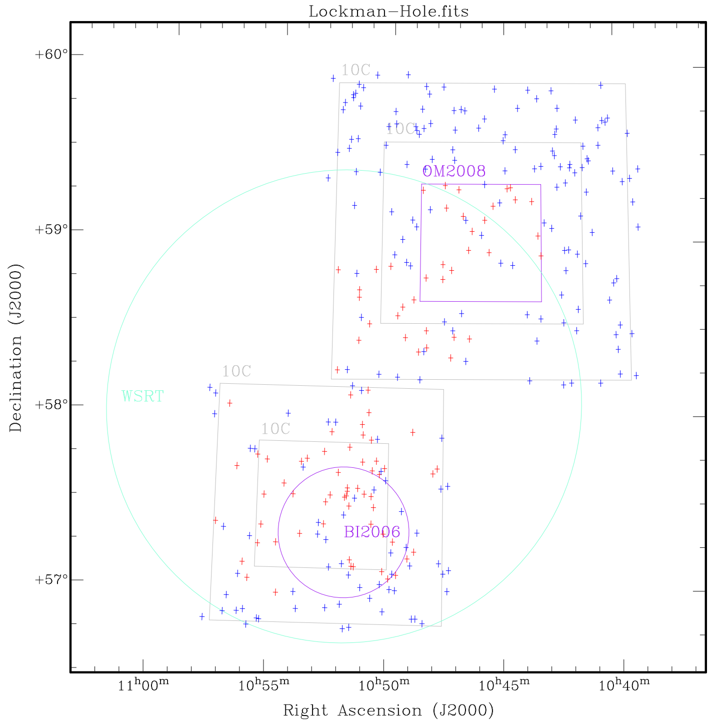

Figure 5.6: Positions of all 296 sources in the 10C Lockman Hole sample. The 96 sources in Sample W are shown in red, and the remaining 200 sources which are not in Sample W are shown in blue. The 10C complete areas are shown in grey (the large rectangles indicate the regions complete to 1 mJy and small rectangles contained within shown the regions complete to 0.5 mJy). The WSRT survey area is shown aquamarine (large circle) and the BI2006 and OM2008 survey areas are shown in purple (small circle).

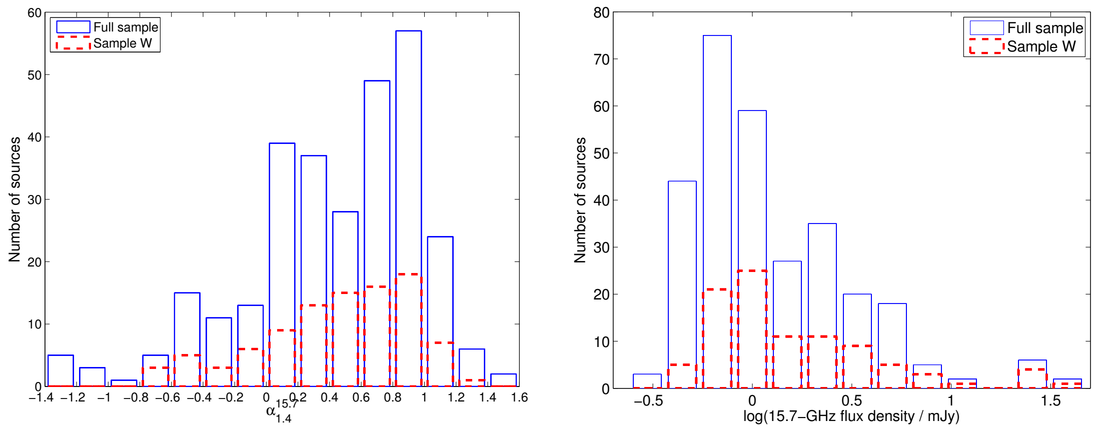

Figure 5.7: Spectral index and flux density distributions for sources in the full sample of 296 sources used in Chapter 2 and Sample W (96 sources) defined here. Left: spectral index, right: 15.7-GHz flux density. Note that the spectral index distribution for the full sample includes 30 sources with upper limits on their spectral indices.

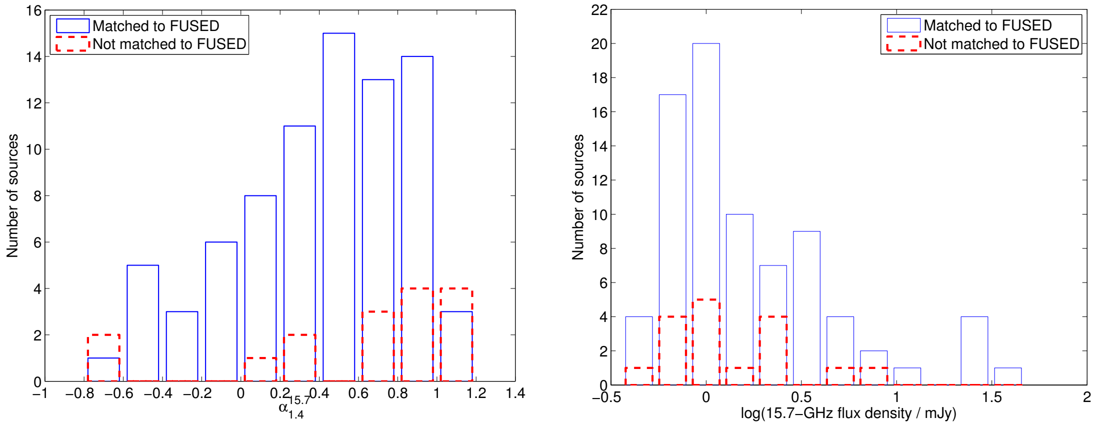

Figure 5.8: A comparison of the spectral index and 15.7-GHz flux density distributions of sources which have a match in the FUSED catalogue and those which do not in Sample W.

are upper limits calculated from the 3σ noise in the WSRT map. The flux density distributions of the full sample and Sample W are also very similar, although none of the faintest sources in the full sample appear in Sample W, as this sample only contains sources above the 10C completeness limits (0.5 and 1 mJy in the deep and shallow regions respectively). The remainder of this chapter concerns the sources in Sample W only.

5.3.1 Properties of sources in Sample W with and without a match to the FUSED catalogue

As described in Section 5.2.2, 80 out of the 96 sources in Sample W have a counterpart in the FUSED multi-wavelength catalogue. The spectral index and flux density distributions of the sources with and without a counterpart are compared in Figure 5.8. The spectral index distributions of the two groups of sources (those with and without a match) are broadly similar, except that a higher proportion of the very steep ($\alpha_{1.4}^{15.7} > 0.8$) sources are unmatched (32 percent of sources with $\alpha_{1.4}^{15.7} > 0.8$ are unmatched compared to 11 percent of sources with $\alpha_{1.4}^{15.7} < 0.8$). This is probably because these very steep sources are likely to be very extended and therefore classified as confused when matching. The 15.7-GHz flux density distributions of the two groups of sources are similar, although all six of the brightest 10C sources have counterparts in the multi-wavelength catalogue.

5.3.2 Matching Sample W to other multi-wavelength catalogues

Sample W was also matched to the F12, RR13 and WISE catalogues. For the 80 sources which have a counterpart in FUSED the catalogues were matched using the position from the FUSED

Table 5.4: A summary of matches to multi-wavelength catalogues for 10C sources in Sample W.

Catalogue	Number of matches to 10C sources
FUSED	80
GS11	59
RR13	57
F12	20
WISE	57

Table 5.5: A summary of the X-ray counterparts found for 10C sources in Sample W.

Field	Number of 10C sources in field	Number with an X-ray match	Percentage with an X-ray match
Chandra	19	7	37
XMM-Newton	13	8	62

catalogue and the nearest match within 1.5 arcsec for RR13 and F12 and 2 arcsec for WISE catalogue is accepted (the shifting procedure described in Section 5.2.2 was repeated for each of the catalogues to chose these match radii). This gave a total of 52 matches to RR13, 20 to F12 and 51 to the WISE catalogue. For the remaining 16 sources without a match in the FUSED catalogue, GMRT (or WSRT where GMRT images were not available) contour plots of each source were printed out, with the positions of the objects from the catalogue which was being matched overlaid. Each source was then examined by eye and if appropriate a match was identified, and the source was allocated one of the following flags:

0 – no match;

1 – match;

2 – confused (several sources within the radio contours);

3 – not in area (relevant for F12 only).

The total number of matches to each multi-wavelength catalogue is summarised in Table 5.4.

5.3.2.1 Matching to the X-ray catalogues

The two X-ray catalogues in the Lockman Hole were matched to the 10C sources, using a 5 arcsec match radius (the analysis in Section 5.2.2 was repeated to determine an appropriate match radius). For those 10C sources with a match to the FUSED catalogue, the FUSED position was used. For the remaining sources the radio position was used, with the radio position chosen in the following order of preference: FIRST, GMRT, BI2006/OM2008, WSRT, 10C. The results of this matching are summarised in Table 5.5. In total, out of 32 10C sources in the two X-ray survey areas, 15 have an X-ray counterpart (47 percent).

5.3.3 Possible matches for confused sources

There are eight sources in Sample W which were classified as confused when matching to the FUSED catalogue. Contour plots and a brief discussion of each of these eight sources is included in Appendix B. Although it is not possible to identify a single counterpart for these sources, some useful information about their nature can be gained by looking at all possible counterparts within the radio contours. Therefore, all objects within one tenth of the peak flux in the GMRT sub-image were selected as possible counterparts for each 10C source. For the one source without a GMRT image, all objects within the 3σ contour in the WSRT map were selected instead. In total, 30 possible counterparts were identified for the eight sources.

5.4 Photometric redshift fitting

The publicly available photometric redshift code Le Phare[b] (Arnouts & Ilbert 2011) was used to compute photometric redshifts for the sources in Sample W with counterparts in the FUSED catalogue. The code takes an input library of spectral energy distribution (SED) templates, which are assumed to represent the SEDs of the observed sample, and shifts them to a range of redshift values. These templates are then fitted to the photometric data, and a least-squares minimisation is used to select the best-fitting SED template for each source. The redshift of the best-fitting template is then adopted as the redshift estimate. The photometric data used here was from the FUSED catalogue (see Section 5.1.1), which has up to ten photometric bands available for each source. Data at 3.6 and 4.5 µm are available from both SWIRE and SERVS for some sources, in which case values from SWIRE were used for the photometric fitting (to maximise consistency across the bands).

Each source was fitted to two different template libraries, the first containing galaxy templates and the second containing AGN templates. These two libraries, and the extinction laws applied, are the same as those used in F12. The galaxy templates used are the library produced by Ilbert et al. (2009). These include nine templates generated by Polletta et al. (2007) – three elliptical galaxy SEDs and six spiral galaxy SEDs (S0, Sa, Sb, Sc, Sd, Sdm) – and 12 starburst galaxy SEDs generated using the Bruzual & Charlot (2003) models (with starburst ages ranging from 3 to 0.03 Gyr). This gives a total of 21 SED templates (Figure 5.9). Ilbert et al. (2009) linearly interpolated between some of the Polletta et al. templates to refine the sampling in colour-redshift space, resulting in a total of 31 templates (Table 5.6). For templates Sb to SB3 (template IDs 11 to 23) extinction is applied according to the Prevot et al. (1984) Small Magellanic Cloud (SMC) law, while for SB4 to SB11 (template IDs 24 to 31) the Calzetti et al. (2000) laws are applied. No additional extinction is applied

[b] http://www.cfht.hawaii.edu arnouts/LEPHARE/lephare.html

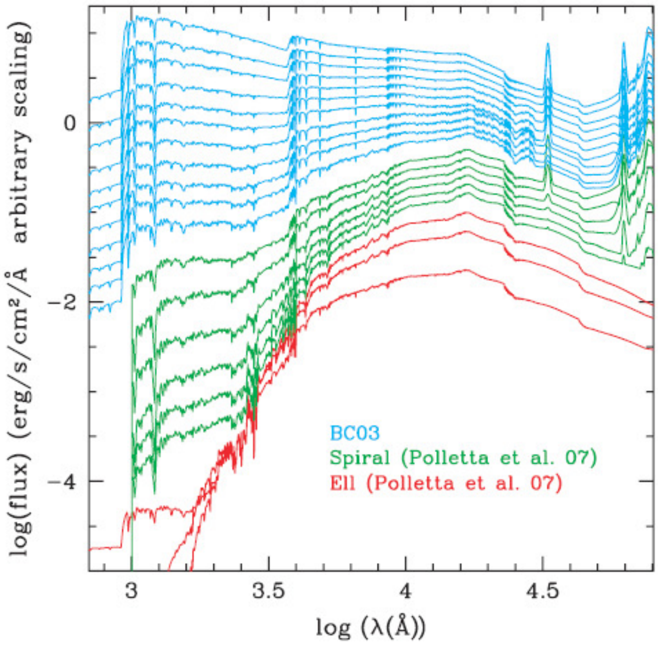

Figure 5.9: SED templates from Ilbert et al. (2009) (the galaxy template library used in this work). The top 12 SEDs (cyan) are generated using Bruzual & Charlot (2003) (BC03) starburst models. The spiral (green) and elliptical (red) SEDs are from Polletta et al. (2007). Flux scale is arbitrary. This figure is taken from Ilbert et al. (2009).

for templates earlier than Sb. The intrinsic galactic absorption is calculated with values of $E(B-V) = 0.00, 0.05, 0.10, 0.15, 0.20, 0.25, 0.30, 0.40$ and 0.50. Emission lines were added to the templates using the option in the Le Phare code as this has been shown to give better results, even in the case of broadband photometry (Ilbert et al. 2009).

The AGN template library was taken from Salvato et al. (2009). This library of 30 templates contains galaxy and AGN templates, as well as a number of hybrid templates. These hybrid templates contain contributions from both galaxy and AGN templates in proportions ranging from 10%:90% to 90%:10% in steps of 10% (see Salvato et al. 2009 for full details). The full template library is shown in Table 5.7 and Fig 5.10. For this template library extinction is allowed to vary from $E(B-V) = 0$ to 0.5 in steps of 0.05.

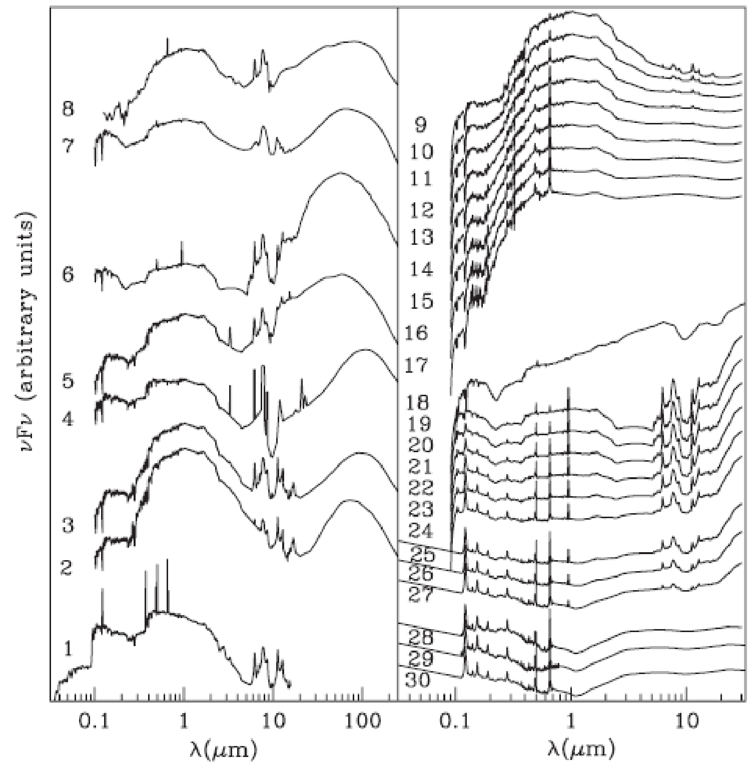

Figure 5.10: SED templates from Salvato et al. (2009) (the AGN template library used in this work). The numbers correspond to the templates listed in Table 5.7. The flux scale is arbitrary. This figure is taken from Salvato et al. (2009).

Table 5.6: Galaxy template library used in this work (templates from Ilbert et al. 2009).

ID	Name	Type
1	Ell1_A_0	Elliptical
2	Ell2_A_0	Elliptical
3	Ell3_A_0	Elliptical
4	Ell4_A_0	Elliptical
5	Ell5_A_0	Elliptical
6	Ell6_A_0	Elliptical
7	Ell7_A_0	Spiral
8	S0_A_0	Spiral
9	Sa_A_0	Spiral
10	Sa_A_1	Spiral
11	Sb_A_0	Spiral
12	Sb_A_1	Spiral
13	Sc_A_0	Spiral
14	Sc_A_1	Spiral
15	Sc_A_2	Spiral
16	Sd_A_0	Spiral
17	Sd_A_1	Spiral
18	Sd_A_2	Spiral
19	Sdm_A_0	Starforming
20	SB0_A_0	Starforming
21	SB1_A_0	Starforming
22	SB2_A_0	Starforming
23	SB3_A_0	Starforming
24	SB4_A_0	Starforming
25	SB5_A_0	Starforming
26	SB6_A_0	Starforming
27	SB7_A_0	Starforming
28	SB8_A_0	Starforming
29	SB9_A_0	Starforming
30	SB10_A_0	Starforming
31	SB11_A_0	Starforming

Table 5.7: AGN template library used in this work (templates from Salvato et al. 2009).

ID	Name	Type
1	BC03	Starforming
2	S0	S0
3	Sb	Spiral b
4	Spi4	Spiral c
5	M82	Starburst
6	I22491	Starburst/ULIRG
7	Sey18	Seyfert 1.8
8	Sey2	Seyfert 2
9	hybrid4_gal90_agn10	Hybrid
10	hybrid4_gal80_agn20	Hybrid
11	hybrid4_gal70_agn30	Hybrid
12	hybrid4_gal60_agn40	Hybrid
13	hybrid4_gal50_agn50	Hybrid
14	hybrid4_gal40_agn60	Hybrid
15	hybrid4_gal30_agn70	Hybrid
16	hybrid4_gal20_agn80	Hybrid
17	hybrid4_gal10_agn90	Hybrid
18	Mrk231	Seyfert 1
19	hybrid_gal90_agn10	Hybrid
20	hybrid_gal80_agn20	Hybrid
21	hybrid_gal70_agn30	Hybrid
22	hybrid_gal60_agn40	Hybrid
23	hybrid_gal50_agn50	Hybrid
24	hybrid_gal40_agn60	Hybrid
25	pl_hybrid_gal30_agn70	Hybrid
26	pl_hybrid_gal20_agn80	Hybrid
27	pl_hybrid_gal10_agn90	Hybrid
28	QSO_SDSS_lum	QSO high lum
29	QSO_SDSS	QSO low lum
30	TQSO1	QSO high IR lum

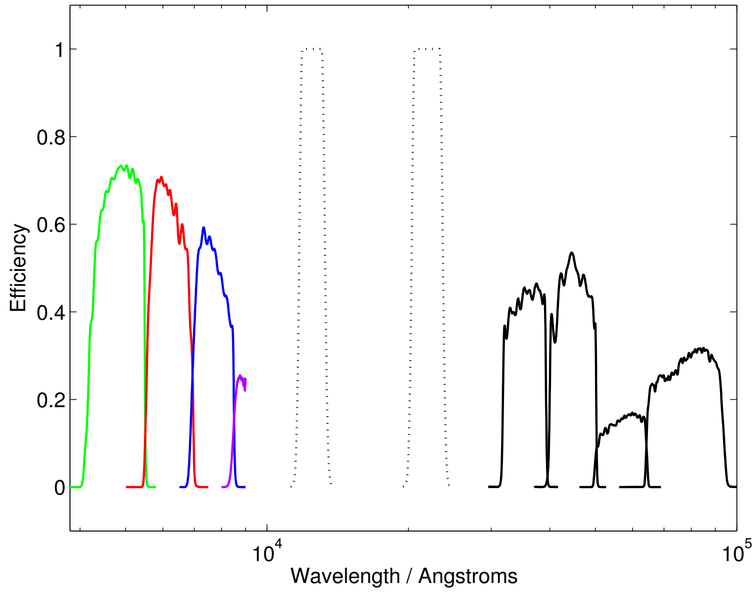

Figure 5.11: Filters used in the photometric redshift fitting. Solid coloured lines are the optical filters (g, r, i and z from left to right), dotted black lines are the two UKIDSS filters (J and K) and the solid black lines are the four IRAC filters.

For both libraries the templates are calculated at redshifts 0–6 in steps of $\Delta z = 0.01$ and in steps of $\Delta z = 0.02$ for redshifts 6–7. The absolute magnitude was restricted to the range $-24 < M < -8$, where M is the absolute magnitude in the g-band.

The filters used in the fitting process for each of the ten photometric bands are shown in Figure 5.11. The two UKIDSS filters and the four *Spitzer* IRAC filters are included in the standard release of Le Phare. The optical filters were constructed by combining the INT WFC filters[c] with the quantum efficiency curve[d]. These curves and the resulting filters are shown in Figure 5.12.

5.4.1 Selecting a final redshift value

Each of the 80 objects in the sample has been fitted to two SED template libraries (the galaxy template library and the AGN template library), so there are two possible redshift values produced for each source. Throughout this section the redshift value resulting from the best-fitting template from the galaxy library is referred to as z_{GAL} and the redshift value resulting from the AGN template library is referred to as z_{AGN}. The two values for each source are plotted against each other in Figure 5.13, with 1σ error bars plotted on the redshift values from the galaxy template library. Note that these errors characterise the goodness of the least squares fit to the

[c]Obtained from: http://www.ast.cam.ac.uk/~wfcsur/technical/filters/
[d]Obtained from: http://www.ing.iac.es/Engineering/detectors/4280qe.htm

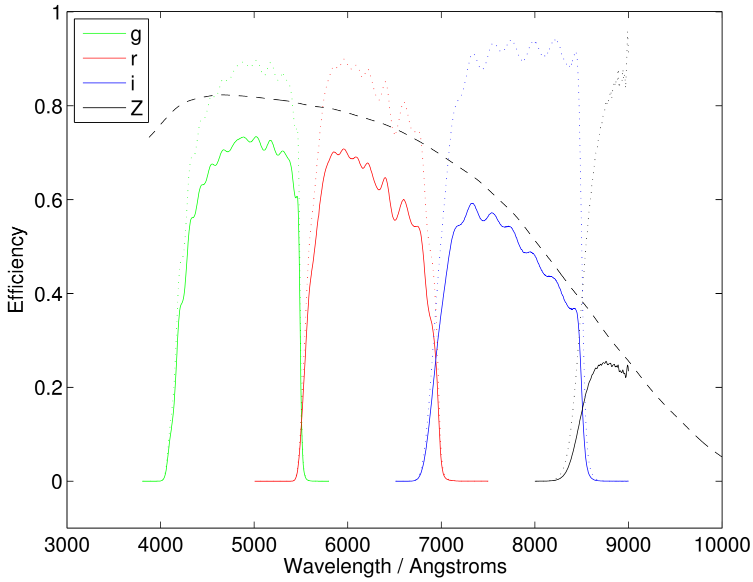

Figure 5.12: INT WFC optical filters. The black dashed line shows the quantum efficiency curve. The dotted coloured lines are the INT WFC optical filters without taking into account quantum efficiency, and the solid coloured lines are the filters with the effects of quantum efficiency applied (these are the filters used in the photometric redshift fitting).

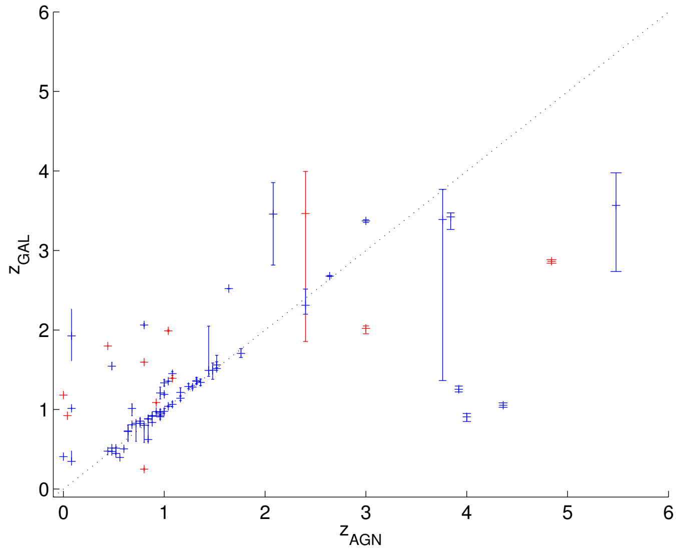

Figure 5.13: Comparison of redshift values resulting from the best fits to the galaxy and AGN libraries. The dotted line indicates where $z_{\rm GAL} = z_{\rm AGN}$. Blue points indicate sources where the $z_{\rm GAL}$ value is selected and red points are sources where the $z_{\rm AGN}$ value is used. 1σ error bars are plotted.

chosen template and that a small error bar does not necessarily mean that the chosen solution is the correct one, but simply that the probability distribution has a narrow peak around a given value. This plot shows that for a significant proportion of sources these two values are in good agreement, with 67 of the values agreeing within 50 percent, while for a thirteen of the sources there is a larger difference between the two redshift values.

It is therefore important to determine which value is the most appropriate one to use for each source. The SED which provided the best fit to the photometric data from each of the two libraries were plotted for each source and these were examined by eye. Both the galaxy and AGN template fits were then qualitatively assigned one of the following template flags to characterise the fit:

1 = good fit;

2 = possible fit;

3 = poor fit.

Three examples of SED plots are shown in Figure 5.14. The top plot is an example where the galaxy fit is significantly better than the AGN fit (these were assigned fitting flags 1 and 3 respectively), the middle is an example where the AGN library fit is significantly better than the galaxy fit (again, assigned flags 1 and 3 respectively). The bottom plot is an example of a situation where both fits appear good (both were assigned flag 1), so additional information is required to identify the best redshift value to use. Note that in this instance, as is often the case when the best-fitting SEDs from the two libraries are equally good, the redshift values resulting from the two fits are very similar.

One of the possible two redshift values was then selected for each source. z_{GAL} was selected if the fit to the galaxy template is better than the fit to the AGN template (i.e. galaxy template flag < AGN template flag). If the fit to the galaxy and AGN templates were judged to be equally good (i.e. galaxy template flag = AGN template flag), then z_{GAL} was selected if the object's optical morphology indicated that it was extended in the optical observations (full details of the optical morphology information is given in Section 6.2.1), and z_{GAL} was also selected if there was no optical morphology information available. z_{AGN} was selected if the fit to the AGN template was better than the fit to the galaxy template (i.e. AGN template fitting flag < galaxy template fitting flag), or if the two fits appeared equally good and the object appeared point-like in the optical. Any source with fewer than three photometric bands available was not assigned a redshift value.

In the final photometric redshift catalogue 63 sources have redshift values from the galaxy templates library and 11 have redshift values from the AGN templates library. This gives a total of 74 sources with redshift values from the Le Phare photometric redshift fitting process. The sources which have final redshift values from the galaxy and AGN template libraries are

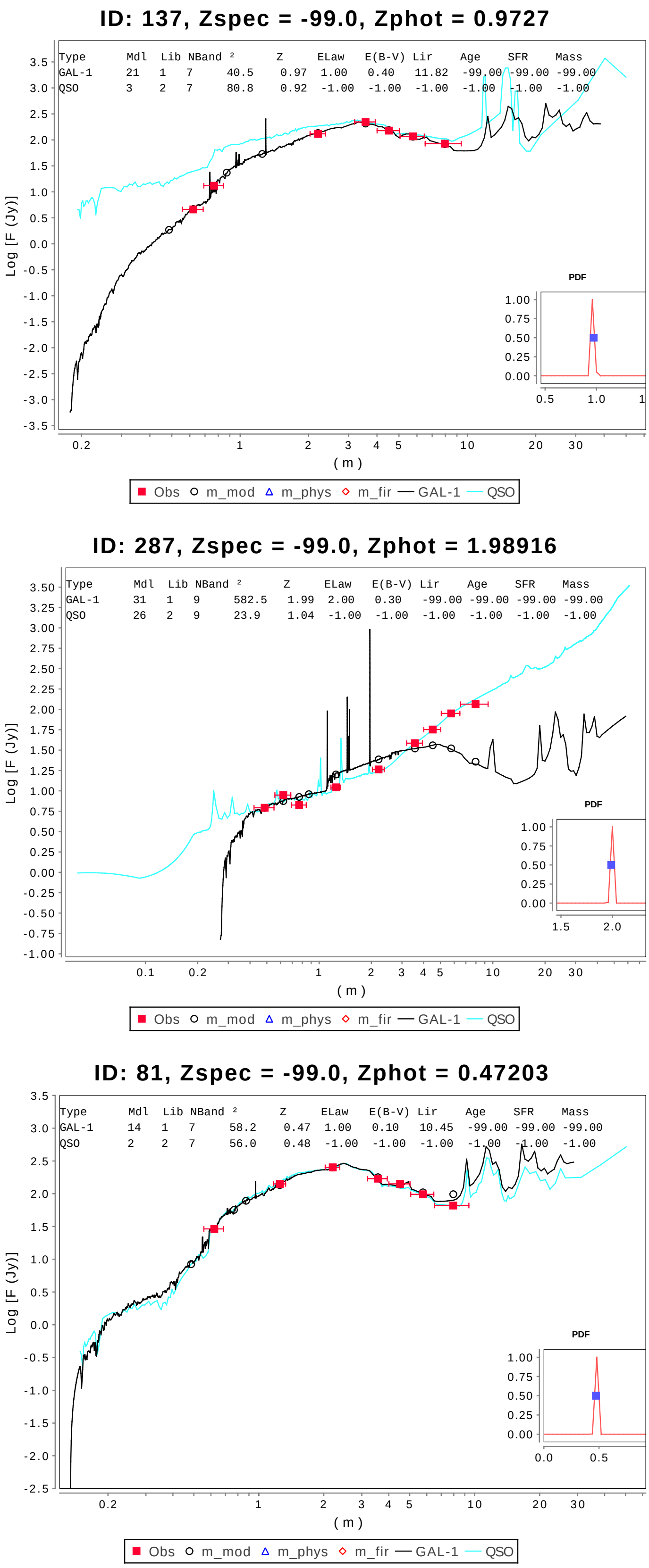

Figure 5.14: Three examples of the best SED fits from the galaxy (black) and AGN (cyan) libraries. The red squares are the observed photometric data.

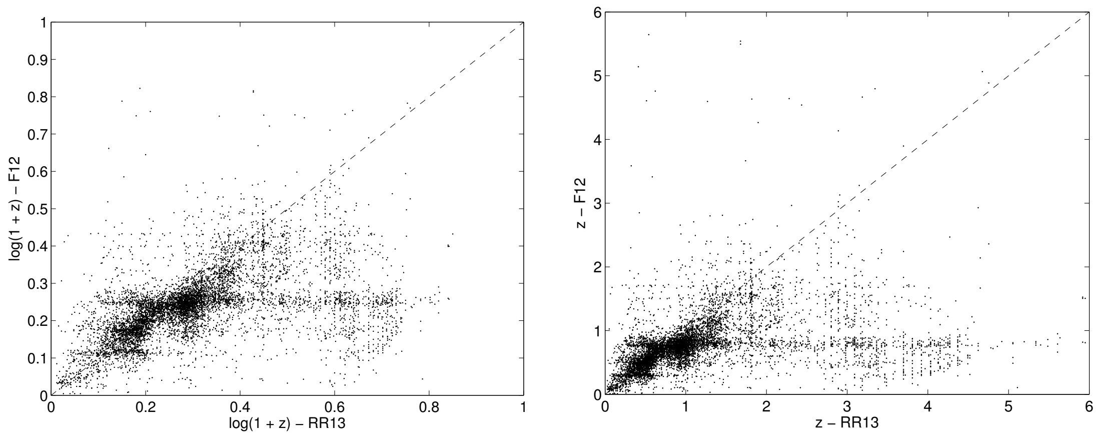

Figure 5.15: Comparison of the redshift values from the RR13 and F12 catalogues. The dashed line indicates where the redshift values from the two catalogues are equal. The same values are plotted in the two panels – in the left-hand panel log(1 + z) is plotted to make it easier to see the high density of points, and the right-hand panel shows z on a linear scale for easier comparison with Figure 5.16.

shown separately in Figure 5.13. All of the sources which have very similar values from the fitting to both the galaxy and the AGN libraries have 'galaxy' values as their final redshift value. This is probably for a combination of two reasons; first, when the templates from both libraries fitted equally well because they were very similar they often gave very similar redshift values, and in this situation the galaxy redshift value was chosen. Secondly, the AGN template library contains a few normal galaxy templates, along with hybrid templates with up to 90 percent contribution from the host galaxy, while the 'galaxy' template library contains no AGN templates. This means that the photometric data from any AGN sources are likely to be a poor fit to all of the galaxy templates, and will therefore probably produce a redshift value significantly different to the value produced by fitting to the AGN library. The photometric data from normal galaxies, however, may well be a fairly good fit to one of the normal galaxy or hybrid templates in the AGN library, and therefore produce a redshift value from the AGN library which is fairly similar to that from the 'galaxy' library.

5.4.2 Comparison with other redshift catalogues

The redshift values obtained from the Le Phare photometric redshift fitting were compared to the F12 and RR13 photometric redshift catalogues. First the two published catalogues were compared to each other – the two catalogues were matched using a match radius of 1.5 arcsec, giving 7895 matches; the redshift values of these matched sources from the two catalogues are compared in Figure 5.15. This plot shows significant scatter, demonstrating that there are some significant disagreements between the two catalogues, highlighting the difficulties in

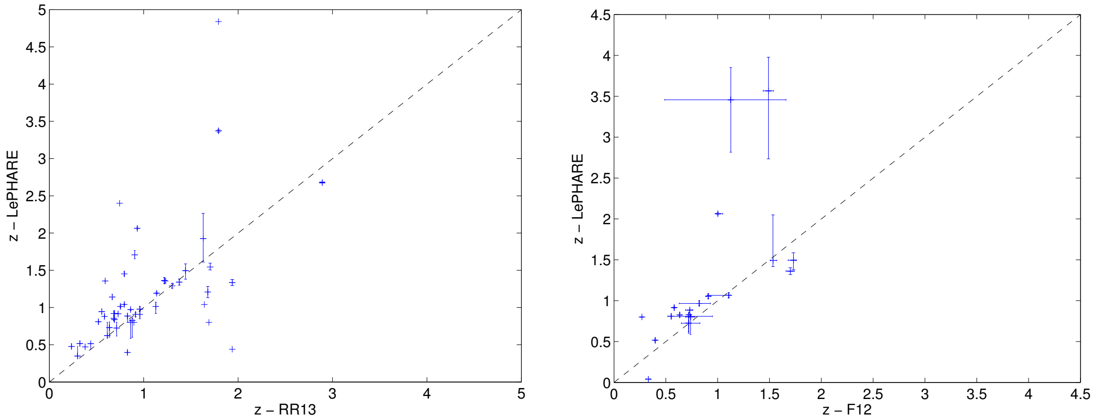

Figure 5.16: Comparison of the redshift values from Le Phare with those from the RR13 (left panel) and F12 (right panel) catalogues. The dashed line indicates where the redshift values from the two catalogues are equal. 1σ error bars are plotted for sources in the Le Phare catalogue with a final value from the galaxy library and values from the F12 catalogue.

achieving reliable redshifts using photometric methods. Redshift values derived in this work are compared to the F12 and RR13 catalogues in Figure 5.16. For the majority of the sources there is a good agreement between the Le Phare values calculated here and the values from RR13 and F12. However, for several sources there are significant differences between the Le Phare values and the values from the other two catalogues, with the values for 11 sources differing by more than a factor of two. Many of the sources do not agree within the error bars, although note that these error bars simply quantify the goodness of the fit of the photometric data to the chosen template, which does not necessarily mean that the chosen template is the correct one. The two points which lie furthest from the $z_{\mathrm{LEPHARE}} = z_{\mathrm{F12}}$ line have the largest error bars.

There are six objects with spectroscopic redshift values available, these spectroscopic redshifts are along with the available photometric redshift values in Table 5.2. For three of the objects the spectroscopic and photometric values are in good agreement, and for a fourth object the F12 and RR13 values are very close to the spectroscopic value but the Le Phare value is a factor of two higher. The photometric values do not agree with the spectroscopic values for the remaining two sources; for one they are a factor of three higher, and for the other the three different photometric values are too different to each other to be able to make a valid comparison ($z_{\mathrm{RR13}} = 1.69, z_{\mathrm{F12}} = 0.27, z_{\mathrm{LE\ PHARE}} = 0.80$).

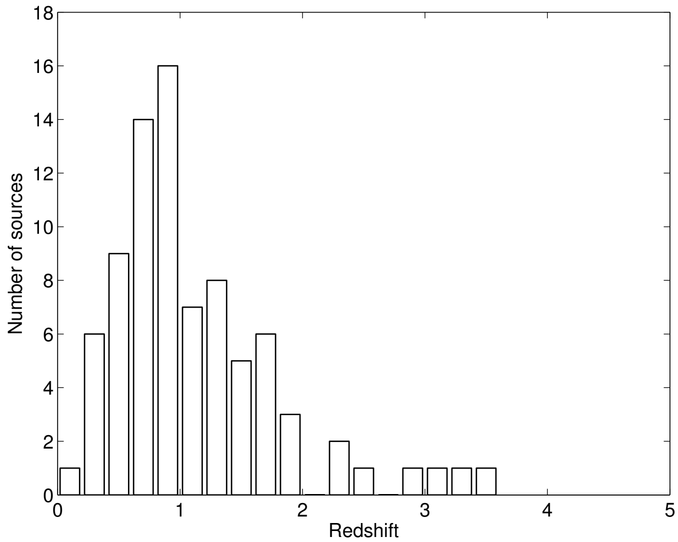

Figure 5.17: Redshift distribution for all sources in Sample W with a redshift estimate.

5.4.3 Compiling the final redshift catalogue

As mentioned, there are a small number of spectroscopic redshifts and two published photometric redshift catalogues available in the Lockman Hole, as well as the new photometric redshifts derived in this work. These were combined to produce a final redshift catalogue with the best available redshift for each 10C source in Sample W. This catalogue is then used to investigate the properties of objects associated with the 10C sources later in this Chapter.

A redshift value for each source is selected in the following order of preference: 1) spectroscopic redshift value (6 sources), 2) photometric redshift from RR13 (53 sources), 3) photometric redshift from F12 (7 sources) and 4) photometric redshift from LE PHARE fitting (16 sources). RR13 values were given preference over F12 values because they are available for a greater number of sources as the RR13 catalogue covers the whole 10C survey area, so this gives the greatest consistency. A full catalogue of the redshifts is given in the appendix.

The redshift distribution of all 82 sources in Sample W with a redshift estimate (or value) is shown in Figure 5.17. The median redshift is 0.93 with an interquartile range of 0.77. The redshift distribution is discussed in Section 5.6 after the possible redshifts for sources classified as confused when matching have been considered.

5.4.4 Confused sources

In Section 5.3.3, a total of 30 possible counterparts were identified for the eight 'confused' sources in Sample W. The LE PHARE photometric code was run on these possible counterparts

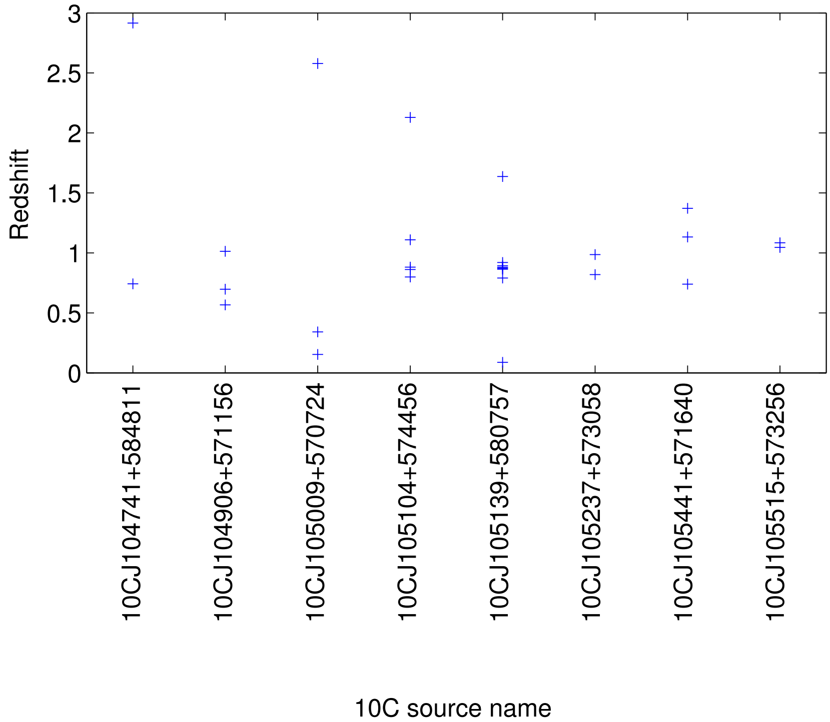

Figure 5.18: Redshift values for the possible counterparts for each 10C source classified as confused.

in exactly the same way as detailed in Section 5.4. The resulting redshift values for all the possible counterparts to each 'confused' 10C source are shown in Figure 5.18.

5.5 Radio to optical ratio

The ratio of the radio and the optical flux densities of a source provides useful information about the nature of the source as radio galaxies have much higher radio flux densities for the same optical magnitude than radio-quiet AGN or starforming galaxies (further details are given in Chapter 1). The radio-to-optical ratio was defined following Condon (1980), using the following expression:

$$R = S_{1.4\ \mathrm{GHz}} \times 10^{0.4(m-12.5)} \tag{5.1}$$

where $S_{1.4\ \mathrm{GHz}}$ is the flux density at 1.4 GHz in mJy and m is the optical magnitude. Sources with radio-to-optical ratios $R > 1000$ are considered to be radio loud (Machalski & Condon 1999), while those with smaller values of R are classified as radio quiet (and are therefore either radio-quiet AGN or starforming sources). i-band magnitudes are used here, as they are the best match to the I-band magnitudes used by Machalski & Condon.

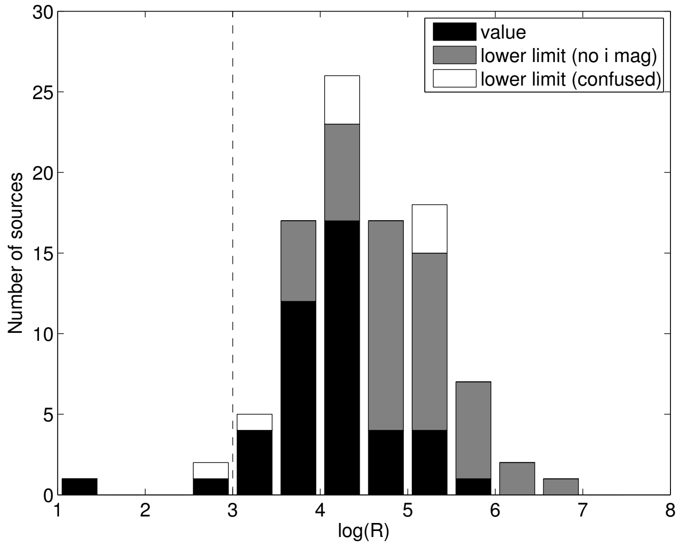

Figure 5.19: Radio-to-optical ratio R for sources in Sample W with a FUSED match. Lower limits are included for those sources without an i-band detection (grey) and for those classified as confused (white); these sources could move to the right on this diagram. Sources with $R > 1000$, indicated by the vertical dashed line, are considered radio loud.

The radio-to-optical ratio, R, was calculated using equation 5.1 for the sources in Sample W which have an i-band magnitude available. Thirty-six sources have a match in the FUSED catalogue but are not detected in the i-band and a further eight are unmatched in the FUSED catalogue. For these 44 sources, lower limits on R are calculated using 23.3 (the limiting magnitude of the i-band observations) as a lower limit on the i-band magnitude. For the eight sources classified as confused when matching, R was calculated using the brightest of the possible counterparts identified in Section 5.3.3, which serves as a lower limit on R.

The radio-to-optical ratio distribution of all sources in Sample W is shown in Figure 5.19, including lower limits for unmatched and confused sources. Based on the study out to $z \sim 0.2$, Machalski & Condon (1999) found that 98 percent of normal and starburst galaxies had $R < 1000$, so this is used as the cut-off point between radio-loud and radio-quiet objects. Figure 5.19 shows that only three sources in Sample W have $R < 1000$, so using this criterion the other 93 are radio loud.

This analysis shows that all but three (97 percent) of the 10C sources in Sample W are radio galaxies. This is confirmed by the VLBI data in Chapter 4, which showed that at least 65 percent of the 10C sources contain an AGN. The nature of these radio galaxies is be discussed further in Chapters 6 and 7.

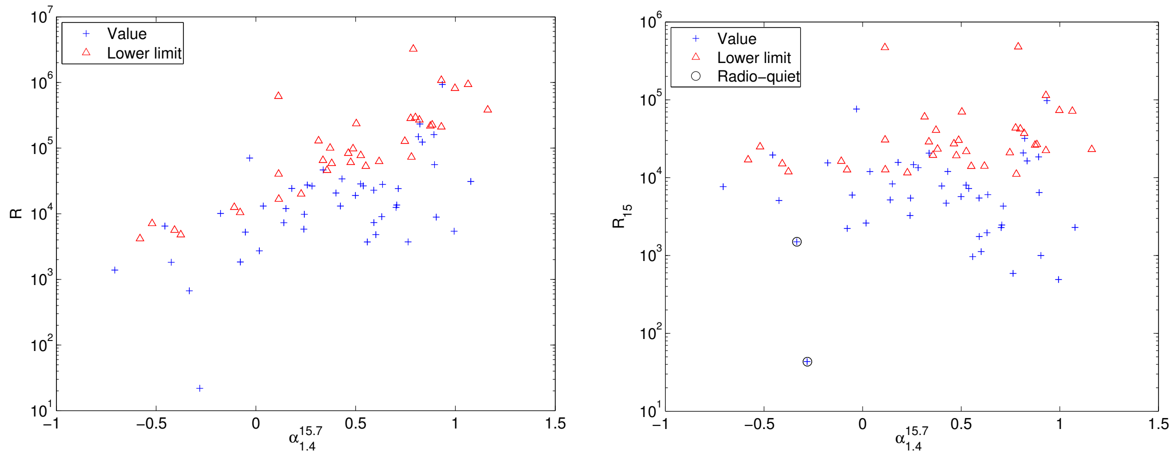

Figure 5.20: Radio-to-optical ratio R as a function of spectral index. Left-hand panel shows R calculated using 1.4-GHz flux density, while the right-hand panel shows R_{15}, calculated using 15.7-GHz flux densities. Red triangles indicate lower limits on R for sources which are not detected in the i band and therefore have a lower limit on i band magnitude. Confused sources are not included. The two radio-quiet sources are circled in the right-hand panel.

5.5.1 Correlations between R and spectral index

The left-hand panel of Figure 5.20 shows R as a function of radio spectral index. There appears to be a positive correlation between R and spectral index; this is, however, a selection effect as the sample is selected at 15.7 GHz but 1.4-GHz flux densities are used to calculate R. To test for any real correlation between radio-to-optical ratio and spectral index R_{15} was calculated using 15.7-GHz flux density, as follows,

$$R_{15} = S_{15.7\ \mathrm{GHz}} \times 10^{0.4(m-12.5)} \tag{5.2}$$

R_{15} is shown as a function of spectral index in the right-hand panel Figure 5.20. The positive correlation with 1.4-GHz radio-to-optical ratio is no longer seen, confirming that this effect was due to the sources being selected at 15.7 GHz.

The three radio-quiet sources (one of which is a lower limit from a confused source, so could in theory be radio loud) all have rising spectra. This means that these sources are very unlikely to be starforming galaxies. The rising spectral shape means these sources have smaller 1.4-GHz flux densities than the majority of the 10C sample, which could explain why they have small values of R. This can be explored by comparing the R_{15} values of these sources with those of the rest of Sample W; the positions of two of these sources are marked by black circles in Figure 5.20, the remaining (confused) source, which is not shown in the figure, has $R_{15} = 2096$. Two of the three sources therefore have values of R_{15} similar to the rest of Sample W, while one has a significantly lower value.

5.6 Source properties

In this section, the radio properties of the sources in Sample W are considered in light of the redshift values derived in Section 5.4.

5.6.1 Summary of radio properties of Sample W

The radio properties of the sources in Sample W (along with those of the full 10C Lockman Hole sample) were presented in Chapter 2. Flux densities are available at a range of frequencies including 1.4 and 15.7 GHz, and radio spectral indices are calculated for all but one source in Sample W (an upper limit is available for the one remaining source). The sources were split into flat-spectrum sources, with $\alpha < 0.5$, and steep-spectrum sources with $\alpha > 0.5$. Best estimates of the angular size of each source were also compiled, with the values of angular size less than the synthesised beam size for the relevant catalogue flagged as upper limits.

5.6.2 Redshift distribution

Redshift values for 82 out of the 96 sources in Sample W were estimated in Section 5.4. The redshift distributions of steep and flat spectrum sources are shown separately in Figure 5.21; the redshift distributions for the two samples appear fairly similar, although the distribution for flat spectrum sources may peak at a slightly higher redshift. A KS test was performed on the two samples and the probability of them being drawn from the same population was 0.19, indicating that the two distributions are not significantly different.

5.6.3 Luminosity distribution

Luminosities were calculated for all sources with a redshift value. The luminosities were k-corrected based on their radio spectral index using the following expression:

$$L_\nu = 4\pi d_L(z)^2 S_\nu[(1+z)^{\alpha-1}] \tag{5.3}$$

where d_L is the luminosity distance.

The 15.7-GHz luminosity distribution for all sources in Sample W with a redshift estimate is shown in Figure 5.22, with steep and flat spectrum sources shown separately. The distributions for the steep and flat-spectrum sources are very similar, suggesting there is no difference in luminosity between the two populations.

To aid comparison with other work, luminosities at 1.4 GHz were also calculated and the luminosity distribution is shown in Figure 5.23. The typical divide between the luminosities of FRI and FRII sources at 1.4 GHz is $10^{24.5}$ W Hz^{-1} (Fanaroff & Riley 1974), with 1.4-GHz luminosities above this value being typical of FRII sources and those below typical of

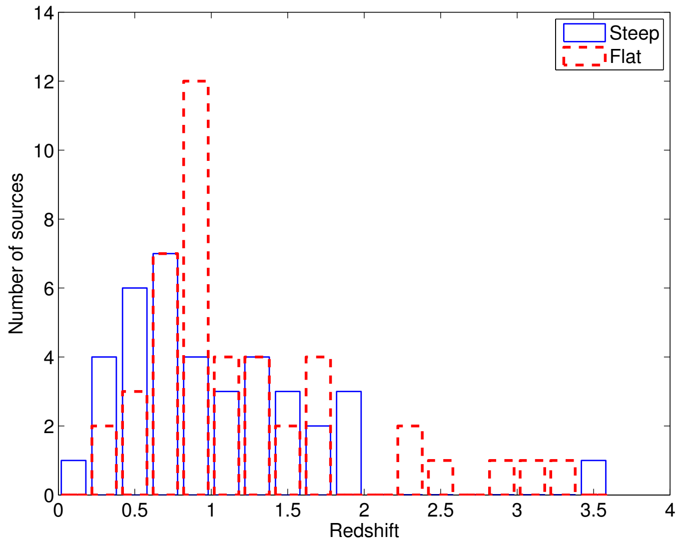

Figure 5.21: Redshift distribution for all sources in Sample W with a redshift estimate, with steep and flat spectrum sources shown separately.

FRI sources. 59 sources have luminosities above this value and 23 have luminosities below it (luminosities are not calculated for the 14 sources without a redshift value), showing that the majority of the sample have luminosities typical of the higher-powered FRII sources. It is clear from Figure 5.23 that the steep spectrum sources tend to have higher 1.4-GHz luminosities than the flat spectrum sources. However, this reflects the fact that the sources are selected at 15.7 GHz, so any steep spectrum sources with relatively low 1.4-GHz flux densities would fall below the detection limit at 15.7 GHz and not appear in the sample; thus the steep spectrum sources in the sample have higher 1.4-GHz flux densities (and therefore luminosities) than the flat spectrum sources. Figure 5.24 shows spectral index as a function of 1.4-GHz luminosity and this effect is evident here.

5.6.4 Linear size distribution

Angular sizes were calculated for all Lockman Hole 10C sources in Chapter 2, using information from a range of different catalogues. Any angular size values less than the synthesised beam size of the relevant catalogue were flagged as upper limits. Linear sizes were then calculated from these angular sizes using:

$$D = \frac{\theta d_L}{(1+z)^2} \tag{5.4}$$

where D is the linear size of the source, d_L is the luminosity distance and θ is the angular size of the source in radians. The linear size distribution is shown in Figure 5.25; the left panel shows the total distribution split into two groups, those with measured sizes and those with

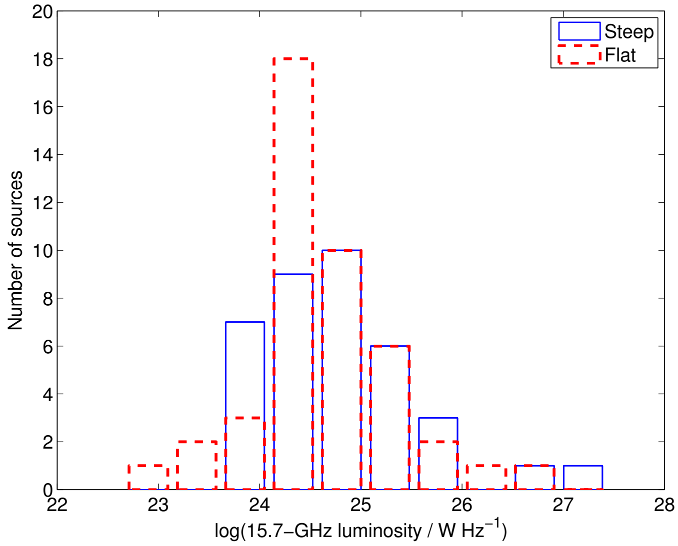

Figure 5.22: 15.7-GHz luminosity distribution for all sources in Sample W with a redshift estimate; the sample is divided into flat and steep spectrum sources.

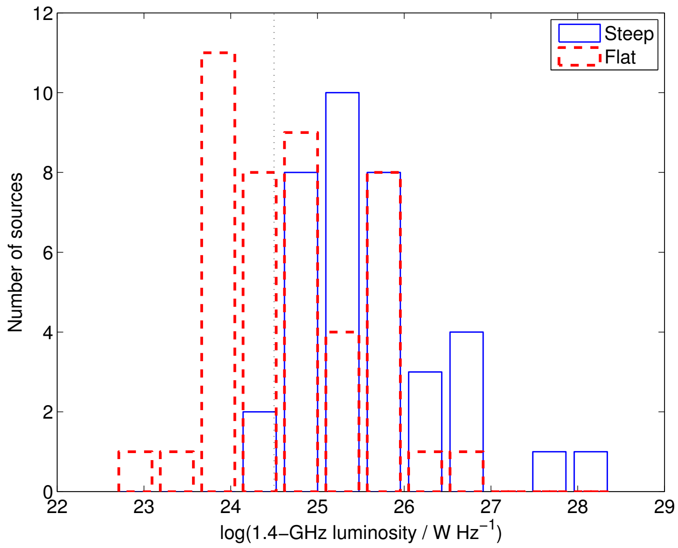

Figure 5.23: 1.4-GHz luminosity distributions for all sources in Sample W with a redshift estimate, with the sample split into flat and steep spectrum sources. The vertical dashed line represents the dividing luminosity between FRI and FRII sources.

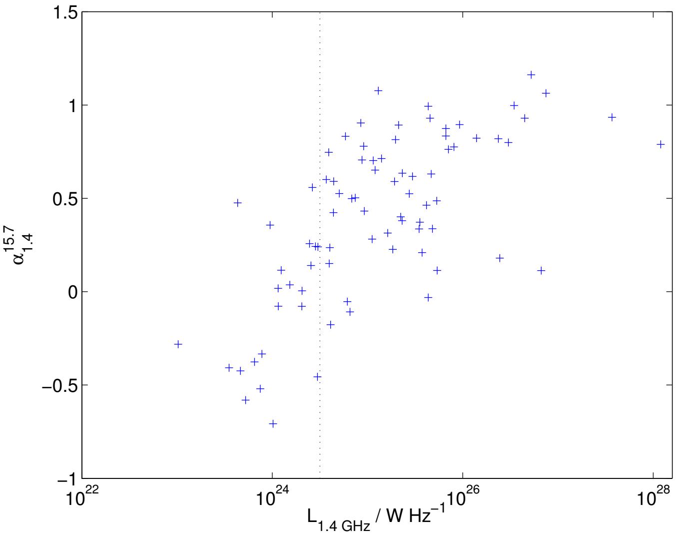

Figure 5.24: Spectral index as a function of 1.4-GHz luminosity for all sources with a redshift value in Sample W. The dotted line represents the FRI/FRII luminosity divide.

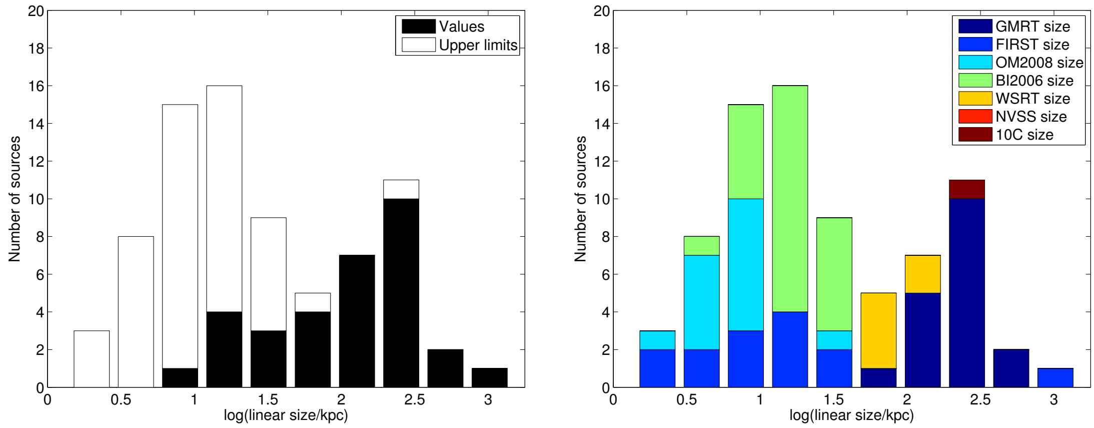

Figure 5.25: Linear size distribution for the sources with redshift values. The left panel shows upper limits and values and the right panel shows the sample split according to the radio catalogue from which the angular size value originates.

upper limits used, and the right panel shows the distributions split according to the catalogues used to determine the angular size (as described in Chapter 2). Note that the 14 sources without a redshift value are not included here. The median linear size of the sample is 21 kpc.

Figure 5.26 shows the linear size distributions for flat and steep spectum sources. It is evident that the flat spectrum sources are on average smaller than the steep spectrum sources. This is expected as the extended components in radio galaxies tend to have steep spectra, while more compact regions tend to have flatter spectra due to self-absorption. While this trend is true for the majority of the population, both steep and flat spectrum sources cover the full range

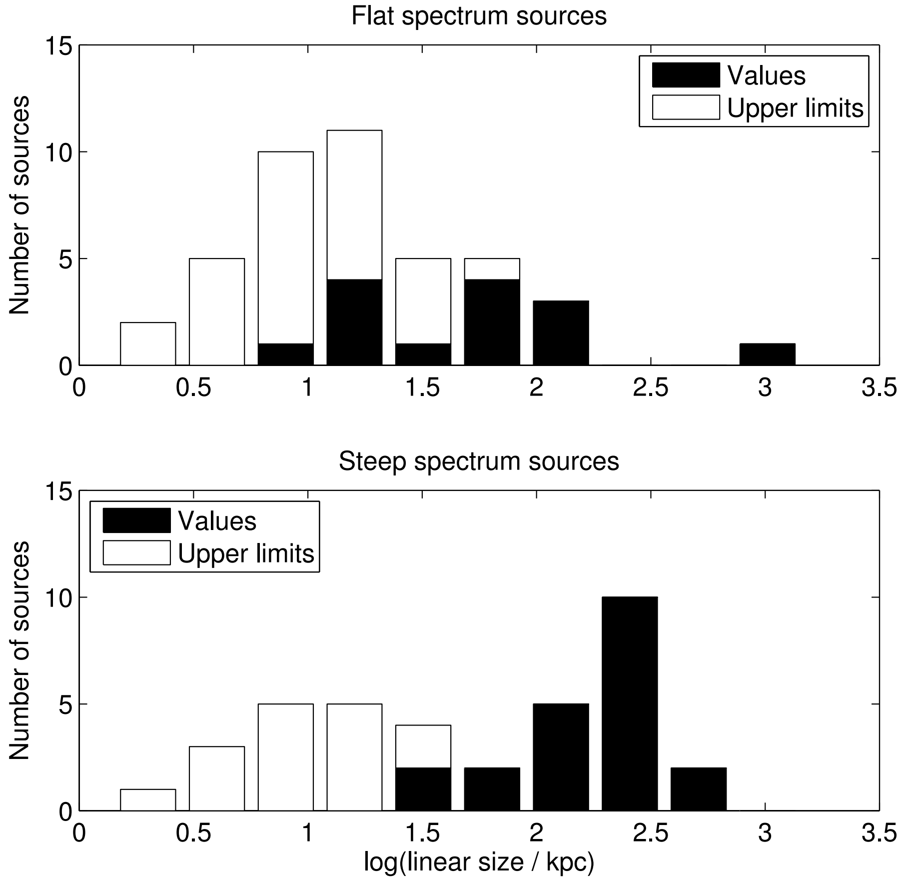

Figure 5.26: Linear size distribution for sources with redshift values. The top panel shows flat spectrum sources and the bottom panel shows sources with steep spectra. Upper limits are shown in white, and could move to the left on these plots.

of linear sizes ($1 \lesssim D \lesssim 1000$ kpc), so there are a number of small steep spectrum sources and large flat spectrum sources. This is consistent with the findings in Chapters 3 and 4 which indicate that there are small populations of both extended, flat spectrum sources and compact, steep spectrum sources in this sample.

Figure 5.27 show both the linear and angular sizes as a function of redshift for all source in Sample W. This shows that, as expected, the sources with larger angular sizes tend to be a lower redshifts, and at $z > 2$ all sources are unresolved.

The linear size of a source can provide some information about its nature; radio galaxies can have a range of linear sizes, from less than 1 kpc for compact radio sources to more than 1000 kpc for some double sources (Blundell et al. 1999), whereas starforming sources are only found at the smaller end of this distribution. This is because the radio emission from starforming galaxies does not extend beyond the physical size of the galaxy, while radio galaxies can have jets extending many hundreds of times beyond the extent of the host galaxy. For example,

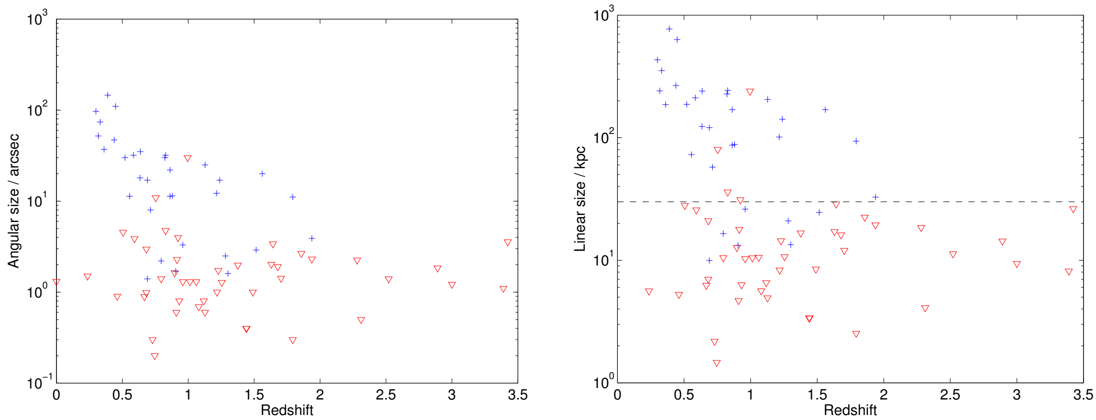

Figure 5.27: Angular and line size as a function of redshift. Red arrows are upper limits on size, blue crosses are values. The dashed horizontal line in the right-hand panel is at $D = 30$ kpc, any sources larger than this value are too large to be starforming galaxies.

Muxlow et al. (2005) used high-resolution JVLA and MERLIN observations to study the structure of 92 faint radio sources with $S_{1.4\ \mathrm{GHz}} > 40$ μJy. All but one of the sources are resolved, and they are classified as either starburst sources or AGN on the basis of their structure and radio spectra. Using the angular sizes and redshifts listed in the Muxlow et al. catalogue, linear sizes were calculated for all sources and it was found that the largest size of any starburst source was 26 kpc, with most having sizes less than 10 kpc. Therefore, sources with linear sizes > 30 kpc are unlikely to be starforming galaxies and are therefore almost certainly radio galaxies. Twenty-five sources in Sample W have linear sizes > 30 kpc, confirming the conclusion presented in Section 5.5 that these sources are radio galaxies.

5.6.5 VLBI information

Information on smaller angular scales can be gained by using VLBI observations. In Chapter 4 the 10C sample was matched to the Middelberg et al. (2013) VLBI catalogue which covers part of the Lockman Hole. Figure 5.28 shows the luminosity and redshift distributions for those sources in the VLBI 'detectable' sample which are also in Sample W, split according to sources which are and are not detected in the VLBI observations. No trends are obvious and the number of sources in this sample are too small to draw any significant conclusions.

5.7 Comparison with the SKADS Simulated Sky

In Chapter 3 a sample of sources with $S_{18\ \mathrm{GHz}} > 0.5$ mJy was selected from the S^3 catalogue; this sample should be directly comparable to the 10C sample. The radio properties of this

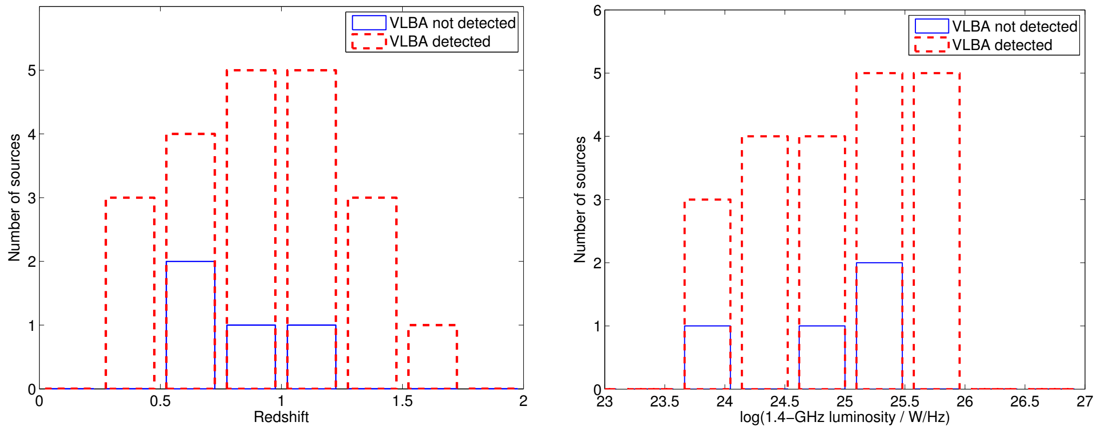

Figure 5.28: Redshift and 1.4-GHz luminosity distribution for sources in both Sample W and the VLBI detectable sample.

sample were compared to the 10C sample, which showed that the simulation fails to accurately reproduce the spectral index distribution of the observed sample. The number of flat spectrum sources is massively underpredicted; there are essentially no sources in the simulated sample with $\alpha < 0.3$, while 40 percent of the 10C sample have $\alpha_{0.61}^{15.7} < 0.3$.

The contributions of different source types to the S^3 sample are given in Table 3.5. This shows that the simulation predicts that the 10C sample should be dominated by FRI sources, making up 71 percent of the population. FRII sources provide the second-largest contribution to the simulated population, and there are only small contributions from starforming sources and radio-quiet quasars. Radio-loud sources therefore make up 87 percent of the simulated sample in total. This is lower than the proportion of radio-loud sources in the 10C sample; the radio-to-optical ratio results presented earlier in this Chapter show that 97 percent of the 10C sample are radio-loud galaxies.

Here I compare the redshift distribution of the S^3 sources and those in Sample W; Figure 5.29 shows the normalised redshift distribution for the two samples. The 10C sample is normalised by the total sample size (96 sources), which includes the 15 sources with no redshift value available. The redshift distributions of the two samples are approximately similar, although the observed sample displays a sharper peak and is missing the low redshift tail which is apparent in the simulated sample. Eleven percent of the sources in the simulated sample have $z < 0.2$, so we would expect to find approximately ten sources in the observed sample in this range if the two distributions are similar. However, there is only one source in the observed sample with a redshift less than 0.2. This might be because the 10C fields were chosen so that they did not include any bright 15.7-GHz sources, and bright sources tend to be some of the closest sources. However, extrapolating the source count from the 9C and 10C surveys

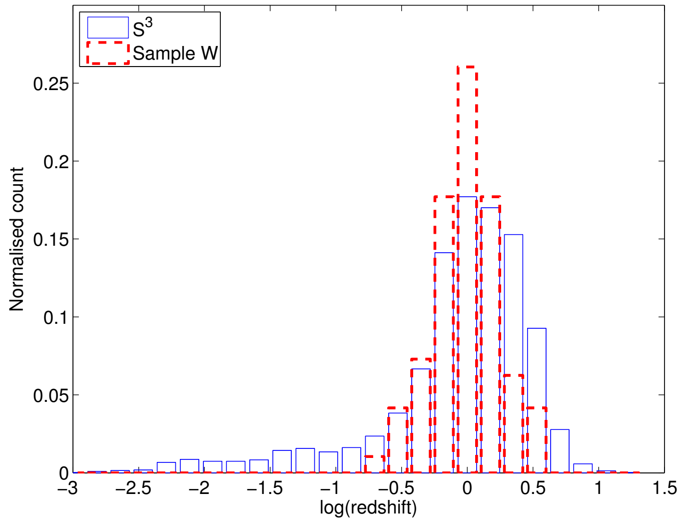

Figure 5.29: Normalised redshift distribution for sources in S^3 and in Sample W. Objects in Sample W with no redshift value have been omitted, but included in the normalisation.

(Davies et al. 2011), we would only expect to find ≈ 0.1 source with $S_{15\ \mathrm{GHz}} > 25$ mJy in an area of sky the size of the Lockman Hole 10C field, so it seems unlikely that it is the cause of the lack of approximately 10 sources. It is possible that some of the 15 sources which lack redshift information and are therefore missing from the observed sample have redshifts less than 0.2. It is unlikely, however, that any of the eight sources without a match are found at this low redshift, as they would have to be very faint in the optical to have $z < 0.2$ and not be detected in the optical or infrared observations. Only two of the 30 possible counterparts for the confused sources have $z < 0.2$, so these sources cannot account for the missing sources in this redshift range.

The majority of the sources with $z < 0.2$ in the simulation are starforming sources, so the fact that the sources in this redshift range are missing from the 10C sample is consistent with the fact that there are no starforming sources in this sample. The incorrect proportion of starforming sources predicted by the simulation could indicate that the spectra of the starforming sources in the simulation is wrong, and they in fact have much steeper spectra than assumed, or that the extrapolation of the luminosity function for the starforming galaxies is not correct.

The peak also appears to be shifted to slightly lower redshifts in the observed sample, with more sources in the bins $-0.25 < \log(z) < 0.1$ but fewer sources in the bins $\log(z) > 0.25$. It is plausible that some of the sources without an optical counterpart have $\log(z) > 0.25$.

5.8 Conclusions

In this chapter the FUSED multi-wavelength catalogue, which contains up to ten photometric bands in the optical and mid-infrared, was matched to the 10C sample and counterparts were identified for 247/296 10C sources. I defined a complete sample of 96 sources with relatively uniform information available (Sample W), 80 of these 96 sources have a counterpart in the FUSED catalogue. Sample W was matched to other catalogues available in the field, including WISE and the *Chandra* and *XMM-Newton* X-ray catalogues.

Photometric redshifts were estimated for all sources in Sample W with sufficient photometric information available using the Le Phare code. This produced redshift estimates for 78/80 sources, albeit with large errors in some cases. The results are compared to two published photometric redshift catalogues (F12 and RR13), and are generally in good agreement, although there are some significant outliers. These catalogues were then combined to produce a final redshift catalogue, which contains redshift estimates for 82 out of the 96 sources in the sample (85 percent). The large errors on some of the redshift estimates, along with the significant discrepancies between catalogues in some cases, mean that photometric methods cannot be used to produce reliable redshifts for every source. They can, however, provide valuable information about the properties of a population as a whole.

The radio-to-optical ratio, R, or a lower limit on R, was calculated for all sources in Sample W. These R values show that 93/96 (97 percent) of Sample W are radio loud. The 10C sample is therefore dominated by radio galaxies. The three radio-quiet sources all have rising spectra, ruling out the possibility that they are starforming galaxies, so they are likely to be radio-quiet AGN.

The overall radio properties of the sources in Sample W are then discussed in light of this redshift information; luminosities and linear sizes are derived for those sources with redshift estimates. This shows that 59/80 sources have luminosities consistent with being FRII sources. The properties of these sources are discussed further in the next chapter.

The redshift distribution for sources in Sample W was compared to the distribution of the S^3 catalogue; both samples have similar distributions, although the sources with $z < 0.2$ which are predicted to be present by the simulation are missing from the 10C sample. These low-redshift sources found in the simulated sample are starforming sources, so the fact that they are missing from Sample W is consistent with the finding that there are essentially no starforming sources in the 10C sample.

CHAPTER 6

INVESTIGATING THE NATURE OF 10C RADIO GALAXIES

The primary aim of the work presented in this chapter is to explore the nature of the objects associated with 10C radio sources. In Chapter 5 Sample W was defined: a complete sample of 96 sources selected from the 10C survey with deep, higher-resolution, 1.4-GHz data available. Counterparts were identified for 80 out of these 96 radio sources and photometric redshifts were derived for the objects with sufficient photometric data. These data were used to show that essentially all ($\gtrsim 97$ percent) sources in this sample are radio galaxies; the nature of these radio galaxies is the subject of this chapter.

It has been known for some time (Hine & Longair 1979) that the properties of radio galaxies are not fully explained by the conventional picture of an AGN, consisting of an accretion disk surrounded by a dusty torus (Antonucci 1993, see Chapter 1 for more details). Based on this conventional picture, we would expect radio-loud objects viewed along the jet axis to show both broad and narrow optical emission lines, while radio-loud objects viewed perpendicular to the jet would only show narrow lines and would have a clear mid-infrared signature of the dusty torus. However, many radio-loud AGN lack the expected narrow-line optical emission and do not display evidence of an obscuring torus.

Subsequent studies have suggested that there are two fundamentally different accretion modes, known as 'hot mode' and 'cold mode' (see Best et al. 2005; Hardcastle et al. 2007) which could be responsible for these discrepancies. Cold-mode accretion occurs when cold gas is accreted onto the central black hole and gives rise to the traditional picture of an AGN (Antonucci 1993). These objects therefore show the expected high-excitation lines in their optical spectra, so are often referred to as high-excitation radio galaxies (HERGs). (This mode is also sometimes referred to as ‘quasar mode’.) ‘Hot mode’ sources, however, are fuelled by the accretion of warm gas and lack many of the typical signatures of AGN, such as strong optical emission lines. These objects are therefore often referred to as low-excitation radio galaxies (LERGs). (This mode is sometimes also referred to as ‘radio mode’.) LERGs typically show no evidence for a dusty torus or for accretion-related X-ray emission. There are also differences in the host galaxies of the two populations, with HERGs found in less massive and bluer galaxies than LERGs. Both HERGs and LERGs are found across the full range in radio luminosities, although LERGs seem to dominate at lower luminosities and HERGs at higher luminosities (Best & Heckman 2012); almost all FRI sources are LERGs, but many FRII sources are LERGs as well.

In this chapter I will use the wealth of multi-wavelength data available in the field to distinguish between these two types of radio galaxy. In Section 6.1 I describe the variety of different methods used to do this, and in Section 6.2 I present the results from these classification methods. In Section 6.3 I then compare the results from the different approaches taken, and define an overall classification scheme. The radio properties of these different types of radio galaxies are discussed in the next chapter.

6.1 Methods of distinguishing between high-excitation and low-excitation radio galaxies

There are many different ways of distinguishing between HERGs and LERGs, using a variety of different wavelengths and object properties. The different methods used in this chapter are summarised here.

6.1.1 Optical compactness

The compactness of an object in the optical image can help to indicate whether it is a HERG. For example, Mahony et al. (2011) compared optical compactness classifications from the superCOSMOS survey (Hambly et al. 2001) to spectral classifications and found that most of the objects which displayed broad emission lines, and are therefore HERGs, were point-like in the optical. However, they found that 27 percent of the objects which were extended in the optical also had broad emission lines. This suggests that if an object is point-like it is a HERG, however, an object which is extended in the optical is not necessarily a LERG.

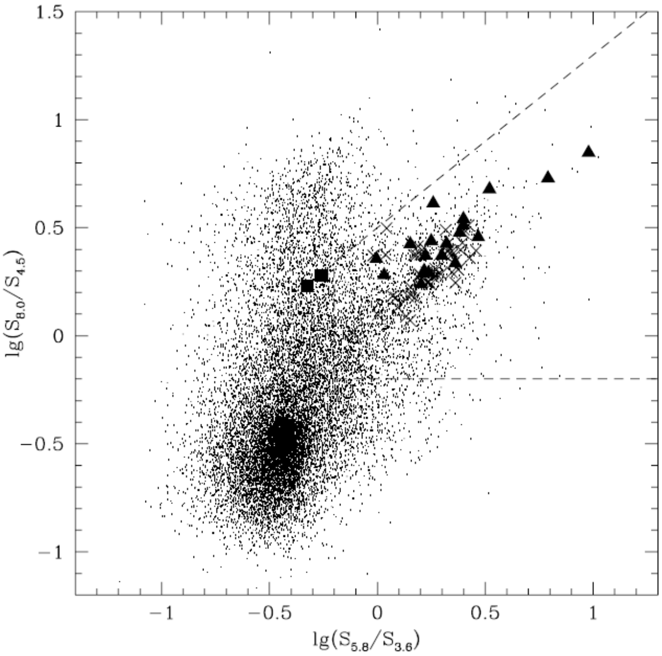

Figure 6.1: The AGN selection region in mid-infrared colour–colour space defined by Lacy et al. (2004) (shown by dashed lines). Dots are 16,000 objects detected by the *Spitzer Space Telescope* First Look Survey. Crosses, squares and triangles represent known AGN. Taken from Lacy et al. (2004).

6.1.2 Mid-infrared colours

Mid-infrared colour–colour diagrams are an effective way of separating HERGs and LERGs, as the characteristic signatures of a dusty AGN torus, typically present in HERGs but missing from LERGs, produces power-law continuum emission which means these objects fall in a particular region on these diagrams (Whysong & Antonucci 2004; Ogle et al. 2006).

Lacy et al. (2004) defined a 'wedge' in the IRAC colour–colour diagram in which objects with power-law continuum emission (produced by a dusty AGN torus) are expected to lie, as shown in Figure 6.1. HERGs are expected to lie inside this 'AGN region', while LERGs are not.

Sajina et al. (2005) simulated an IRAC colour–colour diagram by modelling the source spectra with three components: 1) direct emission from old stars, 2) polycyclic aromatic hydrocarbon (PAH) emission (associated with star-forming regions) and 3) power-law continuum emission (from small dust grains heated by an AGN). They fit this model to a sample of 60 nearby galaxies, including ellipticals, normal spirals, ultraluminous infrared galaxies, starbursts, Seyfert galaxies, and HII galaxies. They include redshift effects ($z \sim 0$ to 2) and add a noise term to generate $\sim 16,000$ simulated objects. Fig 6.2 shows where sources dominated by each of these three components are found to lie on the IRAC colour–colour diagram. Region 1

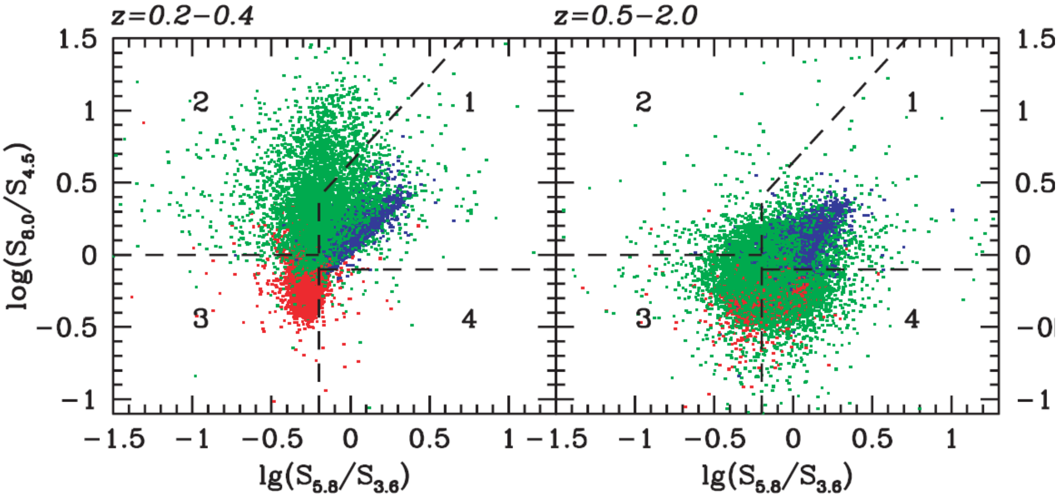

Figure 6.2: Positions of simulated sources on an IRAC colour–colour diagram. Sources dominated by continuum emission (AGN) are shown in blue, those dominated by PAH emission are shown in green and those dominated by emission from stars are shown in red. Region 1 is the region used to select HERGs, region 2 is where low-redshift starforming sources are found, region 3 is the old starlight dominated region, where LERGs are expected to lie. Taken from Sajina et al. (2005).

is the 'wedge' used to select AGN used by Lacy et al. (2004, 2007) in which we expect to find HERGs. Note how at $z > 0.5$ the AGN migrate away from the simple power law, justifying the need for the wedge shape.

Sources dominated by old, red starlight are shown in red in Figure 6.2, and lie in Region 3 outside the bottom left corner of the Lacy AGN wedge. LERGs are generally hosted by old, red elliptical galaxies and are therefore expected to lie in this region. Padovani et al. (2011) studied the properties of 256 faint ($S_{1.4\ \mathrm{GHz}} > 43$ µJy) radio sources observed at 1.4 and 5 GHz with the VLA in the Chandra Deep Field South using the wealth of ancillary data available in the field. They plotted the positions of four known FRI sources and found that all four lay in the old starlight dominated region (Region 3 in Figure 6.2), consistent with the fact that FRI sources (which are mostly LERGs) are predominantly hosted by red ellipticals (e.g. Bonzini et al. 2013).

Low-redshift starforming galaxies are expected to be found in Region 2 in Figure 6.2, the vertical strip $\log(S_{5.8}/S_{3.6}) \sim -0.2$ to -0.8 and $\log(S_{8.0}/S_{4.5}) > 0$. We therefore do not expect to find 10C sources in this region.

Zinn et al. (2012) investigated how well the IRAC colour–colour diagram separated different types of radio sources selected from the Australia Telescope Large Area Survey (ATLAS, Norris et al. 2006; Middelberg et al. 2008). ATLAS covers 7 deg^2 in two separate fields at 1.4 and 2.3 GHz, with detection limits of $\sim$ 100 and $\sim$ 300 µJy respectively. Zinn et al. use spectroscopic classifications of a subsample of these sources by Mao et al. (2012) to investigate where different source types lie on the IRAC colour–colour diagram. They found that the Lacy AGN wedge contained AGN with very little contamination from starforming sources.

Donley et al. (2012) further investigated mid-infrared selection of AGN and defined a narrower wedge, which has significantly lower contamination from starforming sources than the Lacy et al. (2004) wedge but consequently misses some AGN. In this chapter I use the wedge defined in Lacy et al. (2004, 2007), as this provides the most reliable way of selecting all sources with an AGN torus (on the basis that there are essentially no starforming sources in this sample). This region is defined as follows:

$$\begin{aligned} & \log_{10}(S_{8.0}/S_{4.5}) \leq 0.8\log_{10}(S_{5.8}/S_{3.6}) + 0.5, \\ \text{and } & \log_{10}(S_{5.8}/S_{3.6}) > -0.2, \\ \text{and } & \log_{10}(S_{8.0}/S_{4.5}) > -0.2. \end{aligned} \tag{6.1}$$

I will refer to this as the 'Lacy AGN wedge', and classify radio galaxies with host galaxies lying inside this region as HERGs.

6.1.3 SED fitting

The optical and mid-infrared SED template fitting used to estimate photometric redshifts in Chapter 5 can also provide useful information about the host galaxy. Objects can be classified according to the type of SED which best fits the photometric data. LERGs are generally found in early-type galaxies dominated by old, red stars, while HERGs tend to be associated with bluer galaxies. SED type can therefore provide useful information about whether a source is a HERG or a LERG. The template libraries were split into four different object types, listed below (these classifications are similar to those described in Mignano et al. 2008):

1) Early type spectra (ETS) – ellipticals and early spirals (bulge dominated Sa);
2) Late type spectra (LTS) – late spirals (Sb, Sc, Sd) and irregular Magellanic (Im) galaxies;
3) Starbursting spectra (SB) – starburst galaxies;
4) AGN – sources which are fitted by an AGN spectra, including hybrid spectra.

Sources with ETS host galaxies are expected to be LERGs, while sources associated with AGN host galaxies are probably HERGs. The disadvantage of this method is that the results are very sensitive to the input library of SEDs used, as discussed in Section 6.2.3.

6.1.4 X-ray emission

HERGs typically produce X-ray emission, caused by the accretion of matter onto the central black hole. This accretion-related X-ray emission is generally missing from LERGs (Evans et

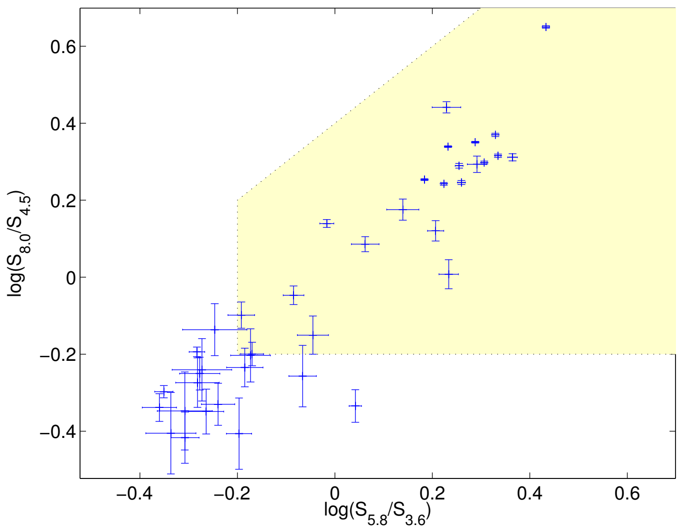

Figure 6.3: An IRAC colour–colour diagram for sources in Sample W with a detection in all four IRAC bands only. Error bars are shown on all points. The yellow shading shows the Lacy AGN region, in which HERGs are expected to lie.

al. 2006; Hardcastle et al. 2006). X-ray observations are therefore a useful diagnostic of radio source type.

6.2 Identifying HERGs and LERGs

6.2.1 Optical compactness

Optical compactness information is contained in the full optical catalogue produced by González-Solares et al. (2011) (details of which are given in Section 5.1). This catalogue contains optical compactness classification flags in each band (r, g, i and z), which are then combined into a merged probability of each object being point-like or extended ('pstar' and 'pgalaxy' respectively). Any source with pgalaxy $>$ 90 percent was considered extended, and any source with pstar $>$ 90 percent was considered point-like.

Optical compactness information is available for 59 sources in Sample W and all 59 fell into one of other of the two categories: nine are classified as point-like, and are therefore probably HERGs, while the remaining 50 are classified as extended.

6.2.2 IRAC mid-infrared colour–colour diagrams

The sources in Sample W which are detected in all four IRAC bands are plotted on an IRAC colour–colour diagram in Figure 6.3, where the Lacy et al. AGN area (described by equation 6.1) is shown in yellow. There are 39 objects included in this diagram and 22 of these lie

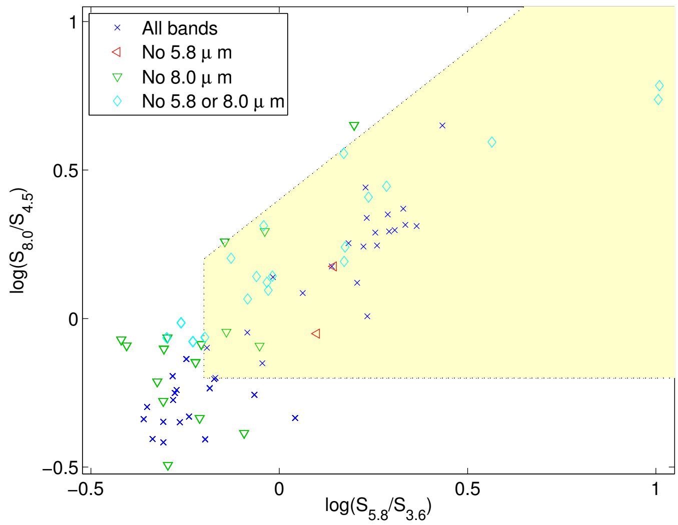

Figure 6.4: An IRAC colour–colour diagram for sources in Sample W, including upper limits for sources which are not detected in one or two of the IRAC bands. Sources without a 5.8 µm detection could move to the left, sources without an 8.0 µm detection could move down, and sources without 5.8 or 8.0 µm values could move left or down. The yellow shading shows the Lacy AGN region, in which HERGs are expected to lie.

Table 6.1: 95 percent completeness limits for the four IRAC bands. These are used as upper limits on the flux density for sources not detected in one or more bands.

Band wavelength / µm	95 % completeness / µJy
3.6	14
4.5	15
5.8	42
8.0	56

inside the AGN area. Error bars are included on this plot but are omitted from all further IRAC colour–colour diagrams for clarity.

Figure 6.3 shows that all the 10C sources with a detection in all four IRAC bands lie along the power-law which objects with a mid-infrared AGN torus are expected to follow, or in the region where sources dominated by old starlight are expected to lie (shown in red in Figure 6.2). As expected, there are no sources in the vertical strip $\log(S_{5.8}/S_{3.6}) \sim -0.2$ to -0.8 and $\log(S_{8.0}/S_{4.5}) > 0$ where low-redshift ($z < 0.5$) young starforming (PAH-dominated) sources would lie. This is consistent with the conclusion drawn from Chapter 5 that there are no starforming galaxies present in the 10C sample.

It is possible to include upper limits for those sources which are not detected in one or two of the IRAC bands by using the 95 percent completeness limit in each band as an upper limit on the flux density of any source not detected in that band. These completeness limits are shown in Table 6.1. This gives information about a further 37 sources, giving 76 sources in total (six additional sources are only detected in one band and therefore cannot be placed on the diagram). Figure 6.4 shows the IRAC colour–colour diagram of these 74 sources, including upper limits where appropriate. In addition to the 22 sources inside the AGN area, there are 21 sources are located inside this region but the nature of their limits mean that they could move outside it, their classification is uncertain. Thirty-one sources definitely lie outside this area, 17 with detections in all four IRAC bands and 14 with upper limits which could not move inside the Lacy AGN region, and these are therefore classified as LERGs. For the remaining 23 sources included on this plot the nature of their upper limits means that it is not possible to determine whether or not they lie inside the Lacy AGN area.

6.2.3 Optical and infrared template fitting

The template which is found to be the best fit to the optical and infrared data in the photometric redshift fitting process described in Chapter 5 can be used to identify different types of sources. As described in Section 6.1.3, the templates are split into four categories; ETS, LTS, SB and AGN. There are three different photometric redshift catalogues available for use here: a) the RR13 catalogue which covers the whole Lockman Hole field; b) F12 which only covers part of the field and c) the Le Phare photometric redshift catalogue resulting from the fitting performed in Chapter 5 (full details of all three catalogues are given in Chapter 5). The F12 and Le Phare catalogues use the same two template libraries: a library of 31 galaxy templates from Ilbert et al. (2009) and a library of 30 AGN templates from Salvato et al. (2009) (these are described in Section 5.4). The RR13 catalogue uses a library of 30 templates which contains both galaxy and AGN templates. The template numbers from each of these libraries which correspond to the four source types listed above are summarised in Table 6.2. The template which provided the best fit to the photometric data and was therefore used to derive the redshift value was used to classify the source into one of these four categories. The overall classifications were assigned in the same way as the overall redshift catalogue was created, with the three catalogues used in the following order of preference; RR13, F12, Le Phare.

Eleven sources are found in all three photometric redshift catalogues and the classifications of these sources were compared, as shown in Table 6.3. The classifications often differ between the different catalogues, suggesting that this is not a robust method of identifying object types. For example, source 10CJ105342+574438 is best fitted by an early-type spectrum template in F12, but to a starburst template in Le Phare; these are very different spectral types.

Table 6.2: Template numbers corresponding to the four object types in each catalogue.

Template library	Template numbers for each object type			
	ETS	LTS	SB	AGN
RR13	1 – 3	4 – 10	11 – 12	13 – 30
Ilbert et al. (2009)[a]	1 – 9	10 – 19	20 – 31	n/a
Salvato et al. (2009)[b]	2	3, 4	1, 5, 6	7 – 30

Notes:
a) Galaxy template library used in both Le Phare and F12.
b) AGN template library used in Le Phare and F12.

Table 6.3: Source classifications based on template type and redshift values for the 11 sources which appear in all three redshift catalogues.

	F12		RR13		Le Phare	
Source	Type	z	Type	z	Type	z
10CJ105007+572020	LTS	1.70	ETS	1.22	LTS	1.36
10CJ105007+574251	ETS	0.72	ETS	0.88	LTS	0.83
10CJ105020+574048	LTS	0.72	ETS	0.71	LTS	0.72
10CJ105039+572339	SB	0.27	AGN	1.69	AGN	0.80
10CJ105039+574200	ETS	0.74	LTS	0.86	LTS	0.80
10CJ105128+570901	ETS	0.55	ETS	0.52	SB	0.81
10CJ105132+571114	ETS	0.40	ETS	0.32	LTS	0.52
10CJ105142+573447	ETS	0.58	ETS	0.73	LTS	0.91
10CJ105142+573557	AGN	1.73	LTS	1.44	SB	1.49
10CJ105148+573245	SB	1.00	ETS	0.93	SB	2.06
10CJ105342+574438	ETS	0.73	LTS	0.83	SB	0.89

6.2.4 X-ray

There are two separate X-ray fields in this 10C survey area; one field observed by *Chandra* (Wilkes et al. 2009) and one by *XMM-Newton* (Brunner et al. 2008). Details of these observations and matching to the 10C catalogue are given in Chapter 5. In total, out of 32 10C sources in Sample W in the two X-ray survey areas, 15 have an X-ray counterpart (47 percent), and are therefore probably HERGs. The other objects may host an AGN which does not produce bright enough X-ray emission to be detected in these surveys, but may on the other hand be LERGs.

6.3 Comparing and combining the different methods

In this section the different methods of classifying sources described in the previous section are compared. The mid-infrared separation of HERGs and LERGs is compared to other classi-

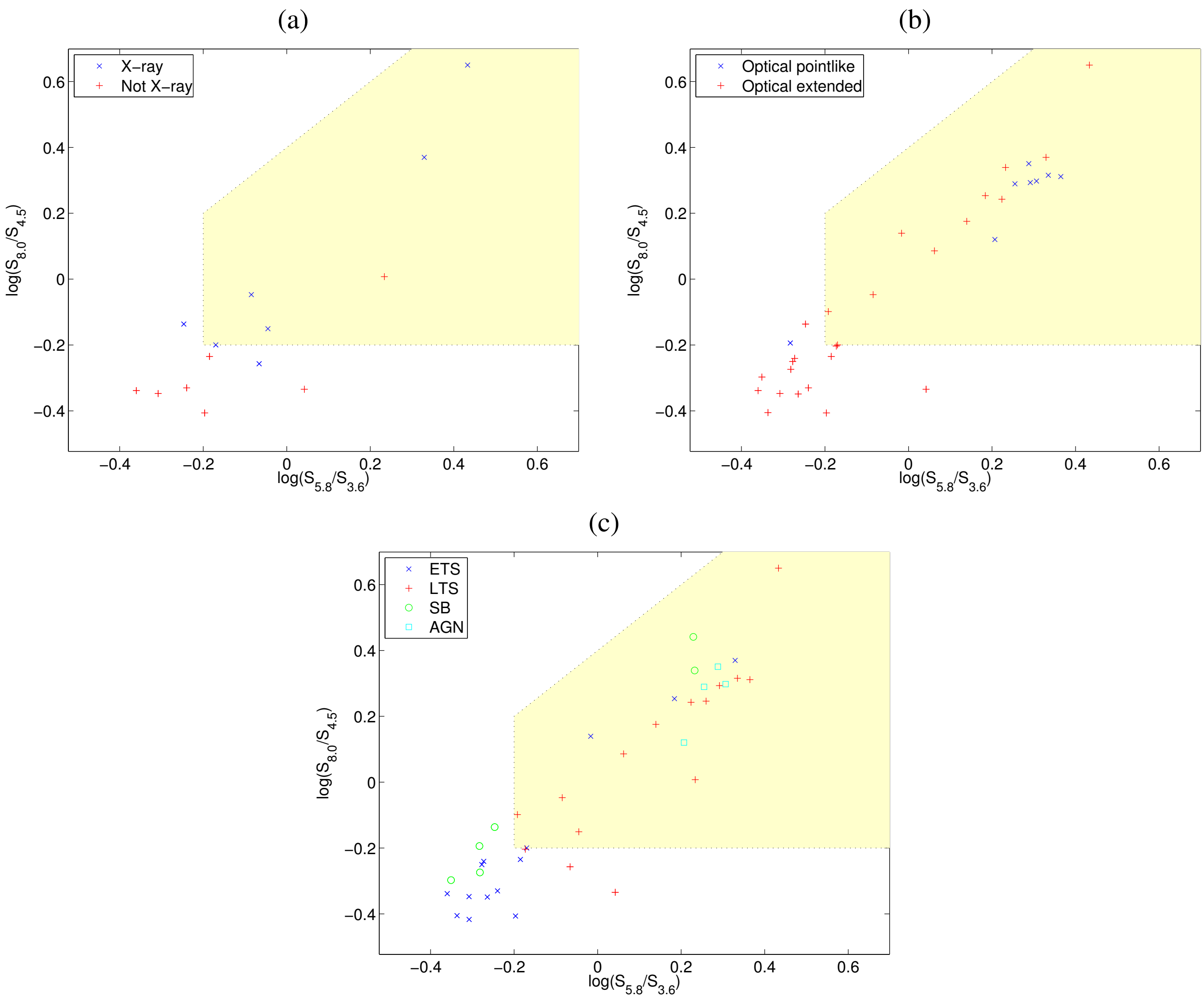

Figure 6.5: IRAC colour–colour diagrams for sources in Sample W classified using other parameters. Only sources with all four IRAC values available are included. The Lacy et al. (2004, 2007) AGN region is shown in yellow. The panels show: (a) sources with and without X-ray detections, (b) sources split according to their optical compactness and (c) sources classified according to their best-fitting template type (ETS = early-type spectra, LTS = late-type spectra and SB = starforming, AGN = active galactic nucleus).

fication methods in Figure 6.5, with the sources split using a different classification method in each panel (only sources with a detection in all four IRAC bands are shown in this diagram).

Sources which have and have not been detected by X-ray observations are shown in panel (a). All but one of the sources not detected in the X-ray lie outside the Lacy AGN area and five of the seven X-ray-detected sources lie inside the Lacy AGN area with the two remaining sources lying close to the boundary. This shows that these two methods of classifying HERGs and LERGs are generally consistent.

Panel (b) of Figure 6.5 shows sources classified according to their optical compactness on the IRAC colour–colour diagram. All but one of the eight sources which are point-like in the optical lie close together in the top right of the Lacy AGN region on this diagram, showing that there is good agreement between the two methods of classifying radio galaxies. However, 12 sources which are extended in the optical also lie inside the Lacy AGN area on this diagram. Most of these sources lie close to the power-law expected for AGN emission, rather than near the edge of the wedge, so would also lie inside the more robust Donley et al. (2012) AGN selection area implying that they are unlikely to be false classifications. This agrees with the findings of Mahony et al. (2011) that while the majority of point-like sources are HERGs, not all HERGs are point-like.

The sources are split according to their broad-band SED classification (as described in Section 6.2.3) in panel (c). Thirteen out of 15 LTS galaxies lie inside the Lacy AGN area, as do all four objects fitted with AGN spectra. Eleven out of 14 ETS sources lie outside the Lacy AGN wedge in the region in which LERGs are expected to lie. There therefore seems to be good agreement between the two classification methods, as HERGs are expected to be hosted by LTS and AGN objects, while LERGs are expected to be hosted by ETS galaxies.

Twenty sources are in an X-ray survey area and have information about their optical compactness available. Eight out of these 20 sources are detected in the X-ray, suggesting they are HERGs, and all eight are extended in the optical. Of the 12 sources which are not detected in the X-ray, 11 are extended in the optical and one is point-like.

All 59 sources with optical compactness information have a template type classification. The four sources which best fit AGN templates are all point-like in the optical. However, these two classifications are not independent – optical compactness information is used when selecting the most appropriate template type in all three photometric redshift catalogues, so it is not surprising that the classifications agree.

Table 6.4: Summary of the properties of host galaxies of 10C sources in Sample W.

10C ID	Optical compactness[a]	Lacy area[b]	X-ray detection[c]	R flag[d]	R^e	Overall classification[f]
10CJ104320+585621	E	Y	Y		31048	HERG
10CJ104328+590312	E	N	N	>	60590	LERG
10CJ104344+591503	E	N	N	>	129536	LERG
10CJ104428+591540		N	Y	>	4179	HERG
10CJ104441+591949	E	N	N	>	10446	LERG
10CJ104451+591929	E	N	N	>	211019	LERG
10CJ104528+591328	E	Y	Y	>	269519	HERG
10CJ104539+585730	E	N	N	>	45965	LERG
10CJ104551+590838	P		N	>	16714	HERG
10CJ104624+590447	E		N	>	382341	LERG
10CJ104630+582748	E	N			5421	LERG
10CJ104633+585816	E	Y	Y	>	5641	HERG
10CJ104648+590956		Y	N	>	12536	HERG
10CJ104700+591903			Y	>	478449	HERG
10CJ104710+582821	E	Y			6482	HERG
10CJ104718+585119	E		Y	>	77304	HERG
10CJ104719+582114	P	Y			24278	HERG
10CJ104733+591244			Y	>	40323	HERG
10CJ104737+592028	E	N	N	>	73125	LERG
10CJ104741+584811			N	c	190000	LERG
10CJ104742+585318	E	N	N		7314	LERG
10CJ104751+574259	E			>	83572	
10CJ104802+574117	E	N			55986	LERG
10CJ104822+582436	E	N			233330	LERG
10CJ104824+583029	E	N			20668	LERG
10CJ104826+584838	E		N		13086	LERG
10CJ104836+591846	P	Y			9015	HERG
10CJ104844+582309	E	N			28484	LERG
10CJ104849+571417	E	N			24155	LERG
10CJ104856+575528				>	225644	
10CJ104857+584103					148904	
10CJ104906+571156				c	13760	
10CJ104918+582801	P	Y			26656	HERG
10CJ104927+583830				>	27579	
10CJ104934+570613	E	N		>	284144	LERG
10CJ104939+583530	E	Y			933182	HERG
10CJ104943+571739	E	Y			1845	HERG
10CJ104954+570456	E	Y			1386	HERG
10CJ105000+585227				>	4805	
10CJ105007+572020	E				26458	
10CJ105007+574251	E				5829	

continued on next page

continued from previous page

10C ID	Optical compactness[a]	Lacy area[b]	X-ray detection[c]	R flag[d]	R^e	Overall classification[f]
10CJ105009+570724				c	3092	
10CJ105020+574048	E	N			13577	LERG
10CJ105028+574522	P	N		⋆	22	HERG
10CJ105034+572922				>	7104	
10CJ105039+572339	P	Y			3730	HERG
10CJ105039+574200	E				7284	
10CJ105039+585118	E	N		>	127447	LERG
10CJ105040+573308				>	18803	
10CJ105042+575233				>	816915	
10CJ105050+580200	E	Y			10116	HERG
10CJ105053+583233		Y		>	3227963	HERG
10CJ105054+580943				>	50143	
10CJ105058+573356			N	>	4179	LERG
10CJ105104+574456				⋆ c	505	
10CJ105104+575415	P	Y			46561	HERG
10CJ105107+575752	E	N			28022	LERG
10CJ105115+573552			Y	>	53486	HERG
10CJ105121+582648				>	936005	
10CJ105122+570854				>	217287	
10CJ105122+584136				>	98197	
10CJ105122+584409	P	Y		>	65186	HERG
10CJ105128+570901	E	N			12494	LERG
10CJ105132+571114		N			4801	LERG
10CJ105136+572944		Y	Y	>	58500	HERG
10CJ105138+574957				>	53068	
10CJ105139+580757				c	30007	
10CJ105142+573447	E	N	Y		2723	HERG
10CJ105142+573557	E		Y	>	100286	HERG
10CJ105144+573313			N	>	263251	LERG
10CJ105148+573245	E	Y	Y		9807	HERG
10CJ105206+574111			Y	>	236090	HERG
10CJ105215+581627	E				34068	
10CJ105220+585051	E			>	292501	
10CJ105225+573323	E	N	N		8880	LERG
10CJ105225+575507				>	616342	
10CJ105237+573058			N	c	130000	LERG
10CJ105240+572322	E	N	Y		19023	HERG
10CJ105243+574817	E	N			27385	LERG
10CJ105327+574546	E				160213	
10CJ105341+571951	E	N	N		13083	LERG
10CJ105342+574438	E	N			22796	LERG
10CJ105400+573324			Y	>	62679	HERG
10CJ105425+573700	E	Y			123351	HERG
10CJ105437+565922				>	493073	
10CJ105441+571640				c	15077	

continued on next page

continued from previous page

10C ID	Optical compactness[a]	Lacy area[b]	X-ray detection[c]	R flag[d]	R^{e}	Overall classification[f]
10CJ105510+574503	E	N			11989	LERG
10CJ105515+573256				c	130000	
10CJ105520+572237		Y		>	20057	HERG
10CJ105527+571607	E	N			3725	LERG
10CJ105535+574636	E	Y			70502	HERG
10CJ105550+570407	E	N		⋆	670	LERG
10CJ105604+570934				>	1080166	
10CJ105627+574221	P	Y			5251	HERG
10CJ105653+580342	E	N			1824	LERG
10CJ105716+572314				>	2764139	

Notes:
a) E = source is classified as extended, P = source is classified as point-like.
b) Y = source is located inside the Lacy et al. (2004) area on the IRAC mid-infrared colour–colour diagram, N = source is located outside this region (including sources with limits which must lie outside this region).
c) Y = sources is detected by an X-ray survey, N = source lies inside X-ray survey area but is not detected.
d) Lower limits on R values are marked '>', confused sources are marked with a 'c' and the three radio-quiet sources are marked with a ⋆.
e) Value of radio-to-optical light ratio calculated in Section 5.5.
f) HERG = source is classified as a 'probable HERG', LERG = source is classified as a 'probable LERG'.

The classifications discussed in this chapter can be combined to produce an overall classification of radio galaxy type. The following three classification methods are used; optical compactness, mid-infrared colour–colour separation and X-ray detections. Optical spectral type is not included due to the discrepancies between the different catalogues. Sources which do not have at least one of these three pieces of information available are not classified. Any source which displays any of the three indicators of high-excitation behaviour (i.e. is point-like in the optical, lies inside the Lacy AGN area, or is detected in the X-ray observations) is classified as a 'probable HERG'. Any source which has mid-infrared information available and lies outside the Lacy AGN area, or is inside the X-ray survey area but is not detected is classified as a 'probable LERG'. Sources which only have optical compactness information available and are extended are not classified as they could be either HERGs or LERGs. The classifications for each source, along with the radio-to-optical ratios, are listed in Table 6.4 and the overall classifications are summarised in Table 6.5. In summary; 34 sources are probably HERGs, 33 are probably LERGs and 29 do not have sufficient information to be classified.

6.4 Summary

A variety of different methods used to distinguish between HERGs and LERGs have been discussed in this chapter. These are; optical compactness, Lacy mid-IR AGN selection, optical

Table 6.5: Summary of HERG and LERG classifications for Sample W.

Classification	No. of sources
Probable HERG	34
Probable LERG	33
No classification	29

template fitting and X-ray observations. These classification methods were compared and generally found to be in agreement. Combining these results to produce overall classifications, a total of 34 sources are probably HERGs, 33 are probably LERGs and 29 are unclassified. The radio properties of these HERGs and LERGs are the subject of the next chapter.

CHAPTER 7

THE PROPERTIES OF HIGH-EXCITATION AND LOW-EXCITATION 10C RADIO GALAXIES

In the previous chapter the nature of the objects associated with 10C sources in Sample W were explored, and where possible were classified as either high-excitation or low-excitation radio galaxies (HERGs and LERGs respectively). Thirty-four sources display evidence of high-excitation properties, and are therefore classified as probable HERGs, while 40 do not and are therefore classified as probable LERGs (a further 22 sources do not have sufficient information to be classified). In this chapter the radio properties of these two groups of sources are compared.

A recent study by Best & Heckman (2012) showed that HERGs and LERGs have distinct accretion rates; HERGs typically accrete at between 1 and 10 percent of their Eddington rate, while LERGs generally have accretion rates much less than 1 percent of their Eddington rate. A picture is emerging where HERGs accrete cold gas at a relatively high rate and radiate efficiently across the whole electromagnetic spectrum. This causes them to produce a stable accretion disc and therefore display the typical properties of an AGN. The requirement for cold gas results in HERGs being more prevelant at earlier cosmic epochs, where higher rates of mergers and interactions provided a steady supply of cold gas. This cold gas leads to star formation, causing the host galaxies of HERGs to be relatively blue.

LERGs, however, slowly accrete warm gas from the X-ray emitting halo of the galaxy or cluster. They radiate inefficiently, emitting the bulk of their energy in kinetic form as powerful jets. They therefore tend to be hosted by massive galaxies, often at the centre of a group or cluster. These galaxies have an old, passive stellar population, and as massive galaxies show little cosmic evolution out to $z \sim 1$, a lack of cosmic evolution is also seen in LERGs.

The fundamentally different accretion modes of HERGs and LERGs cause them to have different properties; we have already seen that HERGs dominate at high luminosities ($L_{1.4\ \mathrm{GHz}} > 10^{26}$ WHz^{-1}), while LERGs dominate at lower luminosities. Mahony et al. (2011) studied the properties of high flux density ($S_{20\ \mathrm{GHz}} > 40$ mJy) HERGs and LERGs in the AT20G sample and found that while both accretion modes display a range of radio properties, a higher fraction of HERGs are extended and have steep spectra. They suggest that this is because HERGs are accreting more efficiently than LERGs, and therefore have a greater chance of producing more luminous jets and lobes. They also find that HERGs display different properties depending on their orientation, with objects displaying broad emission lines tending to be flat spectrum, and objects with narrow lines tending to be steep spectrum, as predicted by orientation models (Antonucci 1993; Urry & Padovani 1995, see Chapter 1). LERGs, however, display no orientation effects. This fits in with the picture where HERGs produce a typical AGN accretion disk and torus while LERGs do not. The 10C sample allows the properties of HERGs and LERGs in a lower flux density regime to be explored, which is discussed in detail in Section 7.1. In Section 7.2 the properties of the 10C sample are discussed in relation to several other studies of the radio sky. Finally, the conclusions of these studies are presented in Section 7.3.

7.1 Properties of HERGs and LERGs

In Chapter 6 the 10C sources were classified as HERGs and LERGs using several different methods, and the results were then combined to produce an overall classification. In this section I first compare the properties of sources classified as HERGs and LERGs in three different ways (optical compactness, X-ray observations and the IRAC colour–colour diagram, see Chapter 6 for details), before comparing the properties of the overall classifications (Section 7.1.2). In Section 7.1.3 the far-infrared – radio correlation is then compared for the two samples.

7.1.1 Properties of HERGs and LERGs split using three different methods

The distributions of four source properties (redshift, spectral index, 15.7-GHz flux density and 1.4-GHz luminosity) are shown in Figure 7.1, with the sample split using three different methods of identifying HERGs and LERGs (optical compactness, X-ray observations and the IRAC colour–colour diagram, see Chapter 6 for details). In all plots the sample shown in red represents sources which display evidence of high-excitation behaviour.

The top row shows objects split according to their optical compactness. The small number of point-like objects makes it hard to draw any meaningful conclusions from these plots for

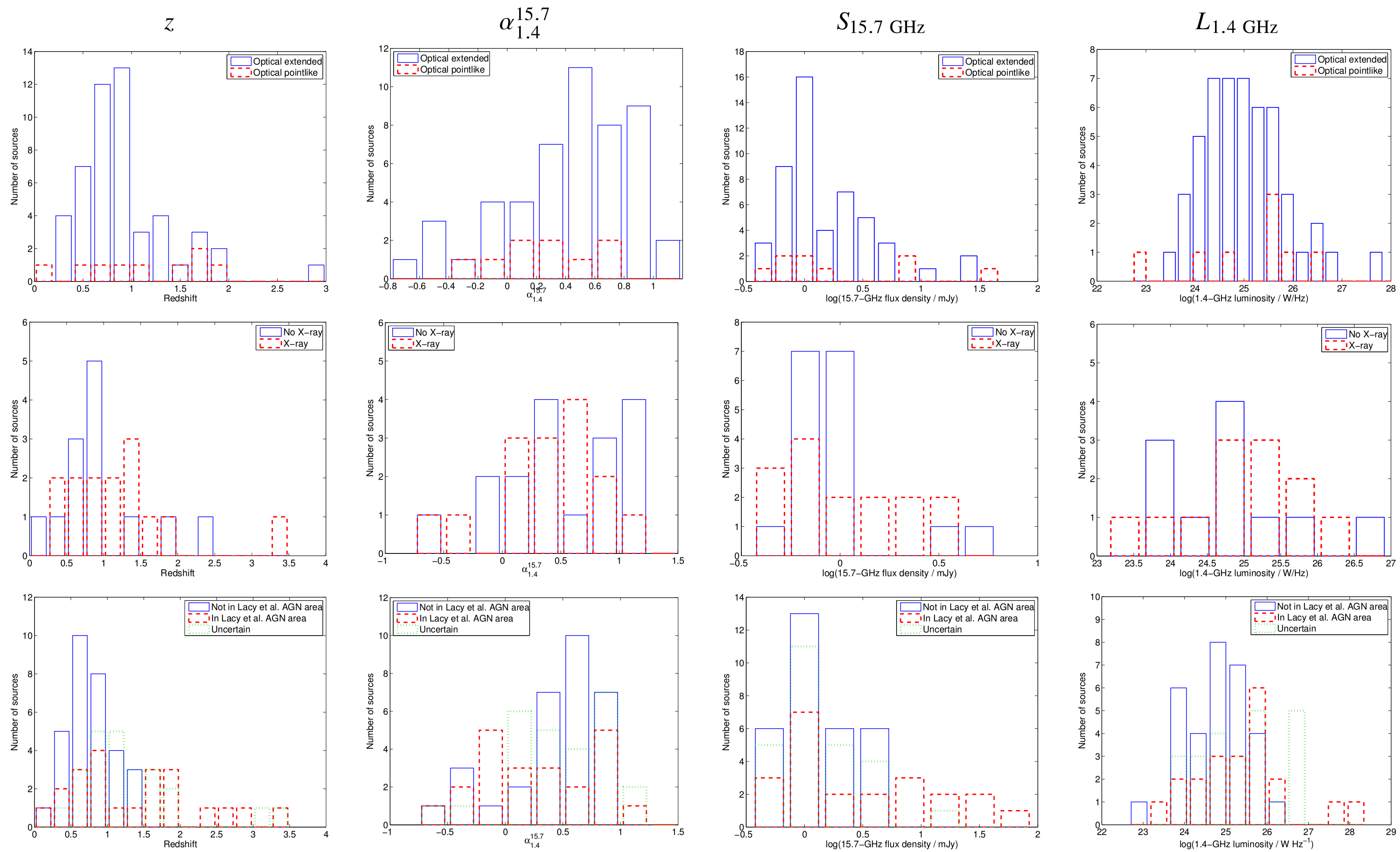

Figure 7.1: Distributions of source properties when the objects are classified using three different methods. Each column contains plots showing the same property; from left to right these are: redshift, $\alpha_{1.4}^{15.7}$, 15.7-GHz flux density and 1.4-GHz luminosity. Each row shows a different method for classifying the sources (as described in Section 6.2); these are optical compactness, X-ray emission and mid-infrared colour–colour diagram. In all plots the sample shown in red represents sources which display evidence of HERG activity.

these objects. The higher proportion of the high-redshift sources which are point-like (5/14, 36 percent, of sources with $z > 1$, compared to 4/46, 9 percent, of sources with $z < 1$) can be attributed to the fact that we expect the objects which appear point-like in the optical to be quasars, and as these sources are rare but very luminous they tend to be found preferentially at higher redshifts where larger volumes are being sampled. There seems to be no significant trend in spectral index with optical compactness, although of the 11 sources with steeply falling spectra ($\alpha_{1.4}^{15.7} > 0.8$) or the four with sharply rising ($\alpha < -0.4$) spectra, none are point-like. Both the point-like and the extended objects cover the same range of flux densities and luminosities.

The second row of Figure 7.1 shows those objects which were and were not detected in the X-ray observations (note that the two different X-ray surveys are combined here). It is clear that a larger proportion of the higher-redshift sources are detected in the X-ray observations, with 9/11 sources with $z > 1$ detected, compared to 6/16 sources with $z < 1$. There is no clear difference in the spectral indices of those sources which are detected in the X-ray and those which are not. The 15.7-GHz flux densities, however, tend to be higher for the X-ray detected sources, with 6/8 sources with $S_{15.7\ \mathrm{GHz}} > 1.2$ mJy detected, compared with 9/24 sources with $S_{15.7\ \mathrm{GHz}} < 1.2$ mJy. Having said this, some of the faintest sources are X-ray detected, with 3/4 sources in the faintest flux density bin with $S_{15.7\ \mathrm{GHz}} < 0.54$ mJy detected in the X-ray observations. There is no significant trend evident with 1.4-GHz luminosity. The small number of sources in the X-ray sample must be borne in mind when considering the significance of these results.

The third row of Figure 7.1 shows the properties of sources which lie inside and outside the Lacy et al. AGN area on an IRAC colour–colour diagram (see Section 6.2.2) along with those whose position on the diagram is uncertain due to the nature of their upper limits. Sources which are found inside the Lacy AGN area are classified as HERGs, while those outside are probably LERGs. There is a clear trend with redshift visible, with all sixteen sources with $z > 1.5$ either lying inside the Lacy AGN area or having uncertain positions on the diagram. There is also a trend with spectral index, with a larger proportion of the flat spectrum sources lying inside the Lacy AGN area (14/41, 34 percent, of flat spectrum sources lie inside the Lacy AGN area, compared to 8/38, 21 percent, of the steep spectrum sources). The 15.7-GHz flux densities of the samples are also significantly different, with the Lacy AGN tending to have higher flux densities (8/9 sources with $S_{15.7\ \mathrm{GHz}} > 5.7$ mJy are inside the Lacy AGN area and the one remaining source is classified as uncertain). This suggests that the composition of the population may be changing with flux density, with fewer HERGs found at fainter flux densities.

All three methods for identifying object types discussed here provide useful information about the population. The Lacy et al. colour–colour diagram appears to be the most effective method of splitting objects with different properties. Sources located inside the Lacy et al. AGN area tend to have flatter spectra, be found at higher redshifts, and have larger luminosities and flux densities. These results therefore support the findings by Best & Heckman (2012) that HERGs tend to be more luminous than LERGs. These results will be discussed in more detail after the properties of the overall classifications are presented.

7.1.2 Combining these classifications

In Chapter 6 the sources were split into three groups; 1) probable HERGs, sources which display one of the three indicators of high-excitation activity (i.e. are point-like in the optical, detected in the X-ray or lie inside the Lacy AGN area in the mid-infrared colour–colour diagram), 2) probable LERGs, sources which do not display any of these three indicators of high-excitation activity and 3) sources with insufficient information available to be classified. The properties of these three groups of sources are shown in Figure 7.2.

Panel (a) of Figure 7.2 shows the redshift distribution of the HERGs and LERGs; the HERG distribution has a high redshift tail, whilst there are no LERGs with $z > 2$. Panel (b) shows the spectral index distributions, which indicates that the HERGs tend to have flatter spectra than the LERGs. However, a KS test on these two distributions shows that there is an 8 percent chance that they are drawn from the sample population. The 15.7-GHz flux density distribution is shown in panel (c); the distributions peak at similar values but the HERG distribution extends to higher flux densities, while the LERG distribution does not (no LERGs have a flux density greater than 6 mJy). The 1.4-GHz luminosity distributions are shown in panel (d), and have similar shapes for HERGs and LERGs. The higher redshifts and 15.7-GHz flux densities of the HERGs combined with their flatter spectra produce a similar 1.4-GHz luminosity distribution to that of the LERGs. Both HERGs and LERGs are found on either side of the FRI/FRII dividing luminosity (shown by the vertical dashed line).

The linear size distribution of HERGs and LERGs is compared in Figure 7.3. Although both HERGs and LERGs cover the full range of linear sizes, the HERGs tend to be more compact.

In summary, HERGs tend to be at larger redshifts, and have larger flux densities, flatter spectra and smaller linear sizes. This is in contrast to the higher-flux-density HERGs in the AT20G sample studied by Mahony et al. (2011), which generally have steeper spectra and are more extended than the LERGs. It is not surprising that sources selected from these two samples do not have the same properties as they are drawn from very different flux density regimes. The fact that the 10C HERGs are flatter and more compact suggests that their cores are more dominant than those of the AT20G sources, suggesting that they have not pro-

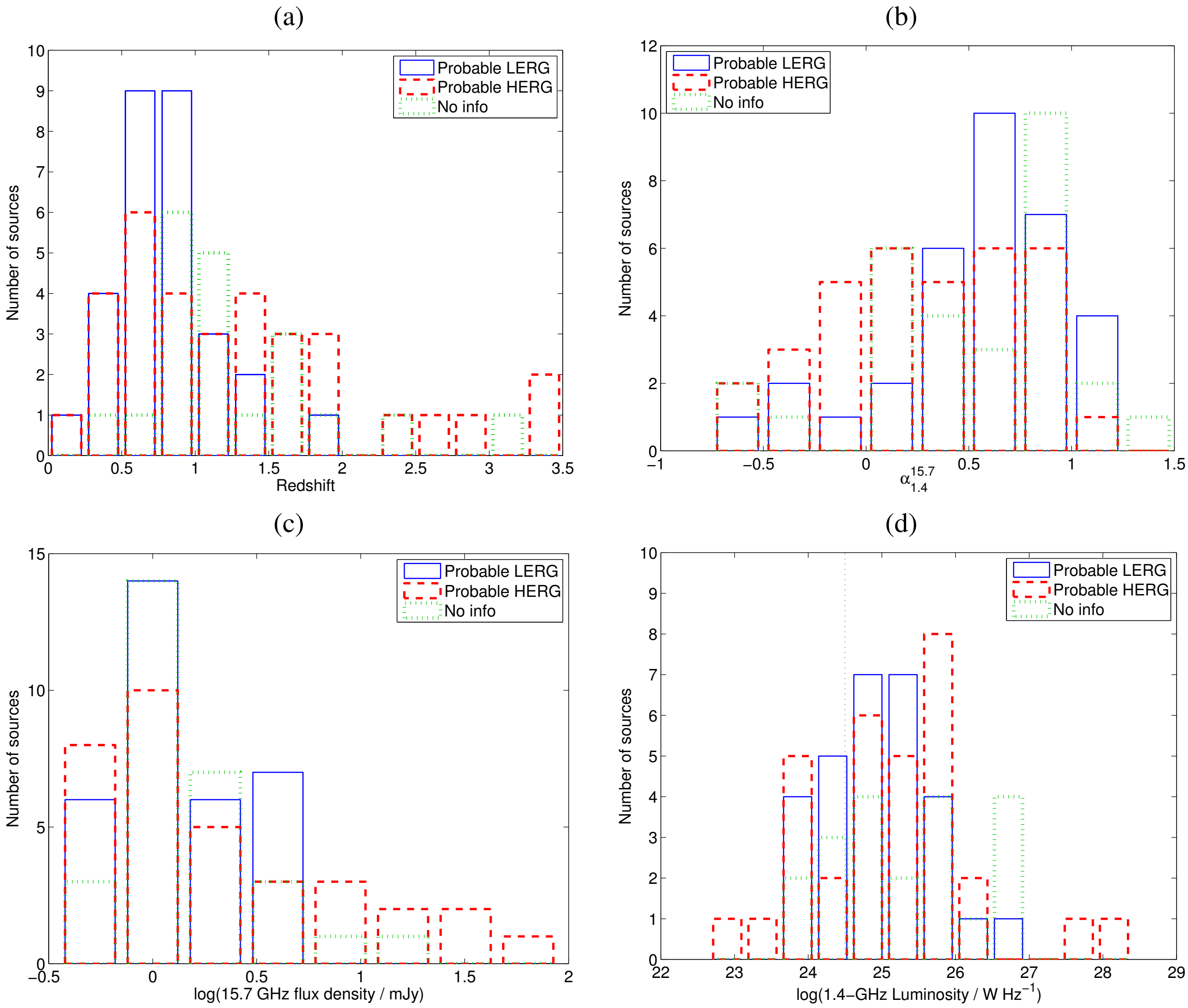

Figure 7.2: Radio properties sources classified as HERGs and LERGs, and those with insufficient information available to be classified.

duced such powerful jets. Best & Heckman (2012) found that although both HERGs and LERGs display the full range of luminosities, HERGs dominate at luminosities greater than $L_{1.4\ \mathrm{GHz}} \approx 10^{26}$ W Hz^{-1}, while LERGs dominate at lower luminosities. The majority of the 10C sample have luminosities smaller than this changeover point, so I may be sampling the low-luminosity tail of the HERG population. This therefore suggests that these HERGs may have lower luminosities because they have not produced the powerful extended emission typical of FRI and FRII sources, and are instead dominated by emission from their cores. The larger linear sizes of the LERGs could be because the inefficient accretion of LERGs tends to produce large jets as most of the energy is emitted in kinetic form, while HERGs accrete efficiently and radiate over the whole electromagnetic spectrum so do not produce such large

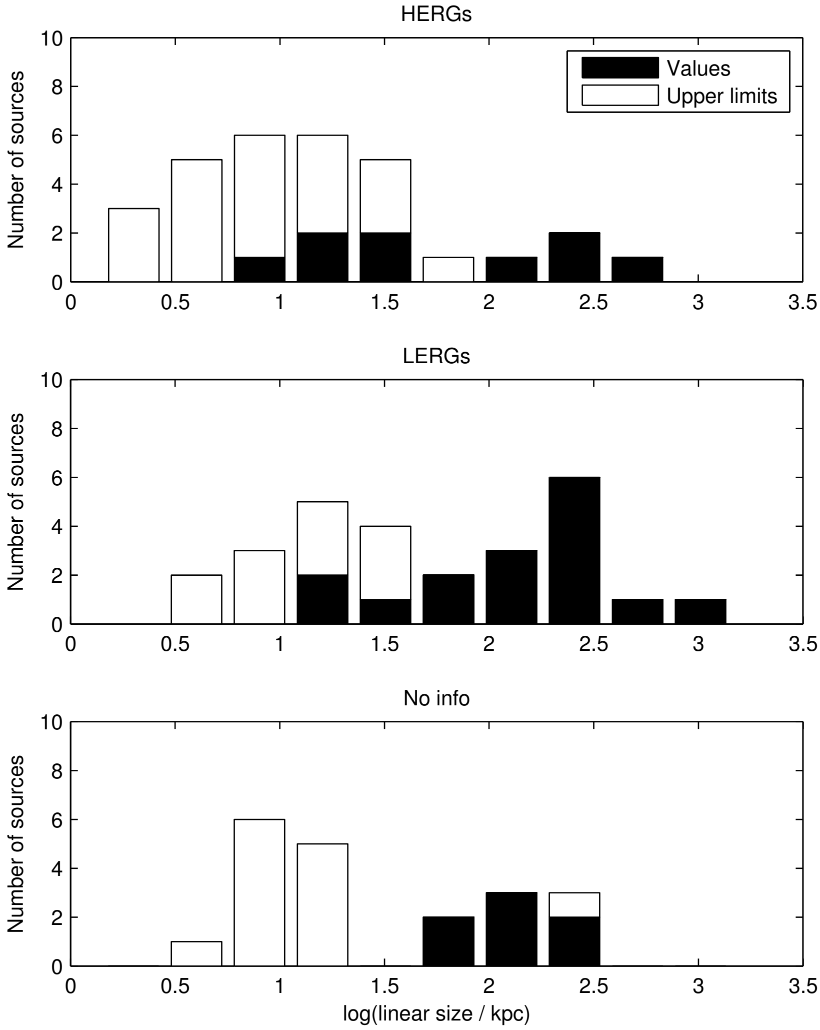

Figure 7.3: Linear size of sources classified as HERGs and LERGs, and those with insufficient information available.

jets.

7.1.3 Far-infrared – radio correlation of HERGs and LERGs

The far-infrared – radio correlation is a remarkably tight correlation over five orders of magnitude in luminosity (e.g. Price & Duric 1992). It is thought to be due to a direct relationship between star formation and cosmic-ray production in supernovae (Harwit & Pacini 1975; Rickard & Harvey 1984; de Jong et al. 1985; Helou et al. 1985; Wunderlich & Klein 1988). While starforming sources and radio-quiet AGN tend to follow the correlation tightly (Roy et al. 1998), radio galaxies do not, as they have radio flux densities significantly larger than predicted by the correlation. To investigate this in more detail, the infrared – radio ratio, q_{IR}, is

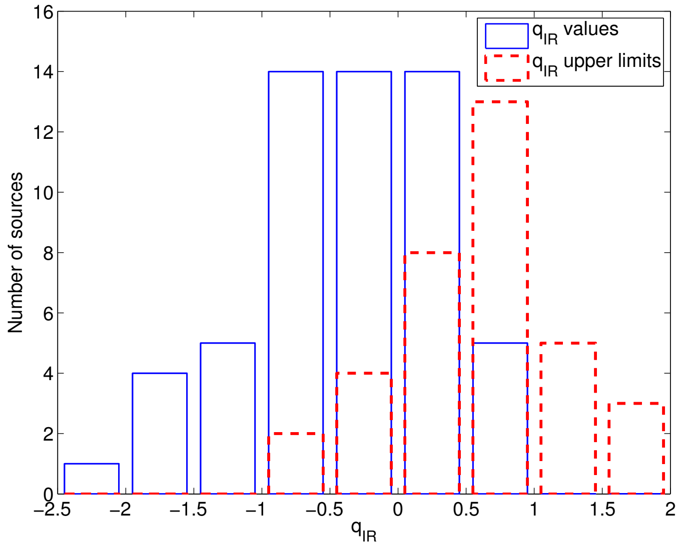

Figure 7.4: Distribution of $q_{\rm IR}$ values for sources in Sample W. Upper limits for sources without a 22µm flux density value from WISE are shown separately (note that the upper limits mean that these sources could move to the left).

often used where

$$q_{\rm IR} = \log_{10}\left(\frac{S_{22\ \mu\rm m}}{S_{1.4\ \rm GHz}}\right) \tag{7.1}$$

Starforming sources and radio-quiet AGN are expected to have positive $q_{\rm IR}$ values, for example, Marleau et al. (2007) found that the typical value of $q_{\rm IR}$ for starforming galaxies was 0.83 ± 0.31. Radio-loud objects tend to have much lower values of $q_{\rm IR}$, with typical values -0.6 to -1.2 (Prandoni 2010b).

The far-infrared to radio ratio, $q_{\rm IR}$, is calculated for each source in Sample W using the 22-µm flux density from WISE (see Section 5.1.2) and the best available 1.4-GHz flux density value (as used to calculate the spectral indices in Section 2.2.3). No k-corrections are applied, as the uncertainties in the redshift values would introduce further errors, as would incorrect assumptions about far-infrared SED-type. The k-corrections are expected to increase $q_{\rm IR}$ by a small amount assuming the spectra is power-law. Fifty-seven sources in Sample W are detected by the WISE survey, and the WISE 95 percent completeness limit of 18 mJy is used as an upper limit on the 22-µm flux density for 35 undetected sources (the remaining four sources are classified as confused when matching to WISE, so no limit could be placed on the flux density of these sources). The distribution of $q_{\rm IR}$ values obtained is shown in Figure 7.4. The majority of the upper limits are larger than the values for those sources detected at 22 µm so they do not provide any significantly useful information about the population.

As expected, the majority of the sources in Sample W which are detected in WISE have $q_{\rm IR}$ values lower than expected for starforming sources or radio-quiet AGN; there are no sources

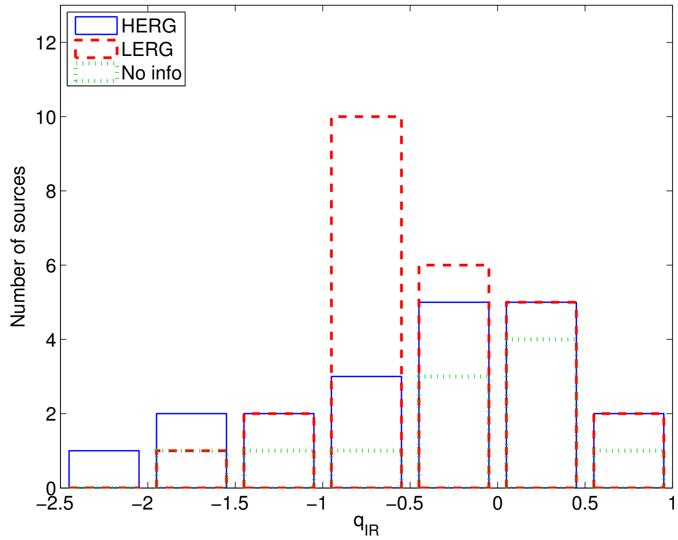

Figure 7.5: Distribution of $q_{\rm IR}$ values for sources in Sample W. HERGs, LERGs and unclassified sources are shown separately. Only sources with a WISE detection are included, upper limits are not plotted..

in this sample with $q_{\rm IR} > 1$, and only five sources with $q_{\rm IR} > 0.5$. This is consistent with the conclusion from Chapter 5 that the majority of the sources in Sample W are radio-loud AGN. It is, however, possible that some of the 21 sources with upper limits on $q_{\rm IR}$ which are greater than 0.5 have values of $q_{\rm IR}$ consistent with starforming sources or radio-quiet AGN.

The $q_{\rm IR}$ distribution for HERGs and LERGs is shown in Figure 7.5. Although both HERGs and LERGs cover the full range in $q_{\rm IR}$, a greater proportion of the LERGs have values of $q_{\rm IR} > -1$. This means that for a given infrared luminosity, HERGs have larger radio luminosities than LERGs.

7.2 Comparing the properties of the 10C sample with other studies

The optical properties of high-frequency sources selected from the Australia Telescope 20-GHz (AT20G) survey were investigated by Mahony et al. (2011). These sources have considerably higher flux densities than the 10C sources studied in this thesis, with AT20G sources typically having $S_{20\,\rm GHz} > 40$ mJy, so the two samples are not directly comparable. However, the AT20G sample provides useful information about the nature of the high-frequency radio population in a different flux density regime.

Mahony et al. investigated the optical compactness of the AT20G sample and found that the dominant population are 'stellar' sources (which are point-like in the optical) and that the

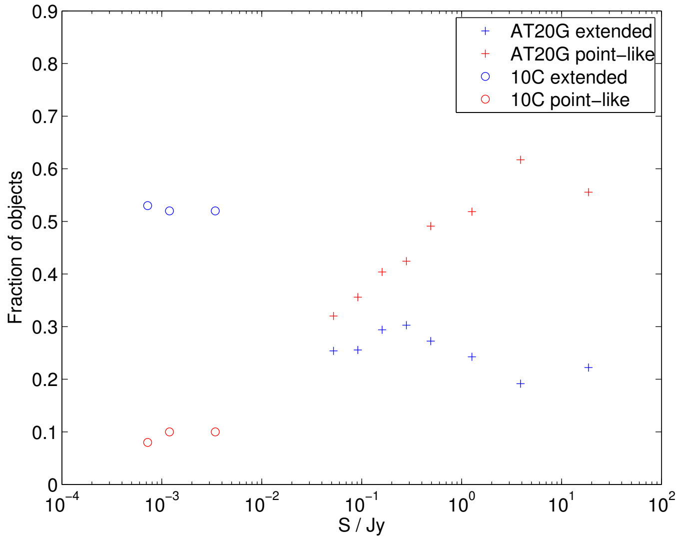

Figure 7.6: Fraction of objects classified as extended and point-like in the optical as a function of flux density in the AT20G and 10C surveys (20-GHz flux density for AT20G sources and 15.7-GHz flux density for 10C sources).

proportion of these sources decreases with 20-GHz flux density. They predict that at lower flux densities the 'galaxy population' would dominate the sample; this is backed up by my fainter observations – only nine percent of the sources with $0.5 < S_{15.7\ \mathrm{GHz}}/\ \mathrm{mJy} < 45$ are point-like in the optical. This is demonstrated by Fig 7.6, which shows the fraction of objects classified as extended and point-like as a function of flux density in the AT20G catalogue and this work. This diagram shows that the population changes steadily from being dominated by point-like objects at high flux densities to being dominated by extended objects at lower flux densities.

Mignano et al. (2008) investigated the properties of a complete sample of 131 radio sources with $S > 0.4$ mJy observed at 1.4 and 5 GHz as part of the Australia Telescope ESO Slice Project (ATESP) 5 GHz radio survey (Prandoni et al. 2006). This sample provides a useful comparison as it has a comparable flux density limit to the 10C survey, albeit at a lower frequency. The ESO Deep Public Survey provides deep multi-colour (*UBVRIJK*) images which cover most of this field, and optical/near infrared counterparts are found for 66 out of the 85 (78 percent) sources in the area covered. Estimates of redshift and source type are obtained for 56 of these 66 sources. These results showed that 78 percent of the ATESP 5 GHz sample had an active nucleus (i.e. they are either quasars or radio galaxies associated with early-type objects), significantly lower that the proportion of radio galaxies found in the 10C sample (97 percent). This is confirmed by looking at the radio-to-optical light ratios of the two samples; approximately 30 percent of the ATESP sources have $R < 1000$ (classifying them as radio quiet), compared to just 3 percent of the 10C sources. This suggests selection at a higher frequency preferentially selects radio galaxies, as the steep-spectrum starforming galaxies drop out of the sample.

Mignano et al. find that those sources in the ATESP sample which have flat or inverted radio spectra and are associated with early-type spectra objects are preferentially compact (with linear sizes < 10 to 30 kpc). They suggest that these sources may be FRIs, due to their low radio powers ($P_{1.4\ \mathrm{GHz}} \sim 10^{22-24}\ \mathrm{W\,Hz^{-1}}$) and the absence of emission lines in their optical spectra. They do, however, note that they would expect FRI sources to have larger linear sizes and steeper spectra. As these sources have flat spectra, we would expect them to also be present in significant numbers in the 15-GHz-selected 10C sample; these could be the flat, core-dominated radio-loud sources which we observe in the 10C sample but which are not predicted by, for example, the S^3 simulation.

Prandoni et al. (2010a) followed up a sample of early-type galaxies selected from the ATESP 5 GHz survey at 4.8, 8.6 and 19 GHz to further investigate their properties. The main aim was to establish whether the AGN population of the sub-mJy sample is more closely related to efficiently accreting systems (such as radio-quiet quasars), or to systems with low accretion rates (such as FRI galaxies), or to low radiative efficiency accretion flows. They compare this AGN population to the much brighter (> 500 mJy) 20 GHz AT20G Bright Source Sample (Massardi et al. 2008) and find strong similarities in the spectra of the two samples. They therefore conclude that the ATESP AGN sources are lower luminosity counterparts of the AT20G FRII radio galaxies, and do not find any compelling evidence for a radio-quiet AGN population. This is consistent with the properties of the 10C sources, as essentially all the sources are radio loud, and there seems to be a population of low-luminosity HERGs present.

Padovani et al. (2009) studied a sample of 256 sources with flux densities $S_{1.4} > 42$ μJy observed at 1.4 and 5 GHz with the VLA using optical and X-ray ancillary data (Mainieri et al. 2008; Tozzi et al. 2009). This survey therefore probes lower flux densities than either the ATESP or the 10C surveys. They find that their sample consists of ~ 60 percent starforming sources, with the remaining 40 percent being AGN (split approximately equally into radio-loud and radio-quiet sources) strikingly different from the composition of the 10C sample (and the other higher flux density samples discussed). This difference stands out when looking at values of the radio-to-optical ratio R; Padovani et al. find that 37 percent of their sample have $R < 1000$[a], while only three percent of the 10C sources have R values in this range.

[a]Using the Padovani et al. definition of radio-to-optical ratio $R_{\mathrm{p}} = 1.4$ is approximately $R = 1000$

7.3 Conclusions

In this chapter the nature of the two distinct types of radio galaxies in the 10C sample (HERGs and LERGs) were explored. The properties of the 10C sample were then compared to other studies.

The HERGs in the 10C sample tend to have larger redshifts, flatter spectra, higher flux densities and smaller linear sizes than LERGs. The majority of the HERGs also have lower luminosities than are typical for these sources. This is in contrast to the HERGs in the higher-flux-density AT20G sample, which have steeper spectra and are more extended than the LERGs. This suggests that the HERGs in the 10C sample lack the powerful extended emission typical of FRI and FRII sources, and instead are dominated by their cores.

This work supports the findings of Mahony et al. (2011) that the proportions of sources associated with point-like objects decreases with flux density, from over 60 percent of sources with $S_{20\ \mathrm{GHz}} > 2$ Jy in the AT20G sample to just 8 percent of sources with $0.5 < S_{15.7\ \mathrm{GHz}}/\mathrm{mJy} < 1$ in the 10C sample.

The proportion of radio-loud sources in the 10C 15.7-GHz selected sample (∼ 97 percent) is significantly higher than the proportion in the ATESP 5-GHz selected sample (∼ 60 percent), which has a comparable flux density range. High frequency surveys are therefore a very effective method of selecting sub-mJy radio-loud AGN.

CHAPTER 8

Deep 15.7-GHz observations of the Lockman Hole and AMI001 fields

The 10C survey is the deepest high-frequency survey to date, and provides a reliable measure of the 15.7-GHz source count down to flux densities of 0.5 mJy. Significantly deeper surveys have been carried out lower frequencies, such as 1.4 GHz, and as a result source counts at 1.4 GHz are constrained to $\sim$ 1μJy. Earlier in this thesis I have demonstrated some of the potential pitfalls of extrapolating from lower frequencies to predict the properties of the higher-frequency population, and discussed why this population is interesting. In this chapter I use new observations made with AMI in both the Lockman Hole and AMI001 fields to estimate the 15.7-GHz source counts down to 0.1 mJy, a factor of five deeper than the 10C count.

8.1 Observations and data reduction

The observations were made with the AMI LA at 15.7 GHz between August 2008 and May 2014. The AMI LA has a primary beam of $\approx$ 5.5 arcmin and a resolution of $\approx$ 30 arcsec. The observations have been made in two fields; 1) the Lockman Hole field, which has been the subject of the rest of this thesis, and 2) the AMI001 field, which is centred on $0^{\rm h}25^{\rm m}, +32^{\circ}$ and covers 3.56 deg^2 (1.69 deg^2 in the deep region). Both fields were initially observed as part of the 10C survey with an integration time of $\approx$ 450 and $\approx$ 1000 hours respectively, and consisted of an outer region complete to 1 mJy, and an inner deeper region complete to 0.5 mJy. Since then $\approx$ 250 hours of additional observations have been made in the Lockman Hole and $\approx$ 400 additional hours in the AMI001 field. This means that these fields contain the deepest

15.7 GHz observations to date. A rastering technique was used to observe the fields with a separation of 4 arcmin between pointings, in the same way as for the 10C survey (full details can be found in Franzen et al. 2011).

In the Lockman Hole field, the new observations were carried out in a hexagon consisting of 37 pointings and centred on $0^{h}52^{m}22^{s}, +57°24'55.0''$. The rms noise in this hexagon is ~ 25 μJy, as shown by the noise map in Figure 8.1. In the AMI001 field the new observations have been made in several hexagons (again, each consisting of 37 pointings), and the rms noise in the centre of the two deepest hexagons (centred on $00^{h}22^{m}19^{s}, +31°46'09.7''$ and $00^{h}24^{m}00^{s}, +31°59'29.5''$) is ~ 16 μJy. The noise map for the AMI001 field is shown in Figure 8.2. These noise maps are produced by averaging by taking the rms noise in each pointing, then applying the primary beam correction and combining the pointings, and is referred to as the 'theoretical noise map'.

The data reduction was performed using the same pipeline as for the 10C survey by members of the AMI consortium. Full details of the data reduction procedure can be found in Franzen et al. (2011). The resulting maps of the two fields are shown in Figures 8.3 and 8.4.

8.2 The source catalogue

8.2.1 Source fitting

The source fitting was performed using the in-house software SOURCE_FIND in the same way as for the 10C survey in order to make the new catalogue as comparable as possible to the 10C catalogue. The procedure implemented in SOURCE_FIND is described briefly here, full details being given in Franzen et al. (2011). The noise maps shown in Figures 8.1 and 8.2 were used to identify component 'peaks' above a given signal-to-noise ratio γ (in this case $\gamma = 4.62$[a]). Initially, all pixels greater than $0.6\gamma\sigma$ (where σ is the local noise) are identified to ensure all peaks greater than $\gamma\sigma$ after interpolation are found. The position and value of each peak ($\mathrm{RA_{pk}}$, $\mathrm{Dec_{pk}}$ and S_{pk}) is then found by interpolation between the pixels, and any peaks less than $\gamma\sigma$ are discarded. The error on the peak flux density (δS_{pk}) is taken to be the thermal noise error combined in quadrature with the five percent calibration error, $\delta S_{\mathrm{pk}} = \sqrt{\sigma_n^2 + (0.05 S_{\mathrm{pk}})^2}$. The integration area, consisting of contiguous pixels down to a lowest contour value of 2.5σ, was then calculated for each component. If more than one peak lay inside the same integration area the sources were classified as a 'group'.

The AIPS task JMFIT was then used to fit a 2D Gaussian to each component. This was used to estimate the integrated flux density, position and angular size (S_{in}, $\mathrm{RA_{in}}$, $\mathrm{Dec_{in}}$ and e_{maj}) for

[a]This value is used, instead of 5σ, to take account of the 1.082 phase error correction factor applied to the flux densities (see Section 8.2.3 for details).

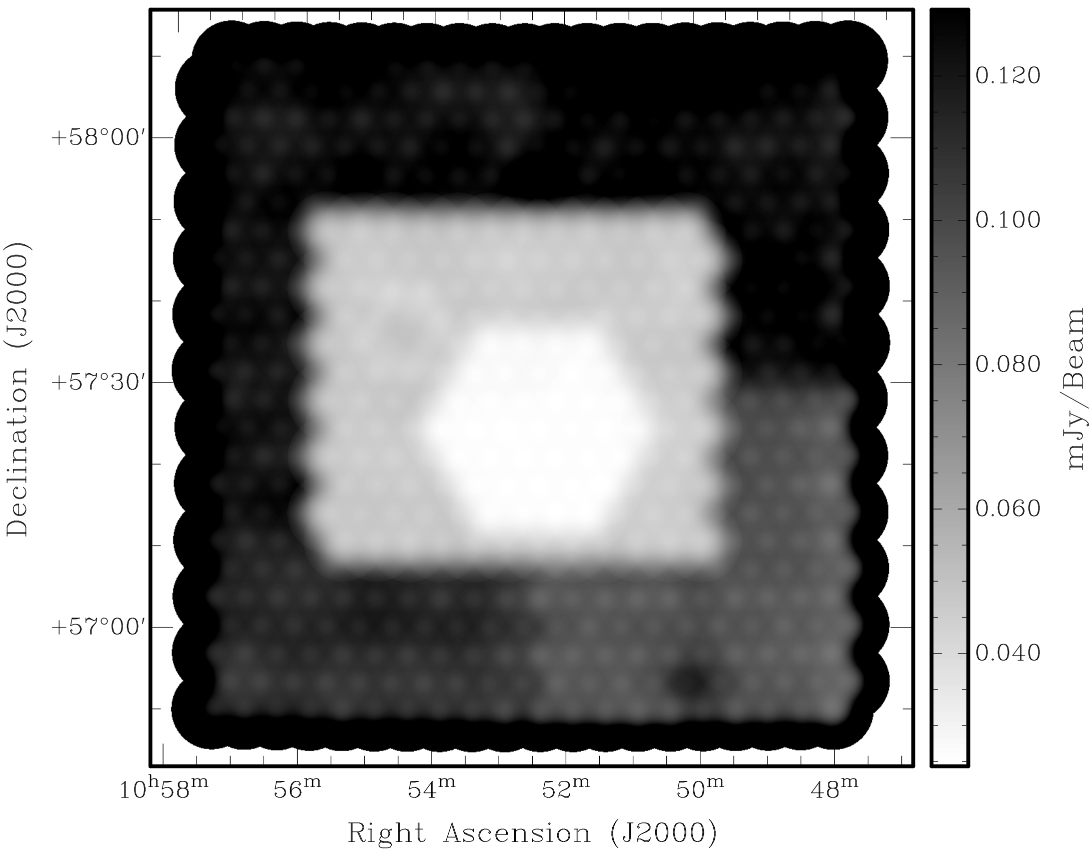

Figure 8.1: The theoretical rms noise in the 15.7-GHz AMI map of the Lockman Hole field.

each component. The error on the integrated flux density ($\delta S_{\rm in}$) was estimated as the error due to thermal noise (estimated by JMFIT) combined in quadrature with the five percent calibration error, $\delta S_{\rm in} = \sqrt{\sigma_{\rm n}^2 + (0.05 S_{\rm in})^2}$.

8.2.2 Exclusion zones

The maps display an increase in noise close to bright (> 15 mJy) sources due to amplitude, phase and deconvolution errors. Because this noise is non-gaussian it is often not included in the noise maps, leading to spurious detections close to bright sources. For this reason, an 'exclusion zone' was defined around any source with a peak flux density greater than 15 mJy during the source fitting process (in the same way as described in Davies et al. 2011), and any source detected within this zone was excluded from the catalogue. Each exclusion zone is a circle centred on the bright source, with a radius defined by:

$$r_e = 12 \left(\frac{S_{\rm pk}}{250\ \rm mJy} \right)^{1/2} \text{arcmin}, \tag{8.1}$$

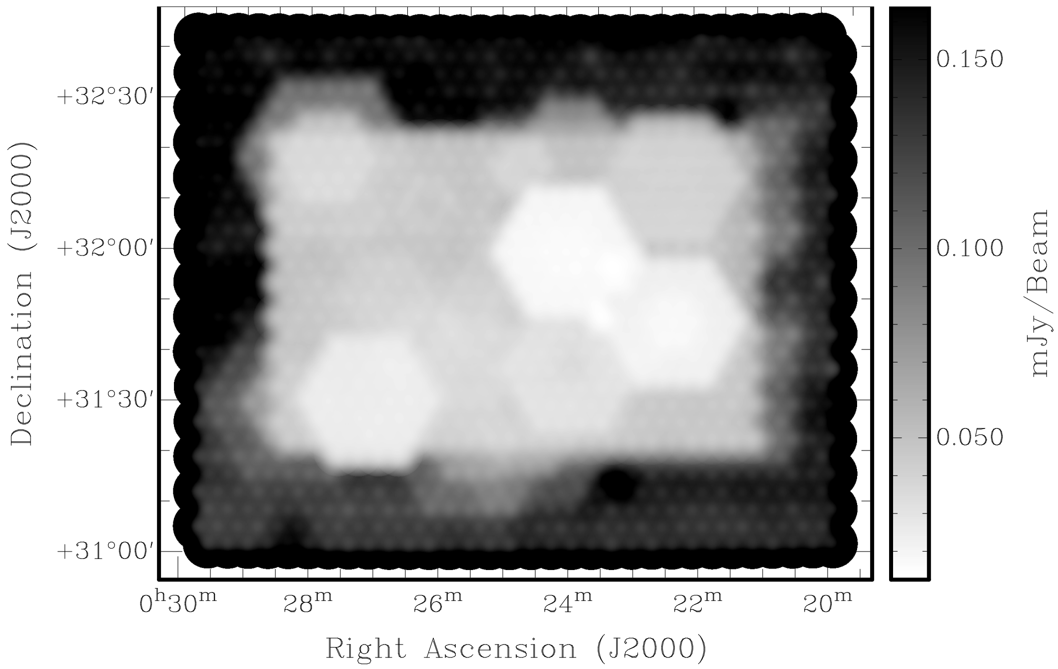

Figure 8.2: The theoretical rms noise in the 15.7-GHz AMI map of the AMI001 field.

where $S_{\rm pk}$ is the peak flux density of the bright source. The positions and radii of these exclusion zones are shown in Table 8.1.

Table 8.1: The positions of the centres of the exclusion zones around bright sources and their radii.

RA	Dec	Radius / arcmin
00:29:33.7	+32:44:52	4.19
00:23:09.8	+31:14:00	3.80
00:21:29.8	+32:26:58	3.41
00:20:50.4	+31:52:28	3.30
00:28:10.5	+31:03:46	3.20
00:29:20.4	+32:16:54	3.06
10:50:07.1	+56:53:37	3.35
10:52:25.1	+57:55:07	3.24
10:54:26.9	+57:36:48	3.69

8.2.3 Final flux density values

The deep AMI images do not have a high enough signal-to-noise to be self-calibrated, so a correction factor was applied to all flux density values to account for the phase errors before inclusion into the final catalogue. The correction factor used here was the same as used for the

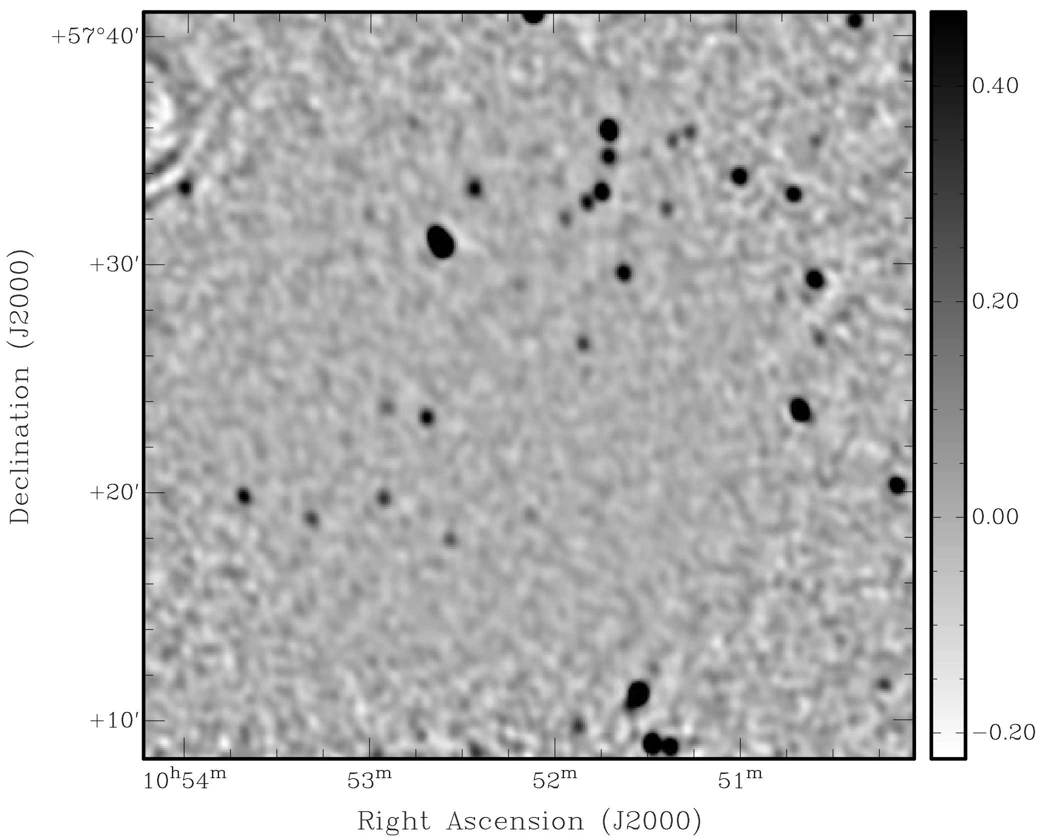

Figure 8.3: The Lockman Hole field image, showing the new deep area only.

10C survey, which was estimated by comparing the flux densities in the 10C raster maps to the flux densities in self-calibrated pointed maps which were used to check the flux density scale. All flux densities were therefore multiplied by 1.082. This correction factor is the reason for carrying out the source-fitting down to 4.62σ – a source near the survey limit which should be detected at 5σ will only be detected at $5\sigma/1.082 = 4.62\sigma$. In total, 358 sources were detected in the AMI001 field and 134 in the Lockman Hole field (including the shallow areas as well as the new deep areas).

A source was considered to be extended if the major axis of the deconvolved Gaussian ($e_{\rm maj}$) is larger than a critical value $e_{\rm crit}$, where

$$e_{\rm crit} = \begin{cases} 3.0 b_{\rm maj}\rho^{-1/2} & \text{if } 3.0 b_{\rm maj}\rho^{-1/2} > 25.0 \text{ arcsec}, \\ 25.0 \text{ arcsec} & \text{otherwise}, \end{cases} \tag{8.2}$$

where $b_{\rm maj}$ is the major axis of the restoring beam and $\rho = S_{\rm pk}/\sigma_n$ (i.e. the signal-to-noise ratio). Sources with $e_{\rm maj} > e_{\rm crit}$ were classified as extended (flag E), otherwise the source was considered point-like (flag P). In total, there are 24 sources classified as extended in the AMI001 field and six in the Lockman Hole field.

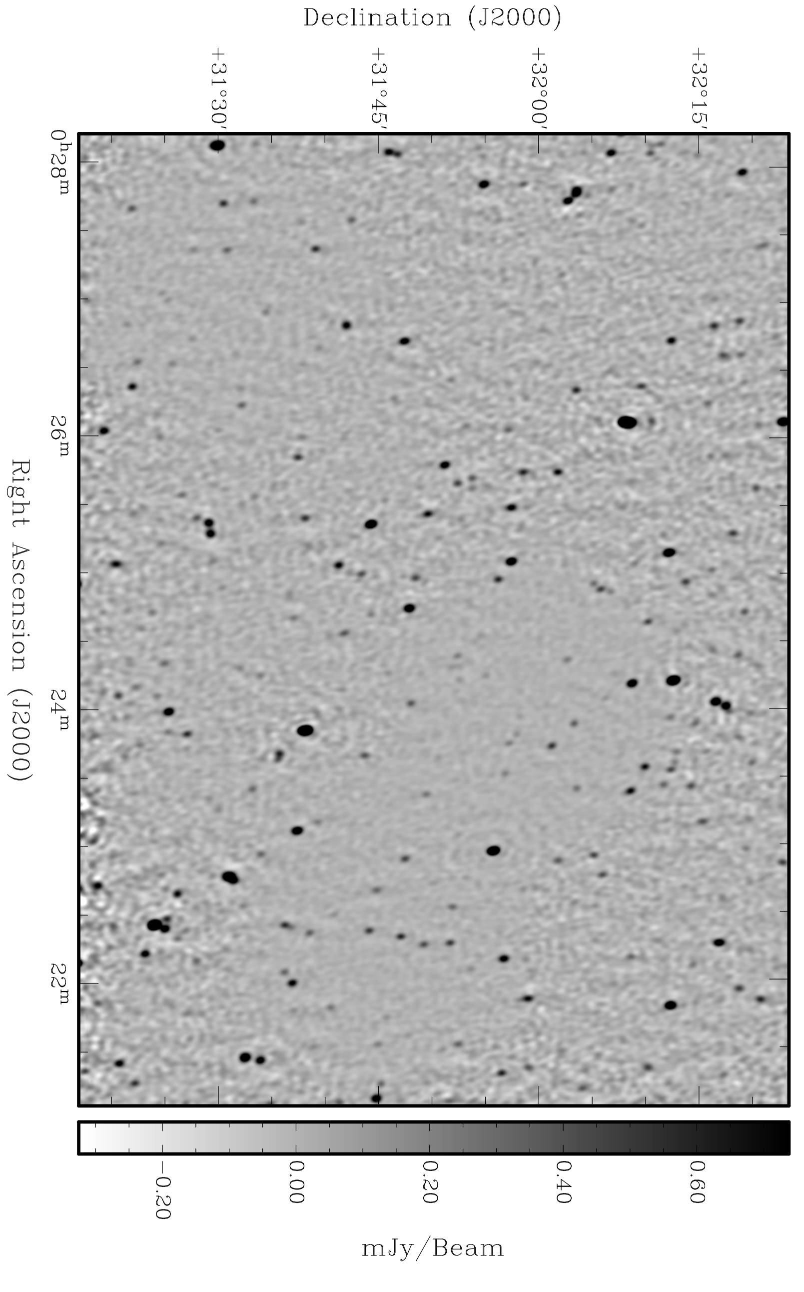

Figure 8.4: The AMI001 field image, showing the deep areas only.

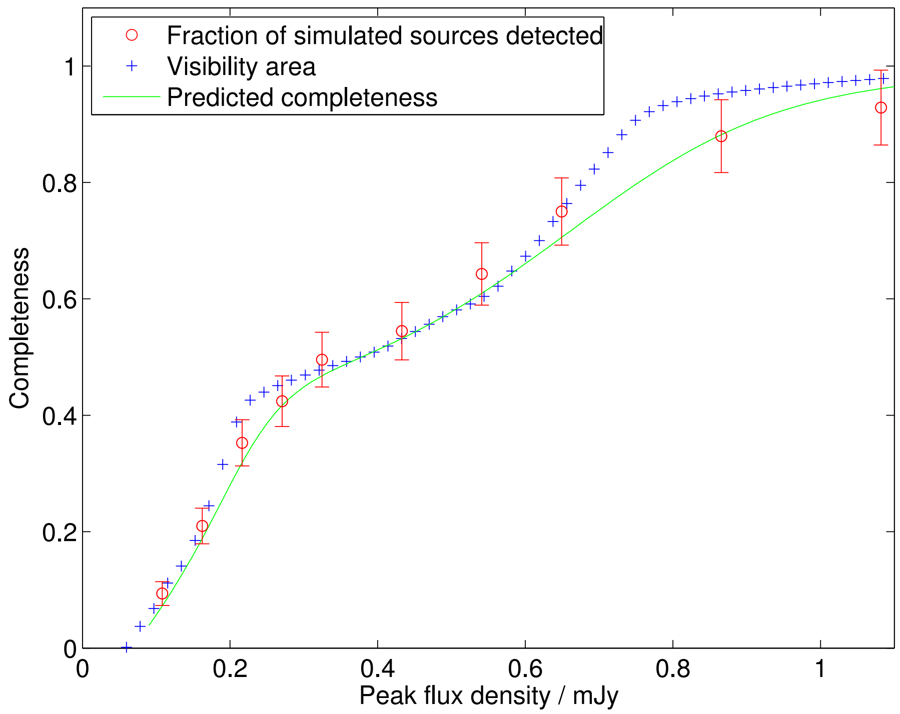

Figure 8.5: Different methods used to estimate completeness in the AMI001 field. The fractions of simulated sources detected at a given flux density are shown by red circles (error bars represent Poisson errors). The completeness curve estimated from the noise map using equation 8.6 is shown by the green line. The blue crosses show the visibility area used to calculate the source counts in Section 3.1.5.

For sources classified as extended, the integrated flux density is used, and for those classified as point-like the peak flux density is used. These values are listed as the 'best flux' in the catalogue, and are the values used for the source count in Section 3.1.5.

8.2.4 Completeness

The completeness of the survey was estimated by inserting 250 sources of equal flux density into the AMI001 map in random positions. The simulated sources were ideal point sources with flux density S and were added to the map in the image plane using the AIPS task IMMOD; no sources were placed in the border 50 pixels wide at the edge of the map, as many of these pixels are blank. Sources which lay within 2 arcmin of another simulated source were removed to avoid the simulated sources interacting, leaving 224 simulated sources. The source fitting was then performed in exactly the same way as described in Section 8.2.1. A simulated source was considered to be detected if there was a source in the output catalogue within 30 arcsec of the simulated source position. This was repeated several times using a range of flux densities $0.1 < S/\mathrm{mJy} < 1$ (keeping the same positions each time) to estimate the completeness as a function of flux density. The fraction of simulated sources detected as a function of flux density is shown in Figure 8.5. The flux densities of the simulated sources are multiplied by 1.082 (the correction factor applied to the final catalogue to account for phase errors, see section 8.2.3) before inclusion on this plot.

The completeness can also be estimated from the noise map assuming a Gaussian noise distribution. The probability of detecting a source of peak flux density S above 5σ is given by

$$P(S) = \int_{5\sigma}^{\infty} \frac{1}{\sqrt{2\pi\sigma^2}} \exp\left(-\frac{(X-S)^2}{2\sigma^2}\right) \mathrm{d}X. \tag{8.3}$$

In reality the noise varies across the map; this can be taken into account by averaging the probabilities of detecting a source at each pixel position in the noise map. The probability of detecting a source in a particular region of the noise map containing N pixels is

$$C(S) = \frac{1}{N}\sum_{i=1}^{N} P_i(S) \tag{8.4}$$

where

$$P_i(S) = \int_{5\sigma_i}^{\infty} \frac{1}{\sqrt{2\pi\sigma_i^2}} \exp\left(-\frac{(X-S)^2}{2\sigma_i^2}\right) \mathrm{d}X \tag{8.5}$$

where σ_i the value of the noise map at the i^{th} pixel. As the source fitting was in fact carried out to 4.62σ and the flux densities were multiplied by 1.082 after source extraction, this equation becomes

$$P_i(S) = \int_{4.62\sigma_i}^{\infty} \frac{1}{\sqrt{2\pi\sigma_i^2}} \exp\left(-\frac{(X-\frac{S}{1.082})^2}{2\sigma_i^2}\right) \mathrm{d}X. \tag{8.6}$$

The outer 50 pixels of the noise map are excluded from this calculation so that the results are directly comparable to the completeness estimated using simulated sources.

The results of both methods used to estimate completeness are shown in Figure 8.5. A similar analysis was performed by Davies et al. (2011) to estimate the completeness of the 10C survey. Davies et al. found that at low flux densities the fraction of detected sources from the simulation was slightly higher than predicted by the completeness curve, while at higher flux densities the fraction of detected sources was slightly lower than predicted. The same effect is visible here, with the fraction of detected sources slightly higher than predicted for $S < 0.8$ mJy and lower than predicted for $S > 0.8$ mJy. Davies et al. suggest several factors which may contribute to this effect. One is source confusion, which will increase the completeness as low flux densities, as two sources below the completeness limit may lie sufficiently close together to be detected as one source; in contrast, at higher flux densities confusion will reduce the completeness as a source may not be detected if it lies too close to a brighter source. Confusion therefore prevents the completeness from reaching 100 percent as quickly as predicted.

The 'visibility area' is also plotted in Figure 8.5. This is the fraction of the total area over which a source of flux density S_i should be detectable, i.e. the fraction of the area with $5\sigma_{\rm local} < S_i$. This is used to calculate the source count and is discussed in more detail in Section 8.4.

8.2.5 Reliability

Assuming that the noise in the map is Gaussian, the expected number of false positives simple due to the noise can be calculated. The total area of the two fields containing the deeper observations is 5.3 deg^2 and the beam area is $\approx$ 700 arcsec^2, so the number of beams covering the two fields is $\approx 100,000$. The probability that a value drawn from a Gaussian distribution is more than 4.62 standard deviations away from the mean is $\approx 1.9 \times 10^{-6}$, so the expected number of false positives is ≈ 0.2. I therefore do not expect reliability to be an issue for this survey.

8.2.6 Multiple sources

There are 38 sources in the AMI001 field which are classified as being part of a 'group', indicating that their fitted Gaussians overlap. Twelve of these sources form four triples, the remaining 26 sources form 13 pairs, meaning that there are 17 groups in total. The separation between the sources in these 17 groups ranges from 27 to 126 arcsec, with an average separation of 49 arcsec. The source counts can be used to estimate the number of sources that would be expected to be overlapping due to confusion alone. Integrating the 10C source counts (given in equation 3.1) between $0.1 < S/\mathrm{mJy} < 25$ (which involves extrapolation from 0.5 – 0.1 mJy), there are expected to be $\approx 7.2 \times 10^5$ sources per steradian in this flux density range. There are a total of 358 sources in the AMI001 field, so the total area within 49 arcsec of another source is $\approx 6.4 \times 10^{-5}$ steradians. Therefore ≈ 46 sources are expected to lie within 49 arcsec of another source and therefore be classified as overlapping. This is higher than the number of overlapping sources observed, which is probably due to the fact that sources as faint as 0.1 mJy (the lower limit on flux density used in this calculation) can only be detected in part of the image. This number can therefore be viewed as an upper limit on the expected number of overlapping sources. Repeating this calculation with a detection limit of 0.5 mJy shows that we would expect $\approx$ 10 sources to be overlapping, we therefore expect there to be between 10 and 46 overlapping sources in the field due to confusion alone. This estimation assumes no source clustering, which would increase the number of overlapping sources.

This analysis suggests that many of the overlapping sources detected in these observations are due to confusion, rather than genuine multiple sources. Therefore, no attempt is made to

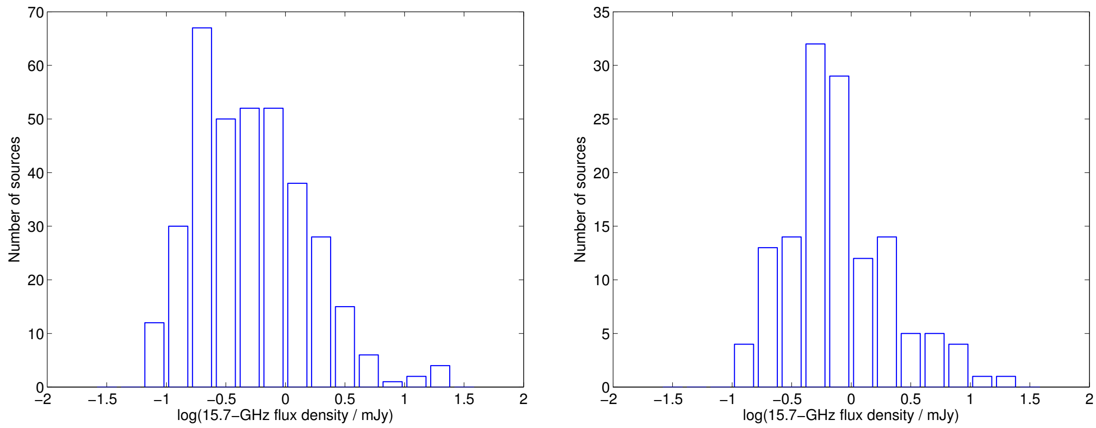

Figure 8.6: Flux densities of sources in the AMI001 field catalogue (left) and the Lockman Hole field catalogue (right).

combine the flux densities of the overlapping sources into a single source; they are listed as separate entries in the source catalogue, but flagged as being part of a group.

8.2.7 The final catalogue

The final source catalogue therefore contains 358 sources in the AMI001 field with flux densities $0.088 < S/\mathrm{mJy} < 34$ and 134 sources in the Lockman Hole field with flux densities $0.15 < S/\mathrm{mJy} < 22$. The flux densities of the sources in these two catalogues are shown in Figure 8.6. Twenty-four of these sources in the AMI001 field and six in the Lockman Hole field are classified as extended. Several tests are performed on the data in the next section, after which the catalogue is used to calculate source counts.

8.3 Checking the catalogue

8.3.1 Comparing to the original 10C catalogue

The source catalogue produced in the AMI001 field was compared to the original 10C catalogue. There are 358 sources in the new catalogue and 290 in the original 10C catalogue; there are 88 sources found in the new catalogue which do not feature in the 10C catalogue and 20 sources in the 10C catalogue which are not found in the new catalogue. In each 10C field two complete areas were defined; one area complete to 1 mJy which encompasses most of the field (the 'shallow' area), and one area complete to 0.5 mJy (the 'deep' area) which is contained within the shallow area.

Figure 8.7 shows the positions of 10C sources which are not found in the new catalogue, colour coded according to their flux density. Four of these sources have flux densities greater

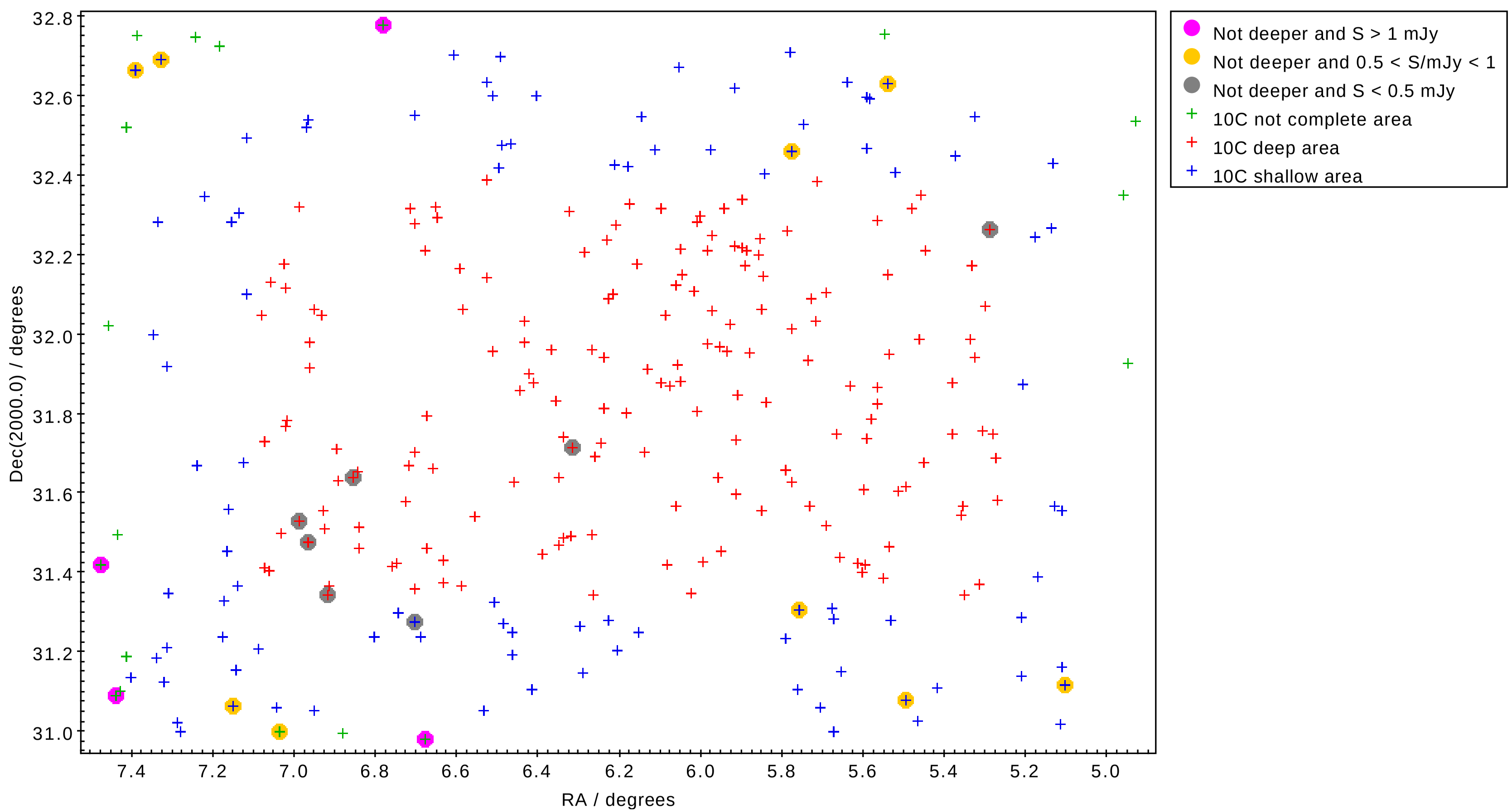

Figure 8.7: Positions of 10C sources in the AMI001 field. Sources which are not found in the new catalogue marked with circles; those with $S < 0.5$ mJy are shown in grey, those with $0.5 < S < 1$ mJy are shown in yellow and those with $S > 1$ mJy are shown in magenta. Red crosses indicate that a source is in the 10C survey area complete to 0.5 mJy, blue crosses show sources in the area complete to 1 mJy and green crosses mark sources outside the complete area.

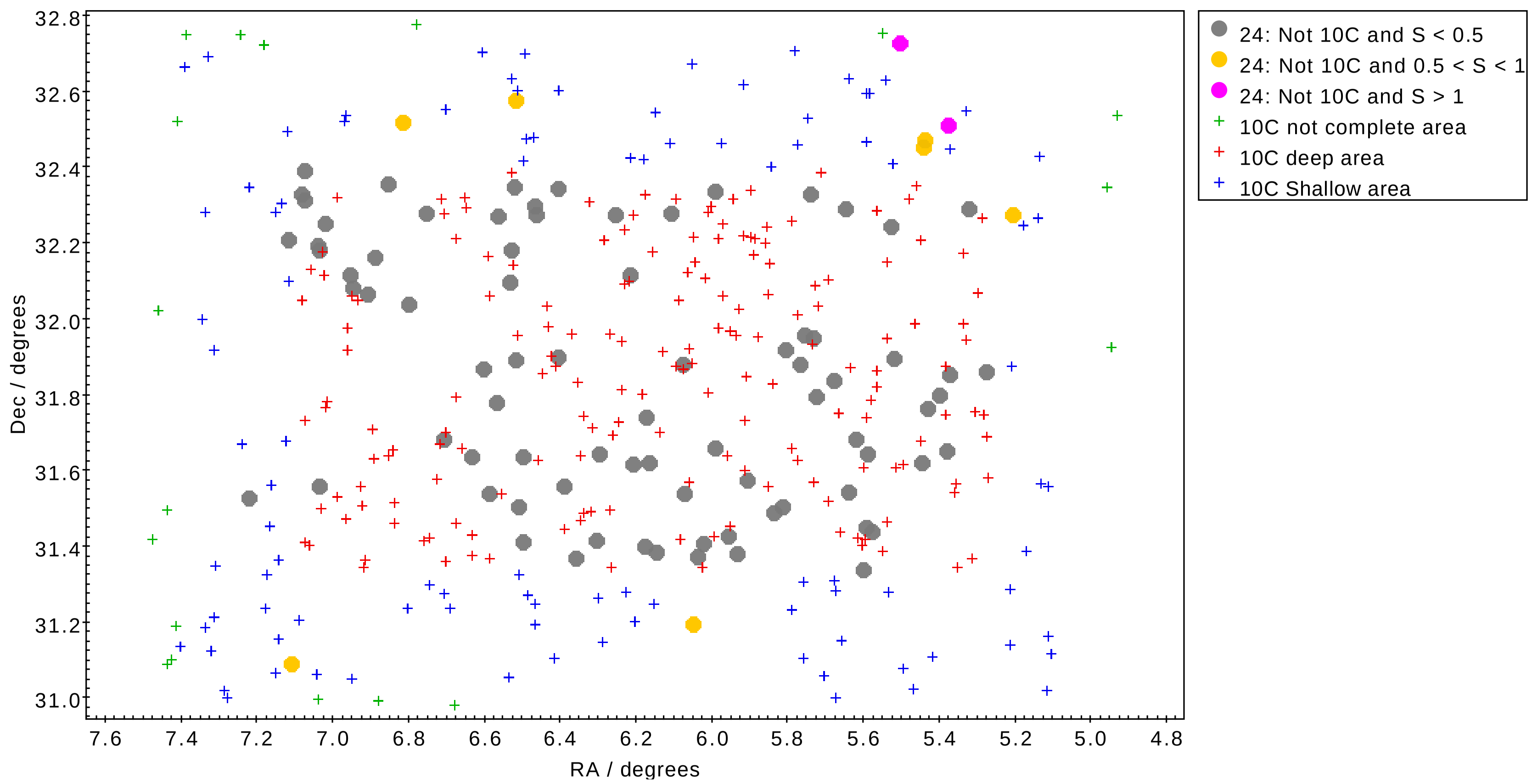

Figure 8.8: Positions of sources in the AMI001 field. Circles show sources in the new deeper catalogue which are not present in the 10C catalogue; those with $S < 0.5$ mJy are shown in grey, those with $0.5 < S < 1$ mJy are shown in yellow and those with $S > 1$ mJy are shown in magenta. All 10C sources in the field are plotted as crosses for reference; sources in the area complete to 0.5 mJy are shown as red crosses, blue crosses show sources in the area complete to 1 mJy and green crosses mark sources outside the complete area.

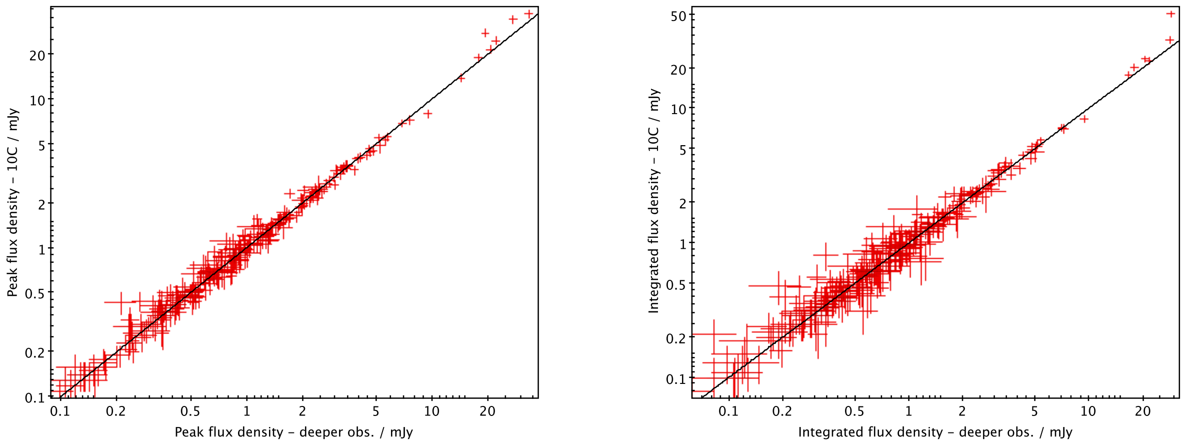

Figure 8.9: Comparison of peak (left panel) and integrated (right panel) flux densities in the 10C and deeper catalogues. The black line indicates where the two flux densities are equal.

than 1 mJy; all four are located outside the complete 10C area (at the edge of the map). Nine sources which are not detected in the new observations have flux densities between 0.5 and 1 mJy, these sources are all found outside the deep complete area. Seven undetected 10C sources have flux densities less than 0.5 mJy (the deep-area completeness limit), six of these are located in the deep area and one in the shallow area. There are therefore no sources found in the 10C catalogue and not in the new catalogue which are above the completeness limit for the region in which they are located. It is also notable that all of the 10C sources located in the area with the lowest noise in the new map (on the right-hand side of the deep area) are found in the new catalogue.

Figure 8.8 shows the sources in the new catalogue which were not found in the 10C catalogue. The majority of these sources are found in the deep area where most of the new observations have taken place. All the new sources found in the deep area have flux densities less than 0.5 mJy. There are eight new sources found in the shallow area, all but one of these have flux densities less than 1 mJy, this one source has a flux density of 1.01 mJy. There are several possible reasons for this source not being included in the original 10C catalogue; it is possible that this source is variable, and its flux density has increased since the observations for the original 10C catalogue were made, or that since its flux density is very close to the completeness limit, that variations in the noise in the map caused this source to not be detected in the original observations and be detected now. The shallow area is 95 percent complete to 1 mJy and there are 106 sources in the shallow complete catalogue in the 10C field; it is therefore expected that at least one extra undetected source may be present.

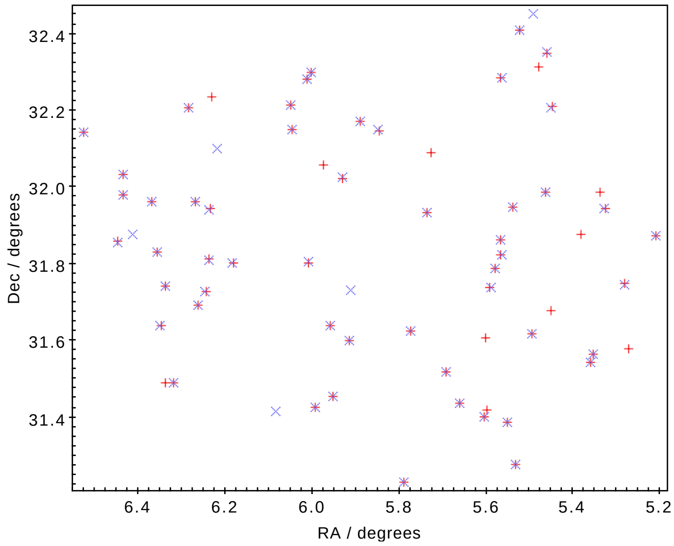

Figure 8.10: Positions of sources in the 'first half' (red) and 'second half' (blue) catalogues when the two halves are imaged separately.

Figure 8.9 shows a comparison of the peak and integrated flux densities of sources which appear in both the original 10C catalogue and the new, deeper catalogue presented here. The flux densities from the two catalogues are generally in good agreement. Similar checks were also performed on the Lockman Hole field and these also showed a good agreement between the new observations and the original catalogue.

8.3.2 Splitting the data in half

A 'jackknife' test was performed on a $\sim$ 1 deg^2 region in the deepest part of the AMI001 field. This involves splitting the data in half according to when it was observed, so all the older observations are in the first half and all the newer observations are in the second half. The two halves are then imaged separately and SOURCE_FIND was run on the two halves to create two catalogues. The 'first half' catalogue contains 63 sources and the 'second half' catalogue contains 57 sources; the positions of these sources are shown in Figure 8.10. The majority of sources are found in both catalogues, however 15 sources are only found in one catalogue. These tend to be the fainter sources (all have $S < 5$ mJy) and this is probably due to the slight difference in rms noise between the two halves. The peak flux densities of the sources which appear in both catalogues are compared in Figure 8.11. Although there is some scatter in this plot the majority of the values agree within the errors, so there is no evidence for any systematic differences between the data observed at the beginning and at the end of the observation run.

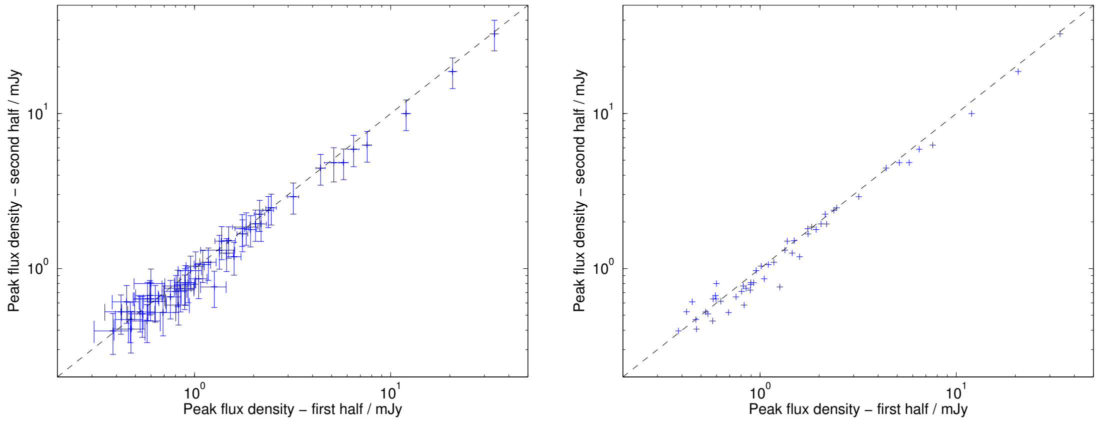

Figure 8.11: Peak flux densities of sources in the 'first half' and 'second half' catalogues. Shown with error bars in the left panel, and without in the right panel for clarity.

8.4 Source counts

8.4.1 Calculating the source counts

The catalogue of sources used to calculate the source counts is described in Section 8.2.7. The integrated flux density is used for sources classified as extended in the fitting process, otherwise the peak flux density is used. The noise varies significantly across both fields, as is demonstrated in Figures 8.1 and 8.2, and this needs to be taken into account when calculating the source counts. To do this the visibility area was calculated (Katgert et al. 1973); this is the fraction of the total area over which a source of a flux density S_i could be detected (i.e. the fraction of the total area with $5\sigma_{\rm local} < S_i$), assuming the theoretical noise map. The visibility area of the two fields are shown in Figure 8.12.

In order to check how sensitive the visibility area is to how the noise map is calculated, two different visibility curves were produced for the AMI001 field, one using the theoretical noise map produced during the data reduction, and one using the noise map produced by the SOURCE_FIND source-fitting algorithm. SOURCE_FIND produces a noise map by calculating the noise at each pixel as the rms inside a square of width 150 arcsec centred on that pixel, and shows more local variation than the original noise map. The visibility curves resulting from the two noise maps are shown in Figure 8.13; both curves have the same overall shape, with a few differences. These differences have a small effect on the source count, as shown in Figure 8.14; the count calculated using the noise map calculated directly from the data is higher in the two faintest bins.

To calculate the source count, each source was weighted by the reciprocal of its visibility

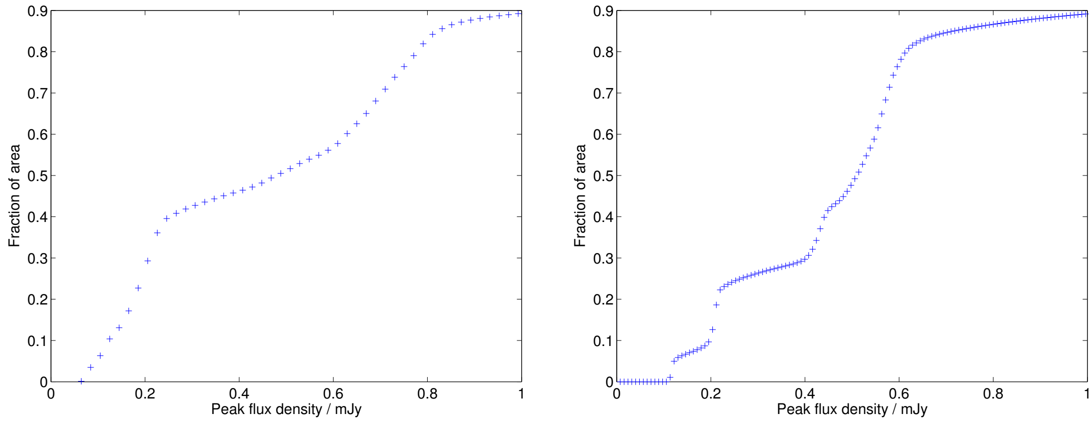

Figure 8.12: Visibility area of the AMI001 field (left) and Lockman Hole field (right) i.e. fraction of the total area over which a source with a given flux density could be detected.

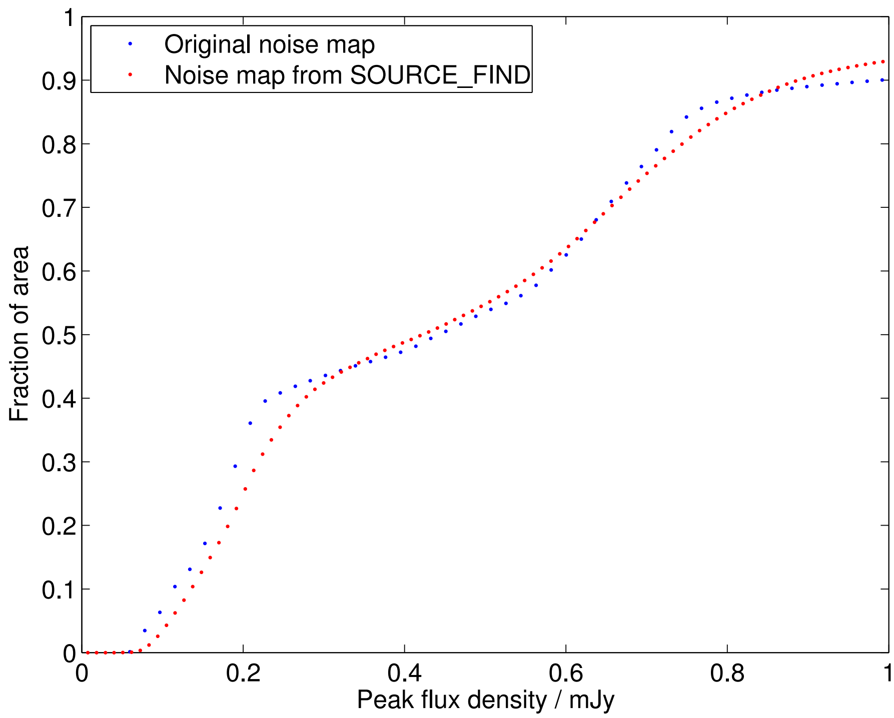

Figure 8.13: The visibility area in the AMI001 field calculated using two different noise maps.

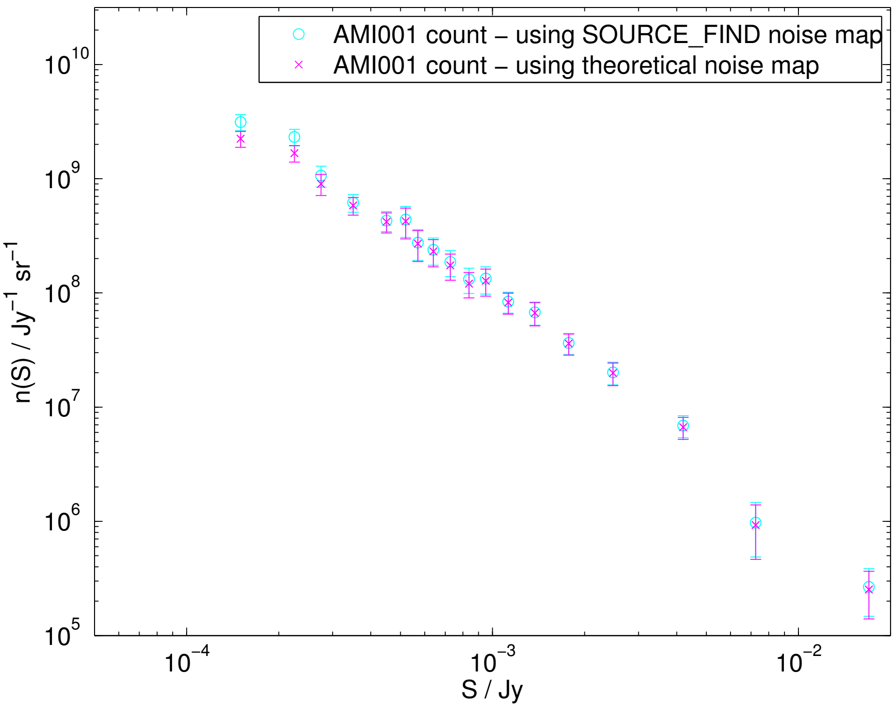

Figure 8.14: The source count calculated using two different noise maps.

area. The source count in each flux density bin is therefore given by the following expression:

$$\frac{1}{A}\sum_{i=1}^{N}\frac{1}{x(S_i)} \tag{8.7}$$

where N is the number of sources in the bin, A is the total area of the field and $x(S_i)$ is the visibility area for a source with flux density S_i.

The differential source counts derived from the two fields are shown in Tables 8.2 and 8.3. They are plotted in Figure 8.15, along with the 10C count for comparison. Higher flux density bins are not included as the fields were chosen to be away from bright sources. The points are plotted at the 'centre of gravity' of each flux density bin (the average of the difference between each flux density and one edge of the bin). The error bars plotted are $\sqrt{N}$ Poisson errors. The new counts are in good agreement with the 10C count where they overlap, and extend the source count by a factor of five fainter in flux density. The counts from the two fields agree within the Poisson errors. In the faintest bin plotted for the AMI001 field ($0.08 < S_{15.7\ \mathrm{GHz}}/\mathrm{mJy} < 0.10$) the count is probably beginning to be incomplete, and due to the poor statistics in this bin it is omitted from Table 8.2 and later discussion.

Table 8.2: Source counts in the AMI001 field.

Bin flux density range / mJy	N	dN/dS / Jy^{-1} sr^{-1}
5.500 – 9.000	4	9.31e+05
2.900 – 5.500	21	6.70e+06
2.050 – 2.900	20	1.99e+07
1.500 – 2.050	23	3.61e+07
1.250 – 1.500	19	6.68e+07
1.000 – 1.250	23	8.25e+07
0.900 – 1.000	14	1.28e+08
0.775 – 0.900	16	1.21e+08
0.680 – 0.775	15	1.76e+08
0.600 – 0.680	14	2.31e+08
0.540 – 0.600	11	2.71e+08
0.500 – 0.540	11	4.27e+08
0.400 – 0.500	25	4.21e+08
0.300 – 0.400	32	5.85e+08
0.250 – 0.300	23	9.10e+08
0.200 – 0.250	37	1.68e+09
0.100 – 0.200	39	2.45e+09

Note: The translation from N to dN/dS is not linear due to the correction for the visibility area (see Equation 8.7.)

Table 8.3: Source counts in the Lockman Hole field.

Bin flux density range / mJy	N	dN/dS / Jy^{-1} sr^{-1}
2.900 – 5.500	6	3.66e+06
2.050 – 2.900	12	2.29e+07
1.500 – 2.050	8	2.41e+07
1.250 – 1.500	5	3.39e+07
1.000 – 1.250	14	9.72e+07
0.900 – 1.000	4	7.06e+07
0.775 – 0.900	14	2.02e+08
0.680 – 0.775	9	1.75e+08
0.500 – 0.680	20	3.03e+08
0.300 – 0.500	17	4.56e+08
0.200 – 0.300	10	6.78e+08

Note: The translation from N to dN/dS is not linear due to the correction for the visibility area (see Equation 8.7.)

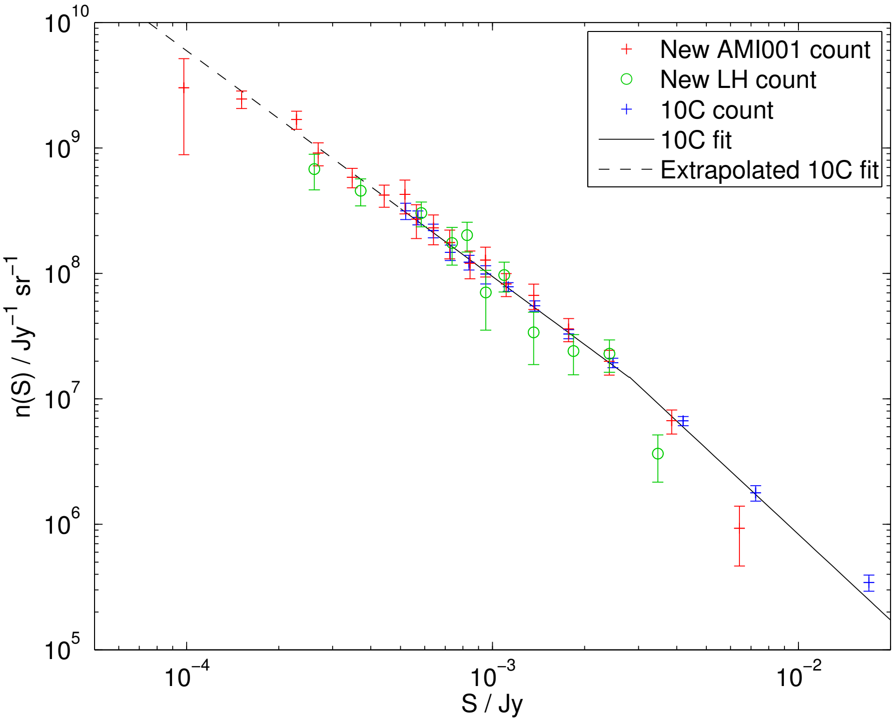

Figure 8.15: New source counts from the AMI001 (red) and Lockman Hole (green) fields. The 10C source counts are also shown (blue) for comparison, as is the fit to the 10C source counts (black line). In the faintest bin plotted for the AMI001 field the count is clearly incomplete, the point is not included in the discussion or subsequent plots.

8.4.2 Sample variance

Heywood et al. (2013) investigated the effects of sample variance induced by source clustering on deep source counts at 1.4 GHz by extracting a series of independent samples from the S^3 catalogue and comparing to observations. They used this to present a method for estimating the uncertainty in the source count caused by sample variance for an arbitrary radio survey. In the AMI001 field there are 0.23 deg^2 with rms noise < 20 μJy and 0.42 deg^2 with rms noise < 25 μJy, as shown in the contour plot in Figure 8.16. It should therefore be possible to detect a source with $S_{15.7\ \mathrm{GHz}} > 0.1$ mJy in an area of 0.23 deg^2; reading off Figure 8.17 (taken from Heywood et al. 2013) for this survey limit and area gives an uncertainty due to cosmic variance of ≈ 14 percent. At higher flux densities, this uncertainty decreases as the area over which a source could be detected (the effective survey area) increases. For example, for a survey limit of 0.125 mJy (equivalent to an rms noise of 25 μJy) and an area of 0.42 deg^2 the uncertainty is 12 percent.

In order to test this further, I extracted all sources with $S_{18\ \mathrm{GHz}} > 0.09$ mJy from eight

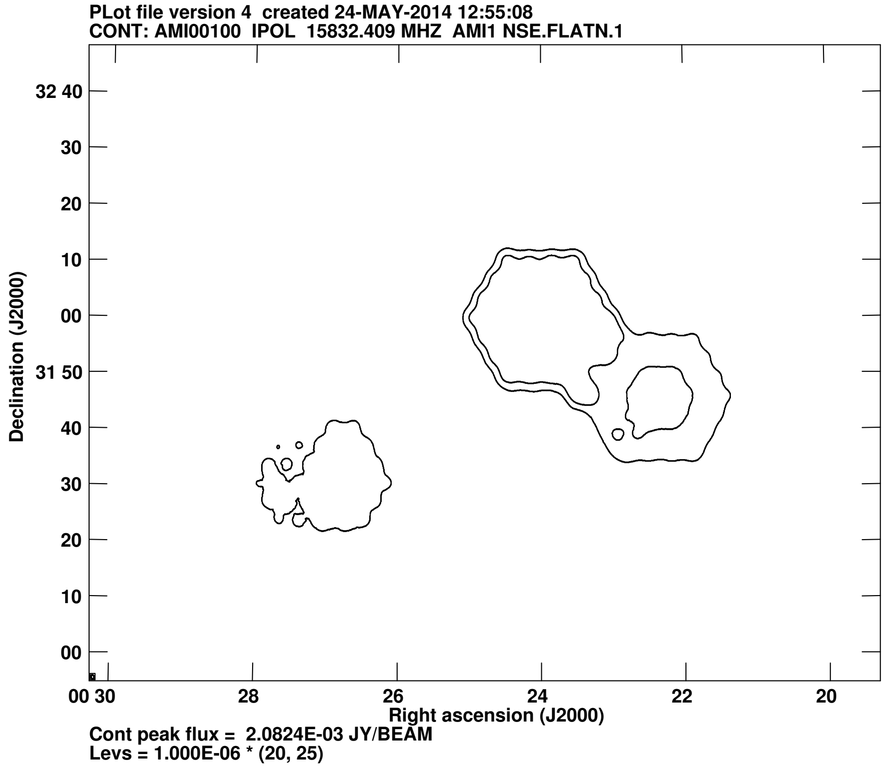

Figure 8.16: Region in the AMI001 field with rms noise < 25 and 20 μJy.

randomly placed regions from the S^3 catalogue, four with an area of 0.23 deg^2 and four with an area of 0.42 deg^2. I calculated the source count in the lowest flux density bin ($0.1 < S_{15.7\ \mathrm{GHz}}/\mathrm{mJy} < 0.2$) for each of these areas. This is shown in Figure 8.18, along with the source count from the AMI001 field in this bin. The cyan point shows the mean count in the four areas selected from S^3, and the standard error in the mean. In the left-hand plot of Figure 8.18 this error bar is a similar size to the error bar on the AMI001 point, which represents the Poisson error. This shows that the error due to cosmic variance is expected to be of a similar magnitude to the Poisson error in this source count bin. In the right-hand plot (which represents the larger area), the error on the mean is smaller than the Poisson error, showing that for larger areas the error due to cosmic variance will be smaller than the Poisson error.

8.4.3 Possible biases

Several effects which could bias the source counts are considered here; however for the reasons discussed no corrections are made for these biases.

1. Variability. Variability in flux densities can cause sources near the edge of flux density bins to move between bins. The shape of the source counts means that at the bottom of

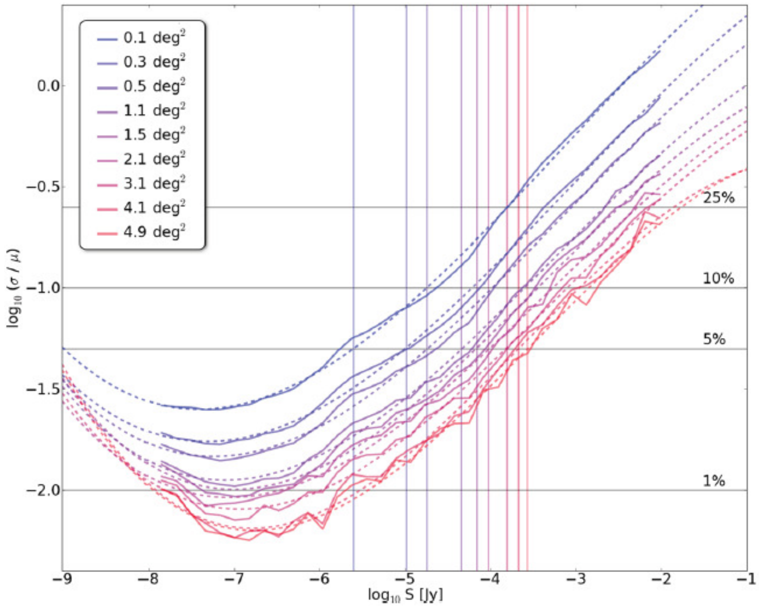

Figure 8.17: The solid lines show standard deviations (σ) per flux density bin for a range of theoretical (colour-coded) survey areas, expressed as a fraction of the mean source counts (μ) in that bin. Polynomials are fitted to the base-10 logarithms of the distributions, as shown by the dashed lines. The vertical lines show the detection thresholds that must be reached in order to deliver 5 per cent uncertainty due to cosmic variance for each area. Taken from Heywood et al. (2013).

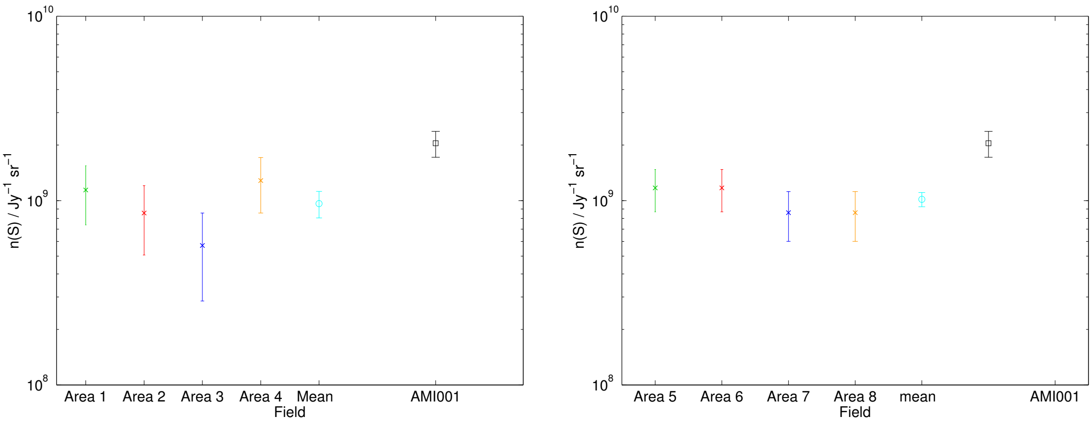

Figure 8.18: Differential source count in the lowest bin ($0.1 < S_{15.7\ \mathrm{GHz}} < 0.2$ mJy) for four areas randomly selected from the S^3 catalogue. For these points, the errors plotted are the Poisson errors. The mean count in the four areas is plotted as a cyan circle; for this point the error plotted is the standard error in the mean. Left panel: area of regions selected from $S^3 = 0.23$ deg^2, right panel: area = 0.42 deg^2 (these are the areas of the AMMI001 field with rms > 20 and 25 μJy respectively). The observed count in the AMI001 field is also shown for comparison (black square, error plotted is the Poisson error.).

the bin, the number of sources in the positive phase of variability which are included in the bin will be marginally higher than the number of sources in the negative phase of variability which are excluded. The opposite effect occurs at the other end of the bin but will not be enough to offset this effect. Therefore, variability will boost the number of sources in the fainter flux density bins.

2. Eddington bias (Eddington 1913). Statistical fluctuations due to thermal noise can alter the flux density of sources and can therefore cause some sources to be put into the wrong bins. If the true number of sources in one bin is greater than in adjacent bins, more sources will be scattered out of that bin than into it. The observed number of sources will therefore be biased low (Jeffreys 1938). The Eddington bias therefore boosts the number in the faintest flux density bin. Davies et al. (2011) estimate that this effect will increase the number of sources in the faintest 10C flux density bin by ≈ 7 percent. As incompleteness is expected to reduce the number of sources in this bin by a similar amount they do not correct for this effect. No correction is applied here for the same reason.
3. Resolution bias. To calculate the source counts a sample which is complete in terms of integrated flux density is required, but the sources are detected according to their peak flux densities. This means that a resolved source of a given total flux density $S_{\rm TOT}$ is more likely to fall below the peak flux density detection threshold than a point source with the same $S_{\rm TOT}$. Due to the relatively large beam size of AMI, only 7 percent of sources in the AMI001 field and 4 percent in the Lockman Hole field are extended, so resolution is not expected to have a significant effect on these source counts.

8.5 Discussion

The new deeper counts are consistent with the extrapolated 10C fit, and do not display any evidence for an inflection point in the flux density range $0.1 < S_{15.7\,\rm GHz}/\rm mJy < 0.5$. There is no sign of the upturn observed in the 1.4-GHz source counts at $S_{1.4\,\rm GHz} \sim 1$ mJy (de Zotti et al. 2010); there is thus no evidence for a new population (e.g. of starforming sources) contributing to the 15.7-GHz source population above 0.1 mJy. This is not surprising, as a typical steep spectrum source ($\alpha = 0.7$) with $S_{1.4\,\rm GHz} = 1$ mJy will have $S_{15.7\,\rm GHz} \sim 0.18$ mJy, and would therefore only have appeared at the bottom of the faintest flux density bin here.

A model of the high-frequency ($\nu > 5$ GHz) source counts was produced by de Zotti et al. (2005), as described in Chapter 1. The new 15.7-GHz source counts presented here are compared to the latest version of the de Zotti et al. model, extracted from their website[b], in

[b]http://web.oapd.inaf.it/rstools/srccnt_tables

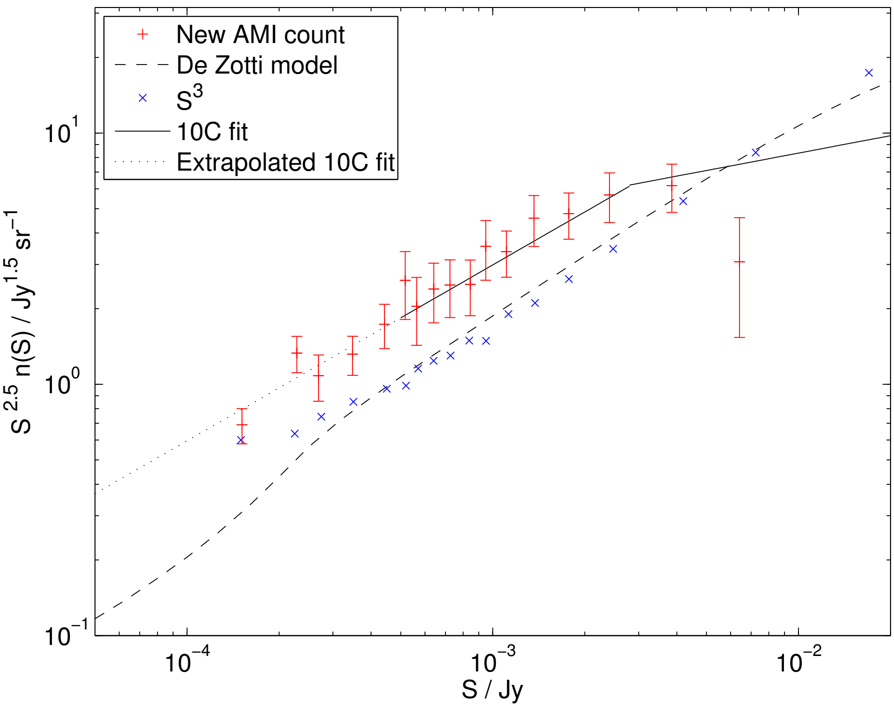

Figure 8.19: Euclidean normalised differential source counts from the de Zotti et al. model (dashed line) and the new 15.7-GHz observations (red points). The 18 GHz count from the S^3 catalogue is shown by blue crosses. Poisson errors are plotted for the observed count.

Figure 8.19. Davies et al. showed that the de Zotti et al. model under-predicts the number of sources in the 10C survey below $\approx$ 5 mJy, and Figure 8.19 shows that the model continues to under-predict the number of sources observed by a factor of two as flux density decreases. In Chapter 3 I showed that the proportion of flat-spectrum sources in particular is too low in the de Zotti et al. model below $\approx$ 1 mJy; it is likely that this under-prediction of the number of flat-spectrum sources in the sub-mJy population is responsible for the discrepancies between the model and the observed count seen here.

The new 15.7-GHz source count is compared to the S^3 catalogue in Figure 8.19. All sources with $S_{18\ \mathrm{GHz}} > 0.09$ mJy were selected from the simulation, and the source count was calculated in the same bins as for the observed count. The simulation under-predicts the observed number of sources, in a similar way to the de Zotti et al. model, but below $\approx$ 0.3 mJy there is a better agreement between the observed and simulated counts. (Note that the S^3 and de Zotti et al. models are not entirely independent as they are both extrapolations from models constructed using low-frequency data.) The slight flattening in the S^3 counts, which is responsible for this better agreement, is due to the greater contribution of starforming sources (both quiescent and starbursting) to the simulated catalogue below $\approx$ 0.3 mJy; starforming sources comprise 21 percent of the simulated sources with $0.09 < S_{18\ \mathrm{GHz}}/\mathrm{mJy} < 0.3$, compared to only 7 percent of sources with $S_{18\ \mathrm{GHz}} > 0.5$ mJy. However, given that there is no flattening in the new AMI count, it is not clear what contribution, if any, a population of starforming sources is making to the observed counts at $S_{15.7\ \mathrm{GHz}} > 0.1$ mJy.

8.6 Conclusions

In this chapter I have presented new very deep (best rms noise = 16 μJy) 15.7-GHz observations in two fields. These are the deepest high-frequency radio observations to date, and enable us to constrain the source counts down to $S_{15.7\ \mathrm{GHz}} = 0.1$ mJy. This is a factor of five deeper than previously achieved with the 10C survey.

The source counts are consistent with the extrapolated fit to the 10C count, and display no evidence for an inflection point in the region $0.1 < S_{15.7\ \mathrm{GHz}}/\mathrm{mJy} < 0.5$. There is thus no evidence for a new population contributing to the 15.7-GHz source counts above 0.1 mJy, suggesting that the high-frequency radio sky continues to be dominated by radio galaxies down to at least this flux density level.

Comparisons with both the de Zotti et al. model and S^3 simulation show that these both underestimate the observed number of sources at low flux densities by a factor of two.

Chapter 9

Conclusions

In this thesis I have investigated the nature of the faint, high-frequency source population using a range of different techniques. A sample of 296 sources were selected from the 10C survey at 15.7 GHz in the Lockman Hole. This sample was matched to several lower-frequency, and higher-resolution, catalogues to investigate the radio properties of the sources. Counterparts were also identified for a subsample of 96 10C sources in a range of multi-wavelength catalogues, including optical, near and far-infrared, and X-ray data. These data were used to further investigate the nature of the 10C sources. New, deep observations at 15.7 GHz were used to extend the source count down to 0.1 mJy, a factor of five deeper than the previous deepest high-frequency source count, 10C. In this chapter I briefly discuss the conclusions drawn from this work.

9.1 Properties of the 15.7 GHz sources

I used the 10C data, along with lower-frequency radio data (e.g. a deep GMRT survey at 610 MHz, a WSRT survey at 1.4 GHz, NVSS and FIRST) to study the variation in spectral index with flux density. This showed that there is a clear increase in the fraction of flat spectrum sources below 1 mJy; the median spectral index between 15.7 GHz and 610 MHz changes from 0.75 for flux densities greater than 1.5 mJy to 0.08 for flux densities less than 0.8 mJy. Thus a population of faint, flat spectrum sources is emerging at flux densities $\lesssim 1$ mJy. I compared this spectral index distribution to that of two samples selected at 1.4 GHz from FIRST and NVSS and found that there is a significant flat spectrum population present in the 10C sample which is missing from the samples selected at 1.4 GHz.

I matched the 10C sample to a recent VLBI survey by Middelberg et al. (2013) and found that 33 out of the 51 10C sources in the VLBI field (65 percent) are detected by the VLBI observations. The high brightness temperature of these VLBI-detected sources indicates that they must be AGN and rules out the possibility that this faint, high frequency population is dominated by starbursting or starforming sources.

The multi-wavelength data were used to investigate the host galaxies of a complete sample of 96 10C radio sources with accurately determined positions. Multi-wavelength counterparts were identified for 80 out of these 96 sources, and these data were used to compute photometric redshifts. The radio-to-optical ratios (or limits on the ratios) of these 96 sources show that essentially all the sources in this sample are radio galaxies. The 1.4-GHz luminosities of these sources show that 59/80 sources have luminosities larger than that of the FRI/FRII divide.

The multi-wavelength data were used to split the radio galaxies into HERGs and LERGs; 34 sources are probably HERGs and 33 are probably LERGs, with 29 which could not be classified at this stage. The properties of these HERGs and LERGs are compared and I find that the HERGs tend to be found at higher redshifts, have flatter spectra, higher flux densities and smaller linear sizes. The flat spectra and compact nature of these sources suggests that they are dominated by emission from their cores. The HERGs observed in this sample have lower luminosities than are typical for this type of radio galaxy; this may be due to the lack of strong extended emission.

The new, deep, 15.7-GHz observations are used to constrain the high-frequency source count down to 0.1 mJy. These deeper source counts are consistent with the extrapolation of the fit to the 10C count, and do not show any evidence for an upturn. There is therefore no evidence for a new population (e.g. of starforming sources) contributing to the 15.7 GHz source count above 0.1 mJy, suggesting that the faint, high-frequency population continues to be dominated by radio galaxies.

9.2 Discussion of the 15.7 GHz radio sky

The results discussed in the previous section show that essentially all the 10C sources are radio galaxies. Here I discuss the nature of these radio galaxies in the context of models of the high-frequency radio sky.

The 10C catalogue was compared to a sample selected from the SKADS Simulated Sky (S^3) and the de Zotti et al. model of the high-frequency source count (both of which are extrapolated from lower frequencies); both these models significantly underpredict the fraction of flat spectrum sources observed, as well as underpredicting the total number of sources observed down to 0.1 mJy by a factor of two. These simulations, which are derived using empirical data from lower-frequency surveys, fail to model the dominance of the flat-spectrum cores and the relative faintness of the extended emission at 15.7 GHz.

The S^3 catalogue predicts that the majority (71 percent) of the sources in the 10C sample are FRI sources, but the 1.4-GHz luminosities of these sources are consistent with the majority of the sample being the higher-luminosity FRII sources. However, given the fact that the spectra from 1.4 to 15.7 GHz tend to be flat, it is likely that the cores of these sources are contributing significantly to the measured luminosities, so these luminosities in fact only represent an upper limit on the luminosity of the extended emission. These sources – which we have seen are drawn from the lower-luminosity tail of the HERG population, along with the LERG population – may be FRIs and FRIIs with very weak extended emission; alternatively they may represent a population of objects which have failed to produce the characteristic powerful extended emission. I have shown that such objects are not well represented in lower-frequency samples so do not appear in models of the high-frequency sky.

The S^3 catalogue predicts that starforming sources will be beginning to contribute to the high-frequency sky at the flux density levels probed here and that ~ 20 percent of the sources with flux densities $0.1 < S_{18\ \mathrm{GHz}}/\mathrm{mJy} < 0.5$ will be starforming. There is, however, no evidence from the source counts for any significant contribution from a population of starforming sources above 0.1 mJy.

9.3 Further work

A natural continuation to the work discussed above is to extend the multi-wavelength study in Chapters 5, 6 and 7 to fainter flux densities. For this purpose, I have made deep optical (U, g, i, r and z) observations with the Isaac Newton Telescope of the AMI001 field, which contains the deepest 15.7-GHz observations presented in Chapter 8. I have also made deep 610 MHz GMRT observations in this field, which will provide the accurate positions required to identify optical counterparts, as well as providing information about the radio spectra. These new data will be used to investigate the radio spectra and nature of these fainter sources (down to 0.1 mJy).

In order to understand the full nature of these faint, flat-spectrum 15.7-GHz sources deep, high-resolution observations at say, 1.4 GHz, are required to look for extended low surface brightness regions. With these data the S^3 and de Zotti et al. models could be updated to better represent the high-frequency sky and, at the same time, give further insights into the very faint low-frequency sky. Such simulations are vital in optimising the design of future radio surveys with next generation instruments (such as MeerKAT and the SKA), which aim to probe the faint radio sky down to unexplored flux density levels (~ 1 nJy).

Appendix A

Source catalogues

A.1 Radio properties

Table A.1: Radio properties of sources in the Lockman Hole 10C sample.

10C ID	RA	Dec	$S_{15.7}^{1}$ mJy	S_{610} mJy	flag[2] 610	$S_{1.4}$b[3] mJy	flag[4] 1.4b	$S_{1.4}$N mJy	flag[2] NVSS	$\alpha_{0.61}^{15.7}$	$\alpha_{1.4}^{15.7}$	$\alpha_{1.4}^{15.7}$ NVSS
J103857+592546	10 38 57.27	+59 25 46.28	2.85	14.9	0	7.81	1	7.81	0	0.51	0.42	0.42
J103859+590548	10 38 59.96	+59 05 48.59	8.858	120.63	0	66.4	1	66.4	0	0.8	0.83	0.83
J103912+591428	10 39 12.78	+59 14 28.18	4.176	180.95	0	67.4	1	67.4	0	1.16	1.15	1.15
J103913+581445	10 39 13.19	+58 14 45.09	1.575	31.61	0	22.9	1	22.9	0	0.92	1.11	1.11
J103920+592235	10 39 20.00	+59 22 35.47	2.311	1.0	0	2.5	1	2.5	0	−0.26	0.03	0.03
J103922+582912	10 39 22.19	+58 29 12.01	5.243	280.48	0	100.3	1	100.3	0	1.23	1.22	1.22
J103923+593805	10 39 23.85	+59 38 05.93	2.28	32.11	0	14.0	1	14.0	0	0.81	0.75	0.75
J103940+592132	10 39 40.09	+59 21 32.12	0.754	0.51	0	1.0	7	1.41	1	−0.12	0.12	0.26
J103952+583215	10 39 52.52	+58 32 15.71	0.81	5.05	0	3.64	1	3.64	0	0.56	0.62	0.62
J103954+581524	10 39 54.87	+58 15 24.55	1.492	0.55	0	2.23	1	2.23	0	−0.31	0.17	0.17
J103959+582354	10 39 59.12	+58 23 54.15	5.254	0.29	1	2.7	1	2.7	0	−0.89	−0.28	−0.28
J103959+584812	10 39 59.53	+58 48 12.69	3.274	122.56	0	53.0	1	53.0	0	1.12	1.15	1.15
J104004+582857	10 40 04.06	+58 28 57.61	2.195	23.81	0	14.7	1	14.7	0	0.73	0.79	0.79
J104005+592513	10 40 05.15	+59 25 13.75	2.424	75.0	0	33.0	1	33.0	0	1.06	1.08	1.08
J104008+584646	10 40 08.02	+58 46 46.36	0.645	1.71	1	1.0	7	1.45	1	0.3	0.18	0.34
J104016+594327	10 40 16.76	+59 43 27.85	1.574	18.34	0	11.7	1	11.7	0	0.76	0.83	0.83
J104019+584053	10 40 19.59	+58 40 53.72	0.69	1.19	1	1.0	7	1.55	1	0.17	0.15	0.33
J104023+594205	10 40 23.75	+59 42 05.20	3.138	17.7	0	21.7	1	21.7	0	0.53	0.8	0.8
J104032+594238	10 40 32.58	+59 42 38.66	2.047	53.89	0	31.1	1	31.1	0	1.01	1.13	1.13
J104033+595446	10 40 33.59	+59 54 46.57	2.431	14.99	0	8.3	1	8.3	0	0.56	0.51	0.51

continued on next page

continued from previous page

10C ID	RA	Dec	$S^{1}_{15.7}$ mJy	S_{610} mJy	flag[2] 610	$S_{1.4}$b[3] mJy	flag[4] 1.4b	$S_{1.4}$N mJy	flag[2] NVSS	$\alpha^{15.7}_{0.61}$	$\alpha^{15.7}_{1.4}$	$\alpha^{15.7}_{1.4}$ NVSS
J104043+593410	10 40 43.90	+59 34 10.25	1.118	13.61	0	9.5	1	9.5	0	0.77	0.89	0.89
J104043+594012	10 40 43.35	+59 40 12.84	0.781	4.65	1	1.0	7	1.61	1	0.55	0.1	0.3
J104046+581222	10 40 46.53	+58 12 22.93	1.494	1.47	1	1.0	7	1.35	1	0.0	−0.17	−0.04
J104103+590414	10 41 03.15	+59 04 14.55	1.043	0.82	0	1.59	1	1.59	0	−0.07	0.17	0.17
J104110+592850	10 41 10.69	+59 28 50.91	0.671	18.18	0	8.9	1	8.9	0	1.02	1.07	1.07
J104114+592934	10 41 14.06	+59 29 34.62	1.576	18.61	0	11.4	1	11.4	0	0.76	0.82	0.82
J104117+591808	10 41 17.31	+59 18 08.10	0.529	1.23	0	1.0	7	1.46	1	0.26	0.26	0.42
J104121+585333	10 41 21.52	+58 53 33.21	0.43	0.83	0	1.0	7	1.46	1	0.2	0.35	0.51
J104124+593356	10 41 24.84	+59 33 56.03	2.555	5.54	0	5.4	1	5.4	0	0.24	0.31	0.31
J104127+592635	10 41 27.79	+59 26 35.39	5.33	60.3	0	33.4	1	33.4	0	0.75	0.76	0.76
J104133+590956	10 41 33.42	+59 09 56.28	0.475	7.43	0	3.7	1	3.7	0	0.85	0.85	0.85
J104142+583751	10 41 42.88	+58 37 51.82	0.559	0.88	1	1.0	7	1.31	1	0.14	0.24	0.35
J104143+585650	10 41 43.38	+58 56 50.32	0.577	0.77	0	1.0	7	1.31	1	0.09	0.23	0.34
J104144+594256	10 41 44.61	+59 42 56.66	1.279	2.25	0	3.1	1	3.1	0	0.17	0.37	0.37
J104147+583031	10 41 47.76	+58 30 31.80	1.108	1.58	0	1.41	5	1.3	1	0.11	0.1	0.07
J104147+592448	10 41 47.85	+59 24 48.90	0.539	1.29	1	1.0	7	1.21	1	0.27	0.26	0.33
J104200+592742	10 42 00.82	+59 27 42.31	4.462	45.27	0	28.7	1	28.7	0	0.71	0.77	0.77
J104202+581232	10 42 02.54	+58 12 32.16	0.874	0.97	1	1.0	7	1.34	1	0.03	0.06	0.18
J104202+592633	10 42 02.14	+59 26 33.12	0.543	1.27	1	1.0	7	1.3	1	0.26	0.25	0.36
J104206+585820	10 42 06.66	+58 58 20.00	5.73	87.64	0	44.7	1	44.7	0	0.84	0.85	0.85
J104213+592121	10 42 13.60	+59 21 21.96	4.089	5.82	0	10.0	1	10.0	0	0.11	0.37	0.37
J104214+585113	10 42 14.32	+58 51 13.96	0.556	12.35	0	4.8	1	4.8	0	0.95	0.89	0.89
J104217+585810	10 42 17.66	+58 58 10.46	1.086	6.61	0	7.1	1	7.1	0	0.56	0.78	0.78
J104221+583317	10 42 21.39	+58 33 17.10	6.453	77.86	0	43.7	1	43.7	0	0.77	0.79	0.79
J104223+581156	10 42 23.48	+58 11 56.53	2.33	66.64	0	31.9	1	31.9	0	1.03	1.08	1.08
J104226+584251	10 42 26.59	+58 42 51.47	0.638	1.08	1	1.0	7	1.34	1	0.16	0.19	0.31
J104226+592656	10 42 26.69	+59 26 56.92	1.417	6.13	0	9.8	1	9.8	0	0.45	0.8	0.8
J104234+594703	10 42 34.40	+59 47 03.40	1.242	0.89	1	1.76	5	1.59	1	−0.1	0.14	0.1
J104236+591956	10 42 36.58	+59 19 56.38	3.378	25.76	0	18.2	1	18.2	0	0.63	0.7	0.7
J104236+593956	10 42 36.95	+59 39 56.12	2.033	33.64	0	20.1	1	20.1	0	0.86	0.95	0.95
J104240+593804	10 42 40.99	+59 38 04.85	1.499	21.19	0	10.7	1	10.7	0	0.82	0.81	0.81
J104242+593048	10 42 42.68	+59 30 48.28	5.974	49.86	0	27.3	1	27.3	0	0.65	0.63	0.63
J104247+593222	10 42 47.76	+59 32 22.90	0.633	1.13	1	1.0	7	1.43	1	0.18	0.19	0.34
J104250+595303	10 42 50.37	+59 53 03.73	0.972	15.42	0	8.0	1	8.0	0	0.85	0.87	0.87
J104251+590547	10 42 51.39	+59 05 47.86	0.671	0.75	1	1.0	7	1.38	1	0.03	0.17	0.3
J104311+590740	10 43 11.67	+59 07 40.89	0.764	13.4	0	7.3	1	7.3	0	0.88	0.93	0.93
J104319+592708	10 43 19.45	+59 27 08.06	0.423	1.61	0	1.0	7	1.78	1	0.41	0.36	0.59
J104320+585621	10 43 20.56	+58 56 21.48	3.265	32.4	0	44.1	1	44.1	0	0.71	1.08	1.08
J104321+583441	10 43 21.78	+58 34 41.18	0.595	9.64	0	5.4	1	5.4	0	0.86	0.91	0.91
J104328+590312	10 43 28.48	+59 03 12.33	0.919	1.5	0	2.9	3	1.29	1	0.15	0.48	0.14
J104329+595021	10 43 29.91	+59 50 21.98	1.995	0.8	1	1.0	7	1.52	1	−0.28	−0.29	−0.11
J104332+582706	10 43 32.57	+58 27 06.08	0.889	0.83	1	0.42	6	1.09	1	−0.02	−0.31	0.08
J104336+592618	10 43 36.74	+59 26 18.41	2.07	41.99	0	21.3	1	21.3	0	0.93	0.96	0.96
J104344+591503	10 43 44.86	+59 15 03.25	2.9	4.21	0	6.2	1	6.2	0	0.11	0.31	0.31
J104352+581324	10 43 52.06	+58 13 24.96	1.338	5.06	0	8.4	1	8.4	0	0.41	0.76	0.76

continued on next page

continued from previous page

10C ID	RA	Dec	$S_{15.7}$[1] mJy	S_{610} mJy	flag[2] 610	$S_{1.4}$b[3] mJy	flag[4] 1.4b	$S_{1.4}$N mJy	flag[2] NVSS	$\alpha^{15.7}_{0.61}$	$\alpha^{15.7}_{1.4}$	$\alpha^{15.7}_{1.4}$ NVSS
J104354+595320	10 43 54.29	+59 53 20.73	0.82	0.7	1	1.67	5	1.46	1	−0.05	0.29	0.24
J104357+583609	10 43 57.93	+58 36 09.40	0.705	0.91	1	0.25	6	1.37	1	0.08	−0.43	0.27
J104422+594706	10 44 22.39	+59 47 06.73	0.768	2.81	0	2.09	5	1.41	1	0.4	0.41	0.25
J104428+591540	10 44 28.93	+59 15 40.44	0.814	0.83	1	0.2	3	1.26	1	0.01	−0.58	0.18
J104428+593255	10 44 28.85	+59 32 55.16	1.012	0.58	1	1.0	7	1.71	1	−0.17	0.0	0.22
J104436+585306	10 44 36.29	+58 53 06.70	0.478	21.32	0	9.7	1	9.7	0	1.17	1.25	1.25
J104441+591949	10 44 41.91	+59 19 49.25	0.605	0.76	1	0.5	3	1.37	1	0.07	−0.08	0.34
J104451+591929	10 44 51.12	+59 19 29.50	1.068	15.19	0	10.1	1	10.1	0	0.82	0.93	0.93
J104456+592537	10 44 56.72	+59 25 37.53	2.685	12.25	0	11.8	1	11.8	0	0.47	0.61	0.61
J104456+593802	10 44 56.31	+59 38 02.67	0.926	3.19	0	4.2	1	4.2	0	0.38	0.63	0.63
J104501+593559	10 45 01.76	+59 35 59.89	1.176	7.71	0	5.4	1	5.4	0	0.58	0.63	0.63
J104507+585353	10 45 07.90	+58 53 53.17	0.399	0.65	1	0.2	3	1.22	1	0.15	−0.29	0.46
J104510+591437	10 45 10.89	+59 14 37.28	0.463	0.82	1	0.6	3	1.19	1	0.18	0.11	0.39
J104525+595343	10 45 25.55	+59 53 43.42	1.051	0.96	1	1.15	5	1.74	1	−0.03	0.04	0.21
J104528+591328	10 45 28.89	+59 13 28.64	1.781	29.18	0	12.9	1	12.9	0	0.86	0.82	0.82
J104539+585730	10 45 39.18	+58 57 30.95	0.929	1.82	0	2.2	1	2.2	0	0.21	0.36	0.36
J104551+590838	10 45 51.06	+59 08 38.97	0.606	0.58	0	0.8	3	1.32	1	−0.01	0.11	0.32
J104551+592056	10 45 51.68	+59 20 56.16	0.48	3.89	0	2.4	1	2.4	0	0.64	0.67	0.67
J104552+594327	10 45 52.67	+59 43 27.15	2.494	5.6	0	3.1	1	3.1	0	0.25	0.09	0.09
J104559+590326	10 45 59.52	+59 03 26.95	0.39	0.77	1	0.4	3	1.38	1	0.21	0.01	0.52
J104608+594018	10 46 08.42	+59 40 18.31	2.069	49.04	0	23.1	1	23.1	0	0.97	1.0	1.0
J104624+590447	10 46 24.75	+59 04 47.51	1.104	34.82	0	18.3	1	18.3	0	1.06	1.16	1.16
J104630+582748	10 46 30.38	+58 27 48.48	5.34	63.63	0	58.9	1	58.9	0	0.76	0.99	0.99
J104633+585816	10 46 33.91	+58 58 16.21	0.723	0.86	1	0.27	2	1.53	1	0.05	−0.41	0.31
J104639+582005	10 46 39.54	+58 20 05.44	0.58	0.74	1	0.05	6	1.17	1	0.08	−1.01	0.29
J104641+590835	10 46 41.75	+59 08 35.91	0.397	0.97	1	0.1	3	1.49	1	0.28	−0.57	0.55
J104646+594612	10 46 46.29	+59 46 12.49	2.477	49.67	0	21.3	1	21.3	0	0.92	0.89	0.89
J104648+590956	10 46 48.93	+59 09 56.89	0.779	0.89	1	0.6	3	1.43	1	0.04	−0.11	0.25
J104651+583630	10 46 51.54	+58 36 30.98	0.369	0.76	0	0.75	2	1.65	1	0.22	0.29	0.62
J104656+594639	10 46 56.52	+59 46 39.82	0.794	9.86	0	0.0	1	5.4	0	0.78	0.79	0.79
J104700+591903	10 47 00.91	+59 19 03.34	2.298	47.62	0	22.9	1	22.9	0	0.93	0.95	0.95
J104710+582821	10 47 10.91	+58 28 21.19	12.226	2.32	0	4.06	2	1.35	1	−0.51	−0.46	−0.91
J104712+593934	10 47 12.35	+59 39 34.39	1.209	30.36	0	13.0	1	13.0	0	0.99	0.98	0.98
J104713+592912	10 47 13.08	+59 29 12.22	0.578	14.45	0	10.8	1	10.8	0	0.99	1.21	1.21
J104714+583034	10 47 14.43	+58 30 34.24	0.671	0.29	0	0.04	6	1.47	1	−0.26	−1.17	0.32
J104715+594617	10 47 15.95	+59 46 17.26	0.665	1.16	1	1.0	7	1.69	1	0.17	0.17	0.39
J104718+585119	10 47 18.80	+58 51 19.82	1.038	3.5	0	3.7	1	3.7	0	0.37	0.53	0.53
J104718+593247	10 47 18.44	+59 32 47.58	4.602	90.88	0	36.0	1	36.0	0	0.92	0.85	0.85
J104719+582114	10 47 19.25	+58 21 14.13	45.705	43.13	0	70.6	1	70.6	0	−0.02	0.18	0.18
J104720+570804	10 47 20.40	+57 08 04.32	1.186	0.86	1	1.12	2	1.12	1	−0.1	−0.02	−0.02
J104723+570051	10 47 23.89	+57 00 51.77	0.909	0.82	1	0.46	2	1.34	1	−0.03	−0.28	0.16
J104724+573703	10 47 24.23	+57 37 03.33	3.283	55.74	0	28.4	1	28.4	0	0.87	0.89	0.89
J104733+591244	10 47 33.98	+59 12 44.57	1.466	1.65	0	1.93	2	1.23	1	0.04	0.11	−0.07
J104734+570651	10 47 34.67	+57 06 51.44	1.399	0.73	1	0.46	2	1.34	1	−0.2	−0.46	−0.02
J104736+583336	10 47 36.59	+58 33 36.49	0.477	10.17	0	4.7	1	4.7	0	0.94	0.95	0.95

continued on next page

continued from previous page

10C ID	RA	Dec	$S^{1}_{15.7}$ mJy	S_{610} mJy	flag[2] 610	$S_{1.4}$b[3] mJy	flag[4] 1.4b	$S_{1.4}$N mJy	flag[2] NVSS	$\alpha^{15.7}_{0.61}$	$\alpha^{15.7}_{1.4}$	$\alpha^{15.7}_{1.4}$ NVSS
J104737+592028	10 47 37.88	+59 20 28.93	0.532	3.25	0	3.5	1	3.5	0	0.56	0.78	0.78
J104740+575336	10 47 40.43	+57 53 36.12	0.962	9.6	0	6.47	1	6.47	0	0.71	0.79	0.79
J104741+573606	10 47 41.50	+57 36 06.59	0.81	0.71	1	0.24	2	1.59	1	−0.04	−0.5	0.28
J104741+584811	10 47 41.93	+58 48 11.58	0.632	25.94	0	8.9	1	8.9	0	1.14	1.09	1.09
J104742+585318	10 47 42.02	+58 53 18.46	0.91	3.38	0	3.8	1	3.8	0	0.4	0.59	0.59
J104744+595419	10 47 44.07	+59 54 19.68	0.836	1.62	1	1.0	7	1.5	1	0.2	0.07	0.24
J104745+571024	10 47 45.90	+57 10 24.17	0.57	1.71	0	1.84	2	1.33	1	0.34	0.48	0.35
J104751+574259	10 47 51.77	+57 42 59.81	1.306	4.93	0	4.0	1	4.0	0	0.41	0.46	0.46
J104802+574117	10 48 02.65	+57 41 17.35	1.011	19.04	0	8.8	1	8.8	0	0.9	0.9	0.9
J104814+592927	10 48 14.05	+59 29 27.15	0.37	0.79	0	1.0	7	1.42	1	0.23	0.41	0.56
J104817+591207	10 48 17.57	+59 12 07.19	0.47	0.42	0	0.87	2	1.34	1	−0.03	0.25	0.43
J104819+594144	10 48 19.22	+59 41 44.65	2.538	29.92	0	13.3	1	13.3	0	0.76	0.69	0.69
J104822+582436	10 48 22.63	+58 24 36.56	2.536	36.86	0	18.5	1	18.5	0	0.82	0.82	0.82
J104823+595151	10 48 23.14	+59 51 51.65	2.166	31.98	0	17.9	1	17.9	0	0.83	0.87	0.87
J104824+583029	10 48 24.03	+58 30 29.27	2.918	9.47	0	7.7	1	7.7	0	0.36	0.4	0.4
J104825+564943	10 48 25.83	+56 49 43.86	0.501	0.75	1	1.26	2	1.27	1	0.12	0.38	0.38
J104826+584838	10 48 26.57	+58 48 38.15	0.567	1.02	1	0.62	2	1.44	1	0.18	0.04	0.39
J104829+582318	10 48 29.98	+58 23 18.76	0.863	3.55	0	6.7	1	6.7	0	0.44	0.85	0.85
J104831+592603	10 48 31.85	+59 26 03.43	0.483	3.28	0	2.8	1	2.8	0	0.59	0.73	0.73
J104831+595426	10 48 31.73	+59 54 26.93	0.813	2.62	0	3.8	1	3.8	0	0.36	0.64	0.64
J104836+591846	10 48 36.94	+59 18 46.90	0.566	2.15	0	2.6	1	2.6	0	0.41	0.63	0.63
J104837+594000	10 48 37.36	+59 40 00.83	1.877	8.28	0	8.5	1	8.5	0	0.46	0.62	0.62
J104839+581335	10 48 39.38	+58 13 35.86	0.99	30.37	0	13.2	1	13.2	0	1.05	1.07	1.07
J104841+572051	10 48 41.79	+57 20 51.76	0.841	9.53	0	8.3	1	8.3	0	0.75	0.95	0.95
J104841+594638	10 48 41.91	+59 46 38.07	4.97	150.15	0	63.0	1	63.0	0	1.05	1.05	1.05
J104843+565117	10 48 43.84	+56 51 17.63	0.52	8.47	0	6.3	1	6.3	0	0.86	1.03	1.03
J104844+582309	10 48 44.00	+58 23 09.09	2.869	24.09	0	10.2	1	10.2	0	0.66	0.52	0.52
J104849+571417	10 48 49.47	+57 14 17.48	1.818	19.82	0	10.2	1	10.2	0	0.74	0.71	0.71
J104849+593800	10 48 49.90	+59 38 00.63	0.975	0.87	1	1.0	7	1.61	1	−0.04	0.01	0.21
J104852+565115	10 48 52.90	+56 51 15.66	0.744	12.55	0	9.2	1	9.2	0	0.87	1.04	1.04
J104853+590610	10 48 53.39	+59 06 10.28	0.855	28.25	0	14.5	1	14.5	0	1.08	1.17	1.17
J104856+575528	10 48 56.04	+57 55 28.46	1.276	19.37	0	10.8	1	10.8	0	0.84	0.88	0.88
J104856+593916	10 48 56.69	+59 39 16.76	0.754	0.88	1	1.0	7	1.88	1	0.05	0.12	0.38
J104857+584103	10 48 57.96	+58 41 03.38	1.479	17.78	0	10.6	1	10.6	0	0.77	0.81	0.81
J104858+570933	10 48 58.99	+57 09 33.03	0.505	2.54	0	1.56	2	1.18	1	0.5	0.47	0.35
J104859+594036	10 48 59.47	+59 40 36.03	1.281	14.13	0	8.0	1	8.0	0	0.74	0.76	0.76
J104904+590829	10 49 04.31	+59 08 29.35	0.396	0.48	0	0.12	6	1.2	1	0.06	−0.49	0.46
J104906+571156	10 49 06.21	+57 11 56.35	1.859	17.62	0	13.9	1	13.9	0	0.69	0.83	0.83
J104908+571552	10 49 08.71	+57 15 52.27	0.516	0.73	1	0.14	2	1.18	1	0.11	−0.54	0.34
J104908+585243	10 49 08.41	+58 52 43.76	0.408	0.89	1	0.39	2	1.28	1	0.24	−0.02	0.47
J104918+582801	10 49 18.95	+58 28 01.49	6.642	25.11	0	24.4	1	24.4	0	0.41	0.54	0.54
J104919+585353	10 49 19.04	+58 53 53.67	0.472	0.95	1	0.83	2	1.36	1	0.22	0.23	0.44
J104922+572812	10 49 22.07	+57 28 12.24	0.58	0.67	1	0.62	2	1.3	1	0.04	0.03	0.33
J104922+592733	10 49 22.16	+59 27 33.89	0.792	13.21	0	6.9	1	6.9	0	0.87	0.9	0.9
J104922+595823	10 49 22.44	+59 58 23.08	4.393	6.86	0	5.7	1	5.7	0	0.14	0.11	0.11

continued on next page

continued from previous page

10C ID	RA	Dec	$S_{15.7}$[1] mJy	S_{610} mJy	flag[2] 610	$S_{1.4}$b[3] mJy	flag[4] 1.4b	$S_{1.4}$N mJy	flag[2] NVSS	$\alpha^{15.7}_{0.61}$	$\alpha^{15.7}_{1.4}$	$\alpha^{15.7}_{1.4}$ NVSS
J104927+583830	10 49 27.22	+58 38 30.47	0.746	3.02	1	1.32	6	1.35	1	0.43	0.24	0.25
J104930+590146	10 49 30.25	+59 01 46.23	2.715	35.88	0	23.6	1	23.6	0	0.79	0.89	0.89
J104934+570613	10 49 34.42	+57 06 13.69	2.086	24.83	0	13.6	1	13.6	0	0.76	0.78	0.78
J104936+570056	10 49 36.70	+57 00 56.69	0.642	0.71	1	0.28	2	1.2	1	0.03	−0.34	0.26
J104938+581422	10 49 38.01	+58 14 22.49	0.733	0.7	1	0.1	2	1.22	1	−0.01	−0.82	0.21
J104939+583530	10 49 39.97	+58 35 30.53	21.12	399.61	0	202.1	1	202.1	0	0.91	0.93	0.93
J104943+571739	10 49 43.82	+57 17 39.14	1.171	0.7	1	0.97	2	1.44	1	−0.16	−0.08	0.09
J104944+570635	10 49 44.12	+57 06 35.92	0.807	1.06	0	1.66	1	1.66	0	0.08	0.3	0.3
J104947+571355	10 49 47.49	+57 13 55.24	0.679	0.85	1	0.65	2	1.51	1	0.07	−0.02	0.33
J104950+570117	10 49 50.50	+57 01 17.79	0.66	6.37	0	5.3	1	5.3	0	0.7	0.86	0.86
J104950+585626	10 49 50.86	+58 56 26.47	0.456	0.88	1	1.46	2	1.48	1	0.2	0.48	0.49
J104952+594125	10 49 52.00	+59 41 25.70	3.883	1.37	0	9.3	1	9.3	0	−0.32	0.36	0.36
J104954+570456	10 49 54.30	+57 04 56.77	5.638	0.72	0	1.02	2	1.48	1	−0.63	−0.71	−0.55
J104954+594540	10 49 54.49	+59 45 40.90	0.791	2.19	0	2.23	5	1.49	1	0.31	0.43	0.26
J105000+585227	10 50 00.75	+58 52 27.97	0.571	0.53	0	0.23	2	1.45	1	−0.02	−0.38	0.39
J105001+591112	10 50 01.24	+59 11 12.30	3.314	41.05	0	21.7	1	21.7	0	0.77	0.78	0.78
J105003+573842	10 50 03.94	+57 38 42.76	0.37	0.48	0	0.27	2	1.46	1	0.08	−0.13	0.57
J105007+565336	10 50 07.11	+56 53 36.86	21.415	0.8	0	3.34	2	1.26	1	−1.01	−0.77	−1.17
J105007+572020	10 50 07.93	+57 20 20.28	1.18	1.7	0	2.33	2	1.32	1	0.11	0.28	0.05
J105007+574251	10 50 07.49	+57 42 51.87	0.716	0.78	0	1.28	2	1.5	1	0.03	0.24	0.31
J105009+570724	10 50 09.71	+57 07 24.56	1.05	6.74	0	5.3	1	5.3	0	0.57	0.67	0.67
J105013+594028	10 50 13.19	+59 40 28.41	1.331	6.94	0	5.2	1	5.2	0	0.51	0.56	0.56
J105015+570258	10 50 15.38	+57 02 58.44	0.51	4.57	0	3.3	1	3.3	0	0.68	0.77	0.77
J105016+574151	10 50 16.32	+57 41 51.52	0.413	0.61	1	0.16	2	1.43	1	0.12	−0.39	0.51
J105019+593402	10 50 19.75	+59 34 02.32	0.362	0.5	0	1.0	7	1.53	1	0.1	0.42	0.6
J105020+574048	10 50 20.57	+57 40 48.46	0.817	9.72	0	4.5	1	4.5	0	0.76	0.71	0.71
J105026+581515	10 50 26.82	+58 15 15.58	0.868	1.21	0	2.02	2	1.26	1	0.1	0.35	0.15
J105027+575252	10 50 27.17	+57 52 52.86	0.7	0.74	1	0.03	6	1.45	1	0.02	−1.3	0.3
J105028+574522	10 50 28.66	+57 45 22.55	0.533	0.63	1	0.27	2	1.34	1	0.05	−0.28	0.38
J105033+573527	10 50 33.47	+57 35 27.77	0.351	0.99	0	0.38	2	1.34	1	0.32	0.03	0.55
J105034+572922	10 50 34.05	+57 29 22.91	1.195	1.14	0	0.34	2	1.21	1	−0.01	−0.52	0.01
J105034+592443	10 50 34.37	+59 24 43.22	0.368	1.16	1	0.9	6	1.54	1	0.35	0.37	0.59
J105038+565810	10 50 38.75	+56 58 10.04	0.536	2.19	0	1.71	2	1.21	1	0.43	0.48	0.34
J105039+572339	10 50 39.56	+57 23 39.77	1.076	3.28	0	6.8	1	6.8	0	0.34	0.76	0.76
J105039+574200	10 50 39.16	+57 42 00.44	0.855	1.86	0	1.2	2	1.46	1	0.24	0.14	0.22
J105039+585118	10 50 39.28	+58 51 18.23	1.004	7.77	0	6.1	1	6.1	0	0.63	0.75	0.75
J105040+573308	10 50 40.65	+57 33 08.68	0.89	1.49	1	0.9	2	1.22	1	0.16	0.0	0.13
J105042+575233	10 50 42.82	+57 52 33.86	3.507	84.65	0	39.1	1	39.1	0	0.98	1.0	1.0
J105046+595803	10 50 46.49	+59 58 03.85	4.393			35.5	1	35.5	0		0.86	0.86
J105050+580200	10 50 50.68	+58 02 00.13	5.672	2.5	0	3.7	1	3.7	0	−0.25	−0.18	−0.18
J105053+583233	10 50 53.98	+58 32 33.17	22.945	289.89	0	154.5	1	154.5	0	0.78	0.79	0.79
J105054+580943	10 50 54.28	+58 09 43.21	1.447	1.35	0	2.4	1	2.4	0	−0.02	0.21	0.21
J105058+573356	10 50 58.64	+57 33 56.08	0.963	0.53	0	0.2	2	1.41	1	−0.18	−0.65	0.16
J105104+570148	10 51 04.45	+57 01 48.35	0.543	4.31	0	4.1	1	4.1	0	0.64	0.84	0.84
J105104+574456	10 51 04.28	+57 44 56.85	1.174	0.84	1	0.21	2	1.33	1	−0.1	−0.71	0.05

continued on next page

continued from previous page

10C ID	RA	Dec	$S^{1}_{15.7}$ mJy	S_{610} mJy	flag[2] 610	$S_{1.4}$b[3] mJy	flag[4] 1.4b	$S_{1.4}$N mJy	flag[2] NVSS	$\alpha^{15.7}_{0.61}$	$\alpha^{15.7}_{1.4}$	$\alpha^{15.7}_{1.4}$ NVSS
J105104+575415	10 51 04.57	+57 54 15.91	8.144	29.39	0	18.4	1	18.4	0	0.4	0.34	0.34
J105107+575752	10 51 07.09	+57 57 52.21	2.887	23.4	0	13.4	1	13.4	0	0.64	0.64	0.64
J105111+580934	10 51 11.29	+58 09 34.09	0.937	7.83	0	5.3	1	5.3	0	0.65	0.72	0.72
J105115+573552	10 51 15.54	+57 35 52.32	0.53	5.48	0	2.56	1	2.56	0	0.72	0.65	0.65
J105116+583441	10 51 16.16	+58 34 41.73	0.733	1.48	1	0.04	6	1.36	1	0.22	−1.2	0.26
J105121+582648	10 51 21.36	+58 26 48.31	3.428	107.88	0	44.8	1	44.8	0	1.06	1.06	1.06
J105122+570854	10 51 22.18	+57 08 54.76	1.256	19.13	0	10.4	1	10.4	0	0.84	0.87	0.87
J105122+584136	10 51 22.64	+58 41 36.44	1.449	7.63	0	4.7	1	4.7	0	0.51	0.49	0.49
J105122+584409	10 51 22.74	+58 44 09.16	1.385	1.14	1	3.12	2	1.28	1	−0.06	0.34	−0.03
J105123+573229	10 51 23.11	+57 32 29.40	0.378	1.83	0	2.5	1	2.5	0	0.49	0.78	0.78
J105124+595339	10 51 24.65	+59 53 39.00	0.779			2.36	5	1.84	1		0.46	0.36
J105128+570901	10 51 28.10	+57 09 01.68	2.251	19.64	0	12.3	1	12.3	0	0.67	0.7	0.7
J105129+564802	10 51 29.96	+56 48 02.43	2.036	7.83	0	5.9	1	5.9	0	0.41	0.44	0.44
J105130+584946	10 51 30.87	+58 49 46.46	0.78	17.37	0	14.6	1	14.6	0	0.96	1.21	1.21
J105131+594718	10 51 31.44	+59 47 18.19	1.961	24.55	0	10.7	1	10.7	0	0.78	0.7	0.7
J105132+571114	10 51 32.63	+57 11 14.59	2.922	8.81	0	12.5	1	12.5	0	0.34	0.6	0.6
J105133+570602	10 51 33.98	+57 06 02.13	0.729	0.91	1	0.13	4	1.59	1	0.07	−0.71	0.32
J105135+581106	10 51 35.18	+58 11 06.88	1.04	10.95	0	8.3	1	8.3	0	0.72	0.86	0.86
J105135+593605	10 51 35.92	+59 36 05.50	0.997	1.48	1	1.0	7	1.61	1	0.12	0.0	0.2
J105136+572944	10 51 36.99	+57 29 44.40	1.117	4.23	0	2.8	1	2.8	0	0.41	0.38	0.38
J105136+595445	10 51 36.96	+59 54 45.94	6.052			117.8	1	117.8	0		1.23	1.23
J105138+574957	10 51 38.15	+57 49 57.66	0.671	2.66	0	2.54	2	1.34	1	0.42	0.55	0.29
J105139+580757	10 51 39.42	+58 07 57.17	2.493	60.5	0	33.7	1	33.7	0	0.98	1.08	1.08
J105139+592444	10 51 39.05	+59 24 44.17	1.595	25.83	0	16.4	1	16.4	0	0.86	0.96	0.96
J105141+591307	10 51 41.44	+59 13 07.56	27.107	429.94	0	221.5	1	221.5	0	0.85	0.87	0.87
J105142+573447	10 51 42.02	+57 34 47.81	0.786	0.69	1	0.82	2	1.44	1	−0.04	0.02	0.25
J105142+573557	10 51 42.07	+57 35 57.97	1.952	8.35	0	4.8	1	4.8	0	0.45	0.37	0.37
J105144+573313	10 51 44.28	+57 33 13.27	0.979	25.59	0	12.6	1	12.6	0	1.0	1.06	1.06
J105145+595139	10 51 45.76	+59 51 39.63	0.852	2.38	0	1.0	7	1.59	1	0.32	0.07	0.26
J105146+564731	10 51 46.14	+56 47 31.33	1.018	7.63	0	5.1	1	5.1	0	0.62	0.67	0.67
J105148+573245	10 51 48.76	+57 32 45.04	0.523	0.67	1	0.94	2	1.38	1	0.08	0.24	0.4
J105149+581638	10 51 49.68	+58 16 38.08	0.765	1.4	0	0.03	6	1.13	1	0.19	−1.34	0.16
J105150+572637	10 51 50.02	+57 26 37.10	0.304	0.75	1	0.38	2	1.35	1	0.28	0.09	0.62
J105151+595008	10 51 51.32	+59 50 08.96	3.247	63.73	0	37.5	1	37.5	0	0.92	1.01	1.01
J105152+570950	10 51 52.33	+57 09 50.63	0.372	5.17	0	2.9	1	2.9	0	0.81	0.85	0.85
J105152+595106	10 51 52.01	+59 51 06.84	1.116	1.05	1	2.32	5	1.66	1	−0.02	0.3	0.16
J105154+593548	10 51 54.10	+59 35 48.04	1.013	34.77	0	13.5	1	13.5	0	1.09	1.07	1.07
J105155+565554	10 51 55.23	+56 55 54.89	0.981	0.72	1	0.33	2	1.3	1	−0.1	−0.45	0.12
J105159+593241	10 51 59.39	+59 32 41.35	4.367	312.06	0	138.2	1	138.2	0	1.31	1.43	1.43
J105206+574111	10 52 06.40	+57 41 11.78	3.35	15.16	0	11.3	1	11.3	0	0.46	0.5	0.5
J105213+594822	10 52 13.47	+59 48 22.65	0.702	3.01	1	1.0	7	1.67	1	0.45	0.15	0.36
J105215+581627	10 52 15.81	+58 16 27.31	1.127	8.61	0	3.2	1	3.2	0	0.63	0.43	0.43
J105216+575826	10 52 16.45	+57 58 26.58	0.728	1.04	1	0.22	2	1.48	1	0.11	−0.5	0.29
J105218+594554	10 52 18.90	+59 45 54.13	0.675	2.23	1	1.35	5	1.7	1	0.37	0.29	0.38
J105220+585051	10 52 20.56	+58 50 51.67	2.027	20.21	0	14.0	1	14.0	0	0.71	0.8	0.8

continued on next page

continued from previous page

10C ID	RA	Dec	$S^1_{15.7}$ mJy	S_{610} mJy	flag[2] 610	$S_{1.4}$b[3] mJy	flag[4] 1.4b	$S_{1.4}$N mJy	flag[2] NVSS	$\alpha^{15.7}_{0.61}$	$\alpha^{15.7}_{1.4}$	$\alpha^{15.7}_{1.4}$ NVSS
J105224+570837	10 52 24.96	+57 08 37.66	0.423	2.36	0	4.2	1	4.2	0	0.53	0.95	0.95
J105225+573323	10 52 25.84	+57 33 23.31	0.585	9.26	0	5.2	1	5.2	0	0.85	0.9	0.9
J105225+575507	10 52 25.43	+57 55 07.62	22.451	12.28	0	29.5	1	29.5	0	−0.19	0.11	0.11
J105230+593112	10 52 30.65	+59 31 12.40	0.722	2.21	0	1.0	7	1.86	1	0.34	0.13	0.39
J105231+565434	10 52 31.72	+56 54 34.33	0.776	10.03	0	8.1	1	8.1	0	0.79	0.97	0.97
J105233+571759	10 52 33.50	+57 17 59.34	0.368	0.79	1	0.11	2	1.39	1	0.24	−0.5	0.55
J105235+575827	10 52 35.70	+57 58 27.07	0.816	1.16	1	0.03	6	1.39	1	0.11	−1.37	0.22
J105237+573058	10 52 37.01	+57 30 58.85	5.16	160.64	0	65.0	1	65.0	0	1.06	1.05	1.05
J105240+572322	10 52 40.87	+57 23 22.96	0.539	2.1	0	1.8	1	1.8	0	0.42	0.5	0.5
J105243+574817	10 52 43.34	+57 48 17.11	0.998	0.96	0	1.86	2	1.2	1	−0.01	0.26	0.08
J105248+595634	10 52 48.61	+59 56 34.44	1.433			8.4	1	8.4	0		0.73	0.73
J105253+572348	10 52 53.86	+57 23 48.65	0.472	0.67	1	0.2	2	1.4	1	0.11	−0.36	0.45
J105254+592218	10 52 54.52	+59 22 18.39	36.435	761.45	0	337.5	1	337.5	0	0.94	0.92	0.92
J105255+571949	10 52 55.07	+57 19 49.35	0.391	4.42	0	3.5	1	3.5	0	0.75	0.91	0.91
J105327+574546	10 53 27.36	+57 45 46.09	0.809	8.8	0	7.0	1	7.0	0	0.73	0.89	0.89
J105337+574242	10 53 37.29	+57 42 42.26	0.383	0.89	0	2.08	2	1.68	1	0.26	0.7	0.61
J105341+571951	10 53 41.01	+57 19 51.29	0.553	2.54	0	1.54	2	1.27	1	0.47	0.42	0.34
J105342+574438	10 53 42.19	+57 44 38.11	1.8	9.11	0	7.5	1	7.5	0	0.5	0.59	0.59
J105345+565400	10 53 45.76	+56 54 00.83	1.183	0.95	1	0.07	6	1.37	1	−0.07	−1.17	0.06
J105353+565949	10 53 53.21	+56 59 49.59	0.724	2.3	0	1.6	2	1.16	1	0.36	0.33	0.2
J105400+573324	10 54 00.97	+57 33 24.63	0.674	4.08	0	3.0	1	3.0	0	0.55	0.62	0.62
J105420+580101	10 54 20.55	+58 01 01.71	0.925	23.14	0	10.4	1	10.4	0	0.99	1.0	1.0
J105425+573700	10 54 25.05	+57 37 00.78	25.473	328.98	0	191.4	1	191.4	0	0.79	0.83	0.83
J105437+565922	10 54 37.19	+56 59 22.76	2.198	0.95	1	23.6	1	23.6	0	−0.26	0.98	0.98
J105441+571640	10 54 41.45	+57 16 40.84	0.777	6.9	0	3.6	1	3.6	0	0.67	0.63	0.63
J105510+574503	10 55 10.35	+57 45 03.49	0.729	1.05	1	1.05	2	1.22	1	0.11	0.15	0.21
J105515+573256	10 55 15.50	+57 32 56.87	0.628	11.39	0	6.1	1	6.1	0	0.89	0.94	0.94
J105517+565003	10 55 17.19	+56 50 03.22	0.634	6.61	0	29.3	1	29.3	0	0.72	1.59	1.59
J105520+572237	10 55 20.58	+57 22 37.32	0.555	0.95	0	0.96	2	1.14	1	0.17	0.23	0.3
J105523+565017	10 55 23.09	+56 50 17.37	1.605	36.37	0	28.9	1	28.9	0	0.96	1.2	1.2
J105527+571607	10 55 27.42	+57 16 07.93	0.83	3.83	0	3.2	1	3.2	0	0.47	0.56	0.56
J105535+574636	10 55 35.51	+57 46 36.74	2.684	2.67	0	2.49	2	1.33	1	0.0	−0.03	−0.29
J105543+574823	10 55 43.46	+57 48 23.10	0.449	2.65	0	2.5	1	2.5	0	0.55	0.71	0.71
J105548+564804	10 55 48.81	+56 48 04.08	2.641	17.72	0	12.8	1	12.8	0	0.59	0.65	0.65
J105548+571828	10 55 48.43	+57 18 28.36	0.81	32.65	0	14.6	1	14.6	0	1.14	1.2	1.2
J105550+570407	10 55 50.85	+57 04 07.56	1.187	1.05	1	0.53	2	1.28	1	−0.04	−0.33	0.03
J105555+574828	10 55 55.40	+57 48 28.07	0.738	0.88	0	0.8	2	1.23	1	0.05	0.03	0.21
J105558+565318	10 55 58.95	+56 53 18.75	3.987	57.92	0	40.9	1	40.9	0	0.82	0.96	0.96
J105604+570934	10 56 04.71	+57 09 34.34	5.466	86.22	0	51.7	1	51.7	0	0.85	0.93	0.93
J105614+565238	10 56 14.46	+56 52 38.50	0.816	1.88	1	0.22	6	1.31	1	0.26	−0.54	0.2
J105614+570520	10 56 14.77	+57 05 20.28	0.698	1.05	1	0.49	2	1.2	1	0.13	−0.15	0.22
J105627+574221	10 56 27.90	+57 42 21.78	1.091	1.52	1	0.96	2	1.45	1	0.1	−0.05	0.12
J105641+565753	10 56 41.16	+56 57 53.45	0.668	1.54	1	1.15	2	1.3	1	0.26	0.22	0.28
J105649+565218	10 56 49.77	+56 52 18.84	0.881	8.21	0	7.8	1	7.8	0	0.69	0.9	0.9
J105653+580342	10 56 53.47	+58 03 42.43	1.951	0.54	0	0.7	2	1.17	1	−0.4	−0.42	−0.21

continued on next page

continued from previous page

10C ID	RA	Dec	$S^{1}_{15.7}$ mJy	S_{610} mJy	flag[2] 610	$S_{1.4}$b[3] mJy	flag[4] 1.4b	$S_{1.4}$N mJy	flag[2] NVSS	$\alpha^{15.7}_{0.61}$	$\alpha^{15.7}_{1.4}$	$\alpha^{15.7}_{1.4}$ NVSS
J105655+572116	10 56 55.72	+57 21 16.74	0.802	1.83	1	0.04	6	1.44	1	0.25	−1.24	0.24
J105716+572314	10 57 16.62	+57 23 14.17	6.416	270.82	0	132.3	1	132.3	0	1.15	1.25	1.25
J105731+575949	10 57 31.47	+57 59 49.16	2.0	8.93	0	8.7	1	8.7	0	0.46	0.61	0.61
J105731+580658	10 57 31.22	+58 06 58.42	2.601	7.87	0	5.5	1	5.5	0	0.34	0.31	0.31
J105739+564958	10 57 39.60	+56 49 58.61	3.456			15.5	1	15.5	0		0.62	0.62
J105747+580848	10 57 47.01	+58 08 48.69	11.982	160.64	0	132.6	1	132.6	0	0.8	0.99	0.99

notes:
1) Peak flux density for sources listed as point sources in the 10C catalogue, integrated flux density for sources listed as extended in the 10C catalogue.
2) 0 = value is a detection, 1 = upper limit.
3) 1.4 GHz values are included in the following order of preference: NVSS, FIRST, WSRT, OM2008, BI2006, upper limit from WRST data the upper limit from FIRST. The value used is indicated by the value of flag 1.4b.
4) Origin of $S_{1.4}$b value: 1 = NVSS, 2 = WSRT, 3 = OM2008, 4 = BI 2006, 5 = FIRST, 6 = limit from WSRT, 7 = limit from FIRST.

A.2 Multi-wavelength properties

Table A.2: Multi-wavelength properties of sources in the Lockman Hole 10C sample. All magnitudes are AB magnitude.

10C ID	g	i	r	z	J	K	SERVS1 μJy	SERVS2 μJy	SWIRE1 μJy	SWIRE2 μJy	SWIRE3 μJy	SWIRE4 μJy	flag^a
10CJ103857+592546													5
10CJ103859+590548	21.94	19.92	20.64			18.00	302.19	218.07	230.99	178.18	132.04	79.54	1
10CJ103912+591428													5
10CJ103913+581445													5
10CJ103920+592235													5
10CJ103922+582912			19.04				512.17	398.62	367.4	309.6	236.62	545.92	1
10CJ103923+593805													5
10CJ103940+592132													5
10CJ103952+583215													4
10CJ103954+581524													7
10CJ103959+582354								26.96	21.57	25.67			6
10CJ103959+584812	22.99	23.19	23.05				25.25	28.06	22.48	27.5			6
10CJ104004+582857													3
10CJ104005+592513													5
10CJ104008+584646													9
10CJ104016+594327													5
10CJ104019+584053													9
10CJ104023+594205													5
10CJ104032+594238													5
10CJ104033+595446													5
10CJ104043+593410													5
10CJ104043+594012													5
10CJ104046+581222													9
10CJ104103+590414			20.66				625.36	546.60	459.45	435.6	352.15	296.33	6
10CJ104110+592850													5
10CJ104114+592934													5
10CJ104117+591808						18.82	194.82	120.78	153.2	96.45	85.39	63.4	6
10CJ104121+585333	17.56	17.62	17.65			17.21	908.70	612.41	688.87	486.35	818.86	4730.12	6
10CJ104124+593356													5
10CJ104127+592635													5
10CJ104133+590956			21.54			19.88	45.07	51.95	45.42	52.41	58.51	140.84	2
10CJ104142+583751													3
10CJ104143+585650							4.05	2.63					2
10CJ104144+594256													5
10CJ104147+583031							18.92	24.17	20.18	30.34	38.43	46.9	1
10CJ104147+592448													9
10CJ104200+592742													5
10CJ104202+581232													9
10CJ104202+592633													9
10CJ104206+585820		22.04	23.09			19.63	80.51	50.52	69.84	45.08	37.39	29.79	2
10CJ104213+592121						20.40	50.98	42.35	41.29	36.2			6
10CJ104214+585113							22.21	22.79	19.63	22.64			2
10CJ104217+585810	21.23	19.38	19.81			17.57	317.91	250.60	251.48	207.71	123.34	77.82	1
10CJ104221+583317							39.03	44.12	34.01	41.8	16.7		6
10CJ104223+581156			22.56				15.94	10.72	16.4	7.05			1
10CJ104226+584251													9

continued on next page

continued from previous page

10C ID	*g*	*i*	*r*	*z*	*J*	*K*	SERVS1	SERVS2	SWIRE1	SWIRE2	SWIRE3	SWIRE4	flag[a]
							µJy	µJy	µJy	µJy	µJy	µJy	
10CJ104226+592656													4
10CJ104234+594703													5
10CJ104236+591956						19.36	115.37	81.77	104.54	73.64	48.82		1
10CJ104236+593956													5
10CJ104240+593804													5
10CJ104242+593048	23.17	22.62	22.81			19.83	60.36		141.2	137.38	135.64	190.78	2
10CJ104247+593222													9
10CJ104250+595303													5
10CJ104251+590547													9
10CJ104311+590740						19.82	87.16	64.91	73.05	61.14			2
10CJ104319+592708	21.62	22.09	21.96			21.01	22.23		22.27	27.06	33.31		6
10CJ104320+585621	21.17	19.62	20.01			17.94	207.74	168.12	175.33	152.47	118.58	96.27	2
10CJ104321+583441							23.34	27.23	18.36	24.94			6
10CJ104328+590312			19.40			17.42	303.22	232.28	264.97	206.65	115.63	94.74	6
10CJ104329+595021													5
10CJ104332+582706							141.89	99.13	123.97	90.07	58.88	37.5	1
10CJ104336+592618	23.76						26.92		23.18	43.77	102.15	247.49	1
10CJ104344+591503							164.69	188.75	140.07	170.76	154.28	79.02	6
10CJ104352+581324		19.44	19.89				298.79	232.52	252.32	204.55	154.67	87.59	1
10CJ104354+595320													5
10CJ104357+583609													9
10CJ104422+594706													5
10CJ104428+591540					21.69	20.22	69.74	60.02	64.62	61.74	55.49	34.17	8
10CJ104428+593255													9
10CJ104436+585306							2.30	1.92					6
10CJ104441+591949					20.89	19.79	111.46	103.01	100.31	97.79	65.54	56.97	8
10CJ104451+591929					20.41	19.50	98.60	67.75	91.08	66.04	34.65		1
10CJ104456+592537													3
10CJ104456+593802													5
10CJ104501+593559													5
10CJ104507+585353			22.83		20.37	19.57	78.12	49.17	70.84	48.95	44.92		8
10CJ104510+591437					22.21	21.45	16.50	16.61	15.63	16.5	15.17		6
10CJ104525+595343													5
10CJ104528+591328					21.77	21.06	34.37	45.52	31.73	44.83	86.0	200.26	6
10CJ104539+585730			20.25		18.54	17.90	192.83	152.48	168.3	140.06	96.94	65.49	1
10CJ104551+590838			24.03			22.77	5.53	4.77	3.83				6
10CJ104551+592056					21.49	20.82	35.90	24.10	32.6	23.49		21.72	2
10CJ104552+594327							94.26		78.55	87.27	65.38	52.31	1
10CJ104559+590326						22.43		7.79					6
10CJ104608+594018					20.67	20.00	58.38		54.46	35.92			1
10CJ104624+590447							2.93	2.89	3.37				1
10CJ104630+582748		17.41	17.57			16.10	1355.66	902.51	1072.43	742.61	477.94	374.37	1
10CJ104633+585816			21.58		20.00	19.44	160.06	119.52	134.25	99.1	110.45	88.94	6
10CJ104639+582005													9
10CJ104641+590835			20.84		18.96	18.27	239.91	151.16	217.42	145.31	136.21	82.73	8
10CJ104646+594612		23.45					126.91						2
10CJ104648+590956						21.59	36.78	41.80	28.45	35.53	48.72	36.16	8
10CJ104651+583630		21.78	22.72			19.55	115.60	70.49	83.37	57.01			6
10CJ104656+594639	23.78	21.26	22.28				96.35	60.52	84.47	54.2	35.03		2
10CJ104700+591903													4
10CJ104710+582821		20.51	21.29			18.33	357.52	378.50	351.19	396.96	536.34	711.65	1
10CJ104712+593934					19.83	19.04	131.24	89.74	116.03	75.93	80.48		6
10CJ104713+592912					22.13	21.61	15.14	17.46	15.71	19.1			2

continued on next page

continued from previous page

10C ID	*g*	*i*	*r*	*z*	*J*	*K*	SERVS1 μJy	SERVS2 μJy	SWIRE1 μJy	SWIRE2 μJy	SWIRE3 μJy	SWIRE4 μJy	flag[a]
10CJ104714+583034													7
10CJ104715+594617													9
10CJ104718+585119			22.86		20.75	20.12	42.82	29.45	35.68	28.47	32.65		2
10CJ104718+593247													3
10CJ104719+582114		18.84	18.42			18.40	325.51	443.00	319.68	434.31	620.55	973.67	6
10CJ104720+570804	22.89	20.73	21.89				262.40	164.19	214.5	150.09	136.95	110.99	2
10CJ104723+570051	19.91	18.72	19.12				741.22	663.82	540.6	494.24	383.8	810.03	2
10CJ104724+573703	21.20	21.34	21.34				44.68	51.32	46.66	53.01	61.1	100.26	2
10CJ104733+591244						21.87	10.41	14.53	11.44	14.26			6
10CJ104734+570651	20.62	19.40	19.77				283.54	247.72	246.79	227.71	172.82	395.68	2
10CJ104736+583336		22.96				21.11	26.05	24.52	23.13	21.72			6
10CJ104737+592028					20.62	19.53	131.04	90.74	114.0	78.66	68.31		6
10CJ104740+575336		23.40					58.26	41.25	50.7	37.88			2
10CJ104741+573606													3
10CJ104741+584811													3
10CJ104742+585318		20.71	21.69		19.34	18.58	189.76	120.75	166.58	107.98	105.92	42.34	2
10CJ104744+595419													5
10CJ104745+571024							48.99	42.49	44.69	38.01			1
10CJ104751+574259	23.47		23.28				30.24	36.07	28.25	35.97			6
10CJ104802+574117	22.59	22.01	22.70				77.07	69.56	71.2	66.97			6
10CJ104814+592927			21.22		19.17	18.50	188.36	121.45	160.5	107.5	83.14		1
10CJ104817+591207	23.24	20.85	21.77	20.47	19.52	18.76	169.95	109.28	141.47	95.69	85.43	43.55	6
10CJ104819+594144			21.68				120.32	78.06	96.58	66.25	50.09		1
10CJ104822+582436		22.75	23.20			19.90	77.20	70.49	69.69	68.42	43.27		6
10CJ104823+595151													5
10CJ104824+583029		21.07	22.12			18.57	237.95	152.17	206.9	134.95	108.09	71.81	1
10CJ104825+564943	22.26	19.94	20.91				259.50	178.32	213.67	159.02	133.29	73.67	1
10CJ104826+584838		23.31				21.40	20.56	15.49	17.0	12.5	26.87		2
10CJ104829+582318		21.68	22.73			19.25	111.45	68.82	97.26	63.13	58.89	29.0	6
10CJ104831+592603			21.40		19.03	18.35	212.89	137.75	175.37	118.85	99.84	56.09	2
10CJ104831+595426													5
10CJ104836+591846	20.81	21.35	21.87	21.38	20.80	20.65	39.23	48.12	35.25	43.57	56.75	57.49	6
10CJ104837+594000					19.17	18.44	219.29	143.05	183.05	134.02	119.83	76.87	2
10CJ104839+581335													3
10CJ104841+572051	23.44	20.95	22.11				189.89	112.73	160.0	99.77	76.5		1
10CJ104841+594638							46.25		39.02	44.71		36.79	2
10CJ104843+565117													4
10CJ104844+582309		21.12	22.26			18.62	274.28	170.77	219.63	149.27	115.99	83.84	1
10CJ104849+571417	23.45	20.94	22.04				160.51	101.35	140.16	91.36	66.5		1
10CJ104849+593800					22.11	21.23	46.16	51.93	39.97	44.62			6
10CJ104852+565115													4
10CJ104853+590610							5.99	8.53	4.79				6
10CJ104856+575528							44.12	44.85	38.34	40.39			2
10CJ104856+593916													9
10CJ104857+584103		22.87				20.20	58.20	37.14	46.2	27.28			6
10CJ104858+570933	23.96	21.84	22.87				107.76	67.62	99.06	63.13	66.43		1
10CJ104859+594036					21.03	20.16	77.55		70.02	80.93	61.77		1
10CJ104904+590829													9
10CJ104906+571156													3
10CJ104908+571552													3
10CJ104908+585243		22.02	22.93		20.23	19.44	101.59	69.99	96.92	65.82	56.9		2
10CJ104918+582801		20.10	20.05			19.00	124.20	142.39	117.07	138.94	210.61	270.57	1
10CJ104919+585353		18.44	18.65		17.50	17.04	450.30	378.13	399.76	360.13	286.13	1142.1	6

continued on next page

continued from previous page

10C ID	g	i	r	z	J	K	SERVS1 µJy	SERVS2 µJy	SWIRE1 µJy	SWIRE2 µJy	SWIRE3 µJy	SWIRE4 µJy	flag[a]
10CJ104922+572812							61.91	53.18	55.43	48.66	42.7	37.24	2
10CJ104922+592733						22.43	15.90	18.04	12.64	14.33			6
10CJ104922+595823													5
10CJ104927+583830													9
10CJ104930+590146	18.02	18.04	17.91		17.73	18.31	82.69	48.51	79.98	50.69			1
10CJ104934+570613			23.87				90.90	68.82	83.47	65.03			2
10CJ104936+570056	24.14	22.57	23.53				146.26	125.25	128.02	112.24	54.71		1
10CJ104938+581422						21.13	27.39	26.68	24.6	25.61		78.96	2
10CJ104939+583530		21.66	22.23			19.60	90.74	93.88	62.57	71.52	72.21	87.13	6
10CJ104943+571739	22.35	20.70	21.48				198.68	129.64	165.34	114.95	106.26	91.62	1
10CJ104944+570635	22.08	20.17	20.77				138.61	106.40	124.54	99.56	77.53		6
10CJ104947+571355			23.83					27.50		31.8			2
10CJ104950+570117													3
10CJ104950+585626					21.37	20.18	76.83	75.13	69.61	69.88	59.44		6
10CJ104952+594125							18.12			20.99		64.16	6
10CJ104954+570456	20.96	20.33	21.06				287.70	348.87	285.32	349.98	477.46	611.71	6
10CJ104954+594540													5
10CJ105000+585227					21.76	20.54	47.27	45.15	43.79	40.31			6
10CJ105001+591112	19.25	19.39	19.35	19.30	18.91	18.69	195.94	337.14	196.32	337.51	690.66	1197.85	6
10CJ105003+573842	19.72	18.57	18.94				386.59	290.75	321.03	236.67	140.01	140.45	1
10CJ105007+565336	20.74	20.89	20.82				64.54	84.34	57.33	68.37	96.51	123.28	6
10CJ105007+572020	23.53	22.64	23.35				82.95	75.08	66.15	64.82			2
10CJ105007+574251	23.83	21.65	22.57					60.81	93.42	62.16	67.62		6
10CJ105009+570724													3
10CJ105013+594028	21.49	19.46	20.12		18.29	17.62	357.21			226.88		108.25	1
10CJ105015+570258	20.57	20.53	20.38				51.49	55.89	46.75	59.21	100.2	140.44	1
10CJ105016+574151		21.65	22.94				67.15	40.50	60.41	37.92	33.13	43.95	2
10CJ105019+593402					21.30	20.22	72.87		65.25	71.26	60.14	63.6	6
10CJ105020+574048		21.20	22.49				125.74	76.71	106.66	67.01	56.93	38.51	1
10CJ105026+581515		20.18	20.88			18.33	227.83	159.58	182.58	137.79	102.28	60.22	1
10CJ105027+575252													9
10CJ105028+574522	18.16	17.28	17.64				1088.85	712.67	905.85	605.93	472.13	387.6	2
10CJ105033+573527							33.60	32.68	29.98	33.44			2
10CJ105034+572922							48.97	49.10	44.9	44.97			2
10CJ105034+592443													9
10CJ105038+565810	21.64	19.79	20.40				189.95	142.83	164.93	129.56	101.17	54.59	2
10CJ105039+572339	19.19	19.35	19.48				125.72	189.30	124.32	183.84	251.84	364.94	2
10CJ105039+574200		21.96	22.77				55.42	34.92	46.17	30.86	33.1		6
10CJ105039+585118			20.19		18.59	17.97	273.96	215.72	205.5	174.39	103.99		2
10CJ105040+573308													4
10CJ105042+575233							55.44	44.15	48.29	40.4			1
10CJ105046+595803													5
10CJ105050+580200	23.28	21.09	22.12			18.90	147.43	113.71	152.26	127.77	146.55	176.16	1
10CJ105053+583233						21.67	18.46	21.91	16.99	19.75	28.79	54.56	2
10CJ105054+580943													4
10CJ105058+573356													7
10CJ105104+570148													4
10CJ105104+574456													3
10CJ105104+575415	21.42	21.01	21.28		20.18	19.99	92.29	139.91	93.06	142.93	201.17	295.42	2
10CJ105107+575752	23.40	20.80	22.07		19.43	18.62	205.92	125.70	178.24	108.21	82.13	42.54	2
10CJ105111+580934					20.78	19.74	130.27	127.17	109.98	112.37	93.36		1
10CJ105115+573552													7
10CJ105116+583441													9

continued on next page

continued from previous page

10C ID	g	i	r	z	J	K	SERVS1 μJy	SERVS2 μJy	SWIRE1 μJy	SWIRE2 μJy	SWIRE3 μJy	SWIRE4 μJy	flag[a]
10CJ105121+582648					21.55	20.47	70.98	81.04	59.12	69.24	52.42		2
10CJ105122+570854						22.96	5.07	8.54	4.14	10.25			6
10CJ105122+584136					22.08	21.08	31.53	28.64	24.34	21.85			6
10CJ105122+584409			23.67		22.09	21.33	26.21	33.52	23.85	31.51	46.68	61.91	6
10CJ105123+573229					21.48	20.38	59.36	51.43	51.31	47.41			6
10CJ105124+595339													5
10CJ105128+570901	22.25	20.02	20.94		18.82	18.14	307.34	204.97	247.26	172.61	134.61	77.27	1
10CJ105129+564802		22.28					111.01	78.49	102.75	73.93	54.38		6
10CJ105130+584946							5.52	5.03					6
10CJ105131+594718													5
10CJ105132+571114	20.68	18.96	19.46		17.89	17.32	383.11	297.39	322.12	256.47	158.6	98.2	2
10CJ105133+570602	23.22	20.92	22.00				150.62	94.76	124.86	78.78	63.38		8
10CJ105135+581106		22.75	23.92		20.65	19.72	97.81	71.73	84.55	61.53	46.66		2
10CJ105135+593605													5
10CJ105136+572944					21.21	20.13	109.31	108.41	92.49	100.3	83.38	70.92	1
10CJ105136+595445													5
10CJ105138+574957							5.60	9.61	4.11	9.2			1
10CJ105139+580757													3
10CJ105139+592444		23.31				20.38	61.05		56.7	68.14	90.7	69.99	2
10CJ105141+591307													5
10CJ105142+573447	23.50	21.30	22.24		19.83	19.06	133.90	79.67	114.69	69.03	45.1		2
10CJ105142+573557					22.48	21.19	31.68	36.43	28.08	32.17			2
10CJ105144+573313													4
10CJ105145+595139													5
10CJ105146+564731	23.66	21.13	22.28				149.01	85.09	122.02	72.89			6
10CJ105148+573245	23.84	22.55	23.21		20.84	19.96	109.27	145.91	99.44	146.91	212.26	344.21	2
10CJ105149+581638													9
10CJ105150+572637					21.33	20.30	65.79	68.41	58.17	63.42	45.36		2
10CJ105151+595008													5
10CJ105152+570950	23.40	22.69	23.07		20.87	19.97	85.00	82.65	79.55	76.13	62.29	79.55	6
10CJ105152+595106													5
10CJ105154+593548													5
10CJ105155+565554	23.50	21.53	22.55				109.30	67.46	95.63	66.24	38.95	43.12	2
10CJ105159+593241													5
10CJ105206+574111					21.78	20.90	39.35	42.88	33.4	35.74		31.8	6
10CJ105213+594822													5
10CJ105215+581627		22.57	23.36		20.74	19.91	66.99	44.09	56.39	35.09			6
10CJ105216+575826	21.68	20.43	20.73		19.13	18.29	163.54	166.16	151.37	158.73	143.98	399.99	2
10CJ105218+594554													5
10CJ105220+585051					21.36	20.44	67.33	58.80	50.97	48.14			1
10CJ105224+570837	21.42	19.65	20.08	19.40	18.42	17.81	217.37	173.30	186.68	153.28	85.8		2
10CJ105225+573323	22.87	20.58	21.59	20.10	19.22	18.51	214.07	133.80	179.69	115.75	88.42	51.99	1
10CJ105225+575507					21.74	20.93	32.02	37.17	30.11	35.91		53.81	6
10CJ105230+593112													5
10CJ105231+565434	23.62		22.16				167.87	101.16	140.75	88.4	78.35		1
10CJ105233+571759		21.91	23.12	21.50	20.46	19.54	77.36	49.40	72.47	47.17	32.24		1
10CJ105235+575827													9
10CJ105237+573058													3
10CJ105240+572322		22.56	23.58	21.68	20.58	19.76	92.68	68.39	81.49	60.31	46.19	44.06	6
10CJ105243+574817		22.92			20.91	19.85	86.32	68.38	83.12	70.87	41.07		6
10CJ105248+595634													5
10CJ105253+572348	23.14	21.98	22.67	21.70	20.63	20.04	49.89	40.01	51.52	48.66	51.81	57.94	2
10CJ105254+592218													5

continued on next page

continued from previous page

10C ID	*g*	*i*	*r*	*z*	*J*	*K*	SERVS1 μJy	SERVS2 μJy	SWIRE1 μJy	SWIRE2 μJy	SWIRE3 μJy	SWIRE4 μJy	flag[a]
10CJ105255+571949		23.25			21.35	19.87	155.01	260.14	150.93	267.84	446.57	643.68	2
10CJ105327+574546		23.40			21.41	20.80	29.49	19.50	28.31	15.57			2
10CJ105337+574242													7
10CJ105341+571951		22.32	23.96	21.78	20.69	19.83	85.41	61.69	76.56	57.85			6
10CJ105342+574438	23.35	21.21	22.26	20.80	19.90	19.19	107.85	71.37	99.56	72.29	66.84	45.27	1
10CJ105345+565400													9
10CJ105353+565949	24.14	21.31	22.52				210.26	128.48	184.58	116.82	108.61	57.73	6
10CJ105400+573324						22.37	10.48	11.75	7.0				6
10CJ105420+580101						21.08	25.46	30.49	24.92	29.72			6
10CJ105425+573700	20.64	19.52	19.81	19.30	18.43	17.79	407.64	480.33	408.28	505.96	696.96	1104.53	2
10CJ105437+565922													4
10CJ105441+571640													3
10CJ105510+574503		22.64	23.17	22.10	20.53	19.69	93.77	68.16	85.7	64.98	43.26		2
10CJ105515+573256													3
10CJ105517+565003													4
10CJ105520+572237					21.39	20.15	96.70	134.44	93.44	138.76	169.92	244.46	6
10CJ105523+565017													4
10CJ105527+571607	22.20	20.16	20.86	19.90	18.91	18.25	190.86	136.30	167.5	121.29	102.93		1
10CJ105535+574636	23.97	23.63	23.74		22.18	21.04	33.48	41.71	32.06	40.03	44.2	59.97	6
10CJ105543+574823	22.85	20.62	21.74	20.33	19.41	18.80	168.82	103.16	149.99	96.13	91.85	39.76	6
10CJ105548+564804		22.57	23.67				102.44	74.97	88.48	69.48	44.2		6
10CJ105548+571828													4
10CJ105550+570407	22.24	20.25	20.95	20.10			170.58	120.56	150.25	106.31	73.9		1
10CJ105555+574828	24.42	22.11		21.39	19.99	19.06	171.90	113.55	154.22	105.53	98.77		6
10CJ105558+565318													3
10CJ105604+570934					21.86	20.64	52.48	44.65	45.26	42.3			6
10CJ105614+565238													9
10CJ105614+570520							98.15	151.60	93.42	152.35	256.92	442.24	2
10CJ105627+574221	21.93	21.84	21.54		21.30	20.75	43.12	57.66	38.13	56.03	88.28	114.76	6
10CJ105641+565753		20.41					200.16	132.63	169.53	120.31	97.78	45.63	6
10CJ105649+565218													3
10CJ105653+580342		21.04	21.97		19.56	18.73	233.12	158.00	169.81	136.17	136.91		6
10CJ105655+572116													9
10CJ105716+572314							9.95	11.53	7.89	10.08			2
10CJ105731+575949					20.26		328.37		251.86	163.11	131.33		6
10CJ105731+580658		21.05	22.20		19.62	18.82	216.45		181.47	133.42	127.38	84.7	6
10CJ105739+564958													5
10CJ105747+580848							15.33		56.85	56.2	58.52	69.17	2

a) Optical matching flag. 1 = extended, probable match; 2 = extended, possible match; 3 = extended, confused; 4 = extended, no match; 5 = not in FUSED area; 6 = compact, match; 7 = compact, no match; 8 = no extended classification but accurate position; 9 = 10C position only.

A.3 Redshift values

Table A.3: Available redshift values for in Sample W with a redshift value available. Redshifts from the Le Phare photometric redshift fitting described in Section 5.4 are given, as well as values from the Rowan-Robinson et al. (2013) and Fotopoulou et al. (2012) catalogues. The 'best' redshift value, used in the analysis, is also listed.

10C ID	Le Phare z	RR13 z	F12 z	Best z^a	z flag^b
10CJ104320+585621	0.35	0.30		0.30	2
10CJ104328+590312	0.48	0.24		0.24	2
10CJ104344+591503	1.71	0.91		0.91	2
10CJ104428+591540	1.28			1.28	4
10CJ104441+591949	1.29	1.30		1.30	2
10CJ104451+591929	0.98	0.96		0.96	2
10CJ104528+591328	3.37	1.79		1.79	2
10CJ104539+585730	0.47	0.38		0.39	1
10CJ104551+590838	2.40	0.75		0.75	2
10CJ104624+590447		1.86		1.86	2
10CJ104630+582748	0.45			0.45	4
10CJ104633+585816	1.45	0.79		0.79	2
10CJ104648+590956	2.31			2.31	4
10CJ104710+582821	1.36	0.59		0.59	2
10CJ104718+585119	0.73	0.64		0.64	2
10CJ104719+582114	1.08			1.08	4
10CJ104733+591244	3.39			3.39	4
10CJ104737+592028	1.04	0.79		0.79	2
10CJ104742+585318	0.88	0.58		0.58	2
10CJ104751+574259	1.93	1.63		1.63	2
10CJ104802+574117	1.34	1.38		1.38	2
10CJ104822+582436	1.36	1.23		1.23	2
10CJ104824+583029	0.92			0.92	4
10CJ104826+584838	0.91	0.96		0.96	2
10CJ104836+591846	0.44	1.94		1.94	2
10CJ104844+582309	0.97	0.86		0.86	2
10CJ104849+571417	0.62	0.61		0.61	2
10CJ104857+584103	0.85	0.68		0.68	2
10CJ104906+571156		0.36		0.36	2

continued on next page

continued from previous page

10C ID	Le Phare z	RR13 z	F12 z	Best z^{a}	z flag^{b}
10CJ104918+582801	0.00			0.00	4
10CJ104927+583830		1.00		1.00	2
10CJ104934+570613	1.01	1.13		1.13	2
10CJ104939+583530	1.54	1.70		1.70	2
10CJ104943+571739	0.92	0.69		0.69	2
10CJ104954+570456	1.02	0.75		0.75	2
10CJ105000+585227	1.22			1.22	4
10CJ105007+572020	1.36	1.22	1.70	1.22	2
10CJ105007+574251	0.83	0.88	0.72	0.88	2
10CJ105020+574048	0.72	0.71	0.72	0.71	2
10CJ105028+574522	0.41			0.41	4
10CJ105034+572922			1.12	1.12	3
10CJ105039+572339	0.80	1.69	0.27	1.44	1
10CJ105039+574200	0.80	0.86	0.74	0.86	2
10CJ105039+585118	0.51	0.44		0.44	2
10CJ105040+573308		0.93		0.93	2
10CJ105042+575233		1.24		1.24	2
10CJ105050+580200	0.92	0.68		0.68	2
10CJ105053+583233	3.42			3.42	4
10CJ105054+580943		2.28		2.28	2
10CJ105104+575415	0.80	0.90		0.90	2
10CJ105107+575752	0.84	0.69		0.69	2
10CJ105115+573552		1.06		1.06	2
10CJ105121+582648	1.56			1.56	4
10CJ105122+570854	3.46		1.13	1.13	3
10CJ105122+584136	1.21	1.68		1.68	2
10CJ105122+584409	4.84	1.79		1.79	2
10CJ105128+570901	0.81	0.52	0.55	0.52	2
10CJ105132+571114	0.52	0.32	0.40	0.32	1
10CJ105136+572944	1.52			1.52	4
10CJ105142+573447	0.92	0.73	0.58	0.73	2
10CJ105142+573557	1.49	1.44	1.73	1.44	2
10CJ105148+573245	2.06	0.93	1.00	0.99	1
10CJ105206+574111	1.49		1.53	0.46	1
10CJ105215+581627	0.91	0.91		0.91	2
10CJ105220+585051	1.34	1.94		1.94	2

continued on next page

continued from previous page

10C ID	Le Phare z	RR13 z	F12 z	Best z^a	z flag^b
10CJ105225+573323	0.83		0.63	0.63	3
10CJ105225+575507	3.00			3.00	4
10CJ105240+572322	1.07		1.11	1.01	1
10CJ105243+574817	1.14	0.67		0.67	2
10CJ105327+574546	0.97		0.82	0.82	3
10CJ105341+571951	1.05		0.91	0.91	3
10CJ105342+574438	0.89	0.83	0.73	0.83	2
10CJ105400+573324	3.57		1.49	1.49	3
10CJ105425+573700	0.04		0.33	0.33	3
10CJ105510+574503	1.19	1.14		1.14	2
10CJ105520+572237	2.52			2.52	4
10CJ105527+571607	0.51			0.51	4
10CJ105535+574636	2.68	2.89		2.89	2
10CJ105550+570407	0.40	0.83		0.83	2
10CJ105604+570934	1.26			1.26	4
10CJ105627+574221	1.04	1.64		1.64	2
10CJ105653+580342	0.95	0.56		0.56	2

a) Final redshift value, description is given in Section 5.4.3.

b) Origin of final redshift value. 1 = spectroscopic (see Table 5.2), 2 = RR13, 3 = F12, 4 = Le Phare.

Appendix B

Confused sources

There are a total of 16 sources without a match to the FUSED catalogue in Sample W, and 14 without a redshift value (the numbers are different because four sources without a match to FUSED have a redshift value from a different redshift catalogue and two of the sources with a FUSED match do not have enough photometric bands to produce a redshift estimate).

The sources without a counterpart in FUSED catalogue fall into two categories; sources which do not have a match because there are no objects in the FUSED catalogue within the match radius (or within the radio contours for an extended source), and sources which are 'confused' because there are several objects within the radio contours. Information about the confused sources is presented in this appendix.

B.1 Comments on individual sources

Contour plots of each of the 10C sources in Sample W classified as confused when matching to the FUSED multi-wavelength catalogue are shown in Figures B.1 and B.2. In some cases circumstantial evidence favours one possible match over others inside the radio contours. Here I briefly discuss each source and its possible counterparts.

10CJ104741+584811

Either of the two sources inside the radio contours could be the correct counterpart for this source.

10CJ104906+571156

Objects 4070 seems the most likely candidate.

10CJ105009+570724

It is possible that this is actually three sources which are blended together in the radio image, in which case the three objects inside the radio contours match to the three blended sources. Another possibility is that this is an FRI-type source, or a head-tail source, and one of the three possible counterparts corresponds to its core.

10CJ105104+574456

This source only has a lower-resolution WSRT contour map available, with a beam size of ≈ 10 arcsec compared to 5 arcsec for the GMRT maps available for the other seven sources. There is no obvious match.

10CJ105139+580757

This appears to be a bent double source, so one would expect the correct counterpart to be at the location of the core of this double. The correct counterpart could therefore be 6709 or 6689, or it could be located somewhere between these two sources and not detected in the FUSED catalogue.

10CJ105237+573058

This appears to be a classic double source, and it seems likely that source 7519 is the correct counterpart.

10CJ105441+571640

This source may in fact be two separate sources which are blended together in the radio images. If this is the case, then the optical counterparts for the two sources are probably 8062 and 8059.

10CJ105515+573256

Either of the two sources inside the radio contours could be the correct match here.

It is therefore only possible to identify a likely counterpart for two of the eight sources classified as confused by using examining the radio images.

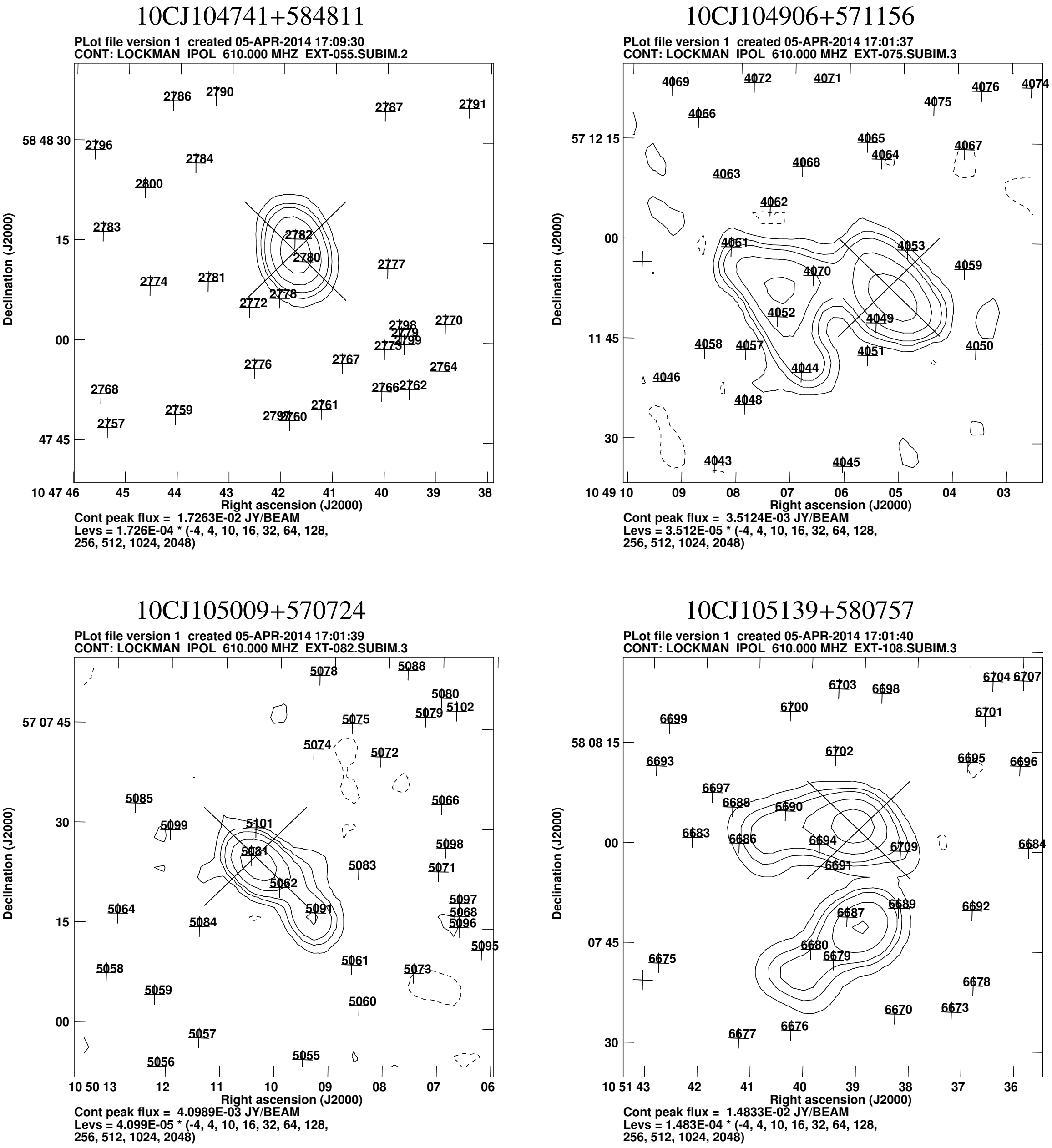

Figure B.1: GMRT contour plots of the sources classified as confused after matching to the FUSED catalogue. The second lowest contour is at one tenth of the peak flux density in the subimages and all FUSED objects within this contour are considered as possible counterparts for the radio source. The big cross represents the radio position used for matching.

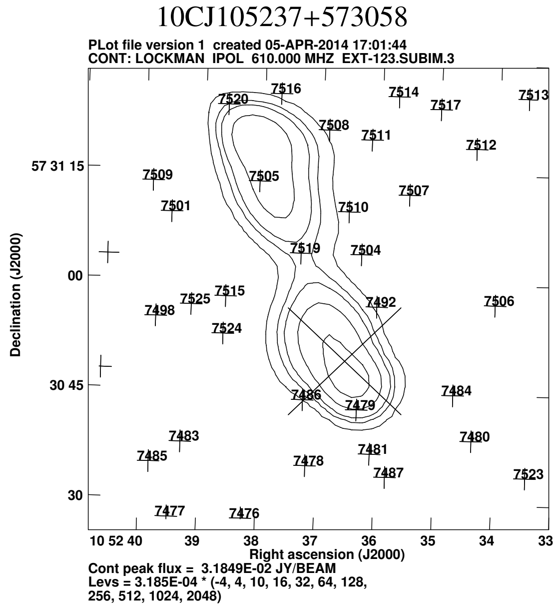

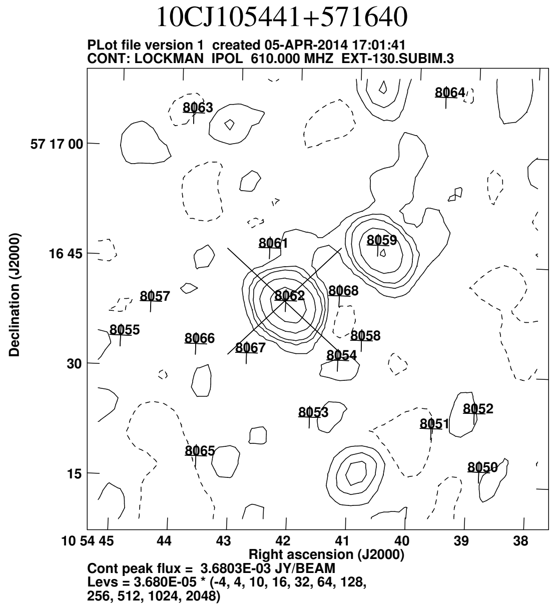

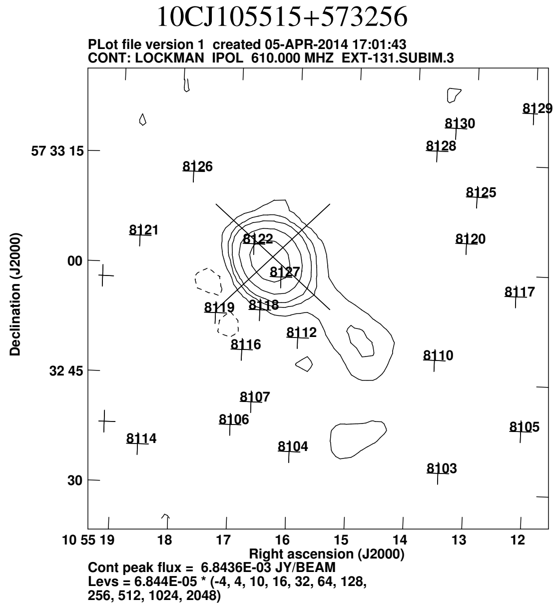

Figure B.1: (cont.) GMRT contour plots of the sources classified as confused after matching to the FUSED catalogue. See previous caption.

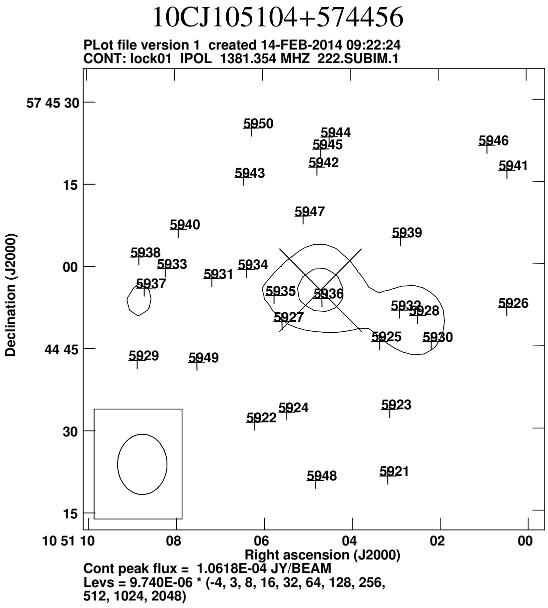

Figure B.2: WSRT contour plots of sources classified as confused after matching to the FUSED catalogue. The lowest contour is at 3σ and all FUSED objects within this contour are considered as possible counterparts for the radio source.

B.2 Properties of possible counterparts for confused sources

All possible counterparts were identified for the eight confused 10C sources, as described in Section 5.4.4, giving a total of 30 possible counterparts. The photometric redshifts for these objects were calculated in Section 5.4.4 and had a similar range to the objects which unambiguously match to of Sample W, with no trend notable. The r-band magnitude distribution for these sources is shown in Figure B.3, and has a similar shape to the magnitude distribution for the objects matched to 10C sources. All of these possible counterparts with two or more IRAC bands available are plotted on a mid-infrared colour–colour diagram in Figure B.4. A large number of the objects have one or more upper limits, making their position on the diagram uncertain. Seven out of 19 objects lie outside the Lacy AGN area, suggesting that if they are associated with the relevant radio galaxy it is a LERG. The remaining 12 sources lie inside the AGN area, but the nature of their upper limits means they could move outside it. These sources occupy a similar area in mid-infrared colour–colour space to the rest of Sample W (shown in Figure 6.4), so there is no evidence from this plot that these confused sources are significantly different to the rest of the population.

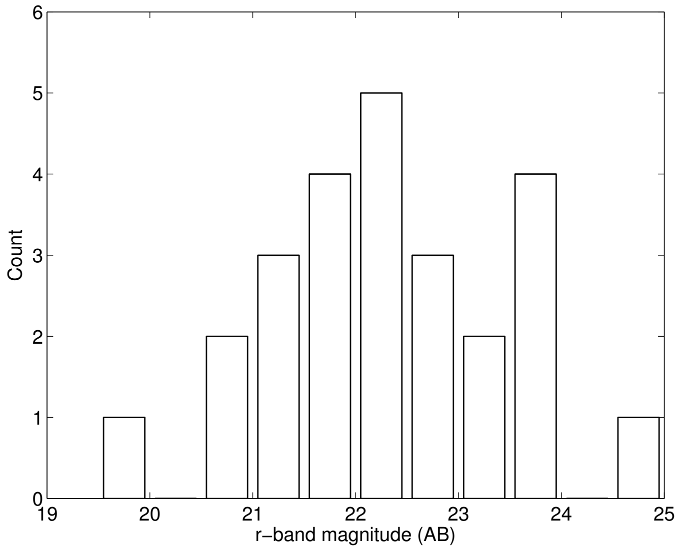

Figure B.3: *r*-band magnitude distribution of all possible counterparts for 10C sources in Sample W classified as confused.

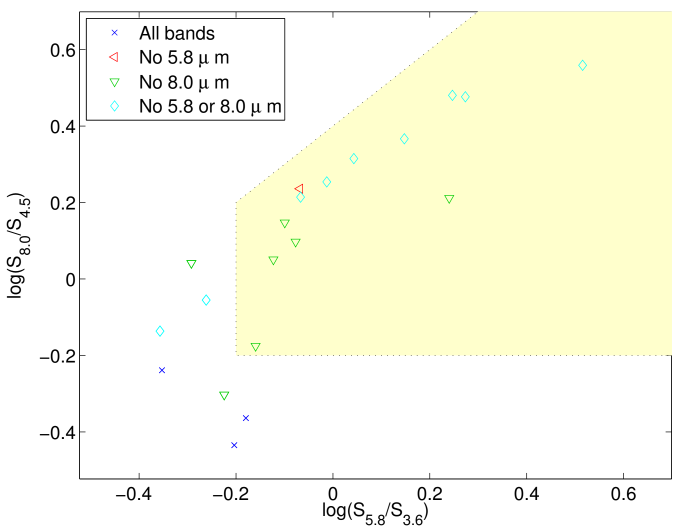

Figure B.4: IRAC colour–colour diagram showing the possible counterparts for the 10C sources classified as confused.

REFERENCES

AMI Consortium: Davies, et al., 2011, MNRAS, 415, 2708

AMI Consortium: Franzen, et al., 2011, MNRAS, 415, 2699

Abdalla F. B., Banerji M., Lahav O., Rashkov V., 2011, MNRAS, 417, 1891

Antonucci R., 1993, ARA&A, 31, 473

Arnouts S., Ilbert O., 2011, *Astrophysics Source Code Library*, record ascl:1108.009

Bertin E., Arnouts S., 1996, A&AS, 117, 393

Best P. N., Kauffmann G., Heckman T. M., Brinchmann J., Charlot S., Ivezić Ž., White S. D. M., 2005, MNRAS, 362, 25

Best P. N., Heckman T. M., 2012, MNRAS, 421, 1569

Biggs A. D., Ivison R. J., 2006, MNRAS, 371, 963

Blundell K. M., Rawlings S., Willott C. J., 1999, AJ, 117, 677

Bolton R. C., et al., 2004, MNRAS, 354, 485

Bolton R. C., Chandler C. J., Cotter G., Pearson T. J., Pooley G. G., Readhead A. C. S., Riley J. M., Waldram E. M., 2006, MNRAS, 370, 1556

Bolzonella M., Miralles J.-M., Pelló R., 2011, *Astrophysics Source Code Library*, record ascl:1108.010

Bonavera L., Massardi M., Bonaldi A., González-Nuevo J., de Zotti G., Ekers R. D., 2011, MNRAS, 416, 559

Bondi M., et al., 2007, A&A, 463, 519

Bonzini M., et al., 2012, ApJS, 203, 15

Bonzini M., Padovani P., Mainieri V., Kellermann K. I., Miller N., Rosati P., Tozzi P., Vattakunnel S., 2013, MNRAS, 436, 3759

Brightman M., Nandra K., 2011, MNRAS, 414, 3084

Brammer G. B., van Dokkum P. G., Coppi P., 2008, ApJ, 686, 1503

Brunner H., Cappelluti N., Hasinger G., Barcons X., Fabian A. C., Mainieri V., Szokoly G., 2008, A&A, 479, 283

Bruzual G., Charlot S., 2003, MNRAS, 344, 1000

Calzetti D., Armus L., Bohlin R. C., Kinney A. L., Koornneef J., Storchi-Bergmann T., 2000,

ApJ, 533, 682
Caputi K. I., 2014, IJMPD, 23, 30015
Carilli C. L., Perley R. A., Dreher J. W., Leahy J. P., 1991, ApJ, 383, 554
Chhetri R., Ekers R. D., Jones P. A., Ricci R., 2013, MNRAS, 434, 956
Ciliegi P., Zamorani G., Hasinger G., Lehmann I., Szokoly G., Wilson G., 2003, A&A, 398, 901
Colla G., Fanti C., Fanti R., Gioia I., Lari C., Lequeux J., Lucas R., Ulrich M. H., 1975, A&AS, 20, 1
Condon J. J., 1980, ApJ, 242, 894
Condon J. J., 1992, ARA&A, 30, 575
Condon J. J., Cotton W. D., Greisen E. W., Yin Q. F., Perley R. A., Taylor G. B., Broderick J. J., 1998, AJ, 115, 1693
Croton D. J., et al., 2006, MNRAS, 365, 11
de Jong T., Klein U., Wielebinski R., Wunderlich E., 1985, A&A, 147, L6
de Zotti G., Ricci R., Mesa D., Silva L., Mazzotta P., Toffolatti L., González-Nuevo J., 2005, A&A, 431, 893
de Zotti G., Massardi M., Negrello M., Wall J., 2010, A&ARv, 18, 1
Donley J. L., et al., 2012, ApJ, 748, 142
Donnelly R. H., Partridge R. B., Windhorst R. A., 1987, ApJ, 321, 94
Dunlop J. S., Peacock J. A., 1990, MNRAS, 247, 19
Eddington A. S., 1913, MNRAS, 73, 359
Evans D. A., Worrall D. M., Hardcastle M. J., Kraft R. P., Birkinshaw M., 2006, ApJ, 642, 96
Fanaroff B. L., Riley J. M., 1974, MNRAS, 167, 31P
Fanti R., Gioia I., Lari C., Ulrich M. H., 1978, A&AS, 34, 341
Feldmann R., et al., 2006, MNRAS, 372, 565
Feigelson E. D., Nelson P. I., 1985, ApJ, 293, 192
Fomalont E. B., Kellermann K. I., Cowie L. L., Capak P., Barger A. J., Partridge R. B., Windhorst R. A., Richards E. A., 2006, ApJS, 167, 103
Fotopoulou S., et al., 2012, ApJS, 198, 1
Franzen T. M. O., et al., 2009, MNRAS, 400, 995
Garn T., Green D. A., Riley J. M., Alexander P., 2008, MNRAS, 387, 1037
Garn T. S., Green D. A., Riley J. M., Alexander P., 2010, BASI, 38, 103
Gendre M. A., Wall J. V., 2008, MNRAS, 390, 819
González-Solares E. A., et al., 2011, MNRAS, 416, 927
Gruppioni C., Zamorani G., de Ruiter H. R., Parma P., Mignoli M., Lari C., 1997, MNRAS, 286, 470

Guglielmino G., Prandoni I., Morganti R., Heald G., 2012, in *Resolving The Sky - Radio Interferometry: Past, Present and Future*, available online at http://pos.sissa.it/cgi-bin/reader/conf.cgi?confid=163, id.22

Hambly N. C., et al., 2001, MNRAS, 326, 1279

Hardcastle M. J., Evans D. A., Croston J. H., 2006, MNRAS, 370, 1893

Hardcastle M. J., Evans D. A., Croston J. H., 2007, MNRAS, 376, 1849

Harwit M., Pacini F., 1975, ApJ, 200, L127

Helou G., Soifer B. T., Rowan-Robinson M., 1985, ApJ, 298, L7

Heywood I., Jarvis M. J., Condon J. J., 2013, MNRAS, 432, 2625

Hine R. G., Longair M. S., 1979, MNRAS, 188, 111

Hopkins A. M., Mobasher B., Cram L., Rowan-Robinson M., 1998, MNRAS, 296, 839

Hopkins P. F., Hernquist L., Cox T. J., Di Matteo T., Robertson B., Springel V., 2006, ApJS, 163, 1

Ibar E., et al., 2008, MNRAS, 386, 953

Ibar E., Ivison R. J., Biggs A. D., Lal D. V., Best P. N., Green D. A., 2009, MNRAS, 397, 281

Ilbert O., et al., 2009, ApJ, 690, 1236

Ishisaki Y., Ueda Y., Yamashita A., Ohashi T., Lehmann I., Hasinger G., 2001, PASJ, 53, 445

Isobe T., Feigelson E. D., Nelson P. I., 1986, ApJ, 306, 490

Jackson C. A., Wall J. V., 1999, MNRAS, 304, 160

Jarvis M. J., Rawlings S., 2004, NewAR, 48, 1173

Jeffreys H., 1938, MNRAS, 98, 190

Katgert P., Katgert-Merkelijn J. K., Le Poole R. S., van der Laan H., 1973, A&A, 23, 171

Kellermann K. I., 1966, ApJ, 146, 621

Kennicutt R. C., Evans N. J., 2012, ARA&A, 50, 531

Lacy M., et al., 2004, ApJS, 154, 166

Lacy M., Petric A. O., Sajina A., Canalizo G., Storrie-Lombardi L. J., Armus L., Fadda D., Marleau F. R., 2007, AJ, 133, 186

Lacy M., et al., 2013, ApJS, 208, 24

Laing R. A., Riley J. M., Longair M. S., 1983, MNRAS, 204, 151

Lawrence A., et al., 2007, MNRAS, 379, 1599

Lehmann I., et al., 2001, A&A, 371, 833

Leipski C., Falcke H., Bennert N., Hüttemeister S., 2006, A&A, 455, 161

Lockman F. J., Jahoda K., McCammon D., 1986, ApJ, 302, 432

Lonsdale C. J., et al., 2003, PASP, 115, 897

Machalski J., Condon J. J., 1999, ApJS, 123, 41

Mahony E. K., et al., 2011, MNRAS, 417, 2651

Mainieri V., et al., 2008, ApJS, 179, 95

Mao M. Y., et al., 2012, MNRAS, 426, 3334

Marleau F. R., Fadda D., Appleton P. N., Noriega-Crespo A., Im M., Clancy D., 2007, ApJ, 663, 218

Massardi M., et al., 2008, MNRAS, 384, 775

Massardi M., Bonaldi A., Negrello M., Ricciardi S., Raccanelli A., de Zotti G., 2010, MNRAS, 404, 532

Massardi M., et al., 2011a, MNRAS, 412, 318

Massardi M., Bonaldi A., Bonavera L., López-Caniego M., de Zotti G., Ekers R. D., 2011b, MNRAS, 415, 1597

Mauduit J.-C., et al., 2012, PASP, 124, 714

McLure R. J., Kukula M. J., Dunlop J. S., Baum S. A., O'Dea C. P., Hughes D. H., 1999, MNRAS, 308, 377

Middelberg E., et al., 2008, AJ, 135, 1276

Middelberg E., et al., 2013, A&A, 551, A97

Mignano A., Prandoni I., Gregorini L., Parma P., de Ruiter H. R., Wieringa M. H., Vettolani G., Ekers R. D., 2008, A&A, 477, 459

Miller P., Rawlings S., Saunders R., 1993, MNRAS, 263, 425

Murphy E. J., 2009, ApJ, 706, 482

Murphy E. J., Stierwalt S., Armus L., Condon J. J., Evans A. S., 2013, ApJ, 768, 2

Muxlow T. W. B., et al., 2005, MNRAS, 358, 1159

Norris R. P., et al., 2006, AJ, 132, 2409

Norris R. P., et al., 2013, PASA, 30, 20

O'Dea C. P., 1998, PASP, 110, 493

Ogle P., Whysong D., Antonucci R., 2006, ApJ, 647, 161

Owen F. N., Morrison G. E., 2008, AJ, 136, 1889

Owen F. N., Morrison G. E., Klimek M. D., Greisen E. W., 2009, AJ, 137, 4846

Padovani P., Mainieri V., Tozzi P., Kellermann K. I., Fomalont E. B., Miller N., Rosati P., Shaver P., 2009, ApJ, 694, 235

Padovani P., Miller N., Kellermann K. I., Mainieri V., Rosati P., Tozzi P., 2011, ApJ, 740, 20

Padovani P., Bonzini M., Miller N., Kellermann K. I., Mainieri V., Rosati P., Tozzi P., Vattakunnel S., 2014 in *Multiwavelength AGN surveys and studies*, IAU Symposium 304, in press (arXiv:1401.1342)

Penzias A. A., Wilson R. W., 1965, ApJ, 142, 419

Planck Collaboration, et al., 2011, A&A, 536, A13

Polletta M., et al., 2007, ApJ, 663, 81

Prandoni I., Gregorini L., Parma P., de Ruiter H. R., Vettolani G., Wieringa M. H., Ekers R. D., 2001, A&A, 365, 392

Prandoni I., Parma P., Wieringa M. H., de Ruiter H. R., Gregorini L., Mignano A., Vettolani G., Ekers R. D., 2006, A&A, 457, 517

Prandoni I., de Ruiter H. R., Ricci R., Parma P., Gregorini L., Ekers R. D., 2010a, A&A, 510, A42

Prandoni I., 2010b, *Proceedings of the ISKAF2010 Science Meeting. June 10 -14 2010. Assen, the Netherlands*. Published online at http://pos.sissa.it/cgi-bin/reader/conf.cgi?confid=112, p.47

Prevot M. L., Lequeux J., Prevot L., Maurice E., Rocca-Volmerange B., 1984, A&A, 132, 389

Price R., Duric N., 1992, ApJ, 401, 81

Rengelink R. B., Tang Y., de Bruyn A. G., Miley G. K., Bremer M. N., Roettgering H. J. A., Bremer M. A. R., 1997, A&AS, 124, 259

Rickard L. J., Harvey P. M., 1984, AJ, 89, 1520

Rowan-Robinson M., et al., 2008, MNRAS, 386, 697

Rowan-Robinson M., Gonzalez-Solares E., Vaccari M., Marchetti L., 2013, MNRAS, 428, 1958

Roy A. L., Norris R. P., Kesteven M. J., Troup E. R., Reynolds J. E., 1998, MNRAS, 301, 1019

Ryle M., Clarke R. W., 1961, MNRAS, 122, 349

Sadler E. M., et al., 2006, MNRAS, 371, 898

Sajina A., Lacy M., Scott D., 2005, ApJ, 621, 256

Salvato M., et al., 2009, ApJ, 690, 1250

Salvato M., et al., 2011, ApJ, 742, 61

Seymour N., et al., 2008, MNRAS, 386, 1695

Simpson C., et al., 2006, MNRAS, 372, 741

Smolčić V., et al., 2008, ApJS, 177, 14

Sopp H. M., Alexander P., 1991, MNRAS, 251, 14P

Steidel C. C., Sargent W. L. W., 1991, ApJ, 382, 433

Stott J. P., Sobral D., Smail I., Bower R., Best P. N., Geach J. E., 2013, MNRAS, 430, 1158

Toffolatti L., Argueso Gomez F., de Zotti G., Mazzei P., Franceschini A., Danese L., Burigana C., 1998, MNRAS, 297, 117

Tozzi P., et al., 2009, ApJ, 698, 740

Tucci M., Toffolatti L., de Zotti G., Martínez-González E., 2011, A&A, 533, A57

Urry C. M., Padovani P., 1995, PASP, 107, 803

Vattakunnel S., et al., 2012, MNRAS, 420, 2190

Vieira J. D., et al., 2010, ApJ, 719, 763

Waldram E. M., Pooley G. G., Grainge K. J. B., Jones M. E., Saunders R. D. E., Scott P. F., Taylor A. C., 2003, MNRAS, 342, 915

Waldram E. M., Pooley G. G., Davies M. L., Grainge K. J. B., Scott P. F., 2010, MNRAS, 404, 1005

White R. L., Becker R. H., Helfand D. J., Gregg M. D., 1997, ApJ, 475, 479

White R. L., Helfand D. J., Becker R. H., Glikman E., de Vries W., 2007, ApJ, 654, 99

Whittam I. H., et al., 2013, MNRAS, 429, 2080

Whittam I. H., Riley J. M., Green D. A., 2014, MNRAS, 440, 40

Whysong D., Antonucci R., 2004, ApJ, 602, 116

Wilkes B. J., et al., 2009, ApJS, 185, 433

Wilman R. J., et al., 2008, MNRAS, 388, 1335

Wilman R. J., Jarvis M. J., Mauch T., Rawlings S., Hickey S., 2010, MNRAS, 405, 447

Wilson A. S., Colbert E. J. M., 1995, ApJ, 438, 62

Windhorst R. A., Miley G. K., Owen F. N., Kron R. G., Koo D. C., 1985, ApJ, 289, 494

Windhorst R. A., Fomalont E. B., Partridge R. B., Lowenthal J. D., 1993, ApJ, 405, 498

Wright E. L., et al., 2010, AJ, 140, 1868

Wunderlich E., Klein U., 1988, A&A, 206, 47

Zinn P.-C., Middelberg E., Norris R. P., Hales C. A., Mao M. Y., Randall K. E., 2012, A&A, 544, A38

Zwart J. T. L., et al., 2008, MNRAS, 391, 1545